THE UNIVERSITY *of* EDINBURGH

Advances in Liquid Electrodes for Spent Fuel Reprocessing in the Nuclear Industry

Andrew Relf

THE UNIVERSITY *of* EDINBURGH

A thesis presented for the degree of

Doctor of Philosophy

The University of Edinburgh

2016

Abstract

For several decades, nuclear power has been of interest as an energy source. Advantages include reliability and zero carbon emissions, however there are disadvantages in waste management and the risk of proliferation. Current research aims to address these by developing proliferation resistant methods to reprocesses the spent fuel and close the fuel cycle.

Whilst aqueous liquid-extraction reprocessing techniques are in use, these are confined to specific fuel types and produce significant additional low-level radioactive waste. Separation of spent fuel in molten salts has been proposed as an alternative to such aqueous methods. These systems include using liquid metals as electrodes at which selective metal deposition takes place. There are several technical and materials hurdles to overcome, these include: characterisation and optimisation of the processes taking place at the liquid electrode/ molten salt interface; and the development of the necessary on-line analysis techniques for process monitoring.

This thesis takes a step-by-step approach to: characterise the behaviour of liquid metal electrodes; explore how molten salts interact with materials to inform the development of microelectrodes for on-line monitoring, and; develop methods to prepare molten salts for rigorous study.

First the fundamental response of liquid cathodes is demonstrated through comparative studies in aqueous systems. By comparing electrochemical studies of mercury cathodes at ambient temperatures and liquid cathodes in molten salts, characteristic responses for deposition, alloying and dendritic growth are observed. In ambient conditions, the bounded Cottrell equation is applied to a liquid cathode for, what is believed to be, the first time to explain alloy formation in the upper layers of a liquid cathode.

The contact angles of lithium chloride - potassium chloride eutectic (LKE) on materials used in microelectrode fabrication have been measured. These wettability measurements confirm silicon nitride and tungsten as suitable materials in design and fabrication of microelectrodes for online process monitoring.

Ensuring the correct speciation is studied in the molten salt is of significant importance in developing a pyroprocessing system. Characterisation must be performed in a high purity, rigorously dry molten salt, and a new method for removing water from lithium chloride-potassium chloride eutectic melt (LKE) has been developed.

Declaration

This thesis has not previously been submitted, in whole or in part, for a degree of any level at either this or any other university. The work is original, and my own, carried out under the direction of Prof. A. R. Mount, and where this is not the case, credit has been duly given.

Andrew Relf

May 2016

Acknowledgements

I would firstly like to thank my supervisor, Professor Andy Mount at the University of Edinburgh and Dr Robert Lewin and Dr Mike Harrison at NNL Ltd for all their guidance and support. Without them I would not have been able to undertake this work or have been able to complete this work.

I would also like to pay a special thanks to Dr Damion Corrigan, without whom I would not have completed this thesis and has proved to be a great teacher, co-worker, and friend. His help and advice in developing electrochemical procedures and understanding analysis methods has been essential in times of difficulty.

I would also like to thank Dr Charlotte Brady, Dr Helena Woodvine, Dr Yifan Li, Dr Jon Terry and Professor Anthony Walton for their assistance, instruction and related discussions.

To everyone else at the University of Edinburgh and NNL with whom I have interacted over the past 4 years and also to NNL and the ESPRC for funding this project.

For all the emotional support I'd like to thank my family and friends.

Finally, and foremost, I would like to give unreserved thanks and apologies to my wife, Dr Kerry Relf, who has stood with me all these years. Without whom I would have given up a long time ago and would surely be lost. I will never be able to sufficiently express my gratitude for the drive and determination she has instilled in me to keep going.

Common Abbreviations

CV Cyclic Voltammogram

SCE Saturated Calomel Electrode

WE Working Electrode

CE Counter Electrode

LKE Lithium Chloride: Potassium Chloride Eutectic

Constants

F Faraday (96485 C mol^{-1})

R Gas Constant (8.3144 J K^{-1} mol^{-1})

Symbols

E Potential

i Current

A Area

P Power

V Voltage

R Resistance

Equations

$$P = V \times i = R \times i^2 = \frac{V^2}{R}$$

$$R = \frac{V}{i} = \frac{V^2}{P} = \frac{P}{i^2}$$

$$V = R \times i = \frac{P}{i} = (PR)^{1/2}$$

$$i = \frac{V}{R} = \frac{P}{V} = \left(\frac{P}{R}\right)^{1/2}$$

Contents

Abstract ... **ii**

Declaration ... **iii**

Acknowledgements ... **iv**

Common Abbreviations ... **v**

Constants ... **v**

Symbols ... **v**

Equations ... **v**

Contents ... **vi**

1 Introduction ... **1**

1.1 Nuclear Energy ... 1

1.2 Fuel Cycle ... 3

1.2.1 Uranium Extraction ... 4

1.2.2 Uranium Enrichment ... 4

1.2.3 Fuel Fabrication ... 5

1.2.4 Fuel Performance ... 7

1.2.5 Nuclear Materials ... 9

1.2.6 Fuel Reprocessing ... 10

1.2.7 Nuclear Waste: Classification, Storage and Disposal ... 13

1.3 Molten Salts ... 17

1.4 Liquid electrodes ... 18

1.5 Reprocessing in Molten Salts ... 19

1.6 Aims of this Work ... 24

1.7 References ... 25

2 Theory ... **28**

2.1 Electrochemistry ... 28

2.1.1 The Three-Electrode System ... 28

2.1.2 Microelectrodes ... 32

2.1.3 Liquid Electrodes ... 34

2.2 Electrochemical Methods ... 35

2.2.1 Cyclic Voltammetry ... 35

2.2.2 Chronoamperometry and Potentiometry 39
2.2.3 Electrochemical Impedance Spectroscopy 41
2.3 Contact Angles 44
2.3.1 Contact angle and Surface tension 45
2.3.2 Contact angle Hysteresis 47
2.3.3 Contact Angle Measurement 49
2.4 References 50

3 Experimental 52
3.1 Electrochemical Experiments 52
3.1.1 Aqueous Experiments 52
3.1.2 Liquid electrodes 53
3.1.3 Molten Salts Experiments 55
3.2 Contact Angle Experiments 57
3.2.1 Substrate Preparation 57
3.2.2 Lithium-Potassium Chloride Eutectic Preparation 61
3.2.3 General Contact Angle Measurement Method 61
3.2.4 Contact Angle Data Analysis 65
3.3 References 66

4 Aqueous Analogues for Detection of Dendritic Growth 67
4.1 Introduction 67
4.2 Electrochemistry of Zinc (II) at a Mercury Pool Cathode 68
4.2.1 Zinc Deposition on a Macro Liquid Metal Electrode 70
4.2.2 EIS of Zinc Deposition on a Macro Liquid Metal Electrode 74
4.3 Electrochemistry of Copper (II) at a Mercury Pool Cathode 76
4.3.1 Copper Deposition on a Macro Liquid Metal Electrode 78
4.3.2 EIS of Copper Deposition on a Macro Liquid Metal Electrode 82
4.4 Detection of Dendritic Growth at Mercury Microelectrodes 85
4.5 Amalgamation of Zinc at a Mercury Microelectrode 86
4.6 Copper Dendrite Detection at a Mercury Film Cathode 92
4.7 Conclusions and Further Work 98
4.8 References 100

5 Contact Angles of LKE on Surfaces of Interest 102
5.1 Introduction 102
5.2 Method Substantiation 102
5.2.1 Accuracy 103

5.3 Wettability of Selected Metal Surfaces 107
5.4 Wettability of Silicon-Based Surfaces by LKE 111
5.4.1 Wettability of Unpolished Silicon Surfaces by LKE 111
5.4.2 Wettability of Polished Silicon Surfaces by LKE 113
5.5 Liquid Metal Contact Angles 116
5.6 Conclusions 117
5.7 References 118

6 Developing an Electrochemical Method for Dry Molten Salt Preparation 119
6.1 The need for dry molten salt 119
6.2 Current Drying methods 119
6.3 The Concept 122
6.3.1 Electrochemical Drying by Cyclic Voltammetry 122
6.3.2 Electrochemical Drying by Alternating Potential Pulsing 125
6.4 Redox Studies in Electrochemically Dried Molten Salt 135
6.5 In-situ drying of LKE containing a redox agent 139
6.6 Conclusions 145
6.7 References 146

7 Detection of Dendritic Growth at Liquid Metal Cathodes in a Molten Salt 148
7.1 Introduction 148
7.2 Stability of a Bismuth Liquid Pool at the Bi-LKE Interface 148
7.3 Deposition of Lanthanum at a Liquid Bismuth Cathode 153
7.4 Growth of Iron Dendrites at a Liquid Cathode in LKE 162
7.5 Conclusions and Further Work 173
7.6 References 174

8 Conclusions and Further Work 176

1 Introduction

Whilst it has been internationally recognised that nuclear energy is a vital low carbon energy source for the future, having stimulated much interest and investment, it is not without significant technical challenges. In order for atomic energy to be more widely adopted and accepted, improvements in proliferation resistance, waste management including reprocessing and economic and generation efficiencies must be investigated.

1.1 Nuclear Energy

Nuclear energy is the use of nuclear reactors to generate electricity by harnessing the thermal energy released during fission reactions. This thermal energy is used to heat water or steam, which then drives conventional turbines. Nuclear energy is experiencing renewed interest as a carbon-free source of reliable electricity generation.

Fission is the process in which the nucleus of an atom splits into lighter nuclei, releasing energy and often producing free neutrons and/ or photons in the process. Nuclear fission was first discovered by Otto Hahn[1] whilst bombarding uranium atoms with neutrons[2]. These reactions formed transuranic elements as the product in an exothermic reaction, releasing large quanta of energy as both heat and electromagnetic radiation. When reacting with a neutron the nucleus of the atom would become unstable, and split into lighter nuclei. The sum of the mass of these product atoms are less than the mass of the original atom, with the loss of mass equating to the energy released in the process[3].

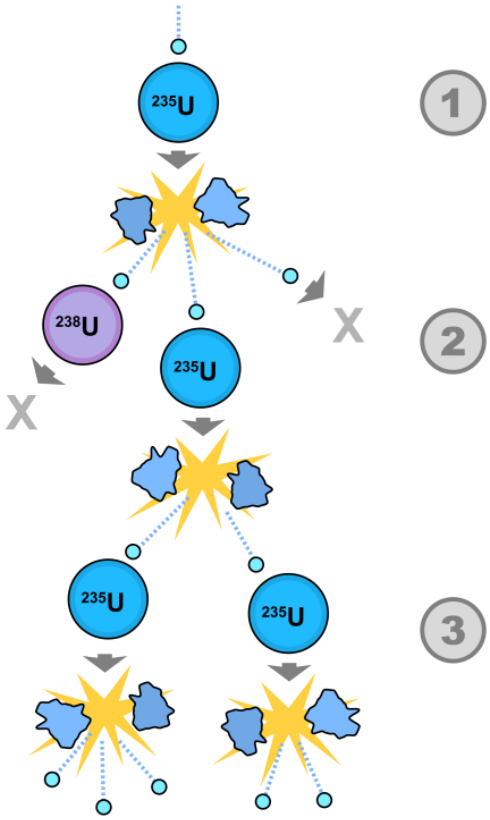

Figure 1.1: A schematic showing a simplified chain reaction that takes place during nuclear fission.

Fission can occur naturally in spontaneous radioactive decay of isotopes, particularly those with very high mass numbers, however in nuclear energy the reaction is induced by a neutron. To maintain these reactions in a nuclear reaction, a chain reaction in which neutrons are also the product of the fission must take place Figure 1.1. The composition of the products of a single nuclear reaction are unpredictable, however a limited series of decay paths are followed such that some elements are prevalent over others. In nuclear reactors self-sustaining reactions are maintained so that the energy is released at a controlled rate.

1.2 Fuel Cycle

The nuclear fuel cycle encompasses the entire life cycle of fuel used in nuclear reactors and the processes which fuel undergoes at each stage. Some of the key stages in the fuel cycle are mapped out in Figure 1.2, showing the order in which they take place. The coloured arrowed represents that the reprocessing of spent fuel to re-use fissile material is an optional step that depends on a country's individual policy. Enhanced reprocessing techniques could lead to closing the fuel cycle, increasing the energy that is extracted from fissile material.

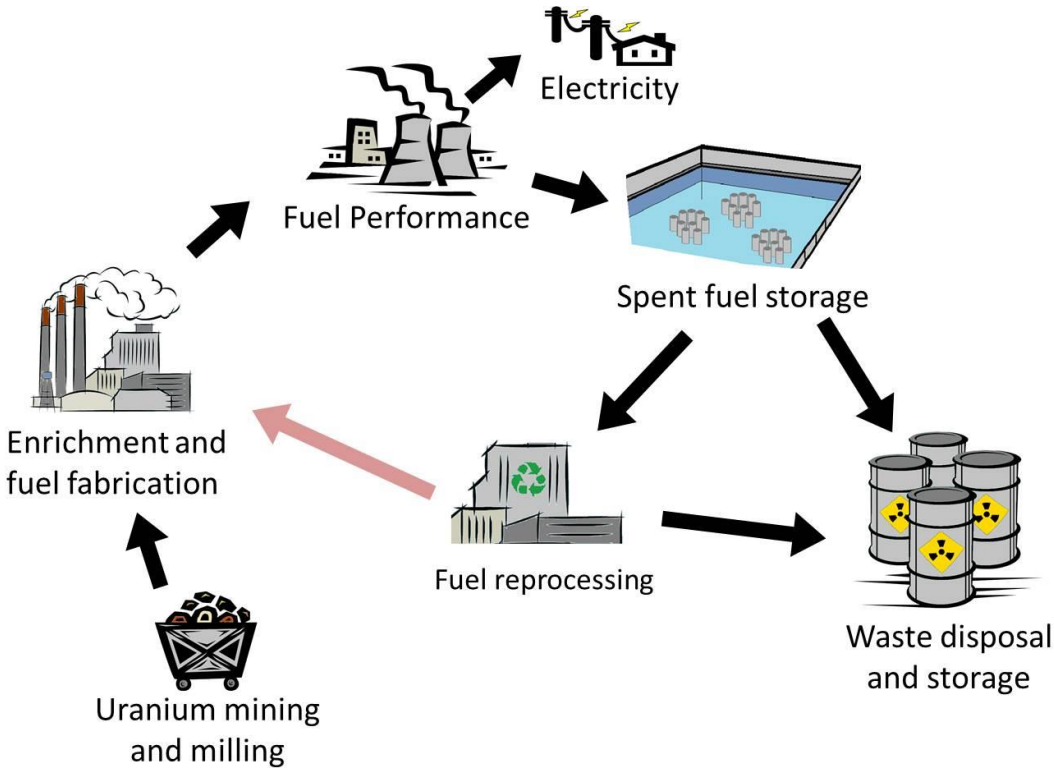

Figure 1.2: The Nuclear Fuel Cycle.

Each of the key stages of uranium enrichment, fuel fabrication, fuel performance, fuel processing and waste disposal and storage, along with materials used in the fuel cycle are discussed in subsequent sections. These sections are intended to provide a general overview,

rather than the specifics for each reactor type, and represent the current industrial processes rather than those in research facilities.

1.2.1 Uranium Extraction

Uranium is a common metal, roughly 500 times more abundant than gold, and about as common as tin. It can be found throughout the world in most soils and rocks, many rivers and in seawater[4]. Almost a third (28%) of the World's most accessible uranium deposits are in Australia, followed by Kazakhstan (16%) and Canada (12%). Large deposits are also found in South Africa (7%), Namibia (6%), Niger (6%), Brazil (6%), Russia (5%), USA (3%), Ukraine (2%), Uzbekistan (2%) and Mongolia (2%). Of these countries, half of the world's supply is produced in Canada (≈28%) and Australia (≈23%).

Uranium ores can be mined from either open pit, or underground mines, and can also be extracted in-situ, being leached directly from the ore. Once mined, the uranium ore is crushed and chemically treated to separate the uranium metal, resulting in a yellow uranium oxide powder, U_3O_8, known as "yellow cake". Conversion to yellow cake increases the uranium concentration to greater than 80%, and provides a stable material for shipping to enrichment facilities.

1.2.2 Uranium Enrichment

Natural uranium ore consists of approximately 99.3% U^{238}, 0.7% U^{235}, and less than 0.01% U^{234} when it is first mined[5]. Only the U^{235} isotope is fissile and the concentration of fissile material in the fuel has a significant influence on the reactor design and the energy output that can be expected from the fuel.

Commercial reactors require a higher concentration of U^{235} than occurs naturally in uranium ore[6]. Once mined, the concentration of U^{235} is increased to between 3% and 5% by isotropic enrichment.

Enrichment can be achieved through one, or combinations of several techniques, however gaseous diffusion and gas centrifuge techniques are the most common. Both of these techniques require the uranium ore to first be converted to uranium hexafluoride (UF_6) gas.

1.2.3 Fuel Fabrication

Aside from the first generation reactors used in the United Kingdom and France that used uranium metal fuel, almost all reactors use uranium oxide fuels. Uranium oxide (UO_2) is a hard ceramic, which was originally developed for use in Light water Reactors (LWRs) that has a high melting point, is resistant to radiation and retains fission products.

UO_2 pellets are clad in zirconium alloy tubes constructed into fuel assemblies, the design of which is dependent on the reactor type and design.

Technical specifications of fuel pellets, such as density, impurity content/composition, porosity and grain size can have a significant influence on performance in the reactor.

Reliability of the fuel is essential to maintain generation capacity and UO_2 has undergone over 40 years of development to achieve high efficiency. In future advanced reactor systems, oxide fuels may be replaced by carbides, nitrides or particulate fuels (or other exotic fuels). However, these will need to demonstrate significant benefits to overcome the dominance of UO_2.

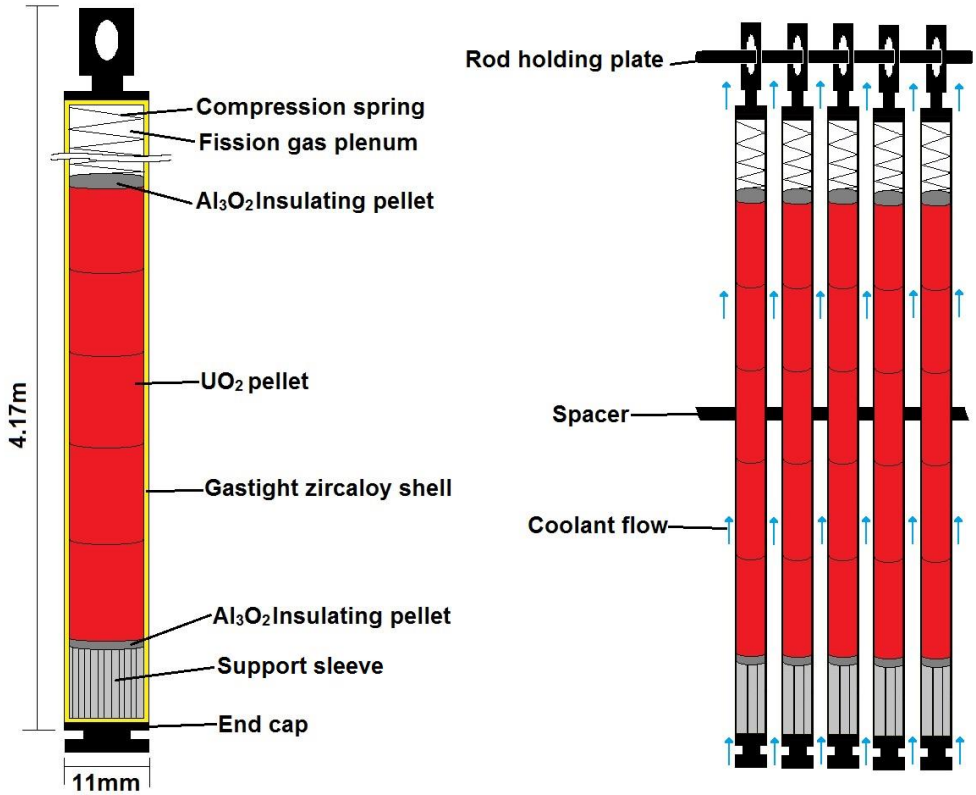

Figure 1.3: Cross-section of a nuclear fuel rod (left). Fuel rod assembly (right).

As fuel needs to reside, intact, in reactor cores for long times (between 4 and 6 years), in-core performance is important. This is governed by a number of conditions and phenomena. Fuel design and operation is regulated to demanding standards to ensure the fuel does not fail. Fuel rods are designed to contain any gaseous fission products, whilst the fuel stack is prevented from moving. This is evident in Figure 1.3, which shows an example cross-section of a fuel rod. A support sleeve, and insulating Al_3O_2 pellet is placed in the bottom of the zircaloy shell, before the fuel pellets are loaded. A further insulating pellet, and a compression spring to hold the fuel in place are added to the fuel rod before the cap is sealed onto the top of the rod. The space around the compression spring acts as a void in which the gaseous products of fission will are retained. Multiple fuel rods are then fixed together in a fuel rod assembly, which will be placed into the reactor core and surrounded by the reactor coolant.

Typically fuel rods are made from zirconium alloys and/or ceramics as failure could lead to the release of fission products, with serious radiological, environmental and safety implications. Severe distortions in fuel rods would also affect safety, as they may no longer move in or out of the reactor as required to control the fission reaction.

Fuel rods need to be resistant to the conditions where chemical oxidation occurs of high pressure (150 atm), high temperature coolant (over 300°C), and high neutron flux (ca $1x10^{18}$ n m^{-2} s^{-1} in Pressurised Water Reactor).

Large radial temperature gradients put a large tensile stress on pellets in circumferential and axial directions. As UO_2 is brittle, stress fractures occur radially and axially. Whilst fuel pellets crack, rod failure is rare, at a rate of approximately 1 in 100,000 fuel rods.

In the reactor, fission takes place and the fuel gets hot as energy is released. As the fuel temperature increases, the fuel expands and cracks, and over time densifies and swells. Extended periods lead to cladding creeping down, and the fuel contacts the cladding, leading to mechanical and chemical interactions between the fuel and the cladding. The cladding oxidises and eventually the fuel temperature changes towards the end of its dwell time.

1.2.4 Fuel Performance

In a nuclear power station, electricity is generated in much the same manner as a conventional coal, gas or oil fired power station, but the heat is generated by the controlled fission reaction rather than by burning fossil fuels. Water is heated to produce high-pressure steam, and, in turn, the steam drives a turbine connected to a generator, which generates electricity. Figure 1.4 shows a simplified diagram of how a nuclear reactor is used to generate steam, driving a turbine to generate electricity. Despite there being many different types of reactor, they almost all use UO_2 fuel, and operate under this principle, mainly varying in the coolant type that is used to transfer heat from the reactor to the steam generator.

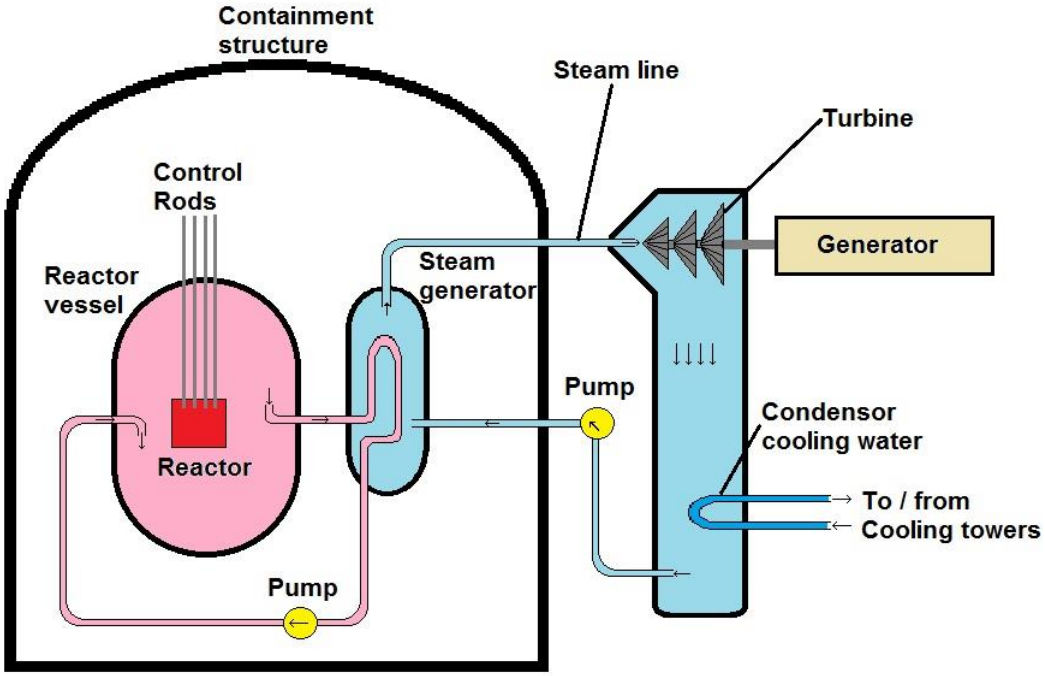

Figure 1.4: Schematic of how a nuclear power station generates electricity.

Fuel resides in the reactor for between 3 and 6 years before it is replaced and transferred to cooling ponds. Approximately every 12 to 18 months, 25% to 30% of the fuel in the reactor is replaced with new fuel in order to maintain a steady reaction rate. This is because after the 3 to 6 year dwell time, the concentration of fissile material in the fuel decreases, and the concentration of neutron absorbing fission products increase, reducing the efficiency of the energy production in the fuel rods.

The spent fuel is still intensely hot, and radioactive due to the natural decay of the fission products and minor actinides, therefore the fuel is initially cooled in storage ponds adjacent to the reactor for 9 to 12 months after the fuel is removed from the reactor. These storage ponds are actively cooled, and the water provides adequate radiation shielding, as well as being an effective coolant. Whilst 50 years of wet storage of fuels has matured the technology, it is relatively high maintenance and tight control of the water's chemistry is required to prevent degradation of the fuel and its cladding.

1.2.5 Nuclear Materials

Materials used in the nuclear fuel cycle have to withstand environments that are unique to the nuclear industry and perform functions that are unique to the fuel cycle. Materials are classified according to reactor duty, fuel cycle processes, waste containment and transport of spent fuels.

Reactor materials have to withstand high temperatures, cyclic loading, corrosive environments, thermal shock, and high neutron and gamma fluxes. Structural materials are typically steels and alloys that have been specially designed to meet these criteria, such as feretic and austenitic steels, inconel and zircaloy.

Fuel processing plants, particularly aqueous reprocessing plants have to be constructed with materials resistant to hot nitric acid. Whilst degradation predominantly arises through chemical oxidation, gamma radiation also enhances the corrosion. Austenitic steel is widely used, however 310L (Nitric Acid Grade) was also developed especially for this task.

It is imperative that waste containers in the nuclear industry are corrosion resistant, have dimensional stability and behave predictably over long time periods (hundreds of years). Any failure in waste containment materials could have serious radiological, environmental and safety consequences. Materials used in waste containment vary depending on the type and classification of waste, which will be discussed in section 1.2.7.

Once fuel has cooled sufficiently at the power station, it is transported to a central facility in specially designed transport flasks. These flasks are filled with water to provide additional cooling and radiation shielding. However, radiolysis can lead to the splitting of water into hydrogen and oxygen. These gasses need to be recombined in the flask in order to prevent an explosion when unloading the flask. Neutron absorbers are added to the water to prevent a criticality event occurring in the water-moderated environment as an uncontrolled criticality event would cause a very high neutron flux, possibly leading to the release of short-lived fission products. As flasks may be transported over large distances, they must be capable of withstanding any conceivable accident; therefore they are drop tested, impact tested and fire tested.

Knowledge of material properties is of fundamental importance to operating a nuclear plant for any part of the nuclear fuel cycle in a safe and economic manner. High fluxes of neutrons

and gamma-rays affect material properties over their service life, so it is crucial that their changes are well understood.

1.2.6 Fuel Reprocessing

Spent fuel management strategies vary depending on each country's political stance, and some countries plan to dispose of intact fuel assemblies in their original form in underground repositories. Other countries rely on some form of spent fuel processing to reduce the volume of waste and/or recycle usable material from spent fuel in an effort to close their fuel cycle.

A closed-loop fuel cycle offers improvements in the energy recovered from fuel, as much of the spent fuel removed from reactors is still fissile, and capable of releasing much more energy. In order to close the fuel cycle, the nuclear industry needs to re-process the spent fuel, to recover uranium and plutonium from the spent fuel, and convert them to solid products, which can be reconverted back into useable fuel. This involves the recovery and purification of uranium and plutonium from fission product wastes. Further discussion on the development of an alternative reprocessing technology will be discussed in section 1.5, but first an overview of the process currently used will be presented.

Reprocessing has taken place since the 1950s, and in the United Kingdom the main reprocessing plants are the original Magnox plant (opened in 1964 to process magnox reactor waste, which cannot be wet stored as it undergoes corrosion in water), and the Thermal Oxide Reprocessing Plant (THORP). Industrially the process of separation is achieved by ambient temperature solvent extraction. The most commonly used solvent extraction process is the Plutonium Uranium Extraction (PUREX) process, which is used internationally following its invention in 1947.

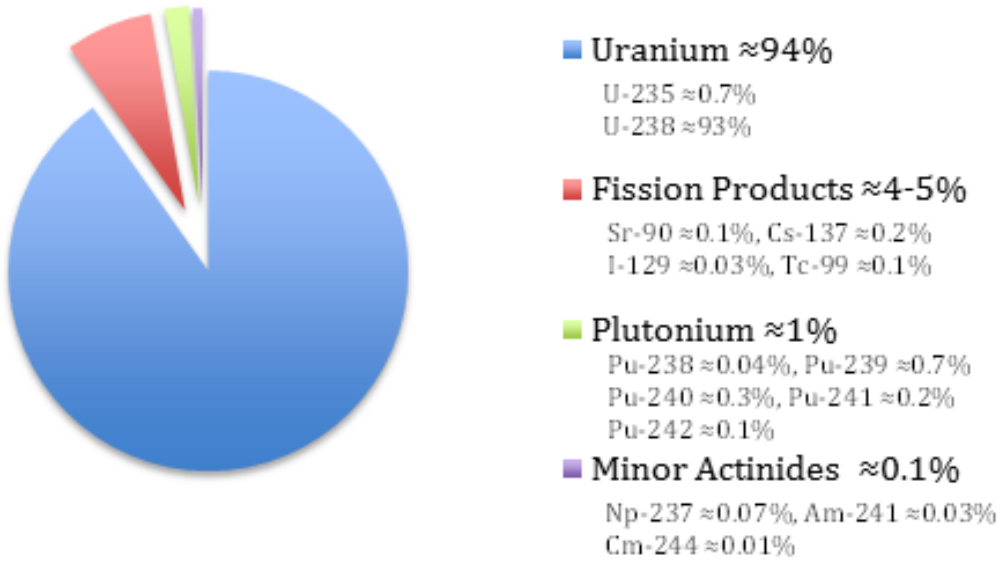

Figure 1.5: Typical constituents of spent fuel[4]

As can be seen in Figure 1.5, spent fuel predominantly consists of the original uranium feedstock. The U-235, and Pu-239 in the spent fuel is fissile, so processing is carried out to conserve resources by recycling these fissile materials. This allows otherwise inaccessible fissile material to be reused so that less ore is required, which is often part of government policy, despite the cost of reprocessing being higher than the cost of uranium ore. In some countries there is a perception that reprocessing increases the likelihood that radioactive materials could be re-directed for use in weapons programmes. Reprocessing is a means of optimising the management of waste, and reduces the volume of highly active waste which would otherwise be placed in a repository, thus reducing the space requirements for a repository, allowing a longer operating life of any single repository.

Reprocessing also allows minor actinides (Np, Am and Cm) to be separated from the spent fuel and there is the possibility that these could be destroyed in a reactor, in a process known as “actinide burning”.

Spent fuel also consists of zirconium, iron and aluminium from the fuel cladding, and iron, nickel and chromium as corrosion products.

The PUREX reprocessing method is industrially established in many countries, and is a complex process for transforming spent fuel into solid oxides suitable for manufacturing into

new fuel. The choice of solvent extraction process is at the heart of reprocessing and dictates the upstream and downstream processes at the tail end of the fuel cycle.

The reprocessing process starts with the fuel assemblies being mechanically sheared from the spent fuel, and then the spent fuel is cut into small fragments which are dissolved in nitric acid. The larger insoluble components from the cladding and assemblies are separated out in a sieve before the finer particles are separated out in a centrifuge. The nitric acid is the aqueous phase for the solvent extraction process and 20-30% tributyl phosphate (TBP) in kerosene is the solvent phase. The PUREX process does not require any further metal salting agents, and high purity separations of U and Pu from the fission products and minor actinides are achievable in 3 solvent extraction cycles.

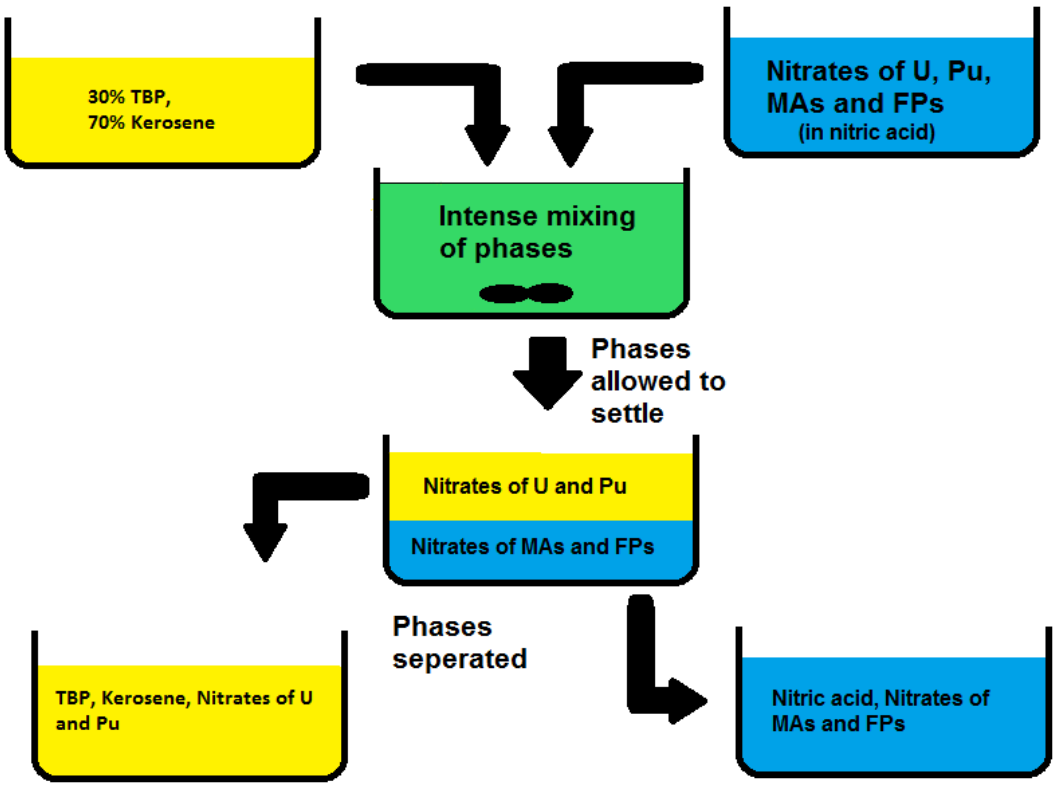

Figure 1.6: Schematic of the solvent extraction stage in the PUREX process, Pu and U are subsequently worked up to their oxide and either stored or returned to the fuel cycle.

Figure 1.6 is a sketch of how when the aqueous and solvent phases are mixed, the nitrates of uranium and plutonium are solubilised preferentially in the solvent phase, whilst the nitrates of the minor actinides (MAs) and fission products (FPs) remain in the aqueous phase.

In the industrial process the PUREX process uses both mixer-settler batteries (where phases are mixed and allowed to separate) and pulsed column (where phases are moved up and down through columns of perforated plates to enhance mixing and settling) methods of extraction.

Once the phases are separated, chemical conditioning is used to separately extract plutonium and uranium from the solvent, before they are converted to stable oxide powders and stored for eventual re-use.

Reprocessing waste experiences difficulties in radiation, radioactivity, solvent degradation and the possibility of criticality events. To avoid these issues remote handling, careful control of the stages and heavy shielding is required. Multistage processes are required to attain the high decontamination factors (10^6 to 10^8), and different streams of subsequent waste treatment are required to dispose of reprocessing waste. Furthermore the liquid nature of the phases represents chemical hazards which would be avoided by keeping the waste in a solid form.

1.2.7 Nuclear Waste: Classification, Storage and Disposal

All nuclear facilities generate wastes of varying degrees of radioactivity. These wastes are classified into three categories according to their radioactivity; high level waste (HLW), intermediate level waste (ILW); and low level waste (LLW). Generally, HLW tend to be in relatively low volumes, whilst there tend to be much larger volumes of LLW.

When compared to other industries, the volume of waste generated from the nuclear fuel cycle and associated activities are small, and despite the hazards, the overall risks are manageable. Current practise is to store the waste in engineered facilities designed to mitigate these risks.

The primary goal of these facilities is to ensure that the radioactive material is immobile and contained to minimise the potential for dispersal. Waste should therefore be kept in a form which is physically and chemically stable, and resistant to significant degradation over the storage period.

In many cases the raw waste will require conditioning to place it in a passively safe form, immobilising the radioactive material. Typical waste forms are gases, liquids, slurries, sludges,

wet solids, powders, particulate material and bulk materials including radioactive materials such as spent fuel. Conditioning processes are usually either encapsulation in cement, or vitrification for liquids and solids.

Waste also presents a technological challenge in storage as long-term exposure of materials (chemical and radiological) in a store or repository could result in alterations in the materials during their service life. Radioactive waste inventory could lead to elevated temperatures, pressures and high levels of radiation. This could give rise to various forms of degradation or corrosion including oxidation resulting in loss of structural integrity through uniform, localised, galvanic, inter-granular, or stress corrosion cracking due to an aqueous environment.

1.2.7.1 High Level Waste

High level waste provides the greatest thermal and radiological challenges in waste management and storage as it predominantly consists of fission product oxides, and wastes from fuel reprocessing. Highly active liquor from historic reprocessing is one of the greatest sources of HLW, and the liquor has to be stored in double-walled tanks, with active heat removal until sufficiently cool to process.

Treatment of HLW involves the waste feed being calcined, where it is heated in air to bring about thermal decomposition and remove volatiles, followed by vitrification in a glass matrix. This glass is cast into stainless steel containers, which are presently stored in air-cooled facilities. The vitrified waste constitutes a more passive form of waste than the original liquor, however the vitrified waste still requires cooling for a further 50 years prior to transfer to a final repository.

The final repository for this waste in the United Kingdom is subject to political and governance decisions, however it is hoped that these will be placed in a deep geological repository, similar to the Onkalo facility which is under construction in Olkiluoto, Finland.

1.2.7.2 Intermediate Level Waste

Intermediate level waste is the most varied waste form, with gas evolution and de-watering issues which are not especially associated with other waste classes. ILW is mainly the remains

of fuel cladding that has been stripped or leached from spent fuel; and materials that have been contaminated with plutonium, such as filters, residues and ion-exchange resins.

ILW comes primarily from processing operations, liquid effluent clean-up, plant and equipment too radioactive to be classed as low level waste, and from development activities in research labs. Large levels of ILW are expected to arise from the decommissioning of nuclear facilities as they are closed.

During the 1950s, 1960s and 1970s, ILW was stored in raw, bulk forms to avoid the foreclosure of options for conditioning and disposal of materials. During the 1980s and 1990s, it was agreed that waste should be immobilised and encapsulated. Design and construction of waste treatment and product storage facilities were implemented, and the treatment of all ILW from commercial operations began.

The majority of the ILW is super-compacted into 500 litre stainless steel drums and is encapsulated directly into a solid matrix, typically cement, although polymer resins are also used for some ion-exchange materials. Not all ILW is encapsulated, with some steel and graphite from the Advanced Gas-cooled Reactors (AGRs) untreated.

In the United Kingdom there is no final repository for intermediate level waste, and it is presently stored in temporary facilities. The long term disposal concept is for the existing steel and concrete boxes to be stored in an underground vault for geological isolation by backfilling the vault.

1.2.7.3 Low Level Waste

Low level waste by far occupies the greatest volume of waste to be treated and disposed of. LLW is made up of discarded equipment, tools, clothing, waste paper from controlled areas, and any other waste arising from controlled areas which could be exposed to contamination. It predominantly consists of miscellaneous structural and packaging materials such as steel, wood, PVC, polythene and fabrics.

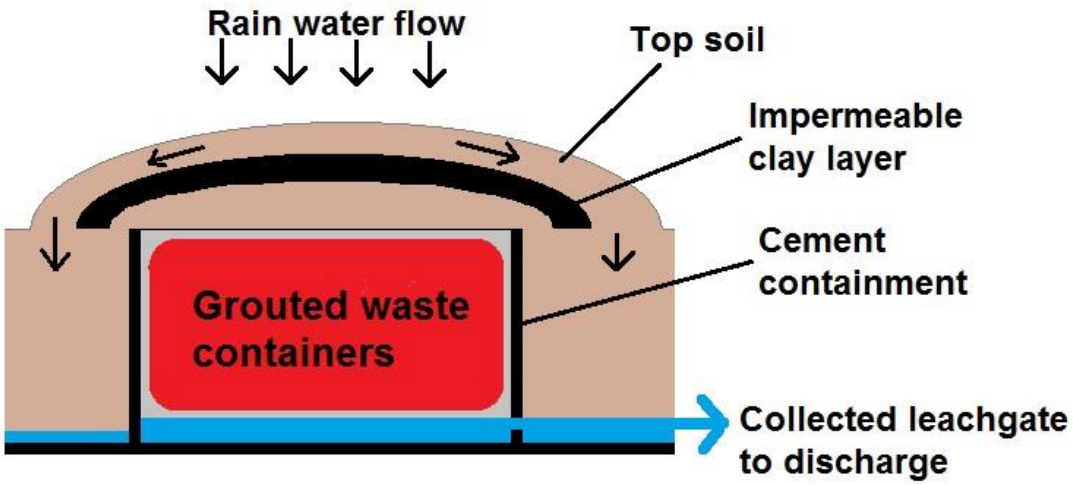

Figure 1.7: Schematic of low level waste repository.

Waste is compacted into an ISO (14000 series) waste container, which is back filled with cement and deposited in a concrete lined trench. In the United Kingdom, the LLW repository is in Drigg, to the south of the Sellafield site in Cumbria, and waste is buried as shown in Figure 1.7.

1.2.7.4 Waste Legacy and Future Prospects

In the United Kingdom, Waste management is complicated by the historic waste legacy, with many different forms of waste having been generated by decades of research activities. There are numerous waste treatment and storage plants, and regardless of whether or not new nuclear reactors are built in the United Kingdom, waste storage and disposal will always be required.

In recent years considerable progress has been made towards the goal of conditioning legacy waste for disposal, however there remains great societal concerns over security and proliferation of spent fuel waste arising from the chequered history of the nuclear weapons program.

1.3 Molten Salts

Molten salts have proven to be suitable media for the extraction and processing of metals, as well as in related materials technologies[7-12]. Molten salts provide a liquid medium with a wide potential window under anhydrous conditions, which allows the preparation and study of highly reactive species that would not otherwise be accessible under aqueous conditions where oxides form spontaneously.

Molten salts are inorganic salts that are heated above their melting point to form an electrically conducting liquid. The ionic nature of the liquid allows the molten salt to act as a solvent which can stabilise any dissolved metal ion species. These inorganic salts can either be used in isolation, or in a combination to form a lower melting point composition. Salts mixed in a ratio which produce the lowest melting point is known as the eutectic molten salts. The most common molten salts are alkali chloride such as lithium chloride, potassium chloride and sodium chloride[12], or ternary mixtures of alkali halides[13]. Fluoride salts are also widely used, however are less common than chloride salts owing to higher melting points and being highly corrosive [14].

Whilst molten salts have been of interest in electrochemistry for several decades, the measurement of fundamental physical properties is complicated by the requirement for high temperatures and rigorous exclusion of impurities. These fundamental measurements are essential for understanding the kinetics of chemical reactions in molten salts, and reliability of measurements are increasing with improving technology. Some physical properties such as melting points, densities[15] and viscosities[16] have been routinely measured, however simulations[17] are still used to overcome the practical complexities.

In this thesis a new method for electrochemically removing hydroxide and oxide contaminants has been developed, so that salts can be rigorously purified in an inert atmosphere, and can be recovered should contamination take place whilst in use.

Whilst the redox chemistry of rare earth metals (lanthanides and actinides) have been studied in molten salts as analogues for radioactive elements[18], separation and purification of these in molten salts is important for recovery from their ores. Electroplating of rare earth metals from

their most stable oxidation to metal has been widely studied using solid macro electrodes such as tungsten, graphite and glassy carbon, which are chemically stable to molten salt[19-23].

Since molten salts can be highly corrosive, and are operated at high temperatures, it is important that compatible materials are used. In this work the wetting of molten salts on selected metal and non-metal surface is investigated to aid the selection of compatible materials and inform future designs of molten salt processing systems.

1.4 Liquid electrodes

The use of liquid metal electrodes is not a new concept. Mercury, with a liquid range from -39°C to 375°C has long been used as an electrode material for electrochemical experiments. Indeed, at ambient temperatures the use of mercury as a liquid metal electrode in the form of a Dropping Mercury Electrode (DME), or a Static Drop Mercury Electrode (SDME) is considered its own field, known as polarography[24, 25]. Polarography has become a generic term for voltammetry at a DME, however the original form, DC polarography, is of great historical importance in electroanalytical chemistry, and became the foundation for most of the electroanalytical methods used to date.

The classical DME had an advantage in that the surface of the electrode would be continually refreshed as the drop grew in size, before falling, and a new drop formed. The dropping action of the droplet also provided a stirring effect in the solution, and so each new droplet was formed in a (locally) fresh solution. There were two principal disadvantages to the DME in that the growing droplet resulted in an ever-increasing electrode area, and the timescale of the experiment was limited by the lifetime of the droplet, constrained to the range of 0.5 and 10 seconds.

To overcome this Princeton Applied Research Corporation developed the Static Mercury Drop Electrode (SMDE)[26, 27].The SDME is an automated device which controls the flow of mercury and fixes the droplet size in terms of mercury volume until mechanically knocked off at an electronic trigger signal. The SMDE can be operated as either a hanging mercury drop electrode, or as a replacement for the DME with a fixed electrode area during measurement.

Mercury also has other characteristics which are of benefit in electrochemical studies. Many metallic ions can be reduced to their metallic state at the surface of mercury metal and readily

form an amalgam with the liquid[28]. This amalgamation of metal into the mercury ensures efficient capture of the metal and ensures the surface of the liquid mercury maintains a stable interface.

The amalgamation of metals is predominantly useful in detecting the presence of metallic species which may not be reduced at a solid electrode. Whilst limited studies have investigated bulk deposition, this attribute could also beneficial in the recovery metals through sustained deposition/ amalgamation with the liquid mercury. The deposition of metals such as nickel, copper, lead, cadmium and zinc have all been extensively studied[29-31] and bulk deposition may be feasible. These target elements can then be recovered by distillation from the high vapour pressure liquid mercury[32].

A similar process has been proposed as the recovery mechanism for TRUs at a liquid cadmium cathode in molten salts reprocessing of spent fuel.

1.5 Reprocessing in Molten Salts

In Section 1.2.6 the present method of spent fuel reprocessing through the PUREX solvent extraction technique has been discussed. This process has its disadvantages, and in the UK the THORP facility is set to close in 2018[33]. The PUREX process is considered responsible for producing copious volumes of liquid waste, resulting in radioactive contamination of ground water at the Hanford site in the United States. There have also been a number of high-profile safety issues at other sites.

As the PUREX process also allows uranium and plutonium to be extracted from spent fuel separately, there is a risk of proliferation of nuclear materials, which could be used in atomic weapons. As a part of the Nuclear Non-proliferation Treaty, the separation and storage of materials that could be used for a weapons programme is to be avoided, adding pressure to cease operations where plutonium inventories are increased.

Molten salt reactors are just one of six key concepts under investigation as a part of the 4th generation of reactors[34, 35]. As well as reactor technologies, molten salt systems are also considered to be an alternative to the PUREX derived extraction techniques for a number of years for the separation and reprocessing of spent fuel[7].

The advantages of a molten salt processing system combines the ability to recover and recycle uranium from the spent fuel, whilst minimising the high level waste generated compared to the PUREX type processes[36]. The disadvantage of this method is the large quantity of energy required to heat the molten salt and drive the electrorefining processes. The mixed plutonium/ transuranic element (TRUs) "waste" of the molten salt reprocessing could also be considered as a fuel for fast reactors[36] that are popular across Asia[37] but not widely adopted in Europe or North America. It is debatable as to whether the accumulation of Pu in the "waste" rather than the fuel (as in PUREX) is an advantage or a disadvantage, however concurrent recovery with other elements is considered a proliferation resistant pathway.

Chloride and fluoride molten salts can ligate and hence stabilise a wide variety of reactive metal species found in spent nuclear fuel. This makes them an ideal medium for electrorefining spent fuel to separate specific value metals such as uranium from plutonium and other minor actinides from the spent fuel.

A previous example of this electrorefining of spent fuel is the ANL process, which was developed alongside the Integral Fast Reactor (IFR) program to include a molten salt fuel recycling process[38-40]. In this process, a vat filled with a mixed lithium chloride/ potassium chloride eutectic salt is heated to 500°C and mechanically chopped up spent fuel is allowed to dissolve through electrochemical action in an anode basket. Once the spent fuel is completely dissolved in the molten salt, by applying a potential to the cathode it is possible to deposit metals selectively on the cathode. It is possible to deposit bulk uranium on an iron cathode, which can be recycled to make new reactor fuel. Selective deposition of other metals such as plutonium codeposited with the remaining uranium (for proliferation resistance) and minor actinides such as neptunium, americium and curium is achieved using a liquid cadmium pool electrode. As cadmium has a low vapour pressure it is then be possible to distil off the cadmium and collect the metals it contains.

Another example of pyrochemical reprocessing is the Research Institute of Atomic Reactors (RIAR) process[41] developed in Russia, using a similar method in a molten salt of 1:2 NaCl:CsCl. Both processes are examples of nuclear proliferation resistant technology as in both cases, Pu is separated with TRUs as a mixed waste rather than weapons grade plutonium.

In each of these examples, uranium as the bulk material in the spent fuel, is deposited at a solid electrode and recovered from the melt. Uranium can be recovered through electrodeposition at a solid cathode with minimal contamination from other spent fuel components. Uranium is more noble than any of the other actinides and applying more positive reduction potential than

the other TRUs will result in the deposition of a high purity deposit. The TRUs are then recovered at a liquid cadmium cathode which favour deposition at the liquid cathode as alloying with the liquid metal stabilises the reduced product[39, 40, 42].

Over periods of operation of these systems without the use of a liquid cathode, fission products (FP) and transuranic elements (TRU) will build up in the melts. This will result in a build-up of heat from the radioactivity of these elements[43], and therefore either they must be removed from the melt, or the melt must be removed from the system to prevent overheating[44]. It is important to note however that the build-up of FP in the melt will be significantly lower than retention of FP by the solvent process, and methods are under investigation to treat the salt and remove FP and TRU from the melt[44].

Initial studies of deposition at a cadmium cathode have demonstrated that deposition of uranium at the surface of liquid cathodes forms a solid product, which forms a dendritic structure, subverting the recovery process[45, 46]. This nucleation of uranium initiates a dendritic growth process where the reduction process is concentrated onto the solid deposition and dominates the recovery process[47].

The occurrence of dendritic growth at these electrodes presents a technological barrier to the use of such systems. The dendritic growth not only prevents the recovery of TRUs in the liquid cathode, but also prevents a risk of shorting the electrochemical circuit. In order for dendritic growth to be avoided, a fundamental understanding of the deposition process needs to be investigated, and tools for monitoring the formation of dendrites developed.

Pyrochemical reprocessing methods directly yield metals as the product, and are well suited to advanced fuels. In the case of metallic alloy fuels, the PUREX process is very cumbersome and costly, due to the number of steps required based on differing fuel types. In the pyrochemical method, the principal steps remain unchanged and conditions can be adjusted so that U and Pu can be recovered together or separately as well as the TRU40. It is interesting to note that whilst studies on such systems have been undertaken since the 1960s[48], Russia is the only country to have employed them on an industrial scale, although the U.S.A. has also conducted some tentative operations[49].

For practical and economic viability of pyrochemical reprocessing, it is important to recover effectively all of the transuranic elements of Pu, Np, Am and Cm from the spent fuel. This is essential for a reactor type such as the AFR concept where the TRU are fabricated into fuel for power generation[50-52].

As discussed above, it is possible to deposit essentially pure U on a solid steel cathode in a molten salt refiner. The remaining TRUs can also be simultaneously deposited at a liquid cadmium cathode, where the deposition is stabilised by alloying with the cadmium[39, 40].

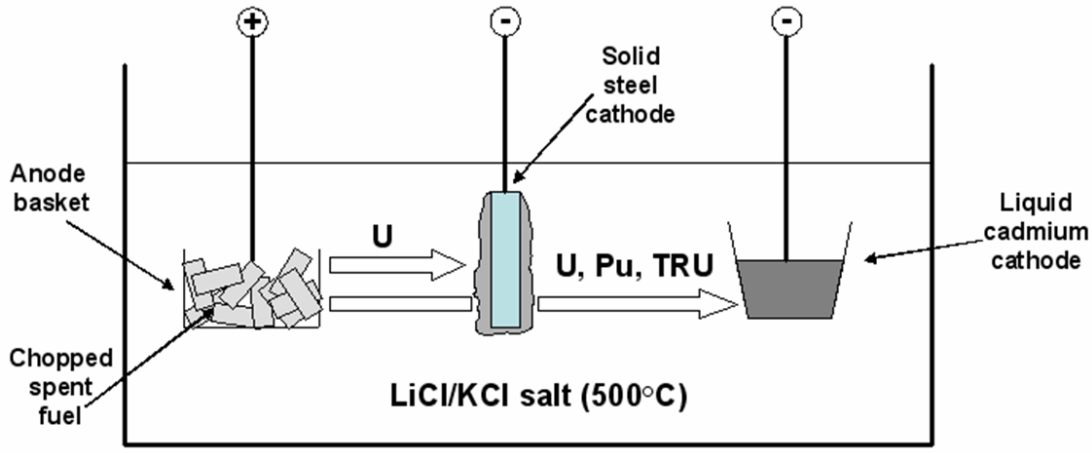

Figure 1.8: Schematic of electrode arrangement in a molten salt reprocessing system.

The recovery of TRUs from a molten salt at a liquid cathode is achieved by arranging the electrodes such that the anode basket where the fuel is dissolved into the salt, is furthest from the liquid cadmium cathode, and the solid steel cathode is somewhere between the two (Figure 1.8). The liquid cathode can be tuned to favour deposition of the TRU over U, thus combining the materials that have applications as atomic weapons and providing a proliferation resistant route to closing the fuel cycle.

It is then possible to apply a potential to the cadmium liquid cathode that will result in deposition of the transuranic elements. As deposition of TRUs at the cadmium occurs at a more positive potential than at a solid cathode, the deposition of transuranic elements is favoured over the deposition of any residual U[40]. This is due to the high activity coefficient of uranium in cadmium, compared to the very low relative activity coefficients of the TRUs[39, 53].

The overall process of dissolution of spent fuel/ deposition at selected electrodes may be limited by the diffusion of the spent fuel in either the molten salt or the liquid metal. During the process the overall rate of separation is limited by the diffusion of TRUs into the liquid metal, limiting the efficiency of the system[53]. Measurements on the evolution of liquid electrode deposition has so far been limited, with few studies being conducted outside of the

former USSR, however research in this area is now gaining some wider focus. Despite research having previously been conducted in the USSR, the nature of the way this has been reported, usually only in Russian language papers, presents problems of access and verification of results.

The primary requirement for the metal used for the liquid cathode is that it is liquid state range matches up to the temperature range of the molten salt operation, i.e. its melting point is below the operating temperature, and its boiling point well above the boiling point. The metal must also not have densities similar to that of the molten salt, as this would prevent to the formation of a stable free-standing interface where the two liquid have a distinct boundary[35]. It so happens that out of the metals that are molten at the LiCl/KCl eutectic operating temperature (about 500°C), bismuth and cadmium are suitable as cathode materials, with cadmium having been chosen for use in the IFR system.

Due to the complexities of molten salt systems – high temperatures, dry inert atmospheres required, aggressive and hazardous nature of the melt – the behaviour of liquid metal cathodes in a molten salt is not well understood, and little fundamental research on their exact behaviour has been carried out. Whilst a liquid metal electrode has been in use in electroanalytical chemistry for many decades, the mercury electrode/ dropping electrode, there are no apparent reports on the behaviour of other metals as liquid electrodes.

It is known that in a melt the deposition process of mixtures of plutonium and uranium at a cadmium liquid cathode has a tendency to be subverted by deposited U forming dendritic structures from the liquid surface[45]. These dendrites result from a nucleation process where the liquid electrode begins to behave as a solid electrode as the diffusion of the U into the liquid is much slower than the diffusion towards the electrode. The behaviour of the cathode as a solid electrode results in further growth of the solid deposit and interrupts the desired deposition process. Whilst a solution to overcome dendritic growth in an industrial process is desired, and under development, an understanding of how these processes occur and how they can be observed are also of interest. Indeed, initial work of this nature has been carried out in a previous studentship within this research group, and studies on ambient temperature mercury were performed[54].

1.6 Aims of this Work

The focus of this work is to address three key issues to overcome in the development of reprocessing spent fuel in a molten salt refiner. These questions are:

- How can dendritic growth at liquid cathodes be detected?
- How are molten salts best prepared to prevent an oxidising or reducing environment and record accurate, reliable electrochemical measurements?
- How do semi-conductor materials interact with molten salt?

First, deposition at liquid metal electrodes are studied in ambient conditions to determine characteristic responses associated with dendritic growth.

Secondly, new methods to measure preclude an oxidising or reducing environment, and thus the chemical formation of oxides in molten salts, are presented. These methods permit electrochemical investigations in molten salt systems without the use of chemical drying agents, which may also react with a liquid metal present in the salt for liquid cathode experiments. These methods are an important progression in understanding liquid cathode behaviour and enable the characterisation of the process that take place during deposition in rigorously controlled and dry molten salt.

Thirdly, the wetting behaviour of molten salt on typical semi-conductor materials is investigated. This involves developing a method to image droplets of molten salt on sample surface in an inert atmosphere and subsequently measuring the LKE-surface contact angle for a set of specific materials of interest.

Finally, having characterised diagnostic electrochemical responses of deposition at a liquid cathode in aqueous experiments, and established suitable methods to prepare the molten salt, dendritic growth at a liquid bismuth cathode in LKE is investigated. Comparisons are drawn to the observations in aqueous conditions, and a diagnostic response of dendritic growth at a liquid cathode is confirmed.

1.7 References

1. O. Hahn, *Scientific American*, 1958, **198** (2) 76.
2. O. Hahn and F. Strassmann, *Naturwissenschaften*, 1939, **27** (1) 11.
3. A. Einstein, *Annalen der Physik*, 1905, **323** (13), 1905.
4. http://www.world-nuclear.org/info/Nuclear-Fuel-Cycle/Uranium-Resources/Supply-of-Uranium/ Accessed 18/02/2015.
5. K.J.R. Rosman, P.D.P. Taylor, *Pure Appl. Chem.*, 1999, **71**, 1593.
6. http://www.nrc.gov/materials/fuel-cycle-fac/ur-enrichment.html Accessed 18/02/2015.
7. D. G. Lovering, Molten Salt Technology, Plenum Press, New York, 1982.
8. G. Z. Chen and D. J. Fray, Novel cathodic processes in molten salts, *Proceedings of 6th International Symposium on Molten Salt Chemistry and Technology,* Shanghai University Press, Shanghai, 2001.
9. G. Z. Chen, D. J. Fray and T. W. Farthing, *Nature*, 2000, **407**, 361.
10. D. J. Fray, *Journal of the Minerals Metals & Materials Society*, **53**, 26 (2001).
11. T. Nohira, K. Yasuda and Y. Ito, *Nature Materials*, 2003, **2**, 397.
12. H. Ito, Y. Hasegawa. *J. Chem. Eng. Data*, 2001, **46** (5), 1203.
13. M. Jafarian, M. G. Mahjani, F. Gobal, I. Danaee. *Journal of Applied Electrochemistry*., 2006, **36** (10), 1169.
14. V. Constantin, A-M. Popescu, M. Olteanu. *Journal of Rare Earths*, 2010, **28** (3), 428.
15. E. R. Van Artsdalen, I. S. Yaffe. *J. Phys. Chem.*, 1955, **59** (2), 118.
16. V. M. B. Nunes, M. J. V. Lourenço, F. J. V. Santos, C. A. Nieto de Castro. *J. Chem. Eng. Data*, 2003, **48** (3), 446.
17. N. Galamba, C A Nieto de Castro, James F Ely. *J. Chem. Phys.*, 2005, **122**, 224501.
18. G. Cordoba, C. Caravaca. *Journal of Electroanalytical Chemistry*, 2004, **572** (1), 145.
19. S.A. Kuznetsov, M. Gaune-Escard. *Electrochimica Acta*, 2001, **46** (8), 1101.
20. Y. Castrillejo, M.R. Bermejo, E. Barrado, A.M. Martínez, *Electrochimica Acta*, 2006, **51** (10), 1941.
21. P. Masset, C. Apostolidis, R.J.M. Konings, R. Malmbeck, J. Rebizant, J. Serp, J-P. Glatz. *Journal of Electroanalytical Chemistry*, 2007, **603** (2), 166.
22. M.R. Bermejo, J. Gómez, A. M. Martínez, E. Barrado, Y. Castrillejo. *Electrochimica Acta*, 2008, **53** (16), 5106.
23. Z.-Y. Qiao, S. Duan, D. Inman. *Journal of Applied Electrochemistry*., 1989, **19** (6), 937.

24. J. Heyrovsky, *Chem. Listy*, 1922, **16**, 256.
25. W.H. Reinmuth, *Anal. Chem.*, 1961, **33** (12), 1793.
26. WM Peterson, *Am. Lab.*, 1979, **11** (12), 69.
27. Z Kowalski, KH Wong, RA Osteryoung, J Osteryoung, *Anal. Chem.*, 1987, **59**, 2216.
28. Y. Shiokawa, K. Hasegawa, K. Konashi, M. Takahashi, K. Suzuki; *J. Alloys. Comp.*, 1996, **255**, 98.
29. G.C. Sayda, L.C. Tao; *J. Chem. Eng. Data*; 1963, **8** (4), 537.
30. C.J. Flora, E. Nieboer; *Anal. Chem.*; 1980, **52** (7), 1013.
31. B.S. Sherigara, Y. Shivaraj, R.J. Mascarenhas, A.K. Satpati; *Electrochim. Acta*; 2007, **52**, 3137.
32. P.J.W. Mallet; *Proc. Roy. Soc. Lon.*; 1908, **80**, 83.
33. http://www.nda.gov.uk/2012/06/nda-publishes-preferred-option-on-oxide-fuels/ Accessed 20th July 2014.
34. http://www.world-nuclear.org/info/Nuclear-Fuel-Cycle/Power-Reactors/Generation-IV-Nuclear-Reactors/ Accessed 28th July 2011.
35. Nuclear Energy Research Advisory Committee and the Generation IV International Forum; Generation IV Roadmap R&D Scope Report for Nonclassical Reactor Systems, Dec. 2002.
36. T. Inoue., *Progress in Nuclear Energy*, 2002, **40** (3–4), 547.
37. K. Nagarajan, B.P. Reddy, S. Ghosh, G. Ravisankar, K.S. Mohandas, U.K. Mudali, K. V. G. Kutty, K. V. K. Viswanathan, C. A. Babu, P. Kalyanasundaram, P.R.V. Rao, B. Raj, *Energy Procedia*., 2011, **7**, 431.
38. C.C. McPheeters, R.D. Pierce, T.P. Mulcahey; *Prog. Nucl. Energy*, 1975, **31** (1-2), 175.
39. J.P. Ackerman, J.L. Settle; *J. Alloys Comp.*; 1993, **199**, 77.
40. J.P. Ackerman; *Ind. Eng. Chem. Res.*; 1991, **30**, 141.
41. O. Skiba, A. Bychkov, S. Vavilov, M. Kormilizym, A. Oscipenco; OECD/NEA Workshop on Pyrochemistry; Avignon, 2000.
42. Y.I. Chang, C.E. Till; *Adv. Nucl. Sci. Tech.*; 1988, **20**, 127.
43. J.P. Ackerman, T.R. Johnson, L.S.H. Chow, E.L. Carls, W.H. Hannum, J.J. Laidler; *Prog. Nucl. Energy*; 1997, **31** (1-2), 141
44. V.A. Volkovich, T.R. Griffiths, R.C. Thied; *J. Nucl. Mat.*; 2003, **323**, 49.
45. B. Krajli, A Review of Prospective Processing Strategies for Uranium Electrorefined in a Molten Salt; BNFL Commercial, 2004.
46. T. Koyama, M. Iizuka, Y. Shoji, R. Fujita, H. Tanaka, T. Kobayashi, M. Tokiwai; *J. Nucl. Sci. Technol.*; 1997, **24** (4), 384.

47. Argonne National Laboratory; CMT Annual Technical Report ANL-88-19; 1988, 95
48. J. Uhlir; OECD/NEA Workshop on Pyrochemistry; Avignon, 2000.
49. Indira Gandhi Centre for Atomic Research, http://www.igcar.ernet.in/lis/nl46/igc-29-1(4p).htm, 27th July 2011.
50. S. DeMuth, B. Boyer, E. Dixon, K. Thomas, S. Tobin, R. Wallace; Los Alamos National laboratory, LA-UR-06-8666, 2007.
51. Y.I. Chang, C.E. Till; *Adv. Nucl. Sci. Tech.*; 1988**, 20**, 127.
52. Economic Modeling Working Group (EMWG); Cost Estimating guidelines for Generation IV Nuclear Energy Systems, Sept. 2005.
53. J.L. Willit, W.E. Miller, J.E. Battles; *J. Nucl. Mat.*; 1992, **195** (3), 229.
54. N Brockie, Ph.D. Thesis, University of Edinburgh, 2011.

2 Theory

This chapter will outline the theory behind the techniques and analysis methods used in this thesis. Techniques that will be discussed include the electrochemical measurement techniques of cyclic voltammetry, chronoamperometry and electrochemical impedance spectroscopy, along with goniometry for the measurement of contact angles. Electrochemistry has been covered in great depth and breadth in literature[1, 2] and therefore this chapter will only discuss the essential aspects of these techniques with respect to the work in this thesis.

2.1 Electrochemistry

Electrochemistry is the field of chemistry dedicated to the study of reaction kinetics and thermodynamics at an electrode surface. Electrochemical reactions are studied by driving and monitoring the movement of electrons across an electron conductor, an "electrode", at an interface between two phases. At this interface chemical redox processes occur (the working electrode), between the electrode and an ion conducting phase, the "electrolyte". Electrodes can either be solid or liquid and either electronically conducting or semi-conducting. Whilst electrolytes are commonly liquid solutions, they can also be molten salts or ionically conducting solids[1]. Electrochemical reactions are known as redox reactions, with either a decrease in the oxidation state of a species through the addition of electrons (reduction) or the increase in the oxidation state of a species through the loss of electrons (oxidation).

2.1.1 The Three-Electrode System

Electrode reactions take place between two electrodes arranged in an "electrochemical cell". However, it is typical to concentrate on the reactions occurring at a single electrode by employing a three-electrode system (Figure 2.1). In this configuration an applied voltage (potential difference) is applied between the working electrode and a reference electrode that has a fixed potential. The constant potential provided by the reference electrode results in the control of the working electrode potential, which is the potential, *E*, of the working electrode with respect to the reference electrode. This potential controls the Fermi level energy of the working electrode and hence the electrode reactivity[1, 2]. The rate of reaction is proportional to

the current which passes between the working electrode, and a third electrode known as the counter electrode. This current is measured to determine the rate, but it is also possible to drive a current between the working and counter electrodes and measure the potential of the reaction with respect to the reference electrode. Experiments where the potential at the working electrode is controlled are said to be under potentiostatic control, and experiments where the current is controlled are said to be under galvanostatic control.

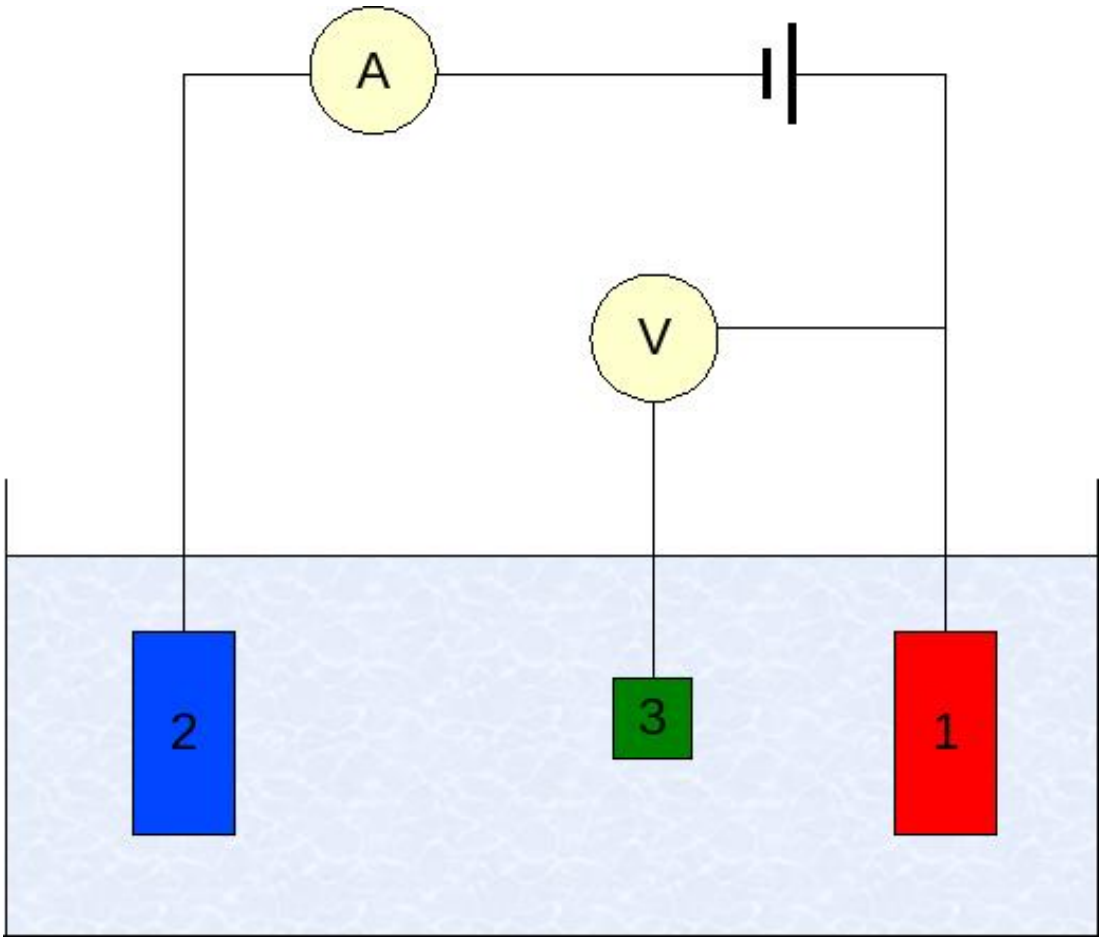

Figure 2.1: Schematic of a three electrode cell, where 1 is the working electrode, 2 is the counter electrode, and 3 is the reference electrode.

In order for electrical neutrality to be maintained at the boundary between the electrode and electrolyte, any charge on the electrode must be balanced by ions of equal and opposite charge forming a layer of charge at the electrode interface. This electrostatic distribution of ions and electrons at the electrode/ electrolyte interface behaves like the two oppositely charged faces

of a capacitor. This structure is known as a double layer[3]. The capacitance of the double layer is a measure of the amount of charge stored for a given potential difference.

Charge transfer between the electrode and the solution alters the concentration of ionic species adjacent to the electrode, thus altering the electric field distribution near the electrode. In turn, this affects the migratory flux of ions towards the electrode, and hence the rate of diffusion of ions (mass transport) to and from the electrode surface. The relationships between ion migration, diffusional mass transport, and charge transfer at the interface during electrochemical reactions can be complex and therefore difficult to control or interpret.

In order to overcome the problems associated with migration and diffusion, experiments are typically carried out in conditions where migration can be neglected. The production of a high concentration of a background electrolyte composed of electrochemically inert ions overcomes the perturbations from migratory effects by maintaining electrical neutrality at the boundary. In solution the background electrolyte is usually present in a concentration typically 50-100 mM. This reduces the double layer thickness to the molecular scale, comparable to the electron transfer distance across the interface. The lack of a potential gradient outside the double layer also nullifies the effects of migration from the bulk solution.

A reference electrode is an electrode with a well-defined reduction potential. Convention is for the thermodynamic scale of oxidation-reduction potentials to be measured against the standard electrode potential, E^{θ}, of hydrogen, which is defined as zero at all temperatures[4]. Owing to practical limitations of routinely using a standard hydrogen electrode (SHE), which requires H_2 gas to be bubbled through an acidic solution at a platinized platinum electrode, other reference electrodes based on the redox reaction between a solid electrode and ions in solution are used. Examples include silver| silver chloride, copper| copper sulphate, and the saturated calomel electrode (SCE).

The saturated calomel reference electrode (SCE) has the redox reaction:

$$Hg_2Cl_{2\,(s)} + 2e^- \rightleftharpoons 2Hg_{\,(l)} + 2Cl^-_{\,(aq)}$$

Equation 2.1

The Fermi level of the underlying Pt electrode is fixed by ensuring that large amounts of the three species, solid Hg_2Cl_2, liquid Hg and Cl^- (by using a saturated KCl solution) are present in the reference electrode chamber. This potential is governed by the Nernst equation:

$$E = E^{\circ\prime} + \frac{RT}{nF} \ln \left[\frac{\alpha_{ox}}{\alpha_{red}}\right]$$

Equation 2.2

Where *E* is the applied potential, *E°'* is the formal potential of the reaction, *R* is the gas constant (8.314 J K^{-1} mol^{-1}), T is the absolute temperature (in Kelvin), F is the Faraday constant (96485 C mol^{-1}) and α is the activity of the oxidised (ox) or reduced species (red) in the bulk solution. Typically the activity, α is substituted for the concentration, *c*, of the oxidised or reduced species in the bulk solution. The formal potential of the reaction is related to the standard electrode potential, E^{θ}, when the ratio of the concentrations of oxidised and reduced species are equal, taking into account the activity coefficients of these species. The larger the concentrations of the species, the less *E* will change, and hence the stability of the reference potential.

In molten salt experiments at elevated temperatures it is not possible to use an aqueous reference electrode. In this thesis, a silver/ silver chloride reference electrode[5] was used for molten salt experiments. These electrodes were fabricated in a similar manner to those previously used in molten salts[5, 6] with a silver wire being sealed in a commercial alumina tube filled with lithium chloride- potassium chloride eutectic (LKE) containing 1 wt.% AgCl.

The counter electrode provides a sink for the current passed by the working electrode in the three electrode system. In order to ensure that the current passed is not limited by the counter electrode, the counter electrode has a much larger area than that of the working electrode (since current is proportional to area). Counter electrodes are usually noble metals and are placed well away from the working electrode to ensure that products at the counter electrode do not interfere with reactions at the working electrode. In this thesis platinum gauze was used as the

counter electrode in all aqueous experiments, and either a tungsten rod or tungsten gauze was used as the counter electrode in molten salt experiments.

All electrochemical systems exhibit a resistance, R_s, arising from the electrolyte concentration that determines the field distribution and the migration of ions in the electrochemical cell.

2.1.2 Microelectrodes

Microelectrodes, electrodes with at least one dimension on the micrometre scale, exhibit lower currents, higher current densities, lower capacitance, increased signal-to-noise and enhanced diffusion of electroactive species to the electrode surface over standard macroelectrodes. These attributes result in a characteristic response in comparison to standard size electrodes. These advantages over standard electrodes in measuring fundamental properties of reactions make microelectrodes highly desirable analytical tools.

On a macro electrode current is proportional to area. On a microelectrode, which has a significantly reduced area, the current density increases in magnitude compared to the current densities observed on larger electrodes. Indeed, in the case of micro-disc electrodes, where the electrode is a disc, the current is directly proportional to the radius of the disc[7]. On a macroelectrode the current would be proportional to the area[2], i.e. πr^2 in the case of a disc. Accordingly this demonstrates that greater current per unit area is passed on microelectrodes than on a macroelectrode, ergo higher current densities are observed.

The diffusion rate to microelectrodes is also vastly improved over that of a macro electrode. In section 2.1.1 the migration of ions was discussed and the concept of adding background electrolyte to the solution in order to facilitate charge transfer was introduced. One of the factors affecting the rate of an electrochemical reaction is the diffusion of the active species of interest to the electrode. The motion of redox active species from the bulk solution to the electrode surface is known as mass transport, and is due to a combination of diffusion, migration and/or convection through the electrolyte[1].

Once an electroactive species at the surface of an electrode has reacted, a concentration gradient develops from the electrode surface into the bulk solution. In order for a reaction to continue, the reaction product must diffuse away from the electrode surface, and fresh reagents must diffuse towards the electrode. Transport of these molecules can be improved by introducing an external source of convection in the solution, such as stirring, although this is

not essential as transport of these molecules is always present through natural convection mechanisms. At microelectrodes this external convection source is unnecessary as mass transport rates to microelectrode are significantly faster.

Figure 2.2: Comparison of diffusion at a) a macroelectrode and b) a microelectrode. The coloured areas represent the electrode area, the lines around the electrode represent the diffusion layers and the arrows indicate the diffusion path of ions towards the electrodes.

When the reagents at the surface of an electrode are consumed by reaction, a diffusion layer develops and as more species near the electrode react, this diffusion layer becomes thicker. Indeed, the thickness of a diffusion layer is proportional to the square root of time[3, 8, 9]. On macroelectrodes, where the diffusion layer thickness grows with $t^{1/2}$, where t is the time, current decays by $t^{-1/2}$ and tends towards zero. As the diffusion layer becomes thicker, the diffusion layer grows linearly (Figure 2.2a) from the electrode. As there is always some natural convection, in practice the current will not reach zero. At a microelectrode, the diffusion layer thickness very quickly develops to be on an equivalent scale to the dimensions of the microelectrode, and then continues to grow hemispherically around the electrode (Figure 2.2b). As the diffusion field is then larger that the electrode, the diffusion (and hence mass transport) to the electrode is far more efficient than the linear diffusion to a macroelectrode. This steady state diffusion is evidenced by a time independent current response in the cyclic voltammogram. Figure 2.2 shows the shapes of the diffusion layers of a macroelectrode and a microelectrode.

The time independent response of a microelectrode allows the mass transport contribution of a redox reaction to be separated from the electron transfer component and allows redox reactions to be far more readily analysed.

When the surface of an electrode becomes charged, ions of opposing charge align themselves across the surface of the electrode. The storage of electrical charge in such a fashion is described as capacitance. Once an electrode surface develops the double layer, it is charged like a capacitor and the potential difference between the electrode and the bulk solution drops

rapidly at the electrode surface. With the double layer charged, the applied potential can drive the electron transfer (faradic) process at the electrode surface. Over time the double layer charging current dies away with a time constant τ:

$$\tau = R_S C_{DL}$$

Equation 2.3

where R_S is the solution resistance and C_{DL} is the capacitance of the double layer. In voltammetry the charging (non-faradic) current is always present as the applied potential is continuously changing. When the potential is swept quickly, or there is a low concentration of redox active material in the electrolyte solution the faradic processes can be dominated by the non-faradic current and separation of the two can be difficult.

Given that capacitance is related to area, microelectrodes have a significantly lower capacitance over macroelectrodes, and as current on a microelectrode is proportional to either radius or edge length (see section 2.2.1) rather than area the Faradic to non-Faradic currents (signal-to-noise) increases as the microelectrodes get smaller.

Reduced capacitance and the subsequent improvements in signal-to-noise ratio, along with fast charging of the double layer, owing to reduced area, and reduced iR distortion make electrodes more sensitive than macroelectrodes and more suitable for analysing fast reaction kinetics.

2.1.3 Liquid Electrodes

Historically, the use of liquid electrodes has been largely restricted to polarography and the use of either a static mercury drop (SMDE) or dropping mercury electrode (DME). SMDEs and DMEs consist of a capillary filled with mercury metal, which is liquid at room temperature. Electrical connection is made to the liquid mercury within the capillary, and an open end of the capillary is submerged in the electrolyte solution exposing the suspended mercury as the electrode surface.

Developed during the 1920s by Jaroslav Heyrovsky, polarography is a form of linear sweep voltammetry over cathodic potentials, where the liquid mercury was used for its renewable

electrode surface. The current response during polarography is determined by diffusion/ convection/mass transport to the electrode and produces a sigmoidal plot of current against the applied potential. On the plot, there are oscillations, which correspond to drops of mercury falling from the electrode (capillary) and the electrode surface being refreshed.

Recent interest in liquid electrodes has been predominantly as a cathode for recovering metals in molten salts systems, particularly in the reprocessing of spent nuclear fuels. Desirable for economic, political and environmental reasons, liquid cathodes present a viable means of concurrently recovering almost all of the transuranic elements (plutonium, neptunium, americium and curium) from the waste, which is dissolved into a molten salt.

Fundamentally, the liquid cathode enables these elements to be deposited at the cathode surface, and then incorporated into the electrode through either diffusion into the liquid pool, or amalgamation/ alloying with the liquid metal. The formation of alloys/ amalgams of these elements of interest with the liquid cathode metal are thermodynamically favourable compared to deposition of these elements at a solid cathode. This effect is represented by a relative shift in the standard reduction potentials of these elements and thus facilitates the recovery when it wouldn't otherwise be possible within the potential window of the molten salt.

In practice, the use of liquid cathodes in molten salts has not yet been fully developed and is fraught with complications. This thesis aims to address the use of liquid electrodes as a tool for recovery of metals, and understand the limitations associated with dendrite formation arising from deposition of solids at the surface of the liquid electrode.

2.2 Electrochemical Methods

2.2.1 Cyclic Voltammetry

One of the simplest, and most commonly used methods of electrochemical study, is cyclic voltammetry. In cyclic voltammetry the potential of the working electrode is swept from a starting potential between defined upper and lower potential limits at a constant sweep rate. During the potential sweep the current, *i*, is measured and plotted against the applied potential. The voltages selected to be the upper and lower limits for the sweep are chosen based on the potential at which an electroactive species in the solution will undergo a redox reaction and

from the potential of the reaction and the current response, it is possible to determine thermodynamic and diffusional properties of the species.

For a typical one electron oxidation,

$$A \rightleftharpoons B + e^-$$

Equation 2.4

when the applied potential, E, is swept above the standard reaction potential, E^{θ}, the current response will change with E as determined by the equation:

$$|i| = nFAc_A k_{ox}$$

Equation 2.5

Where, $|i|$ is the magnitude of the current, A is the electrode area, c_A is the concentration of A at the electrode surface and k_{ox} is the rate constant for the oxidation reaction. When E is significantly negative of E^{θ}, no current will be passed at the electrode as no reaction will occur, however, as E approaches E^{θ}, the current response is governed by the rate of the oxidation reaction, calculated as:

$$k_{ox} = k^{\theta} \exp\left[\frac{\propto_{ox} nF(E - E^{\theta})}{RT}\right]$$

Equation 2.6

where, k^{θ} is the standard rate constant for the electron transfer and α_{ox} is the transfer coefficient that describes the position of the transition state on the reaction co-ordinate between 0 and 1[2].

Initially, as E becomes increasingly more positive the current, i, increases exponentially with E and the charge transfer reaction rate at the electrode controls the rate of the reaction. However, as species A is oxidised to species B, more of species A must diffuse to the electrode surface from the bulk solution in order for the reaction to continue. As depletion of species A

occurs, this diffusion becomes increasingly difficult. With the applied potential being swept increasingly greater than E^{θ}, the diffusion layer spreads into the bulk solution and the reaction becomes rate limited by the rate of mass transfer, k_{MT}, to the electrode.

On a macroelectrode this mass transfer limit causes the current to drop to with time as the diffusion layer becomes greater. These two rate controlling processes, k_{ox} and k_{MT}, are the underlying factors which lead to the typical curved and peaked response of current in a cyclic voltammogram (Figure 2.2a). On microelectrodes the current response in the cyclic voltammogram differs from that of macroelectrodes. In the case of microelectrodes, the advantages of enhanced hemispherical diffusion results in faster diffusion of species from the bulk solution to the electrode and mass transfer is steady state. As the rate of diffusion of species A to the electrode surface is time independent, k_{MT} is constant and there is no peak to the current response. Without this peak, the current response for the reaction becomes a wave shape (Figure 2.2b).

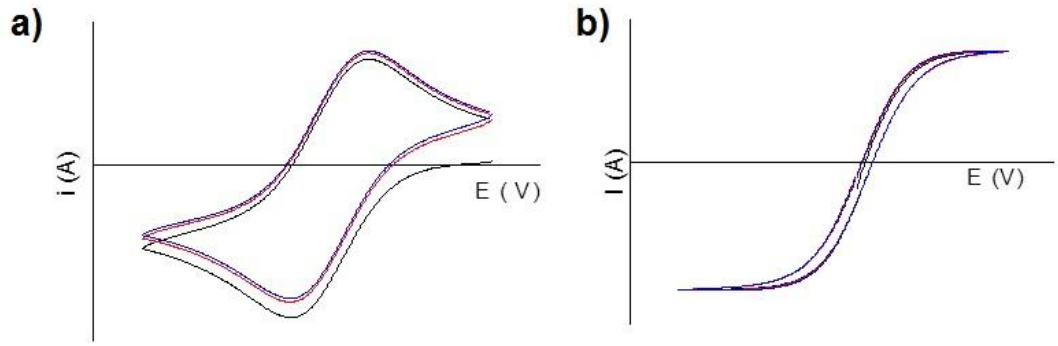

Figure 2.3: Characteristic cyclic voltammograms for a) a macro electrode with curved and peaked response and; b) a microelectrode wave response.

On a microelectrode, the height of the oxidation or reduction wave is defined experimentally as the limiting current. Calculation for this current is fundamentally dependent on the

microelectrode shape, however initially the equation for calculating the limiting current on a disc shaped electrode[1, 10] was derived by Oldham[11] to be:

$$i_L = 4r_0nFDc_\infty$$

Equation 2.7

Where i_L is the limiting current; r_0 is the radius of the disc electrode; D is the diffusion coefficient for the redox species in solution; and c_∞ is the bulk concentration.

Microelectrodes produced, studied and previously characterised within the group are square shaped, and to reflect this difference in microelectrode geometry Equation 2.7 must be modified. To do this, the electrode radius property r_0 is replaced by the edge length of the square, l, and a geometric factor, B, is introduced. For a square microelectrode, B was found using simulations and experimental validation to be 2.63[12]. The equation for calculating the limiting current of a microsquare can be taken as:

$$i_L = BnFDlc_\infty$$

Equation 2.8

2.2.1.1 Deposition of Reaction Product

In the previously described example, oxidised product B has diffused away from the electrode and is not directly observed at the electrode. An alternative case would be a redox reaction where the product is deposited in some form at the electrode. In the case of metals, it is possible to reduce the ion to metal which is deposited at the electrode.

On a macroelectrode the deposition of metal continues to be limited by, k_{red} and k_{MT}, with the same initial peak and curve, however as the potential is swept further beyond E^θ, metal continues to deposit on the electrode surface and the electrode area increases as the deposited metal forms a new active surface. The growth of the electrode surface, and hence area, as metal continues to deposit causes the current to increase again, even when the potential is reversed, until the applied potential approaches E^θ. When the applied potential is swept above E^θ and

the metal is oxidised from the electrode, the reaction is limited by the rate of reaction, k_{ox}, and the amount of material that has been reduced. This typically results in a large oxidation peak as the material is rapidly oxidised, with the rate of mass transfer away from the electrode, k_{MT}, having very little effect as the active species is already at the electrode surface.

On a microelectrode these features are more pronounced, as the enhanced diffusion enables a greater proportion of metal to be deposited at the electrode, and similarly when the metal is oxidised the resulting oxidation peak is very sharp.

At liquid cathodes, the reduced metal can, at the extremes, follow two routes. Either the reduced metal can be dissolved into or alloy with the cathode metal; or the deposited metal can form a solid crust over the liquid metal cathode eventually blocking the underlying liquid and resulting in the electrode behaving as a solid electrode. The behaviour of species being reduced at a liquid electrode can be governed by multiple factor such as alloying between the cathode metal and the reduced metal; the miscibility between the two metals; the solubility of the reduced metal in the cathode metal; and the density of the two metals.

2.2.2 Chronoamperometry and Potentiometry

Chronoamperometry is the measurement of current when the potential is fixed. Typically, the potential is fixed and the current is measured with respect to time, and it is also possible to step the potential and monitor the current response. Similarly, potentiometry is the measurement of potential with time at a controlled current.

At a fixed potential for the reaction shown in Equation 2.4, where the fixed potential, E, is greater than E^{θ}, the current response the current response initially follows the large peak observed in cyclic voltammetry where species A at the electrode surface is oxidised. Once the reaction is under mass transport control the current response as a function of time can be described by the Cottrell equation:

$$|i| = \frac{nFAc_A\sqrt{D_A}}{\sqrt{\pi t}}$$

Equation 2.8

As t tend to ∞, $|i|$ tends to zero, as the active species (in this example A) is consumed and c_A decreases.

Fick's second law predicts concentration changes due to diffusion over time for a thin layer of thickness l:

$$\frac{\partial c}{\partial t} = D \frac{\partial}{\partial l^2}$$

Equation 2.9

The modified Cottrell equation is derived by integration of Fick's second law with the Cottrell equation,

$$|i| = \left[\frac{D}{\pi t}\right]^{1/2} \frac{\Delta q}{l}\left[1 + 2\sum_{m=1}^{\infty}(-1)^m e^{\left[-\frac{m^2 l^2}{Dt}\right]}\right]$$

Equation 2.10

to describe the current response with changing concentration over time t, in thin layers of thickness l, due to diffusion, D, for a system with defined boundaries. The experimental time course for current response described by the modified Cottrell equation is controlled by the parameter D/l^2.

In practice, the application of chronoamperometry for measurement of current over time under Cottrell conditions requires awareness of the instrumental and experimental limitations[1].

In theory, very high currents will be passed for a short time period, but in practice the current will be limited by the characteristics of the potentiostat being used. Uncompensated resistance (R_u) and double layer capacitance (C_{dl}) will result in the flow of a non-faradic current that will decay exponentially with a time constant R_uC_{dl}. This charging current will contribute to the measured current. In addition to these limitations, over longer time periods the build-up of a

density gradient combined with natural convection will disrupt the diffusion layer, and often results in larger currents than theory would predict.

Chronoamperometry and potentiometry are complementary techniques that can be used to understand the evolution of the diffusion layer as a reaction proceeds. These techniques are also used to drive continuous reactions such as electrodeposition of metal(s), or, as in the case in Chapter 6, oxidise or reduce species to generate volatile species which are subsequently removed from the solution.

2.2.3 Electrochemical Impedance Spectroscopy

The third, and arguably one of the most informative, electrochemical methods is electrochemical impedance spectroscopy (EIS). EIS allows the investigation and determination of a broad range of processes at an electrode surface, in some cases allows for simultaneous processes to be analysed separately at a single electrode[13]. Whilst resistance, R, describes the opposition to a flow of current in a resistor, as defined by Ohm's law[14],

$$R = \frac{E}{i}$$

Equation 2.11

it only accounts for direct opposition of current. In the presence of an alternating current, then the phase difference between the oscillating potential and the oscillating current produce an imaginary component in the response. The complex case for describing the opposition of current in terms of the real (resistance) and the imaginary (reactance) components is collectively known as the impedance.

When an oscillating current, *i* (t), is induced by an oscillating sinusoidal potential, E (t), then the impedance Z can be described as:

$$Z\,(f) = \frac{E\,(t)}{i\,(t)} = \frac{E_{amp}\sin(2\pi f t)}{i_{amp}\sin(2\pi f t + \theta)}$$

Equation 2.12

where f is the frequency of oscillation, E_{amp} is the maximum amplitude of the potential, i_{amp} is the maximum amplitude of the current and θ is the phase difference between the sinusoidal waves.

Rearranging this equation allows impedance to be described in terms of the real and imaginary components by the expression:

$$Z\,(f) = Z' \sin(2\pi f t) - Z'' \cos(2\pi f t)$$

Equation 2.13

where Z' is the real component of the impedance and –Z'' is the imaginary component which is out of phase. This mathematical representation of impedance gives rise to a plot of Z' and –Z'' as the x and y axis respectively. This plot is a typical method of graphically presenting impedance data, and is known as the Nyquist plot[13].

Beyond the Nyquist plot, the analysis of impedance at a macroelectrode can be performed by comparison to an equivalent circuit, and subsequent fitting to the response which would be expected for that circuit. Before these comparisons and subsequent analysis can be undertaken, a simple understanding of fundamental electrical circuit components, and the physical process being studied is required.

The simplest impedance response is that of a capacitor, which, on a Nyquist plot appears as a line perpendicular to the x-axis. In an electrical circuit model a capacitor represents the charging of the double layer of ions that form across the surface of the electrode. If a capacitor is in series with a resistor, the position of the perpendicular line on the Nyquist plot is the sum of the resistance of the capacitor and that of the resistor to give the total impedance. In an electrochemical cell, a resistor in the equivalent circuit represents various simple resistive properties such as the electrolyte resistance or a charge-transfer resistance.

If a resistor is added in parallel on the equivalent circuit, then there are two paths for the current to pass through the circuit. When presented with such circuit, current always travels the path of least resistance, which in an electrochemical cell is dependent on the frequency of oscillation. At low frequencies, the capacitor is quickly charged and presents an extremely high resistance and so the resistor is the favoured path for current to flow. At high frequencies

however, the path containing the capacitor is favoured. Intermediate frequencies are composed of some combination of double layer charging and current passing through the resistance and thus the response varies across the frequency range. In real (experimental) conditions, the double layer must always charge before an electron transfer reaction can take place, so this equivalent circuit arrangement is typically found for charge transfer resistances.

A circuit representing a true electrochemical cell is far more complicated than just a capacitor and a resistor in parallel, and so other circuit elements must be introduced to better reflect the processes taking place during the electrochemical reaction. For instance, the initial resistance of an electrolyte between the working and reference electrodes must first be overcome by a current flow before charge transfer or double layer charging will take place. This initial resistance will be added to the plot, shifting the resistance at the intercept of the Z'-axis more positive by the value of the electrolyte resistance.

On macro electrodes, there is an additional feature on the Nyquist plot which gives the linear response describing the linear mass transport from the bulk to the electrode surface. This 45° line in known as the Warburg impedance (W) and is a common element in modelling electrochemical systems and semi-infinite linear diffusion. As microelectrodes have different mass transport properties, the microelectrode response differs to that of a macroelectrode[15]. On a microelectrode, linear diffusion rapidly advances to hemispherical diffusion, and is no longer described by the Warburg impedance.

By combining the described electrical components, it is possible to compose an equivalent circuit which represents the behaviour of an electrochemical cell. The most common circuit, representing the basic electrochemical cell is the Randles circuit (Figure 2.4). In the Randles circuit R_S is the solution resistance, R_{CT} is the charge transfer resistance and C_{DL} is the capacitance of the double layer at the electrode surface. W is the Warburg impedance element describing the frequency dependence of diffusive transport, which for a microelectrode is placed in parallel to a resistor, R_{NL}. At low frequencies, diffusion over a longer time changes the concentration more significantly. This resistor is used as an approximation to describe the

non-linear diffusion to the microelectrode where the response in the Nyquist plot returns to the Z'-axis at lower frequencies[16].

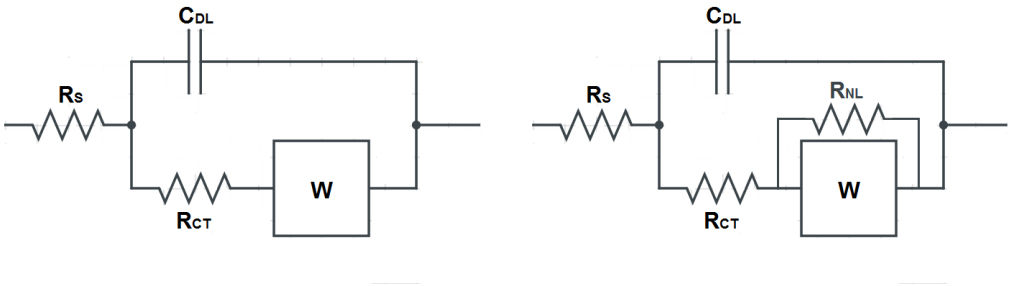

Figure 2.4: Circuit diagram of the Randles circuit (left) and modified Randles circuit for microelectrodes (right).

In this thesis, EIS is used to probe the surface of macro- and micro- electrodes during deposition at liquid cathodes and measure the change in resistance as an indication of dendritic growth. Fitting to an equivalent circuit was not possible as the equivalent circuit for a liquid electrode could not be established. Instead raw, as-measured data is presented, and discussed.

2.3 Contact Angles

The principle of wetting plays a significant role in numerous industrial processes such as oil recovery, lubrication, paints and coatings, printing and adhesives[18-21]. Wetting studies are of interest both fundamentally and in application owing to the ever-increasing list of potential applications, for example in self-cleaning surfaces[22] and electrowetting[23].

Wetting studies typically involve the measurement of the contact angle to indicate the degree of wetting when a liquid interacts with a solid.

The work of adhesion of a liquid drop to a solid surface is defined by the Young-Dupre equation, $W = \gamma_L (1 + \cos \theta)$, where γ_L is the surface tension of the liquid and θ is the contact

angle. Work of adhesion, *W*, is generally considered to be equivalent to the free energy of adhesion.

Large contact angles (greater than 90 °) correspond to poor wettability of the surface and small contact angles (less than 90 °) correspond to high wettability.

2.3.1 Contact angle and Surface tension

Contact angle measurement techniques can be classified in two main groups: direct optical measurement; and indirect force methods. Contact angle values can then be used to calculate the surface tension of the solid material. In this thesis direct optical measurements shall be used to determine the behavioural trend of contact angles between lithium-potassium eutectic and selected surfaces. To date, insufficient data has been determined for the surface tension of rigorously dry lithium-potassium eutectic droplets to allow further calculations.

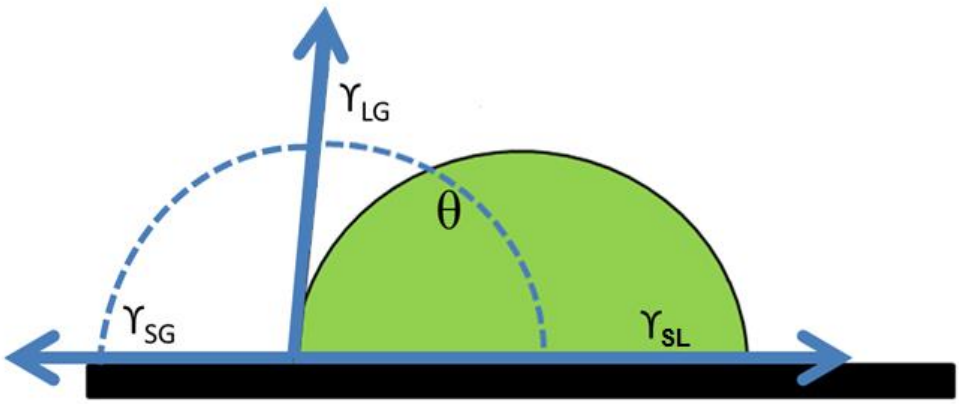

Figure 2.5: Contact angle measured between the three phases, where S, L and G represent solid, liquid and gas.

The contact angle is defined as the angle formed at the intersection of the liquid-solid/ liquid-vapour interface. This is geometrically acquired by taking a tangent line from the liquid-solid contact point and following the liquid-vapour interface of the droplet profile (Figure 2.5) and measuring the angle θ with respect to the horizontal surface.

In Figure 2.6 it can be seen that when a liquid spreads across the surface, a low contact angle is observed. In the most extreme instances of spreading it can be very difficult to measure the contact angle. Contact angles approaching 0 ° indicate complete wetting of the surface. Conversely, when the contact angle is large, it generally means that wetting of the surface by the liquid is not favoured, and the liquid will keep its contact with the solid to a minimum. This forms a compact liquid droplet, and in the more extreme cases, showing almost no contact between the liquid and the solid. For example, the measurement of a water droplet on a super-hydrophobic surface has contact angles greater than 150 °, similar to that of water on a lotus leaf[24].

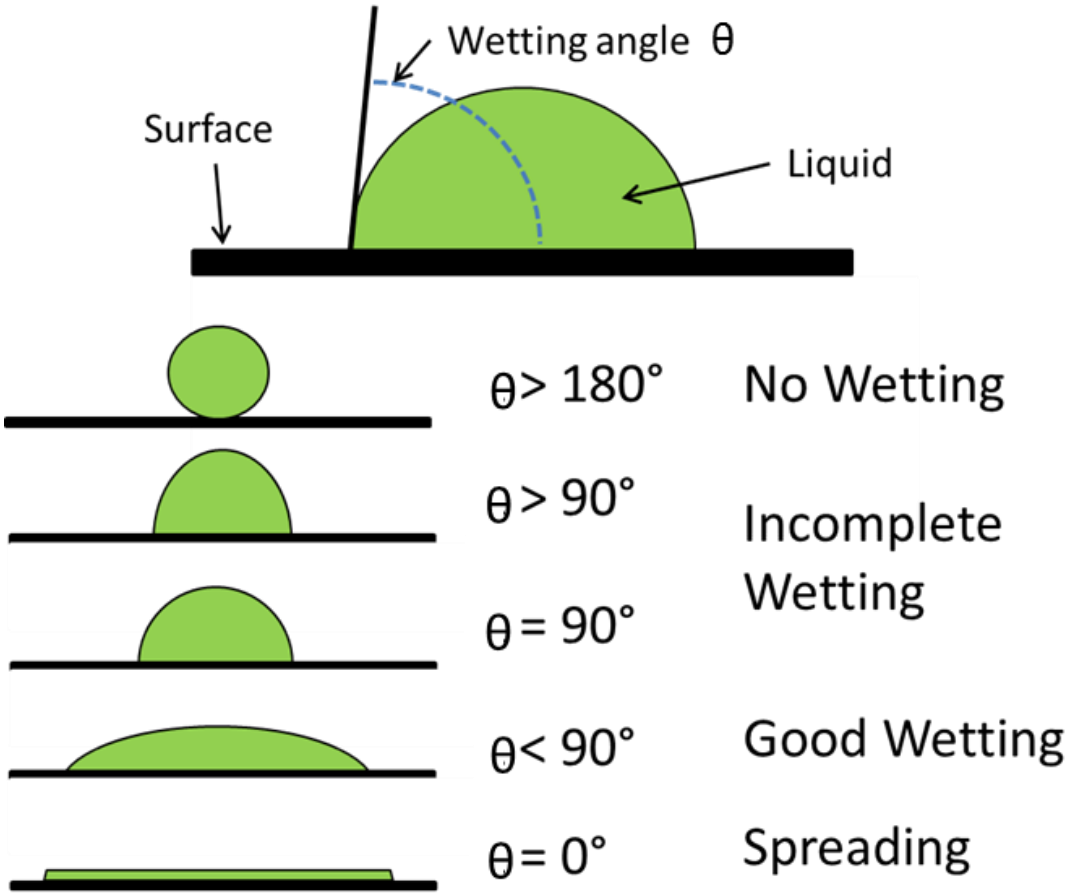

Figure 2.6: Types of interactions arising between a liquid and a solid surface.

Contact angles are not solely limited to the liquid-vapour interface on a solid, and can be applied to liquid-liquid interfaces on solids, however these more complicated scenarios will not be considered in this thesis.

In ideal cases, a liquid droplet's shape is governed by the surface tension of the liquid. In pure liquids, the molecules in the bulk interact equally with its neighbour molecules in all directions, resulting in a net force of zero. At the droplet surface however, neighbouring molecules are not present in all directions. Instead of a balanced force, the outer molecules are pulled inwards by the neighbouring molecules to create an internal pressure. The liquid maintains its lowest surface free energy by deliberately contracting its surface area. For a fixed volume in free space, the minimum surface area is achieved by taking the form of a sphere, but in practice the droplet is deformed by external forces e.g. gravity. Theoretically, the contact angle of a liquid-solid system in a specific environment should be characteristic of the system[25].

The contact angle of a liquid on an ideal surface is defined using Young's equation[26] by the mechanical equilibrium of the drop under the action of each of the three interfacial tensions,

$$0 = \gamma_{SV} - \gamma_{SL} - \gamma_{LV} Cos\theta_c$$

Equation 2.14

where γ_{SV}, γ_{SL}, and γ_{LV} are the solid-vapour, solid-liquid and liquid-vapour interfacial tensions respectively and θ_c is the contact angle. θ_c in the context of this equation is usually referred to as Young's contact angle, θ_Y.

2.3.2 Contact angle Hysteresis

Young's equation sets the scene that contact angle is a static state, dependent on three thermodynamic parameters. In practice there are multiple metastable states a droplet can exhibit on a solid, and the experimentally measured contact angle is rarely equal to Young's contact angle. Liquid on a surface moves to refresh its surface and to wet the fresh surface of the solid. If the three-phase contact point is in continuous motion, the contact angle produced is called a dynamic contact angle. This is particularly prevalent in an expanding or contracting liquid. When a liquid is expanding, the contact angle is called the advancing angle. Conversely,

when a liquid is contracting, the contact angle is called the receding contact angle. These angles form a range, with the advancing angle approaching a maximum value, and the receding angle approaching a minimum value. The difference between the advancing angle and the receding angle is called the hysteresis.

Contact angle hysteresis has been exhaustively studied, with the general conclusion that surface roughness and heterogeneity lead to a greater hysteresis of the contact angle. For surfaces that are not homogeneous, some regions will be non-wetting, presenting a barrier to the droplet and increasing the contact angle. Other regions will be more wetting, drawing the droplet onto the surface and reducing the contact angle. Surface roughness can act in one or both of these roles with microscopic variations in the surface acting as barriers or channels for the liquid, with microscopic features presenting as macroscopic changes in contact angle.

The contact angle phenomena is highly complex, and the experimentally observed contact angles are not always equal to the Young's contact angle[27] as Young's equation does not account for the surface topography. The observed contact angle is only observed to be the Young's contact angle on ideal surfaces, and interpreting contact angle data can often be misleading. On a smooth, chemically heterogeneous solid surface the contact angle may not be equal to Young's contact angle, yet may still be expected to be a good approximation of θ_Y, however the angle may have less reproducibility owing to liquid sorption or solid swelling[28]. On rough surfaces the measured contact angle and θ_Y are likely to have no correlation, and contact angles on rough surfaces are largely considered to be meaningless for fundamental study.

Despite the negative impact of a large surface roughness on the relationship between measured contact angle and θ_Y, there is no defined limit at which a surface is considered too rough to provide an accurate contact angle. As a general guide, surfaces should be prepared as smooth as possible, free from surface contaminants and be inert to the liquid being used in the measurement.

In this thesis, only static contact angles will be measured owing to the complexities of manipulating a liquid droplet with a high temperature melting point and the requirement to maintain an oxygen and moisture free environment. By studying carefully prepared samples

and maintaining a rigorously controlled environment, it is possible to measure the trend in contact angle on smooth, homogeneous surfaces, without the distortion from hysteresis.

2.3.3 Contact Angle Measurement

The simplest and most widely used method for measuring contact angles is a direct, optical measurement of the tangent at the three-phase intercept on a sessile drop profile. The first dedicated instrument of this kind was set up by Bigelow et al.[29], which they called a "telescope-goniometer" and used to measure contact angles of various liquids on polished surfaces. Whilst the word telescope has been dropped from the name in general parlance, the principle behind this technique remains unchanged.

The apparatus consists of a horizontal stage on which the solid surface is mounted, and a micrometer pipette is used to form a liquid droplet on the surface. A diffuse light source is positioned behind the surface and droplet, and a telescope equipped with a protractor device was used to measure the angle through an eyepiece. In modern equivalents, the telescope has been replaced with a high resolution camera and lens, with the measurement of the angle being carried out using computer software. High magnification lenses allow for relatively detailed examination of the three-phase contact point and the profile of the drop.

Direct optical measurement of this type has the advantage of being simple, relatively low cost, and allows the study of small samples, both liquid and surface substrate. Smaller size samples can increase the impact of impurities; however, this can be mitigated by the care taken by the operator. Similarly, the accuracy and repeatability of measurements rely on the consistency of the operator, especially in the assignment of the tangent line, although with the increasing use of computer based analysis this becomes less of a concern.

Direct measurement of contact angles with a goniometer has some disadvantages. The first being that droplets are often not symmetrical in shape, owing to either surface defects or from the surface not being perfectly horizontal. To overcome this, the contact angle should be measured on both sides of the drop, and repeat measurements taken so that a representative angle can be determined. Secondly, small contact angles, below about 10 ° cannot be accurately measured due to the uncertainty in defining the three-phase contact point when the profile is almost flat and the silhouette of the droplet could be distorted. Finally, variations in the surface at the contact point can also cause variations in the observed contact angle;

however, these can also be overcome by numerous repeat measurements and by discarding any obvious outliers.

Measurement of sessile-drop type contact angles using a goniometer is largely considered to be a convenient and well-practiced method of contact angle measurement, and accuracy is largely considered to be about ± 2 °[30].

2.4 References

1. A.J. Bard, L. R. Faulkner. Electrochemical Methods: Fundamentals and Applications, John Wiley & Sons, 1980.
2. A.C. Fisher, Electrode Dynamics, Oxford University Press, 2009.
3. H. L. F. von Helmholtz, *Ann. Physik*, 1853, **89**, 211.
4. A. D. McNaught and A. Wilkinson. IUPAC. Compendium of Chemical Terminology, 2nd ed. Blackwell Scientific Publications, 1997.
5. W. Zhang, C.R. Pulham, A.R. Mount, N. Brockie, R. Lewin, *Energy Materials*, 2008, **3** (2), 132.
6. H. Wang, N.J. Siambun, L. Yu, G.Z. Chen, *J. Electrochem. Soc.*, 2008, **159** (9), H740.
7. J. Heinze, *Angew. Chem. Int. Ed. Engl.*, 1993, **32**, 1268.
8. G. Guoy, *Compt. Rend.*, 1910, **149**, 654.
9. D.L. Chapman, *Phil. Mag.*, 1913, **25**, 475.
10. R. Compton, C. E. Banks, Understanding Voltammetry, 2nd Ed., Imperial College Press, 2011.
11. K.B. Oldham. *J. Electroanal. Chem.*, 1981, **122**, 1.
12. H.L. Woodvine. PhD Thesis, University of Edinburgh, 2011.
13. E. Barsoukov, J.R. Macdonald, Impedance Spectroscopy; Theory, Experiment, and Applications, 2nd ed., Wiley Interscience Publications, 2005.
14. G. Ohm, Die Galvanische Kette: Mathematisch Bearbeitet, Riemann, Berlin, 1827.
15. P. Łoś, G. Żabińska, A. Kisza, . Christie, A. Mount, P.G. Bruce. *Phys. Chem. Chem. Phys.*, 2000, **2,** 5449.
16. L. Christie, P. Los, P.G. Bruce. *Electrochimica Acta*., 1995, **40**, 2159.
17. K.N. Prabhu, P. Fernandes, G. Kumar, *Mater. Des.*, 2009, **2**, 297.
18. X. Zhao, M.J. Blunta, J.J. Yao, *Pet. Sci. Technol. Eng.*, 2010, **71**, 169.
19. Y.Q.Wang, H.F. Yang, Q.G. Hang, L. Fang, S.R. Ge, *Adv.Mater. Res.*, 2010, **154–155**, 1019.

20. M. Sakai, T. Yanagisawa, A. Nakajima, Y. Kameshima, K. Okada, *Langmuir*, 2009, **25**, 13.
21. Y. Son, C. Kim, D.H. Yang, D.J. Ahn, *Langmuir*, 2008, **24**, 2900.
22. B. Bhushan, Y.C. Jung, K. Koch, *Langmuir*, 2009, **25**, 3240.
23. Y.S. Nanayakkara, S. Perera, S. Bindiganavale, E.Wanigasekara, H. Moon, D.W. Armstrong, *Anal. Chem.*, 2010, **82**, 3146.
24. A. Lafuma, D. Quere, *Nat. Mater.*, 2003, **2**, 457.
25. J.H. Snoeijer, B. Andreotti, *Phys. Fluids*, 2008, **20**, 057101.
26. T. Young, Philos. *Trans. R. Soc. Lond.*, 1805, **95**, 65.
27. A.W. Neumann, *Adv. Colloid Interface Sci.*, 1974, **4**, 105.
28. R.V. Sedev, J.G. Petrov, A.W. Neumann, *J. Colloid Interface Sci.*, 1996, **180**, 36.
29. W.C. Bigelow, D.L. Pickett, W.A.J. Zisman, *Coll. Sci.*, 1946, **1**, 513.
30. A.W. Neumann, R.J. Good, in *Surface and Colloid Science: Experimental Methods*, vol. 11, Plenum Publishing, New York, 1979.

3 Experimental

In this thesis a number of different experiments have been carried out to develop the understanding of deposition at liquid cathodes and in molten salts. This chapter will discuss the methodologies used in these experiments, and the fabrication processes of the substrates studied in the contact angle measurements.

3.1 Electrochemical Experiments

This section will set out the two main experimental arrangements, for aqueous and molten salts, applied in this thesis. The electrochemical methodologies used have already been described in Chapter 2.

Electrochemical measurements were collected at the University of Edinburgh using a PGSTAT 12 potentiostat (Autolab, Netherlands), and in NNL's central lab using an iviumstat (Ivium, Netherlands).

Electrochemical experiments were controlled using the associated software (GPES or FRA at University of Edinburgh, and IviumSoft at Central Lab) for each potentiostat. For the Autolab potentiostat at the University of Edinburgh, GPES was used for the data collection and initial analysis of cyclic voltammetry, chronoamperometry and chronopotentiometry, whilst FRA was used for the collection and analysis of electrochemical impedance spectroscopy data.

Origin 8.5 (OriginLab, USA) data analysis and graphing software was used for data presentation and additional analysis performed on the data, and has been used to present the data in this thesis.

3.1.1 Aqueous Experiments

Aqueous experiments were solely conducted at the University of Edinburgh. Both microelectrodes and macroelectrodes were used as working electrodes, with all of these being fabricated in house. Planar electrodes were fabricated by the Scottish Microelectronics Centre

(SMC), whilst the mercury metal macroelectrodes were fabricated as part of the experiments where they were used.

Ambient electrochemical experiments were performed in a Faraday cage to limit electromagnetic interference, or Radio Frequency (RF) noise, in electrochemical experiments. Electrochemistry was carried out using a three-electrode system with a cell of a 7.5 cm crystallisation dish (Pyrex) and using a 1.5 cm^2 platinum gauze counter electrode, either a saturated calomel or a double junction silver-silver chloride reference electrode, and either a planar working electrode supplied by the SMC or the liquid macroelectrode as described above.

Redox agents, purchased from Sigma Aldrich, were used in concentrations ranging from 10 mM to 100 mM, and KNO_3background electrolyte concentration was consistently 0.1 M. Solutions were made using 18 MΩ deionised water and degased with argon for 20 to 30 minutes prior to use. Argon gas was then blown across the surface of the solution to prevent ingress of free oxygen to the solution during the experiments.

As mercury can react with chloride ions to form the insoluble product calomel (Hg_2Cl_2), experiments using mercury in any form (metal or redox species) were carried out in nitrate solutions using the double junction reference electrode. All apparatus was thoroughly cleaned in water and rinsed with nitrate background electrolyte prior to use such that calomel could not form on the surface of the liquid mercury electrodes.

3.1.2 Liquid electrodes

Due to the liquid nature of mercury at ambient conditions, the desired working electrode was formed by corralling Hg metal in a small ceramic crucible (CC9, Almath, UK). The electrical connection was then made to the liquid metal using a platinum wire fed through a ceramic tube to preclude electrical connection between the wire and the electrolyte solution (Figure 3.1). The mercury was constrained by the dimensions of the insulating ceramic crucible, and any

surface deposits upon the electrode surface should, at least initially, be formed at the surface of the liquid metal.

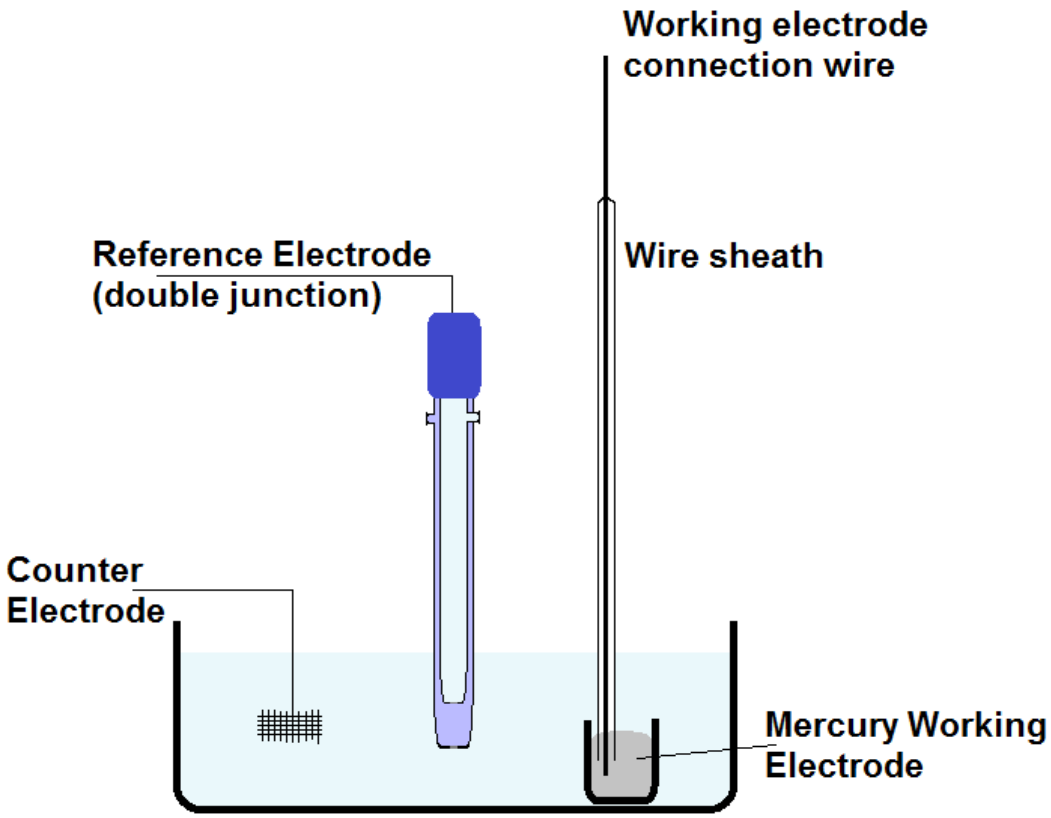

Figure 3.1: Schematic of apparatus for experiments with a liquid metal macroelectrodes.

The crucibles (CC9, Almath, UK) used for constructing the mercury electrodes have a maximum capacity of 0.6 mL After accounting for the displacement of the ceramic tube and wire, the total volume of mercury used in the macroelectrode was 0.6 cm^3. The cross sectional area of the crucible was approximately 0.45 cm^2, significantly larger than the area of a microelectrode. This area does not take into account the convex meniscus[1] of the mercury, which would further increase the effective electrode area (Figure 3.2).

Figure 3.2: Image of the meniscus on the mercury macroelectrode used in this thesis.

Note that this arrangement for the liquid electrodes was used for both aqueous and molten salt experiments, and is comparable in terms of electrode area, with only a subtle difference due to the shape of the meniscus at the mercury-water interface and bismuth-LKE interface.

3.1.3 Molten Salts Experiments

As discussed in Chapter 1, molten salts have unique properties that make them of significant interest in the pyrochemical processing of metals. The corrosive nature, and importance of maintaining an anhydrous, oxygen free atmosphere create handling and contamination issues that must be avoided.

In order to maintain an inert atmosphere around the molten salt, and prevent ingress of oxygen into the melt, molten salts experiments were carried out in a sealed cell (H. Baumbach & Co, Ipswich, UK), operated under either vacuum or a flow of anhydrous argon.

The lower section of the cell was a flanged quartz vessel with an outer diameter of 72 mm and a 5 mm wall thickness. The upper, lid section was made from borosilicate glass and was also flanged so that the 2 sections can be joined together to make a gas-tight seal. The lid had either three, four or five vertical ports in the top and two side ports at about 40° from the vertical, to which gas lines are connected. These ports were threaded so that screw connectors with O-rings or silicone washers could be used to seal the connections.

The LKE was contained in a glassy carbon crucible (GAT10, Sigradur®, HTW Germany) which was placed in the lower quartz section of the cell. Once assembled, with the required electrodes fed through the upper vertical ports of the cell lid, the cell was sealed at the flanges using high temperature vacuum grease. The cell was then suspended in a vertical tube furnace (Carbolite, Derby UK) to heat the LKE to 500 °C (Figure 3.3).

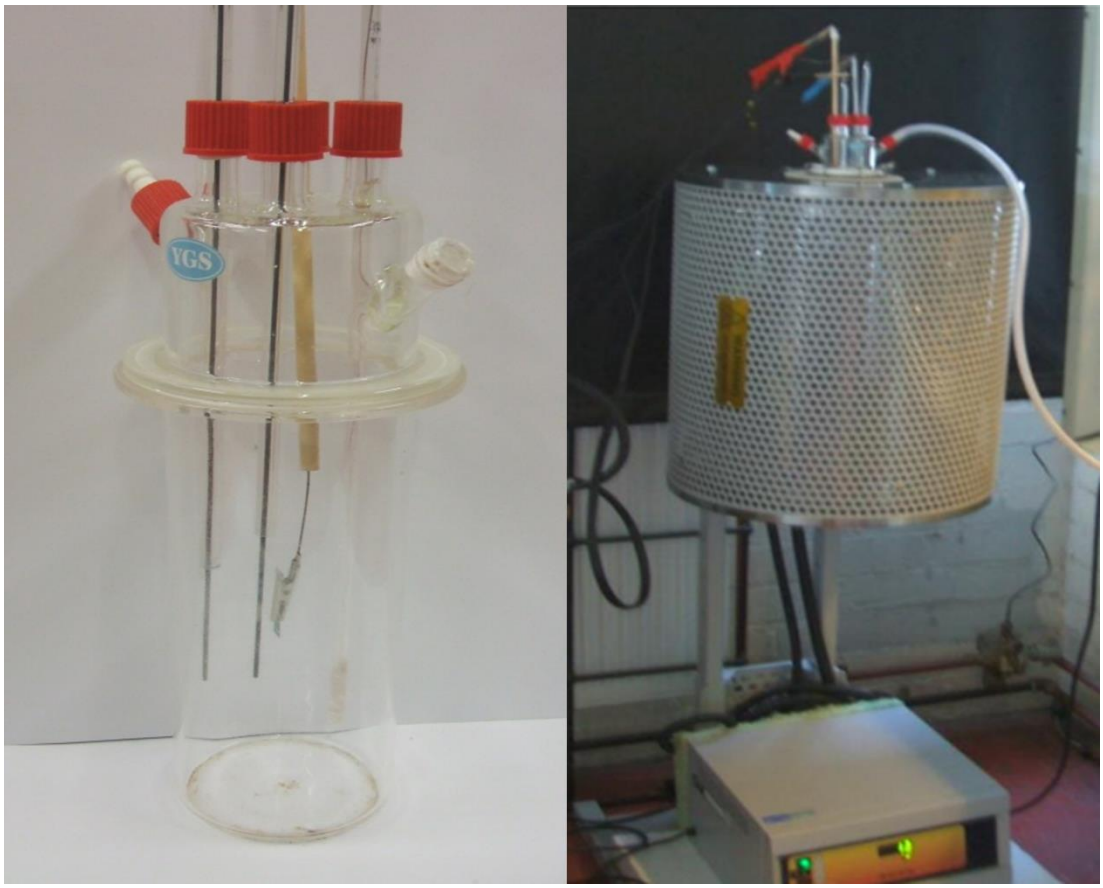

Figure 3.3: Photos of high temperature cell and cell operating in the tube furnace.

For molten salts experiments the counter and working macroelectrodes were 1.6 mm diameter tungsten rods, which were fed through a glass tube and sealed at one end to support the sealing of the cell. The reference electrode was made from a silver wire dipped into a mullite tube (Almath, UK) which was filled with 1% AgCl in LKE and sealed to form an Ag|AgCl reference electrode. The mullite ceramic material is conducting, and thus allows current to flow, whilst the silver –silver chloride reaction fixes the potential as discussed in chapter 2.

Similarly to the aqueous liquid electrodes, macro liquid electrodes were made for the molten salts experiments by filling small ceramic crucibles (CC9, Almath, UK) with 1 to 3 mm beads of bismuth metal (Sigma Aldrich, UK) which were melted and subsequently cooled in an inert argon environment. These crucibles of bismuth were then placed in the bottom of the glassy carbon crucible so that when the LKE was melted, the Bi metal would also melt under the LKE and an oxide film would be prevented from forming over the surface of the liquid pool. An electrical connection was made to the liquid pool via a sheathed tungsten wire, with the sheath also being partially submerged in the liquid bismuth to prevent the wire being exposed to the salt.

Molten salts experiments were carried out at both the University of Edinburgh and at NNL's central lab facility. The above set up was mirrored at NNL's central lab facility; however, at central lab the cell could only be kept under an inert argon atmosphere and not held under vacuum. At central lab the cells were assembled in a glovebox, where moisture and oxygen levels were controlled to be less than 10 ppm using a recirculation system (Saffron, UK) which passed the argon through molecular sieve (Saffron, UK) and desiccant (Saffron, UK). This was confirmed using two oxygen meters (Rapidox, Cambridge-Sensotec, UK; Systech 600 Series Mk III oxygen transducer, USA) and a hydrometer (Mitchell Cermet II Hygrometer, UK), precluding the need for the rigorous exclusion and removal of moisture from the cell during initial fusing of the salt.

3.2 Contact Angle Experiments

3.2.1 Substrate Preparation

Silicon substrate (76 mm diameter, n-type <100> silicon wafers, IDB Technologies) based surfaces, similar to those of interest in the fabrication of microelectrodes for uses in molten

salts were prepared by Dr Jonathan Terry at the Scottish Microelectronics centre. The surfaces used were: native and polished samples of thermally grown silicon oxide; plasma-enhanced chemical vapour deposited (PECVD) silicon oxide; plasma-enhanced chemical vapour deposited (PECVD) silicon nitride; and low pressure chemical vapour deposited (LPCVD) silicon nitride. Samples of titanium, titanium nitride and tungsten, deposited by sputtering were also supplied by the Scottish Microelectronics Centre. Further details on surface fabrication are given below.

Samples of brushed and mirrored 316 stainless steel (RS Supplies, UK) and glassy carbon (Sigradur®, HTW Germany) were also investigated to establish the molten salt wetting characteristics of system relevant materials.

3.2.1.1 Oxide Surface Fabrication

Layers of thermal oxide are produced by the conversion of surface silicon on the wafer to silicon oxide by heating in oxygen and is a common insulator in microelectronics. The oxidising mixture reacts with the surface to produce silicon dioxide by oxidation of the silicon in the wafer. As the layer of silicon dioxide grows into the wafer, the oxidising agents must diffuse through the oxide layer to further react with the underlying silicon. This diffusion rate slows the rate of oxidation of the silicon, and so the thicker they layer of the oxide, the longer the process takes[2].

Chemical vapour deposition (CVD) is a process where one or more volatile precursors are exposed to the substrate and react and/or decompose onto the substrate to produce a high-purity, high-performance solid film. Two types of CVD were used to prepare films of silicon oxide and silicon nitride for measuring contact angles with LKE. PECVD was used to deposit silicon oxide and silicon nitride films, whilst LPCVD was used to deposit silicon nitride films.

Plasma-enhanced chemical vapour deposition (PECVD) is used to deposit thin films from gaseous precursors which react after plasma is created from the gases and deposit as a solid

product on the substrate. The plasma is generated by passing the reacting gases between two electrode and passing an RF (AC) frequency discharge between two plates.

The thermal oxide layers were grown by wet oxidation in an O_2/H_2 mixture in a furnace at 1100 °C.

The PECVD silicon oxide films were deposited from silane (SiH_4) and nitrous oxide (N_2O) precursors in nitrogen using a parallel-plate PECVD reactor (Surface Technology Systems). The chamber pressure was maintained at 600 mTorr and the RF power that generated the plasma was set at 20 W with a frequency of 13.56 MHz. The PECVD deposition time was targeted to deposit a film thickness of 500 nm SiO_2. However, the actual thickness on each wafer was measured using a Nanometrics Nanospec automatic film thickness system.

3.2.1.2 Nitride Surface Fabrication

Silicon nitride is a common ceramic material used in the semiconductor industry. As "silicon nitride" can be used to describe a broad range of stoichiometric and non-stoichiometric ratios of silicon and nitrogen, precise control of the composition is required. As a ceramic it has a low thermal expansion coefficient, low thermal conductivity and has a high strength across a wide temperature range.

Low pressure chemical vapour deposition (LPCVD) is where the CVD process is carried out at sub-atmospheric pressures to reduce unwanted gas-phase reactions and improve film uniformity. Stoichiometric silicon nitride films were deposited from dichlorosilane (SiH_2Cl_2) and ammonia (NH_3) in a LPCVD tube furnace using gas flows of 5 sccm and 20 sccm respectively at a temperature of 800 °C.

The PECVD silicon nitride films were deposited using a parallel-plate PECVD reactor (Surface Technology Systems), from silane (SiH_4) and ammonia (NH_3) at gas flows of 40 sccm and 55 sccm respectively in a nitrogen (N_2) stream of 1960 sccm at a temperature of 350 °C.

The chamber pressure was maintained at 900 mTorr, and the RF power that generated the plasma was set at 20 W with a frequency of 13.56 MHz.

Both PECVD and LPCVD deposition times for the silicon nitride layers were controlled to produce a film thickness of 200 nm. PECVD produced nitride films of SiN:H, whilst LPCVD films were stoichiometric Si_3N_4.

3.2.1.3 Surface Polishing

Samples of each of the thermal oxide (≈1 μm thickness), PCVD oxide (≈500 nm and ≈1 μm thickness), LPCVD nitride and PECVD nitride were polished by chemical mechanical polishing (CMP) in an effort to overcome any surface roughness issues that may arise as described in Chapter 2.

CMP is a process whereby the surface of a wafer is polished with abrasive, corrosive slurry on a polishing pad. The wafer is held in a chuck by vacuum, which is rotated as it presses the wafer into a polishing pad. The polishing of the wafer is achieved chemically and mechanically, with the slurry chemically etching and weakening the material and the mechanical action of the pad removing debris from the surface.

Polishing was performed on a Presi Mecapol 460 polisher using a Klebosol 30H50 colloidal slurry chilled to 10 °C. Each wafer underwent 40 seconds of slurry-based polishing and 90 seconds of rinsing with 1% (w/v) tetramethylammonium hydroxide (TMAH) solution. After the wafers had been removed from the polisher, they were rinsed in 10% (w/v) TMAH solution for 10 minute followed by a cleaning cycle in an Ultratech mask scrubber to remove any slurry particulates that remained on the surfaces.

3.2.1.4 Deposited Metal Surface Fabrication

Titanium, titanium nitride and tungsten surfaces were prepared by DC magnetron sputtering. The titanium and titanium nitride layers were deposited to a thickness of 20 nm. In the case of the tungsten, a 10 nm adhesion layer of titanium was sputtered onto the wafer to relax the stress in the subsequent 200 nm layer of tungsten.

During sputtering, high energy argon ions (Ar^+) are used to bombard a large metal target. These ions physically knock metal atoms off the surface of the target, and these atoms are

transported *in vacuo* to the process wafer where they deposit on the surface. This process results in an even coating of the substrate in the metal atoms. Film thickness is controlled and measured during the deposition process using a quartz crystal microbalance incorporated into the instrument. Film thicknesses were also checked after deposition using a profilometer. In the case of the tungsten samples, the adhesion layer is deposited in the same process cycle, without the vacuum being broken, to ensure that oxide could not build up on the surface of the adhesion layer.

Once the samples were fabricated and surfaces prepared, the wafers were diced into quarters using a diamond-tipped scribe and stored in container until required to prevent contamination.

3.2.2 Lithium-Potassium Chloride Eutectic Preparation

Lithium chloride – potassium chloride eutectic was fused and dried using the method described in Chapter 6. Once fused and electrochemically dried, an anhydrous argon environment was maintained over the LKE and the crucible of LKE was transferred to a rigorously dry argon atmosphere glove box.

Once the fused LKE had been removed from the crucible, the salt was broken up and ground to beads of approximately 3 to 5 mm diameter (≈ 0.1 g) with a mortar and pestle and placed into sealed vials for storage until required for measurements.

When required, these sealed vials were removed from the glove box in an air-tight container and were not opened to expose the salt to the air until transferring the salt bead onto the substrate. Although the transfer of the bead onto the substrate did result in the bead being transiently exposed to the atmosphere, the time of exposure was restricted as far as reasonably practicable by flushing the chamber with argon immediately.

3.2.3 General Contact Angle Measurement Method

To benchmark the method and ensure no optical aberrations were introduced by the glass hood, contact angles of 5 µL droplets of deionised water were measured on each of the surfaces using and existing goniometer (Figure 3.4). The camera, stage and backlight of the goniometer were

all adjustable to ensure the correct alignment to achieve the best possible image for measuring the contact angle of the droplets on the surfaces.

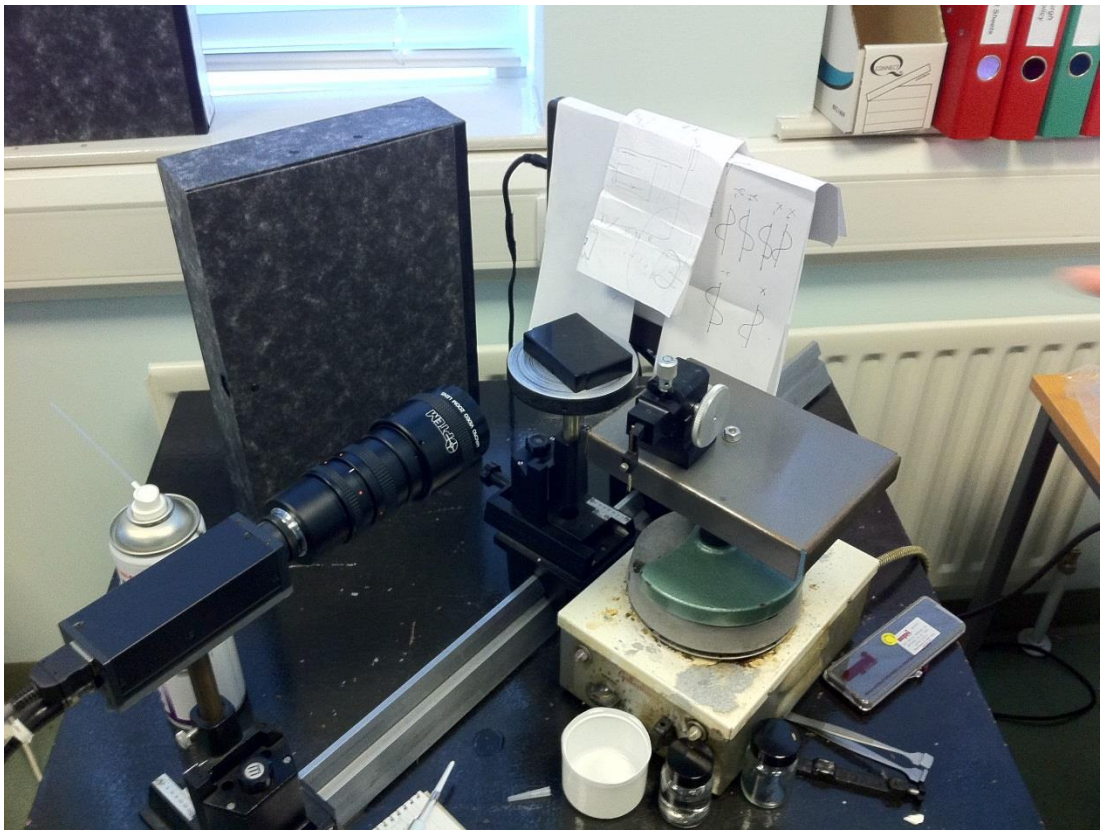

Figure 3.4: Standard goniometer used for measurement of contact angles at ambient conditions.

In order to measure the contact angles of molten salt droplets on the substrates in an inert atmosphere at 400 °C, the existing goniometer was adapted to be suitable for the task. In order for the salt to be melted on the substrates, the standard stage, on which substrates were

normally placed, was replaced by a ceramic hotplate capable of maintaining temperatures of up to 450 °C (Figure 3.5).

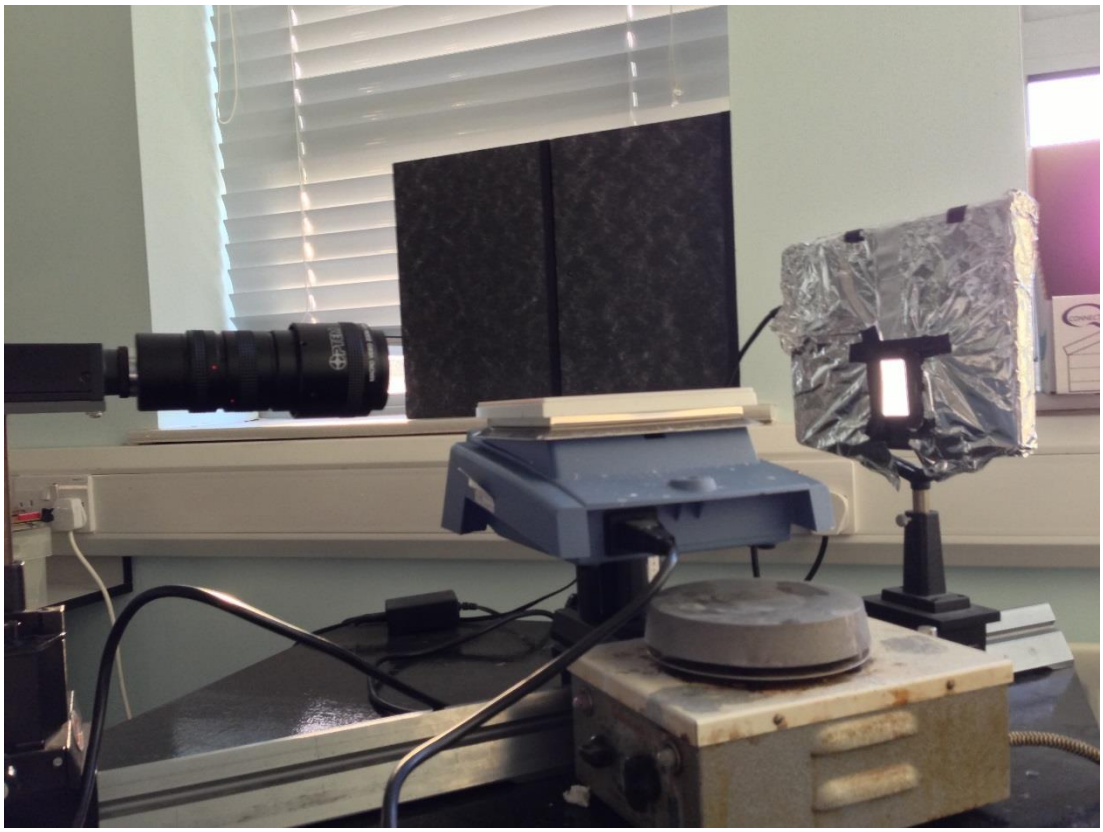

Figure 3.5: Goniometer stage replaced by a ceramic hotplate.

As in-situ measurement of the hotplate temperature was not possible owing to practical limitations of the glass hood design, and the position of the sample on the hotplate, the hotplate was calibrated using an independent thermocouple. The hotplate was then tuned to a fixed setting, where it repeatedly and accurately heated to, and maintained 400 ºC during each heat cycle.

The arrangement of the apparatus can be seen in Figure 3.6. In the centre of the apparatus, the hotplate was situated on a custom designed platform with adjustable feet allowing the hotplate to be raised, lowered and levelled. To the left is the camera used to capture images of the droplet/ surface interface and to the right is a diffuse light source. A steel framed glass hood enclosed the ceramic plate of the hotplate, and dry argon gas was fed into the resulting chamber

in order to maintain a dry, inert atmosphere. Gas was vented from the chamber using fortuitous leakage paths around the perimeter of the hotplate between the ceramic plate and the glass tank. In order to maintain the inert atmosphere within the chamber, a positive flow rate equivalent to 2 gas exchanges per minute was maintained.

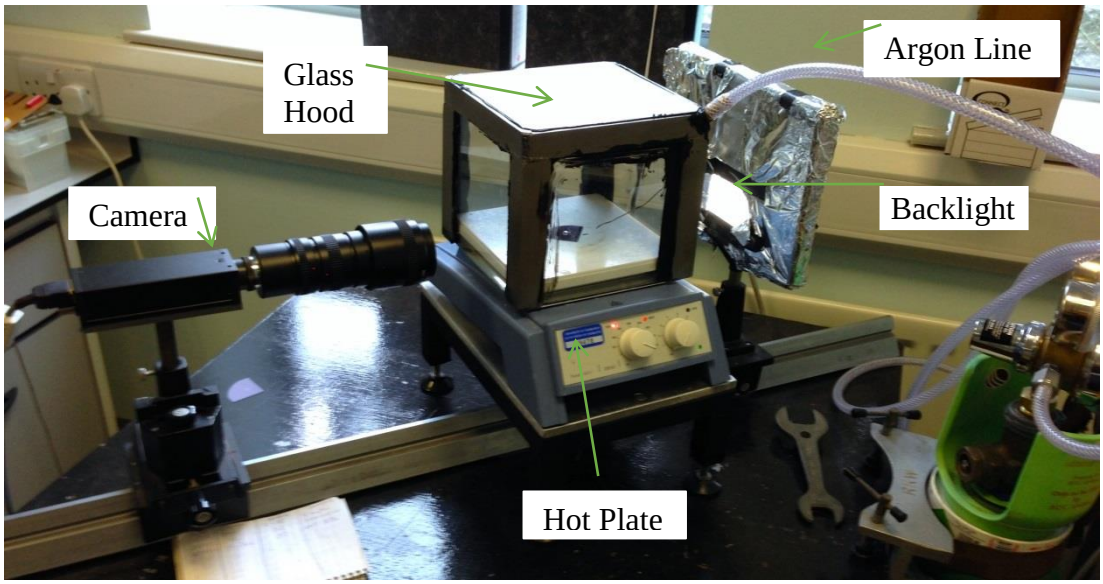

Figure 3.6: Experimental set-up for contact angle of molten salt measurements.

The hotplate was adjusted to be aligned with the existing camera and backlight and the LKE samples were placed on the substrates as solid beads of eutectic salt. The chamber was then purged with argon before the substrate was heated and the contact angle measured once the salt had fully melted. Once an image of the contact angle of the molten salt in argon had been captured, the argon supply was shut off, and the hood removed to measure the contact angle of the molten salt in air.

This apparatus was repeatedly tested for reliability and shown that the salt beads were readily melted on the surfaces within the glass hood (Figure 3.7).

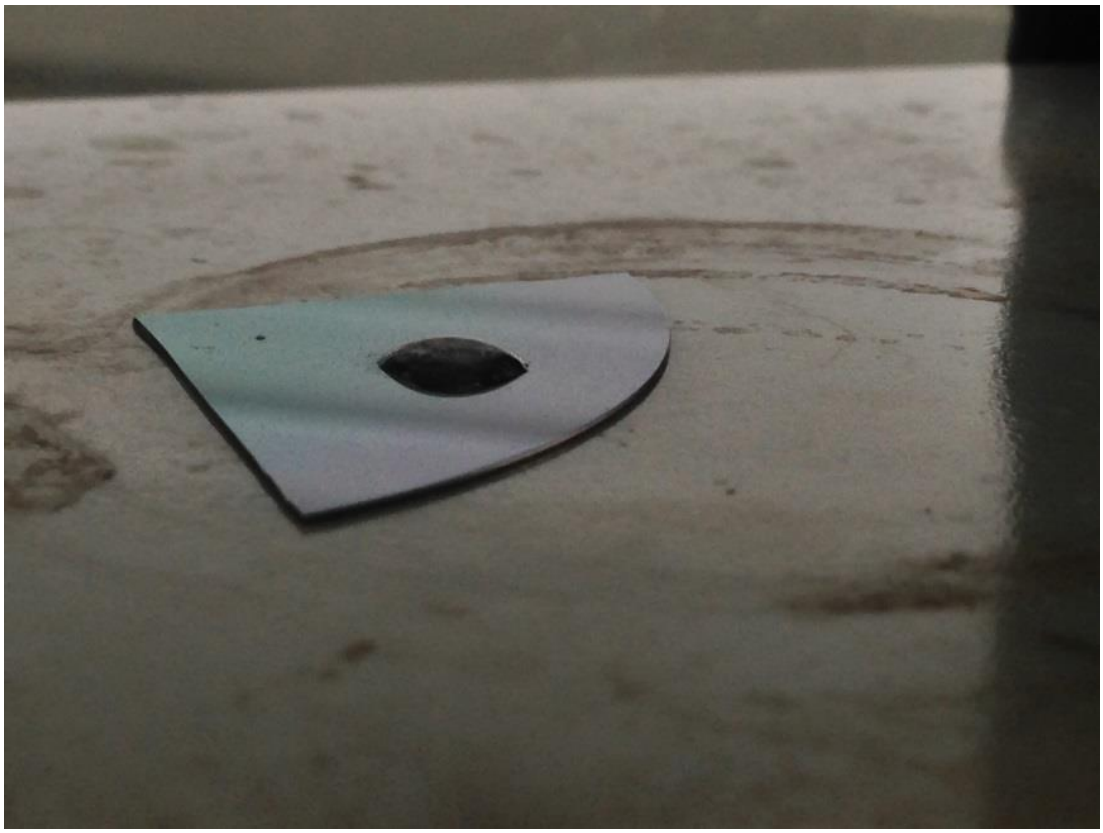

Figure 3.7: Image of LKE droplet melted on a substrate at 450°C in the modified goniometer.

Between measurements the hotplate was allowed to cool before the next sample was placed on the hotplate, a fresh bead of salt was placed on the substrate and the hood replaced over the hotplate and purged with argon prior to heating.

3.2.4 Contact Angle Data Analysis

Images of the contact angles were recorded as video clips, from which stills were extracted and analysed using the Dropsnake plug-in[3, 4] for ImageJ software[5]. The accuracy of contact angle measurement was determined by a combination of the software (0.01°) and the image resolution. For the purposes of this thesis, contact angles were only measured to the nearest degree, and instrument error assumed to be zero. As explained in chapter 2, contact angles which were measured as less than 10° were deemed to be unreliable, and were therefore simply recorded as the salt spreading on the surface.

Images of droplets of LKE on each of the surfaces were repeated at least 8 times, with each measurement producing two measurements (i.e. 16 measurements), for each of the left and right three phase points observed. Once these angles had been measured, and the anomalies excluded, the remaining angles were averaged to determine a representative contact angle for each of the surfaces.

The contact angles measured on each of the surfaces are presented in Chapter 6, along with the discussion of these results.

3.3 References

1. H. Sha, R. Diedrichs, K. Schwerdtfeger, *Metallurgical and Materials Transactions B*, 1996, **27**, (2), 305-314
2. B. E. Deal, A. S. Grove, *Journal of Applied Physics*, 1965, **36** (12), 3770–3778
3. A.F. Stalder, G. Kulik, D. Sage, L. Barbieri, P. Hoffmann, *Colloids And Surfaces A: Physicochemical And Engineering Aspects*, 2006, **286**, (1-3), 92-103
4. A.F. Stalder, T. Melchior, M. Müller, D. Sage, T. Blu, M. Unser, *Colloids and Surfaces A: Physicochemical and Engineering Aspects*, 2010, **364**, (1-3), 72-81
5. C.A. Schneider, W.S. Rasband, K.W. Eliceiri, *Nature Methods*, 2012, **9**, 671-675

4 Aqueous Analogues for Detection of Dendritic Growth

4.1 Introduction

As discussed in chapter 1, to enable the concept of full recovery of fissionable material and reactive fission products from spent nuclear fuel to be achieved in molten salts, the use of a liquid cathode is essential. The proposed system relies on a range of materials, largely fission products, being safely, and simultaneously captured by alloying these materials in a liquid cathode. Producing an alloyed product is vital for a pyroprocessing system to be considered proliferation resistant, as selectively recovering highly active fission products would be politically untenable.

If such a pyroprocessing system is to be adopted, then a fundamental understanding of the reduction processes at liquid cathodes and the resulting products must be established. Given the technological challenges in carrying out rigorously controlled experiments in molten salts, it would be prudent to first understand the fundamental processes in analogous systems at room temperature.

This chapter expands on previous work at the University of Edinburgh by Dr Nathan Brockie[1], which focused on visual observation of the reduction processes and the surface structures of deposits on the liquid surface. In Nathan's thesis zinc and copper are identified as suitable analogues for metals deposited at liquid cathodes in molten salts which amalgamate with the liquid metal cathode and form solid dendrites respectively. Zinc was chosen for two reasons; it readily forms amalgams with mercury, which do not become solid until 30 atomic percent zinc[2]; and the diffusion coefficient of zinc in mercury (10^{-5} cm^2 s^{-1}) is similar to uranium in cadmium or bismuth liquid cathodes[3, 4]. Copper was selected as it amalgamates with mercury to a much lesser extent, and deposition forms the solid thermodynamic product Cu_7Hg_6, belendorffite, at all concentrations.

Here the electrochemical response during deposition of zinc and copper at a liquid mercury cathode are studied on macro- and micro- electrodes. The electrochemical response observed during dendritic growth has been investigated at macro- and micro- electrodes, and compared to demonstrate a characteristic indicator of when dendritic growth is occurring. To eliminate the possibility of calomel formation on the surface of the mercury electrodes influencing the

results, experiments were carried out using nitrate solutions and were kept free from chloride contamination.

4.2 Electrochemistry of Zinc (II) at a Mercury Pool Cathode

First, the deposition of zinc, which is known to form an alloy with mercury, at the macro mercury electrode was investigated to establish the behaviour that can be expected when the desired process of recovery in a molten salt is achieved.

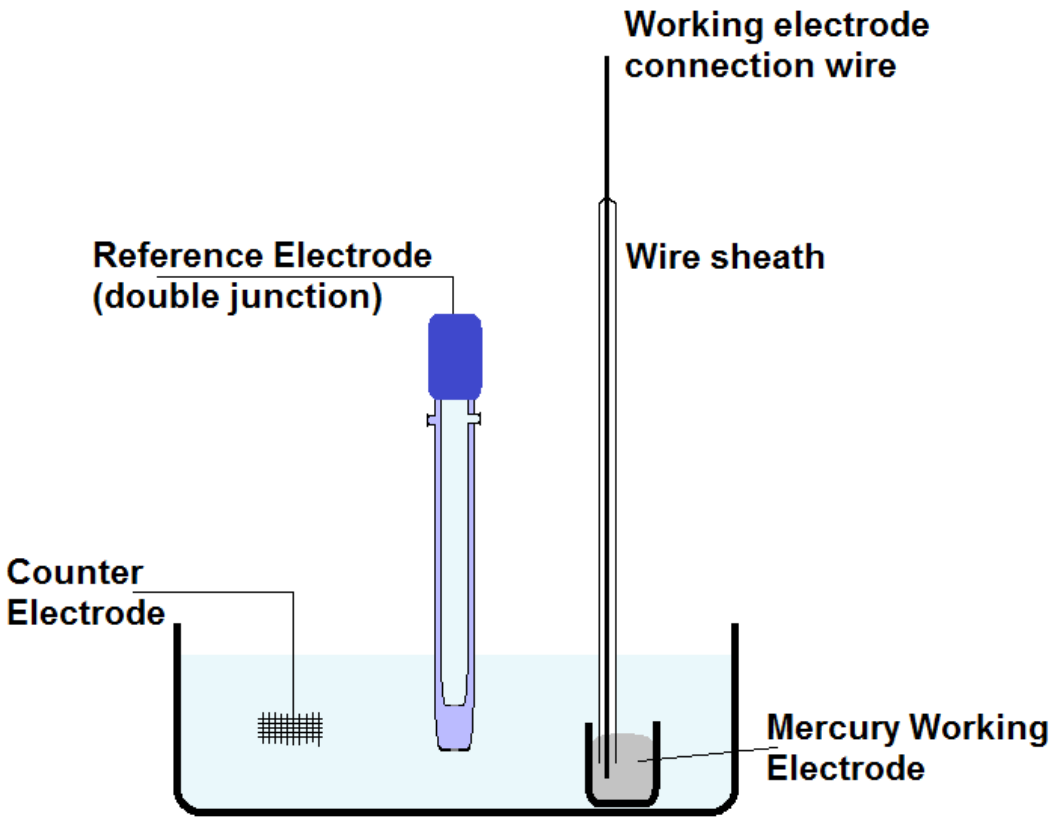

Figure 4.1: Experimental set-up for liquid macroelectrode experiments.

Figure 4.1 shows the schematic of the 3 electrode cell where the working electrode is a crucible filled with mercury, and an electrical connection is made through a sheathed wire. The apparatus and method for the liquid macroelectrode experiments is discussed in detail in section 3.1.2.

In solution, zinc ions exist as Zn^{2+}, which is reduced in a single, 2 electron process to Zn^{0}, and oxidised back to Zn^{2+}. At the mercury cathode, the reduced zinc forms an alloy with the mercury metal as shown on the phase diagram in Figure 4.2.

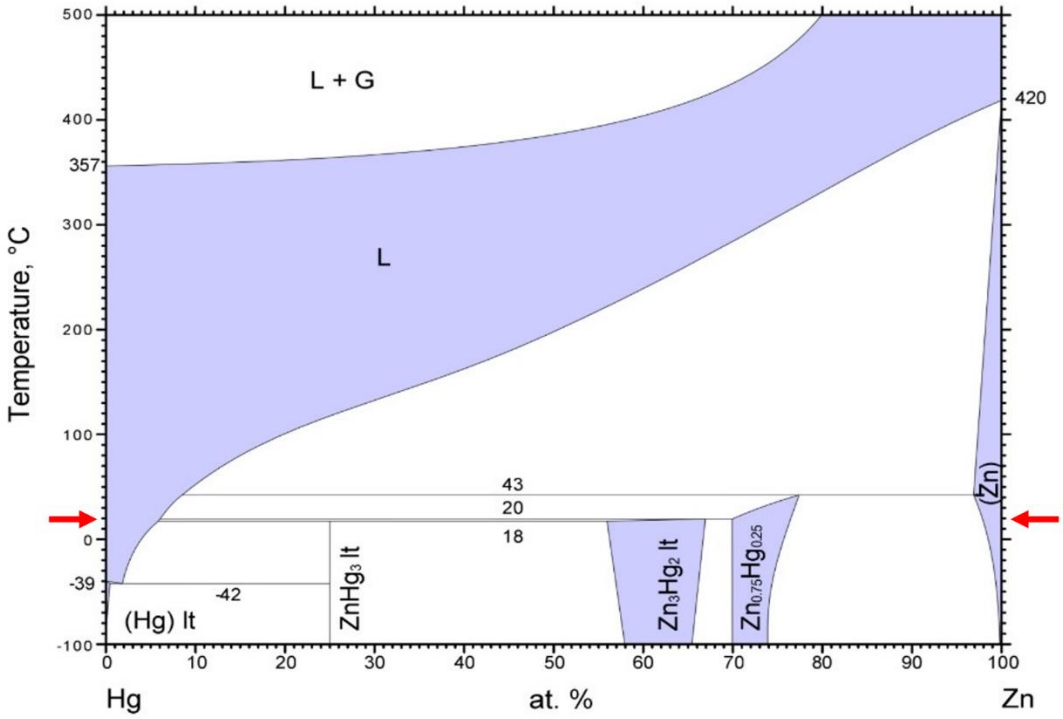

Figure 4.2: Phase diagram of mercury-zinc system[5] showing their alloys. White sections indicate a two-phase field, whilst shaded sections indicate a single-phase field with its composition noted. The red arrows indicate the approximate temperature at which the experiments were conducted.

The phase diagram in Figure 4.2 shows that at room temperature (indicated by the red arrows) there are three distinct alloys of mercury and zinc. In order of increasing zinc content, these are $ZnHg_3$, Zn_3Hg_2 and $Zn_{0.75}Hg_{0.25}$. As zinc is reduced at the electrode, it is not clear whether

the alloy formation is limited to the surface of the electrode, the alloy diffuses into the mercury metal, or whether the alloy is solvated within the mercury pool.

As the proportion of zinc increases, the density of the alloy decreases from a density of 14.4 g cm^{-3} for pure Hg[6] to a density of 9.47 g cm^{-3} for the alloy $Zn_{0.75}Hg_{0.25}$[7]. The density of zinc is 7.4 g cm^{-3} [8]. As zinc is reduced at the surface of the electrode, the alloy formed floats on the denser mercury pool, and the boundary between the alloy and the mercury grows into the pool rather than a homogeneous mix of the alloy and the mercury metal.

4.2.1 Zinc Deposition on a Macro Liquid Metal Electrode

The typical current time transient of zinc reduction at a mercury liquid cathode is shown in Figure 4.3.

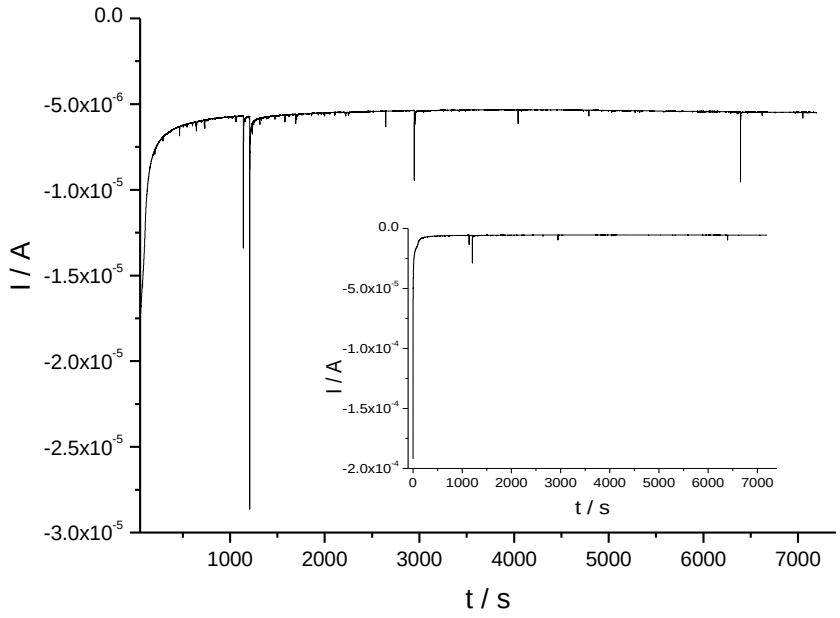

Figure 4.3: Current -time transient for the reduction of Zn (II) at a mercury electrode at -0.2 V vs Ag/AgCl with 100 mM $Zn(NO_3)_2$ in 0.1 M KNO_3. Note spikes are electrical noise and there is a background current of -5 x 10^{-6} A on the Zn-Hg amalgam.

In Figure 4.3 the current response is as would be expected for a continuous reduction. Spikes in the transient are due to electrochemical noise from adjacent equipment, and external convection from other activities in the lab. After around 1500 seconds the current reaches a background current of $-5x10^{-6}$ A. At this point a Zn-Hg alloy has formed at the electrode surface and although a background current was observed the deposition had become diffusion limited.

Having deposited Zn at the electrode surface, the potential was switched to oxidise the zinc and the current time transient is shown in Figure 4.4.

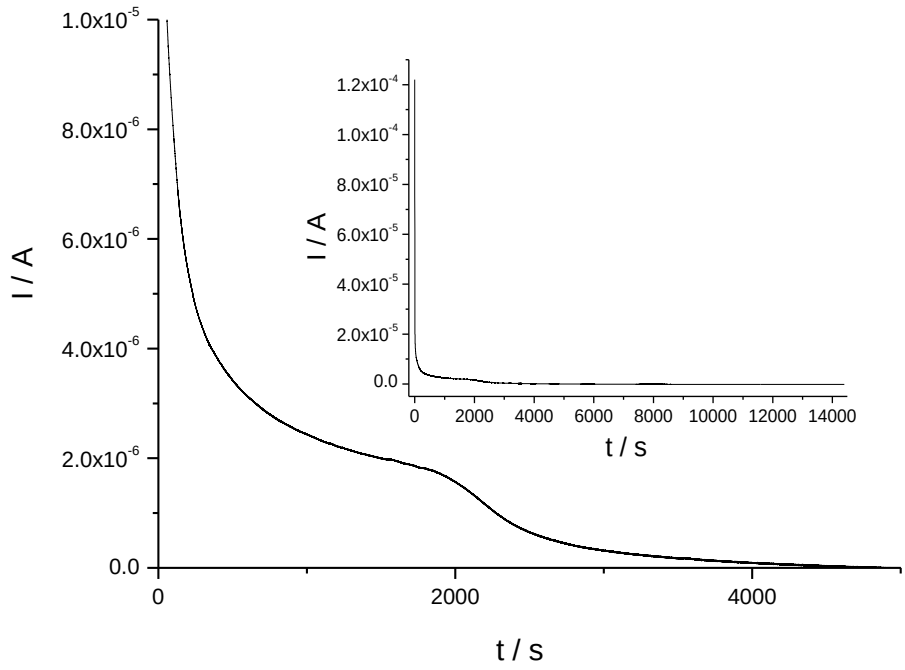

Figure 4.4: Current-time transient of the oxidation of zinc from a liquid mercury electrode at 0.5 V vs Ag/AgCl with 100 mM $Zn(NO_3)_2$ in 0.1 M KNO_3.

In Figure 4.4 the zinc oxidation current initially jumps as the diffusion layer is charged and the current decays as the reaction is diffusion limited by the rate of zinc diffusing out of the mercury pool. After around 2000 seconds the current response changes as the zinc is depleted

from the mercury and the reaction is limited by the last of the zinc ions diffusing away from the electrode surface.

Comparison of the reduction and oxidation charges (less the background current) indicates that all the deposited zinc is stripped from the liquid pool during the oxidation step. Almost 90% of the reduction current was passed during the oxidation of the zinc (3.15 mC passed during oxidation vs 3.54 mC passed during reduction). As the reduction charge includes what is likely to be a small background current, and the oxidation current returned to, and held at zero A, it is assumed that all of the zinc reduced at the mercury cathode was re-oxidised electrochemically and there were no losses of zinc due to competing mechanisms.

Furthermore, the shape of the oxidation curve is characteristic of a bounded Cottrell (Section 2.2.2) systems in solid films on planar electrodes, where the concentration of an electroactive species changes noticeably over a short space of time. This effect is observed where the electroactive species is in a thin layer similar in thickness *l* to the diffusion layer.

The application of the bounded Cottrell equation to reduction and oxidation at liquid metal cathodes has not previously been reported. To confirm the behaviour at around 2000 seconds could be attributed to the bounded Cottrell system, the current-time transient was plotted as current vs $t^{-1/2}$ in Figure 4.5.

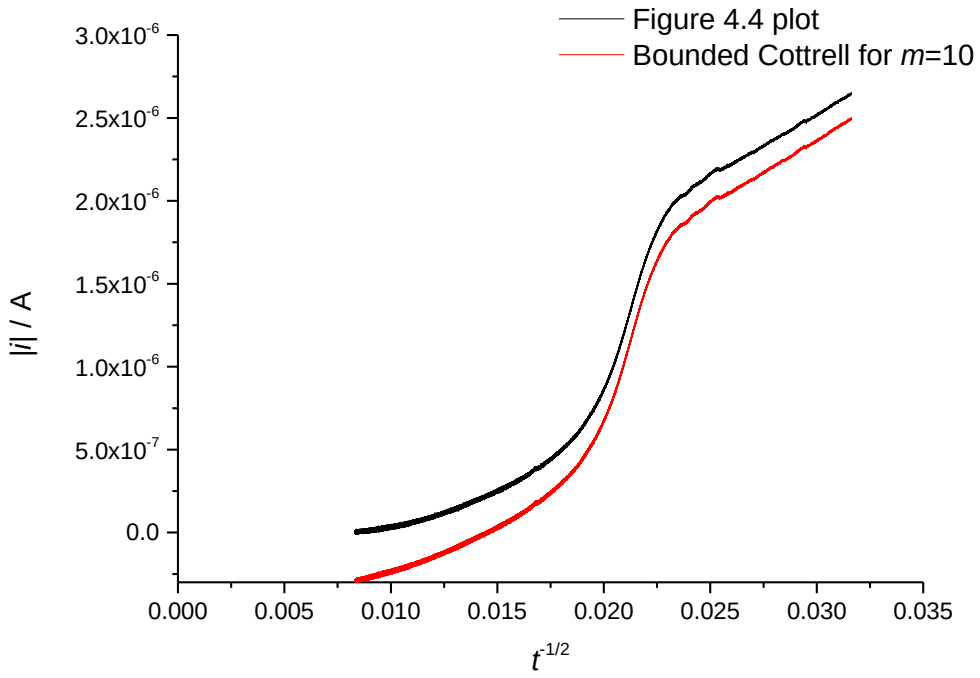

Figure 4.5: Plot of *i* vs $t^{-1/2}$ for the oxidation of Zn from the mercury cathode at 0.5 V vs Ag/AgCl with 100 mM $Zn(NO_3)_2$ in 0.1 M KNO_3 and the fit line to the bounded Cottrell equation for m = 10, truncated to *t* = 1000 to 5000 seconds.

Here, the straight line component of the plot (where $t^{-1/2}$ is greater than 0.025) represents the diffusion controlled oxidation of Zn, where the gradient is equal to the diffusion coefficient. The gradient of the straight line segment in Figure 4.5 (above $t^{-1/2}$ = 0.025) is 3.39×10^{-5} cm^2 s^{-1} which is in close agreement to the literature diffusion coefficient value for zinc in mercury metal of 1.46 - 3.35×10^{-5} cm^2 s^{-1} [4].

This response indicates that the reduced zinc ions extend only into a portion of the total depth of the liquid cathode. This depth, *l*, is the depth to which the Zn-Hg alloy is formed during deposition, and is proportional to the density of the alloy formed and the amount of zinc reduced. This phenomenon also suggests that the Zn-Hg alloy formed during Zn reduction

does not form a homogeneous liquid with the Hg metal, and instead floats at the surface of the liquid electrode.

Unfortunately, the density of the $ZnHg_3$ alloy is not precisely known. However, if it were, it would be possible to determine the precise layer thickness from the density and the charge passed during the oxidation. Using the time taken for the zinc to diffuse from the mercury pool and the rate of diffusion of zinc in mercury, it is possible to estimate that the thickness of the alloy layer was 6.78×10^{-3} cm. As this layer thickness is much smaller than the depth of the mercury pool, the assumption that the mercury does not distribute equally through the electrode and behaves in line with the bounded Cottrell equation could be valid.

Should a molten salt reprocessing system be adopted, complicated monitoring solutions would need to be engineered to optically determine whether solid deposition or indeed dendritic growth is occurring at the liquid electrode surface. Electrochemical monitoring is preferential, as this will reduce the complexity of the system, and provide accurate early warning to the formation of dendritic growth. Preventing such growth is critical to achieving the desired recovery of species from the melt, and in preventing the loss of solid material to the containment structure or shorting of the electrochemical circuit.

4.2.2 EIS of Zinc Deposition on a Macro Liquid Metal Electrode

In previous work, electrochemical impedance spectroscopy was investigated as a potential tool for monitoring the electrodeposition characteristics and determination of when solid deposition was taking place. The concept is that by taking short impedance measurements during the deposition experiments, the solution resistance can be monitored, and changes in solution resistance equated to solid formations on the liquid electrode surface. Solution resistance is proportional to the electrode area and any increase in electrode area owing to solid dendrite growth will be measured as a drop in solution resistance.

During the course of the deposition of zinc, electrochemical impedance at OCP of the liquid electrode surface was measured at intervals to detect changes at the electrode/ solution interface.

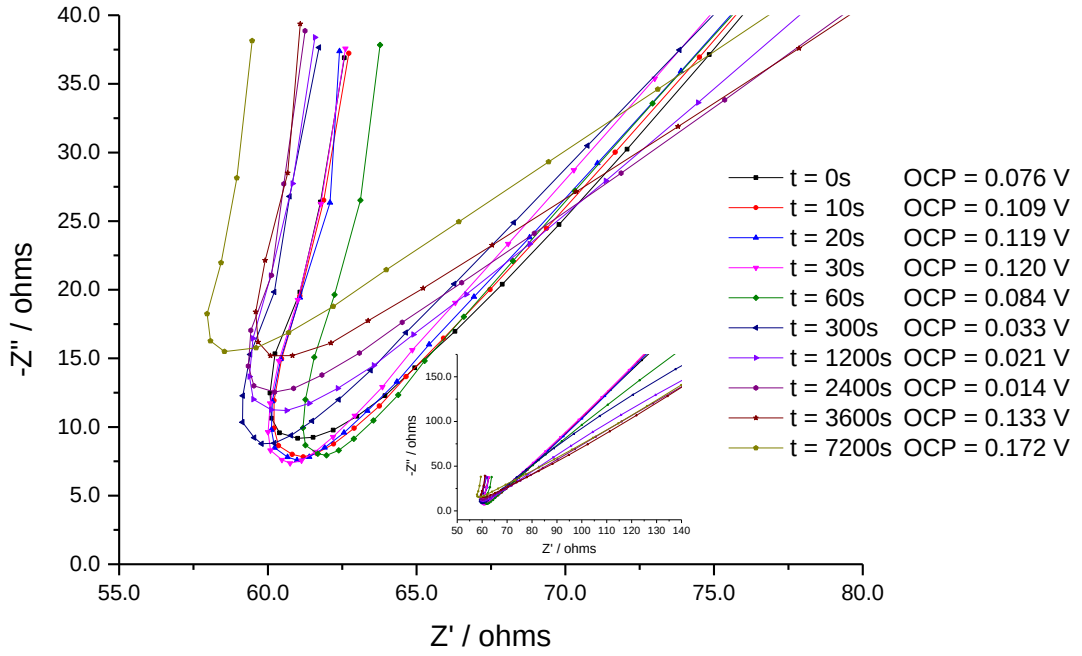

Figure 4.6: Nyquist plots of impedance spectroscopy at OCP of a liquid electrode during deposition of Zn.

On the Nyquist plot the high frequency limit on the Z' axis gives rise to the solution resistance, R_s. In general, there is no significant difference between the value for R_s in each plot in Figure 4.6, with the solution resistance being 61 Ω to 2σ confidence.

The angle of the straight line produced in the nyquist plot can also be indicative of changes at an electrode surface. In Figure 4.6, the slope of this line is 45° on the scans for 0 to 300 seconds of deposition, however the angle decreases in the plots after longer deposition times. This is common when the Warburg impedance is supressed by a constant phase element and is typical for when the electrode surface changes from 2d (smooth) to 3d (roughened).

As mercury has a high surface tension, the surface of the electrode is almost perfectly smooth at the outset of the experiment (save for any small external contaminants). As zinc is reduced at the mercury surface, the zinc initially forms an alloy with the mercury and diffuses into the bulk mercury. As the mercury at the surface of the cathode alloys with the zinc, less free mercury is available to combine with the zinc being reduced at the interface. This results in an increase in the localised concentration of zinc reduced at the electrode which deposits as either

a solid, or forms a solid alloy with a higher zinc content, roughening the surface of the electrode.

The Nyquist plot in Figure 4.6 also shows that over the duration of the reduction of zinc, the OCP increases. This increase in the OCP would indicate that the increase in localised zinc concentration at the electrode surface is more stable to further zinc deposition, and may ultimately result in dendritic growth. Where zinc had been deposited at the surface of the liquid electrode, the OCP was found to be stable for at least 30 minutes, providing further evidence for the stability of the zinc reduction product.

4.3 Electrochemistry of Copper (II) at a Mercury Pool Cathode

In contrast to zinc, where long deposition times were required to initiate solid growth from the liquid electrode surface, copper is known to grow dendrites when deposited at a mercury cathode[1]. The electrochemical response when copper is reduced at a macro mercury electrode was investigated to establish the behaviour that can be expected when the dendrites form in a molten salt reprocessing system.

The phase diagram for copper and mercury is shown in Figure 4.7.

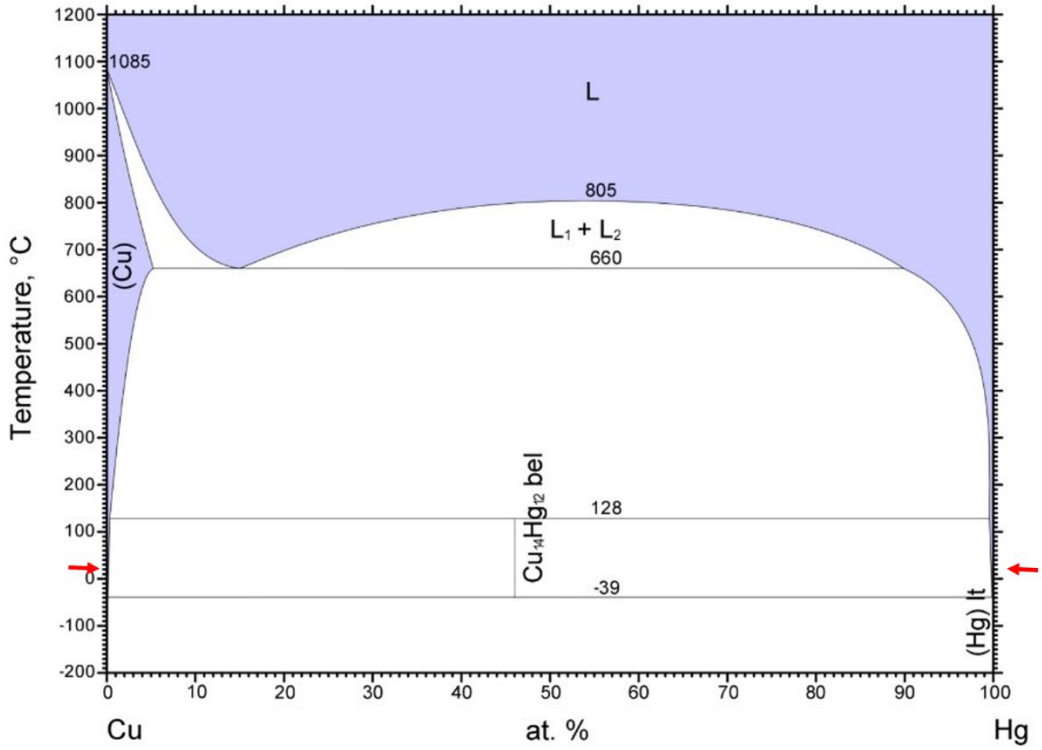

Figure 4.7: Phase diagram of mercury-copper system[9] showing their alloys. White sections indicate a two-phase field, whilst shaded sections indicate a single-phase field with its composition noted.

In the phase diagram in Figure 4.7, a single, thermodynamic alloy of Cu-Hg is identified as forming between -39 °C and 128 °C when the copper is reduced at the mercury electrode. This alloy, $Cu_{14}Hg_{12}$ is a solid at room temperature with a density of 13.17 g cm^{-3} [10]. Again, this alloy is less dense than mercury metal (14.4 g cm^{-3}) and denser than copper, which has a density of 8.93 g cm^{-3} [11]. In each case of the alloy and copper metal, solid deposits can be expected to float on the surface of the mercury cathode.

Studies of bulk electrodeposition of copper (0) at a liquid mercury cathode in chloride solutions have previously been reported[1]. In these studies, the electrochemistry was complicated by the irreversible formation of calomel, which formed a solid product at the electrode regardless of copper deposition taking place or not. This study seeks to investigate dendritic growth of copper at a liquid cathode without the complication of calomel formation,

and determine characteristic indicators of when dendritic growth is taking place as a model for molten salt systems.

4.3.1 Copper Deposition on a Macro Liquid Metal Electrode

As in Section 4.2, the electrochemical cell was set up as shown in Figure 4.1: Experimental set-up for liquid macroelectrode experiments. Figure 4.1, with the liquid mercury cathode formed from liquid mercury bound within a crucible and an electrical connection made through a sheathed wire. The copper solution was prepared from copper nitrate and potassium nitrate background electrolyte to prevent a solid calomel (Hg_2Cl_2) crust forming on the liquid electrode surface, and degassed with argon.

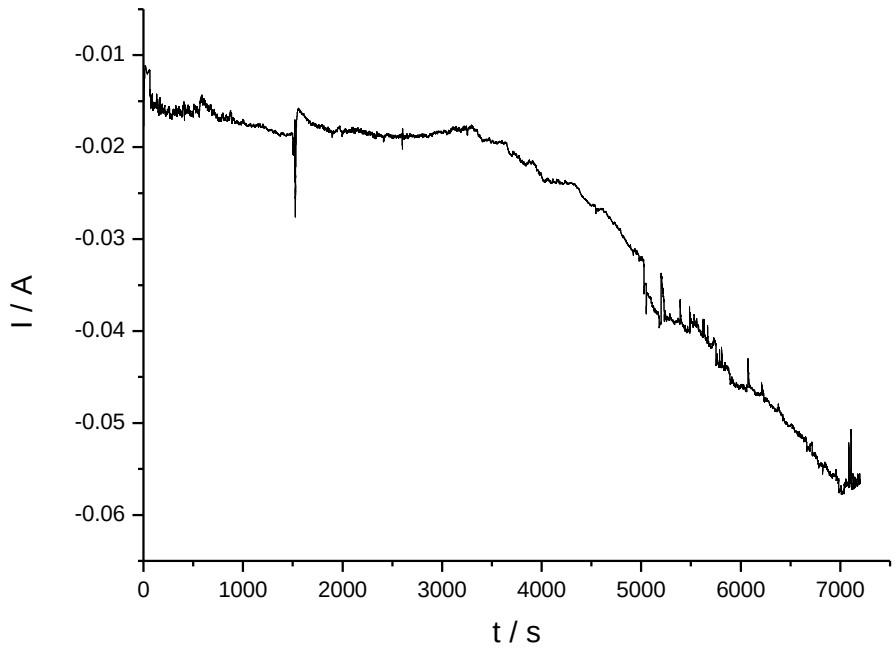

Figure 4.8: Current - Time transient of reduction of Cu (II) at a liquid mercury electrode at -0.7 V vs Ag/AgCl with 100 mM $Cu(NO_3)_2$ in 0.1 M KNO_3

Figure 4.8 shows a typical current-time transient for the deposition of copper at a liquid electrode surface. Unlike the transient observed for zinc deposition, the current in the transient

for copper deposition increases in magnitude throughout the period the reduction potential was applied.

Initially the current grows slowly with rapid fluctuations in the measured current, typically associated with noise, occurring at irregular intervals. Drops in the magnitude of current flowing occur at approximately 650 seconds and 1500 seconds, however in each case the current stabilises, and again gradually increases immediately after the drop. After approximately 3500 seconds the rate of increase in current quickens, and the current steadily increases threefold over the next 3500 seconds, albeit with increasing fluctuations after 5000 seconds.

The increase in current during the reduction shown in Figure 4.8 is indicative of an increasing electrode area. Here this is most likely due to a solid crust, or dendritic growth from the liquid surface, such that the copper metal becomes an extension of the electrode, increasing the area of the electrode. Further growth then occurs from the solid deposit, so the electrode continues to grow in size. The drops in current observed during the reduction, could be explained by a loss of electrode area caused by some of these solid growths detaching from the liquid electrode, the diffusion field of two fractal growth tips joining or the active sites on the electrode becoming passivated in some way.

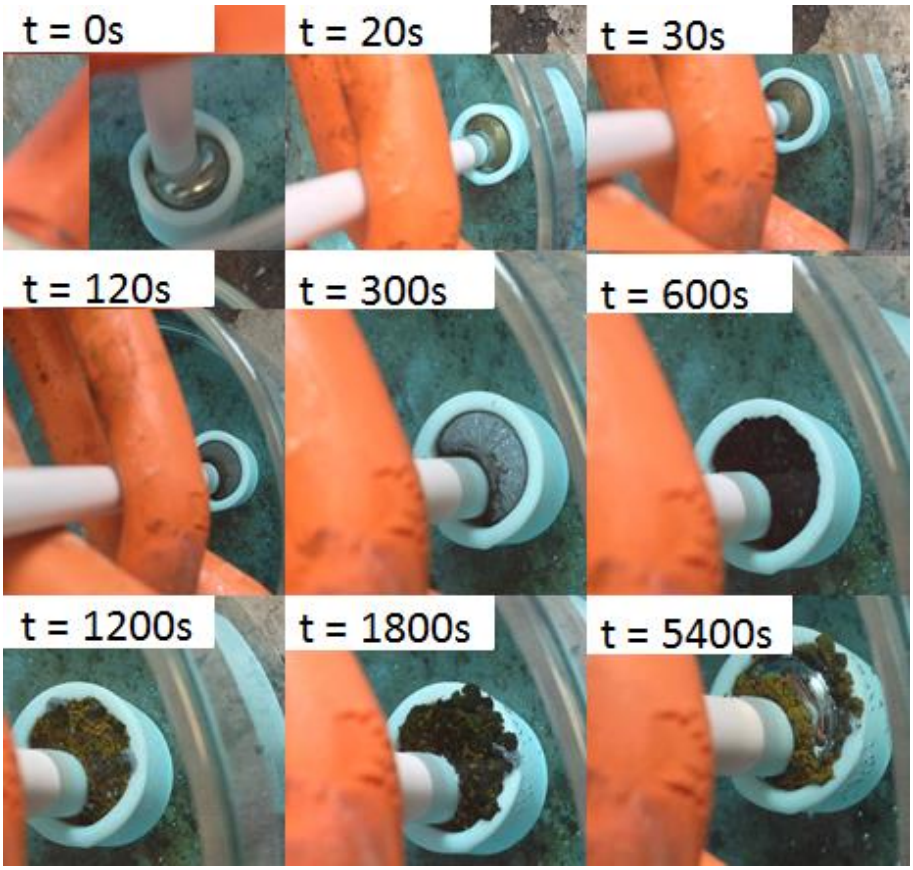

Figure 4.9: Images of the mercury cathode surface during Cu deposition. After 1800 s the current was reversed to oxidise the Cu from the electrode, however after 5400 s solid deposits were still visible on the electrode surface.

To confirm that dendritic growth, and subsequent detachment of dendrites is responsible for the variation in current, the experiment was repeated over 1800 second reduction whilst pictures of the electrode were captured. After 1800 seconds, the potential was switched to an oxidising potential, and a further image captured after 5400 seconds. Figure 4.9 shows pictures of the mercury electrode surface at t = 0, 20, 30, 120, 300, 600, 1200, 1800 and 5400 seconds.

In these images, the initial nucleation of copper on the mercury surface, and subsequent growth of dendrites can be clearly seen. These deposits are substantial in size, but fragile in structure, and are easily disturbed by solution turbulence and hydrogen evolution. The nature of the dendritic growth essentially consists of fine nano-wires that grow from the tips where the current density is greater, and hence diffusion from the solution is unimpeded (as opposed to diffusing to the surface of the mercury). In the 1200 second and 1800 second images, the

dendrites can be seen to exceed the boundary of the ceramic crucible. Whilst not immediately obvious in these pictures, solid copper deposits have detached from the liquid electrode surface and collected in the bottom of the flask.

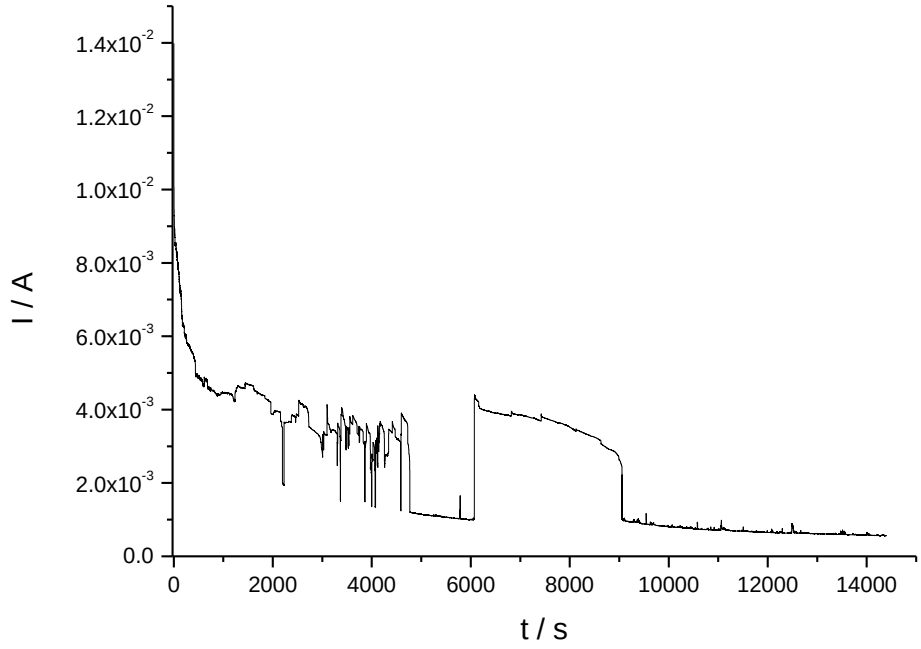

Figure 4.10: Current- Time Transient of the oxidation of copper from a liquid mercury electrode at 0.6 V vs Ag/AgCl with 100 mM $Cu(NO_3)_2$ in 0.1 M KNO_3.

Figure 4.10 shows the corresponding current-time transient of oxidation of copper from the liquid cathode to the reduction shown in Figure 4.8. As with the reduction, the oxidation transient shows large fluctuations in the current as dendrites are oxidised in an irregular pattern. The drop in oxidation current between 4800 seconds and 6000 seconds can be accounted for as a significant detachment of the fern-type growth from the surface of the electrode, which then reconnects with the electrode as the fragile network of deposited copper collapses from either gravity or convection/ external vibration.

During the reduction of copper, 200 mC of charge is passed, however during the oxidation phase, 35 mC is passed. The difference between these charges can be explained through the loss of the reduced product from the electrode surface due to physical mechanisms. Such

processes have already been observed under optical observation (Figure 4.9) where dendrites have detached from the electrode under their own mass, and fallen to the bottom of the crucible.

The current-time transient observed for the deposition of copper on the mercury electrode provides a diagnostic “finger print” for when dendritic growth is taking place but cannot be directly observed due to constrains of the system. In Section 4.2, the reduction of zinc followed the classical decay to a steady state current during deposition, dendrites were not explicitly observed. Rather in the case for long depositions of zinc, the electrode surface only dulled in appearance. The behaviour in the current time transient for copper deposition, where dendritic growth was confirmed through visual observations, is diagnostic of dendritic growth, and has been observed over many experiments in this work, and also in the preceding work by Dr Nathan Brockie.

In isolation, observing this behaviour in a current transient can be used to identify when dendritic growth has taken place. This indication is of little use in a reprocessing system where such growth can be detrimental to the overall process, so it would be preferential to determine a diagnostic which can warn of the early onset of dendritic growth.

4.3.2 EIS of Copper Deposition on a Macro Liquid Metal Electrode

As with the zinc experiments in Section 4.2, the electrochemical impedance at OCP was measured periodically throughout the deposition.

As discussed in Section 2.2.3, electrochemical impedance is an important tool in studying changes at an electrode surface, and can give a detailed insight into the processes taking place at the electrode-solution interface.

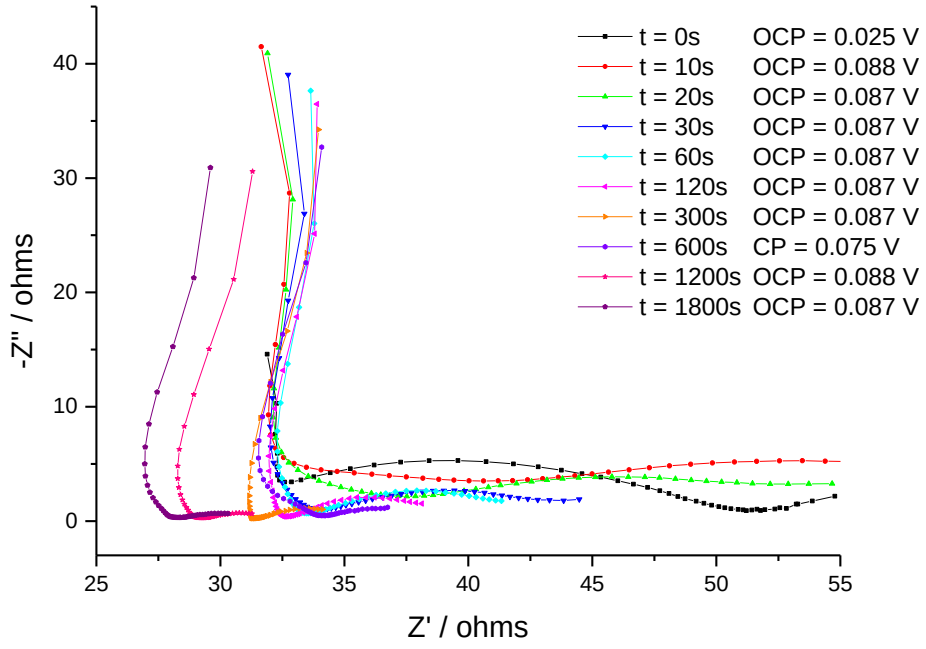

Figure 4.11: Nyquist plots of impedance spectroscopy at OCP of a liquid electrode during deposition of copper from 100 mM $Cu(NO_3)_2$ in 0.1 M KNO_3

Figure 4.11 shows the Nyquist plots measured by electrochemical impedance spectroscopy during the deposition of copper at the liquid mercury electrode. In this plot, the solution resistance R_s can be seen to decrease over the course of the deposition, particularly in the impedance spectra for 1200 seconds and 1800 seconds of copper deposition. Even after only 330 seconds, where dendritic growth is minimal (Figure 4.9), a reduction in the solution resistance can be observed. Typically, the deposition of a metal at an electrode would be expected to have little effect on the solution resistance, which is generally a function of the distance between the working electrode and the reference electrode, and the effective electrode area. Under dendritic growth, both the electrode distance decreases, and the electrode area increases.

This EIS response is a further diagnostic for determining when dendritic growth is taking place. In a reprocessing system a reduction in the solution resistance could be used as a trigger to stop the deposition process before a critical failure can occur.

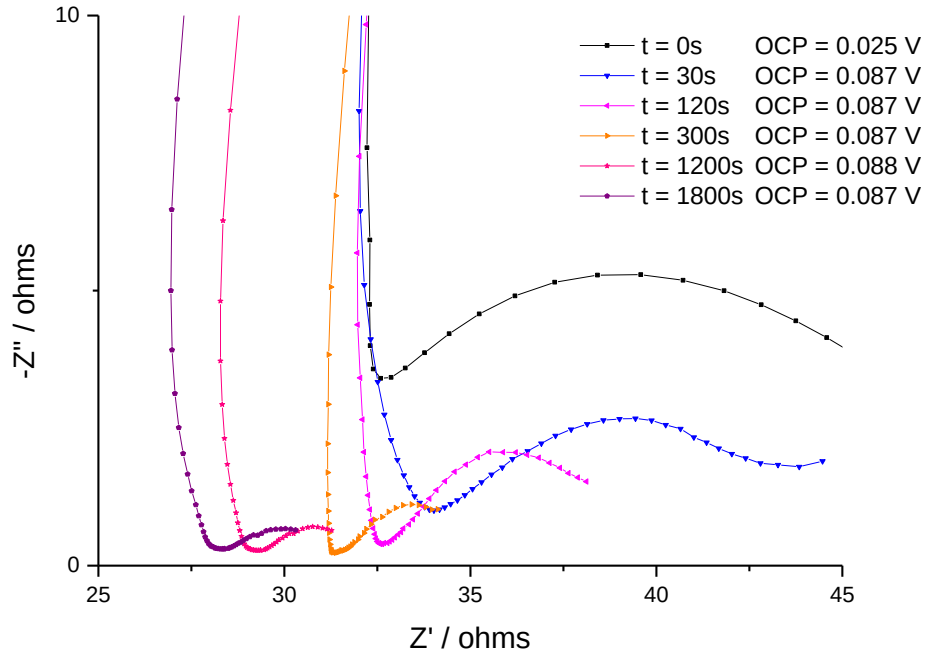

Figure 4.12: Expanded Nyquist plot of impedance spectroscopy at OCP of a liquid electrode during deposition of copper from 100 mM $Cu(NO_3)_2$ in 0.1 M KNO_3 at t = 0, 30, 120, 300 1200 and 1800 seconds.

In addition to the change in solution resistance the charge transfer semi-circle can clearly be seen to be decreasing in size as reduction of copper at the electrode becomes easier (lower energy) and then resistance drops for Cu on Cu deposition. This is even more evident in Figure 4.12, which is an expanded plot of Figure 4.11, where the peak of the charge transfer semi-circle prior to deposition halves after only 30 seconds from 5 Ω to 2.5 Ω, and then halves again by 300 seconds.

This change in charge transfer resistance is even more prominent during the early stages of dendritic growth than that of the change in solution resistance. This characteristic is also a useful diagnostic tool to indicate when dendritic growth is occurring, and is arguably more sensitive to dendritic growth, and therefore can provide earlier warning to prevent failure of the reprocessing system.

4.4 Detection of Dendritic Growth at Mercury Microelectrodes

As discussed in earlier chapters, microelectrodes are known to be far better diagnostic tools owing to their intrinsic properties of greater signal to noise and greater sensitivity. Ideally, a reprocessing system will employ microelectrode sensors instead of having to perform diagnostic tests on the bulk liquid cathode used for recovery of species, which would require halting the process at a regular interval.

Parallel work is ongoing to develop microelectrodes that are resistant to molten salts that can be utilised in the proposed reprocessing system, however, it is also important to understand how the use of microelectrodes will influence the characteristic behaviour of dendritic growth.

To provide an analogous study of the electrochemical response that can be expected from liquid microelectrodes, mercury was plated on the planar platinum electrodes using a previously reported method [12] to replace the mercury pools in the experiments in sections 4.2 and 4.3.

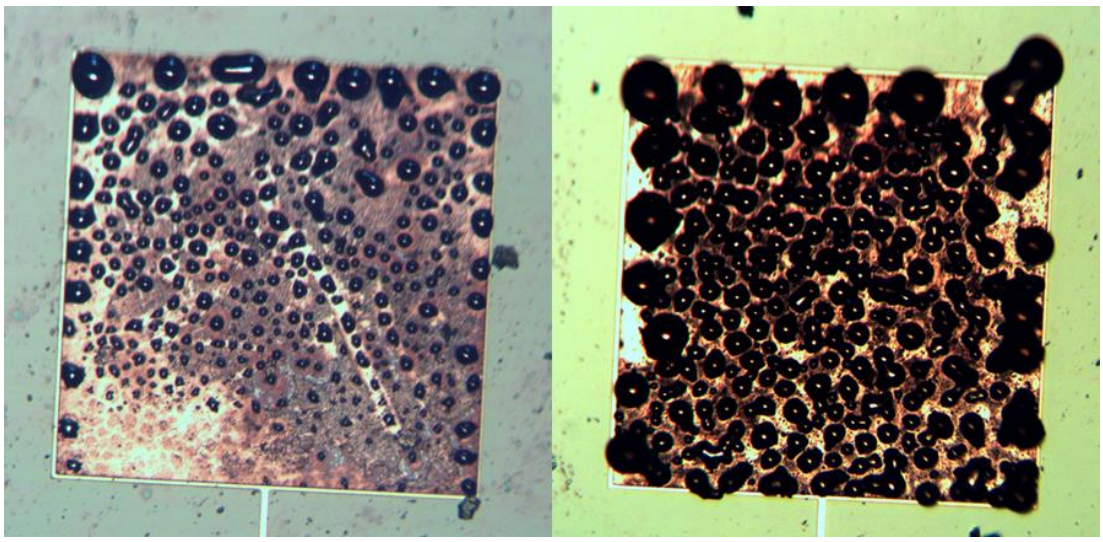

Figure 4.13: Images of mercury deposited onto 500 µm square Pt electrodes. Rather than depositing as a homogenius film, the mercury accumulated in small droplets, which acted as a randomly distributed microarray.

Figure 4.13 shows the typical result of depositing mercury onto the platinum microelectrodes. This deposition formed small droplets of mercury distributed across the platinum square to

form a randomly distributed array of mercury electrodes. Arrays of this nature on the micron scale benefit from hemispherical diffusion, and have been shown to be useful as high-performance sensors[133-15].

Once prepared, images of each of these mercury electrodes were captured and those with the greater coverage of mercury, as shown in the right hand image in Figure 4.13 were used in investigating the deposition behaviour of zinc and copper.

4.5 Amalgamation of Zinc at a Mercury Microelectrode

In Section 4.2, zinc was seen to, at least initially, alloy with mercury when reduced at the surface of a liquid mercury cathode. On a liquid metal microelectrode, the total volume of liquid metal will be greatly reduced, with only a thin layer covering the underlying electrical connection. The diffusion to a micro electrode is also greatly enhanced, and it could therefore be possible that dendritic growth could occur far more readily at a liquid microelectrode than on a macro pool.

To determine the effect of using a microelectrode on the electrochemical response of deposition and possible dendritic growth of zinc at liquid mercury, the experiments from section 4.2 were repeated at a square mercury microelectrode with edge length of 100 μm.

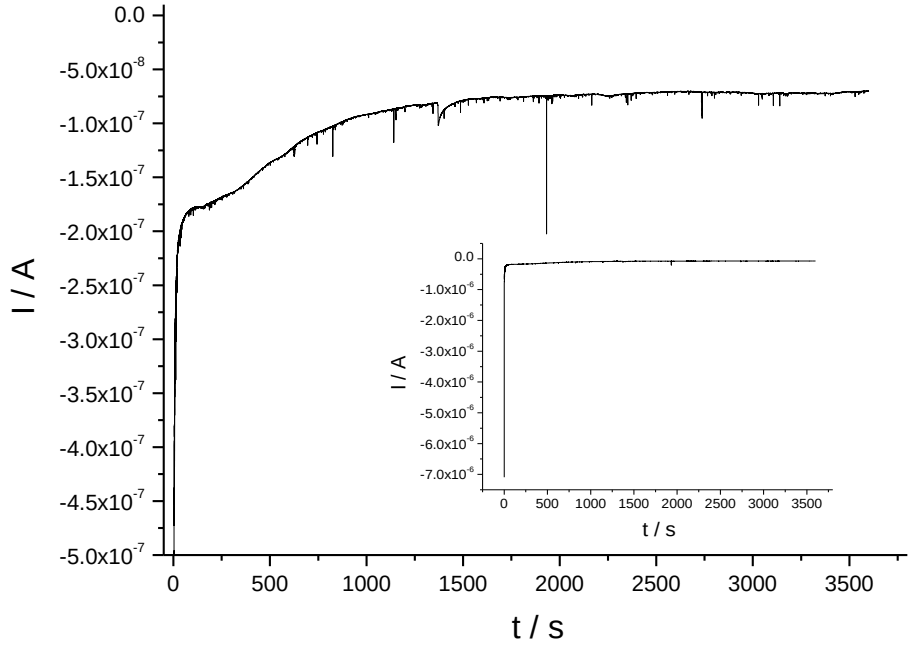

Figure 4.14: Current - time transient of reduction of Zn (II) at a 500 µm square electrode with a liquid mercury film at -0.2 V vs Ag/AgCl with 10 mM $Zn(NO_3)_2$ in 0.1 M KNO_3. Note that the current stabilises at a background current of $-7x10^{-8}$ A after 2000 seconds.

Figure 4.14 shows the current-time transient of the deposition of zinc at a mercury microelectrode, similar to that shown in Figure 4.13. Over the course of the deposition, 88 µC of charge is passed and the current stabilises at a constant background current of $-7x10^{-8}$ A. This background current is most likely due to a secondary process taking place at exposed electroactive sites on the underlying platinum microsquare.

In this current time transient there are two obvious points at which the gradient of the decay changes, at 160 seconds and 540 seconds. There is also a feature in the transient at 1400 seconds where the current spikes and demonstrates diffusion-limited decay.

One possible explanation for these feature lie in the geometry of the mercury deposited onto the platinum square, where there are hemispherical drops of mercury sitting above the exposed, planar platinum electroactive area. However, the most likely explanation is that the first two features correspond to a change in rate of diffusion as the reduced zinc initially forms the alloy $ZnHg_3$, before saturating the exposed mercury and going on to react with the alloy at a slower rate to form the solid alloy Zn_3Hg_2. The feature at 1400 seconds was likely caused by

external diffusion exposing an active site on the mercury, as the spike decays back to the dominant curve.

After 3600 seconds of reduction, the potential of the electrode was switched to an oxidising potential, and the current-time transient for oxidation of the zinc was measured.

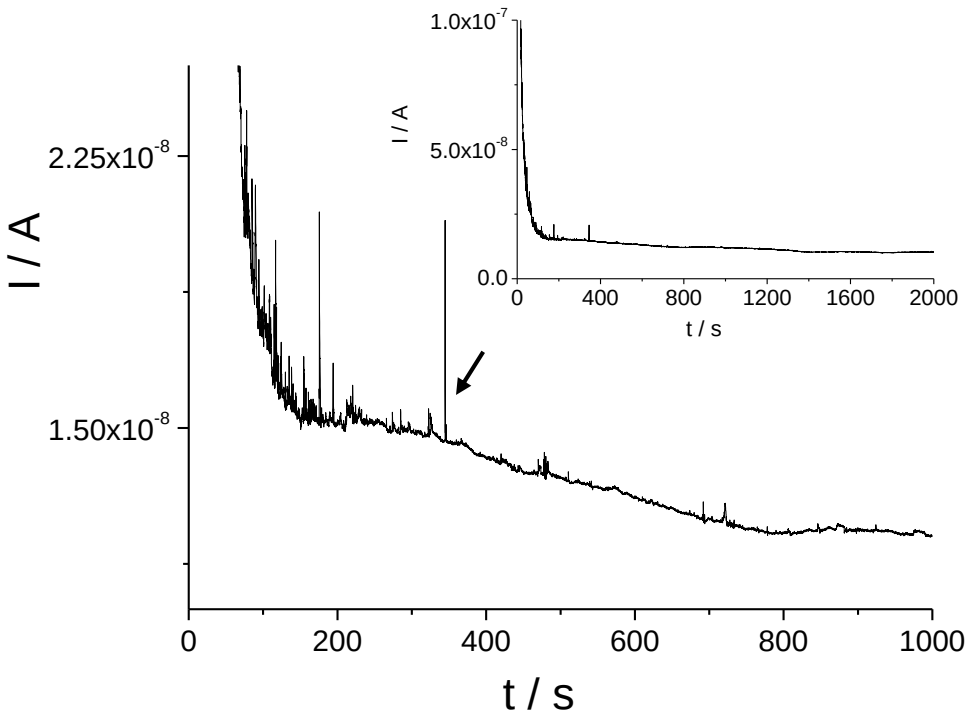

Figure 4.15: Current- time transient of the oxidation of Zn from a liquid mercury electrode cathode at 0.5 V vs Ag/AgCl with 10 mM $Zn(NO_3)_2$ in 0.1 M KNO_3.

In Figure 4.15 the current-time transient for the re-oxidation of zinc initially appears to be controlled by a single diffusion limited rate. On closer inspection however, an inflection in the current curve is apparent at approximately 360 seconds.

This change in rate indicates that the oxidation reaction changes, and can be interpreted as a change in the species being oxidised. It is assumed that the second diffusion limited rate is

mercury diffusing out of the liquid mercury, with the initial rate being the oxidation from the alloy Zn_3Hg_2 to the alloy $ZnHg_3$.

Over the course of the re-oxidation, 70 μC of charge is passed and the current stabilises at a constant background current of $1.1x10^{-8}$ A. This charge equates to 80% of the charge passed during the reduction, however does not take into account the background currents in both steps.

Images were then captured of the electrode after the reduction and re-oxidation of zinc to compare with the initial images from the preparation of the mercury microelectrodes.

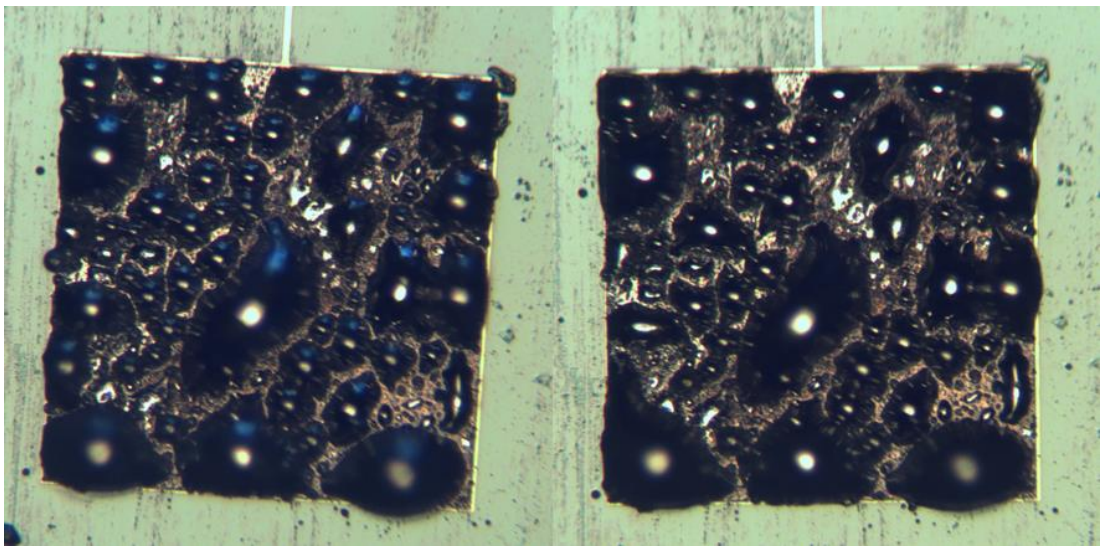

Figure 4.16: Images of the mercury electrode before (left) and after (right) the zinc deposition and re-oxidation shown in Figure 4.14 and Figure 4.15.

As can be seen in Figure 4.16, the mercury droplets on the liquid microelectrode were not greatly affected by the reduction and oxidation of zinc from the electrode, however small areas of the underlying platinum electrode did change slightly in appearance.

Optical appearance through a microscope can be deceiving and the slight change in colouration of the platinum could be considered circumstantial. To confirm that the mercury microelectrodes were not being structurally altered during the deposition and subsequent oxidation, the process was repeated over a number of iterations, with the electrodes studied under a microscope at varying stages of reduction and oxidation.

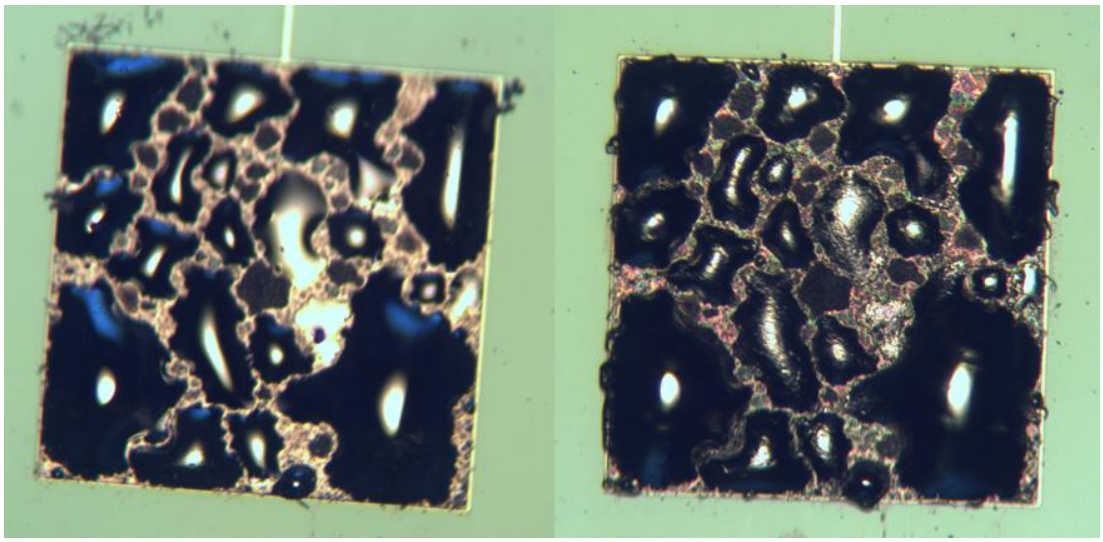

Figure 4.17: Images of the mercury electrode before (left) and after (right) zinc deposition over 3600 s. The electrochemical impedance of this electrode was recorded during the course of the deposition and the Nyquist plots are shown in Figure 4.18.

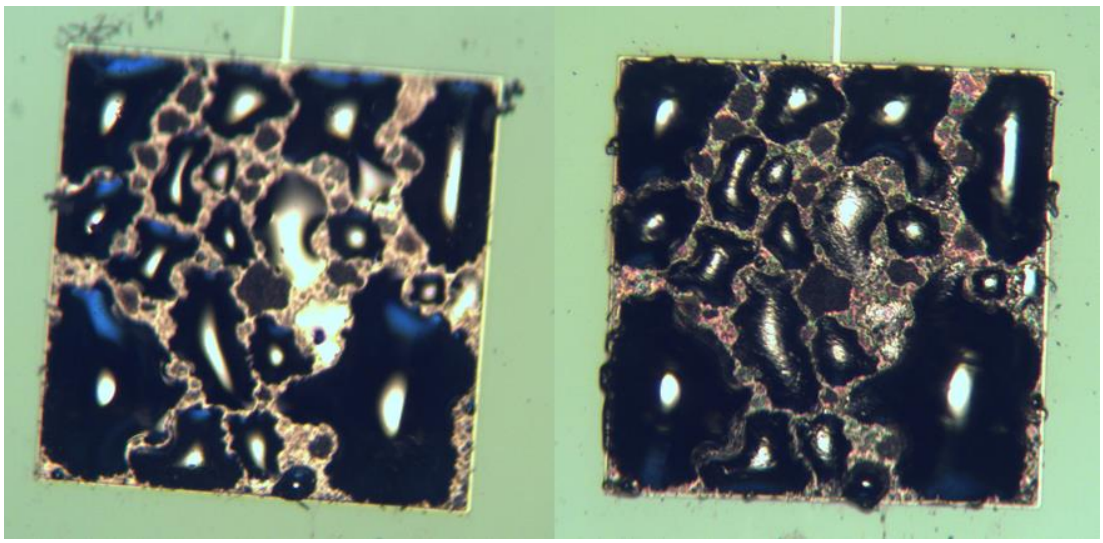

Figure 4.17 shows images of a mercury microelectrode before and after the deposition of zinc. As with Figure 4.16, the location of the mercury has not changed across the electrode, however it is clear that the surface of the liquid metal has become textured. The zinc-mercury amalgam on this electrode was found to have formed a solid film across each of the mercury droplets as was predicted from the change in diffusion rates in the current-time transients for reduction (Figure 4.14) and oxidation Figure 4.15).

As the mercury microelectrodes have a much thinner layer of mercury than in the bulk pool experiments, the mercury becomes saturated with Zn more quickly. Instead of the Zn-Hg alloy

diffusing into the bulk mercury metal and forming a mixed solution, here the reduction of zinc results in the solid alloy remaining at the surface of the electrode, as there is insufficient liquid mercury for the alloy to dissolve into.

As with the experiments of zinc reduction at a bulk mercury pool, electrochemical impedance spectroscopy was used to measure changes at the electrode surface as a function of deposition time.

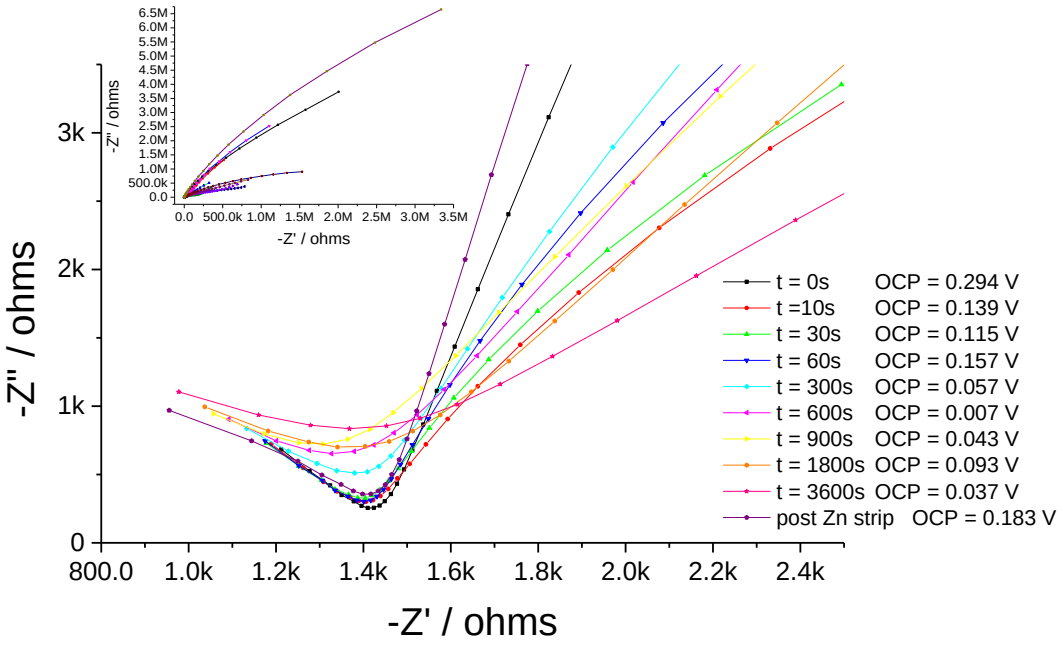

Figure 4.18: Nyquist plots of impedance spectroscopy at OCP of a liquid film electrode during reduction of Zn (II) at a liquid mercury electrode cathode at -0.2 V vs Ag/AgCl with 10 mM $Zn(NO_3)_2$ in 0.1 M KNO_3.

Figure 4.18 shows the Nyquist plots from the impedance measurements taken during the deposition of zinc. In these plots, the previously identified indicators of dendritic growth from the previous sections are present, specifically the solution resistance drops from 1424 Ω to

1380 Ω between 0 and 300 seconds; and the angle of the straight line decreases significantly over time.

After the zinc is oxidised from the electrode, the Nyquist plot shows that the electrode surface returns to its original state, with the solution resistance post oxidation measured as 1417 Ω and the slope of the line being similar to that recorded for 0 seconds.

The observation of these characteristics shows that the diagnostic behaviour seen at macro liquid electrodes also applies to micro liquid electrodes. Unlike the zinc experiments at the bulk mercury pool, it was possible to readily form a solid crust at the surface of the micro mercury electrode. The increased sensitivity of microelectrodes is as equally valid on liquid electrodes as it is on solid electrodes, and micro liquid electrodes lend themselves to being used as sensors in a molten salt reprocessing system to detect when dendritic growth is occurring.

4.6 Copper Dendrite Detection at a Mercury Film Cathode

The process of copper deposition at mercury has already been shown to readily form dendrites. To confirm that the observations made with the mercury microelectrode during the deposition

of zinc are truly representative of dendritic growth, the deposition of copper at liquid micro electrodes was also investigated.

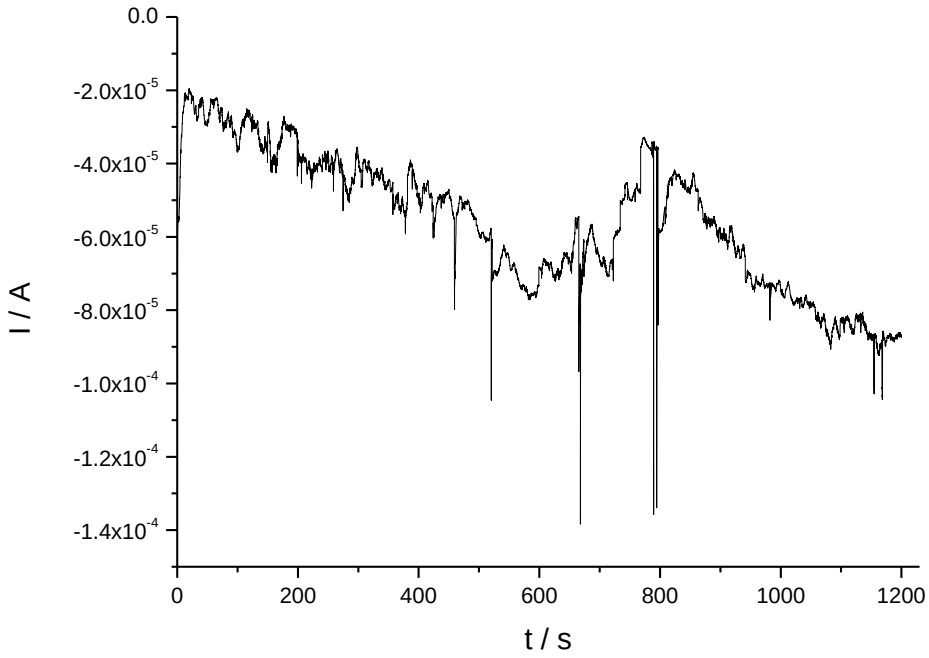

Figure 4.19: Current - time transient of reduction of Cu (II) at a 100 µm square liquid mercury electrode at -0.7 V vs Ag/ AgCl with 10 mM $Cu(NO_3)_2$ in 0.1 M KNO_3.

Figure 4.19 is the current-time transient of the deposition of copper at a mercury microelectrode, similar to that shown in Figure 4.8. Over the course of the deposition, 66 mC of charge is passed, which is a significantly large charge for a microelectrode. Furthermore, the current increases with deposition time following an irregular pattern of peaks and troughs.

Such a large current is passed as copper deposits as a solid, increasing the electrode area and providing more active sites for solid copper to deposit as it is reduced. As this growth propagates from the electrode surface into the solution, some of the dendrites mechanically detach from the electrical connection, either under gravity (as the microelectrode is vertically orientated) or some other external convection. This results in momentary reductions in the

magnitude of current, however this is quickly overcome as the rate of dendrite growth exceeds the rate of detachment.

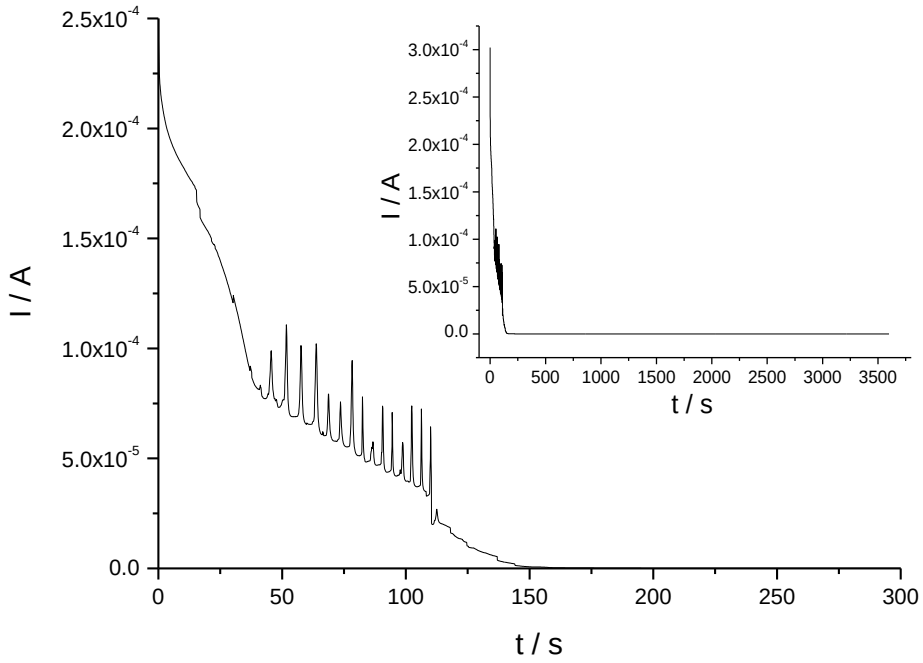

Figure 4.20: Current- time transient of the oxidation of Cu from a liquid mercury electrode at 0.6 V vs Ag/AgCl with 10 mM $Cu(NO_3)_2$ in 0.1 M KNO_3.

Figure 4.20 shows the current-time transient for the re-oxidation of copper from the mercury microelectrode. During oxidation, the current returned to zero after only 150 seconds, with only 11 mC of charge passed. At first the current jumps and falls smoothly as could be expected for a diffusion limited reaction, however between 45 and 110 seconds the current shows a regular pattern of spikes before falling to zero after 150 seconds.

This spiking pattern occurs as copper from the dendrites close to the electrode is reduced. The electrical connection to the remainder of the dendrites structure is broken and the site on the original electrode surface which had previously been blocked by the dendrite is exposed. This causes an increase in current which drops quickly as the concentration of the reduced species at the electrode is consumed and no reaction can take place.

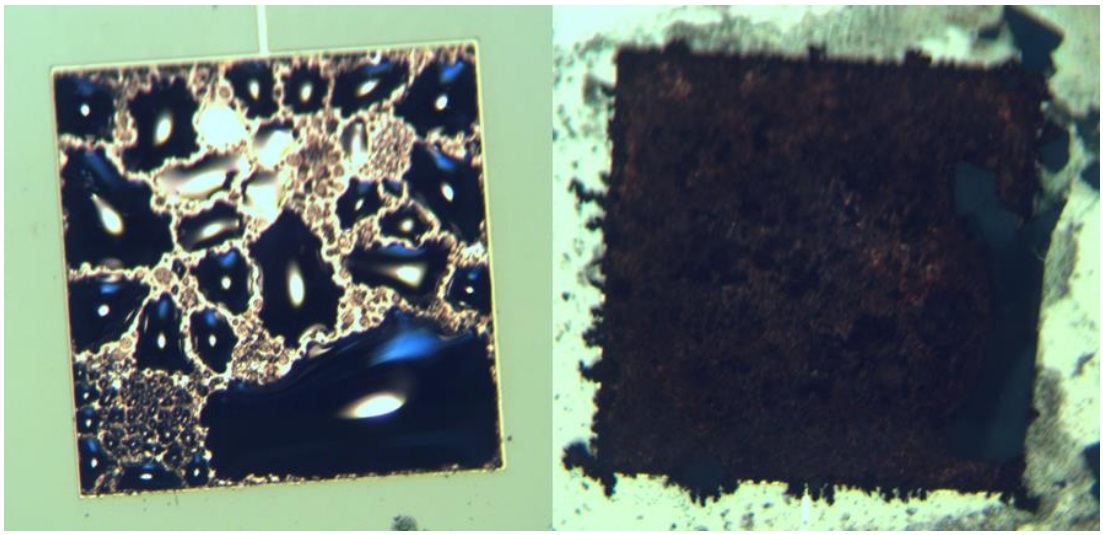

Figure 4.21: Images of the mercury electrode before (left) and after (right) the copper deposition and re-oxidation shown in Figure 4.19 and Figure 4.20. It can be seen that after the re-oxidation of the copper, dendrites are still apparent around the edges of the square, and it is not possible to identify the mercury deposits.

Figure 4.21 shows the before and after images of the mercury microelectrode used to measure the transients in Figure 4.19 and Figure 4.20. In the left hand image, the mercury droplets can be seen to be distributed across the underlying square electrode like a random array. After the deposition and oxidation of copper dendrites, the right hand image, the mercury droplets are no longer visible. In place of the mercury, the underlying platinum square is covered in a solid, black "wool-like" deposit. This deposit is similar in appearance to the copper dendrites seen in Figure 4.9 for deposition on the macroelectrode after 600 seconds of reduction, and to the detached dendrites which collected in the bottom of the beaker. It is assumed that during the re-oxidation of copper from the microelectrode, the mechanical detachment of the dendrites also leads to the removal of much of the mercury. The black material shown in the right hand image consists of detached dendrites, which are not electrically connected to the electrode, but have remained attached to (or been drawn onto) the electrode as it was removed from the cell.

In support of this, further deposits of a similar nature were found on the passivating material surrounding the microsquare electrode. It is most likely that this material, which was freely floating in the solution, was drawn onto the electrode by the surface tension of the water as the electrode was removed from the solution. Drying of the electrode in a 120 °C oven and

gently blowing over the surface with argon removed almost all of this material, so it was not strongly bound to any point of the electrode device.

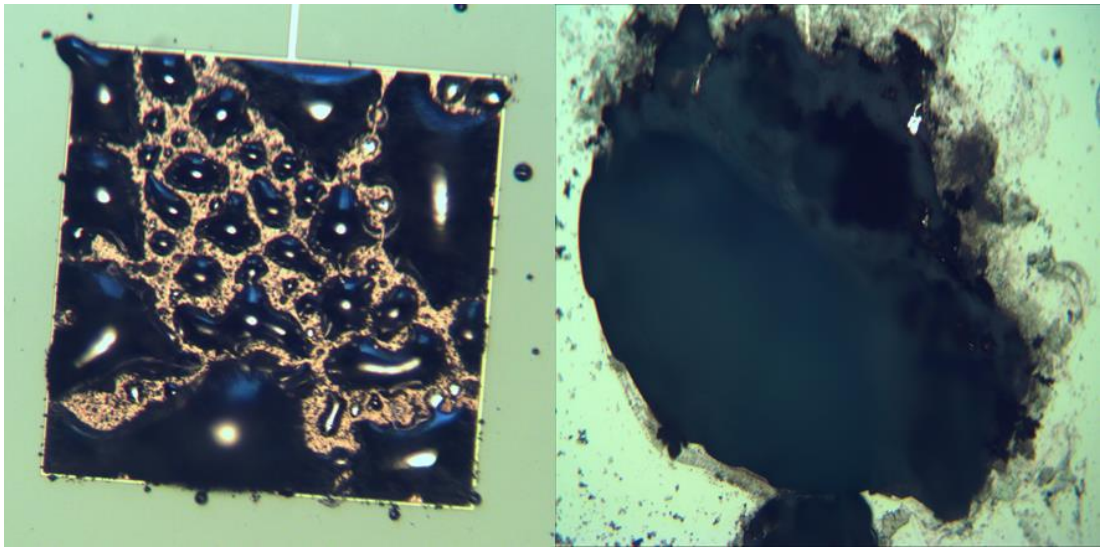

Figure 4.22: Images of the mercury electrode before (left) and after (right) copper deposition over 1800s for the impedance measurements in Figure 4.23.

Figure 4.22 shows a before and after image of the reduction of copper at a mercury microelectrode. Whilst the "after" image (right) is not clear, optical inspection revealed the dendrites had collapsed onto the electrode surface as it had been removed from solution. The dendrite material covered a large area over the electrode, and the underlying square was not visible even after gently blowing argon gas over the electrode surface. The material could be removed by gently scraping across the surface of the electrode, but at such a small scale, a viable sample for investigation could not be collected.

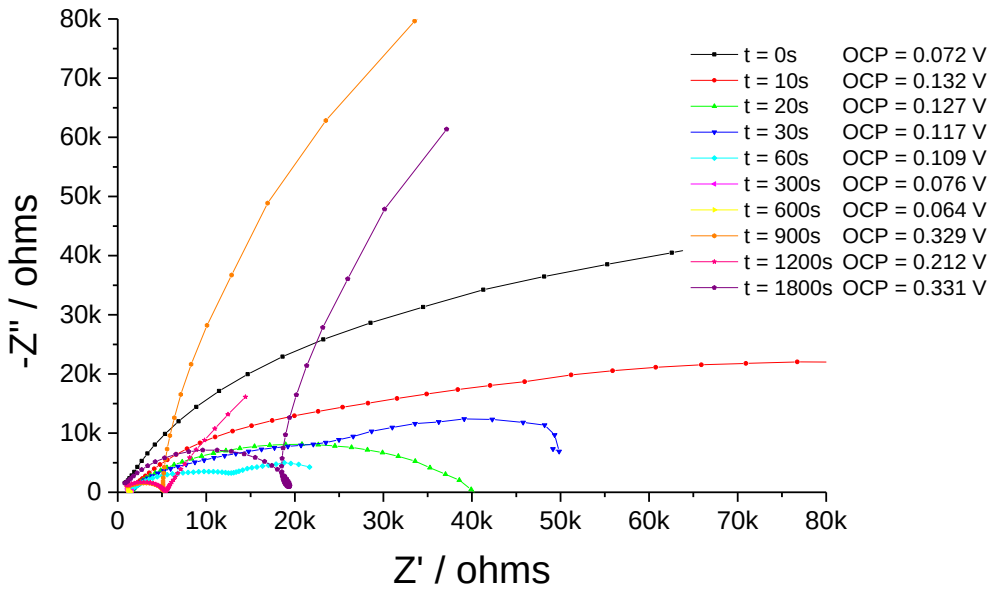

Figure 4.23: Nyquist plots of impedance spectroscopy at OCP of a liquid mercury electrode during deposition of Cu.

Figure 4.23 shows the Nyquist plots of electrochemical impedance spectroscopy recorded as a function of time for the deposition of copper at the mercury microelectrode. Unlike previous EIS spectra of dendritic growth, the plots do not follow a trend in sequence with time. Whilst in general, the 1st charge transfer semi-circles decrease in size with time, an explicit trend is not discernible.

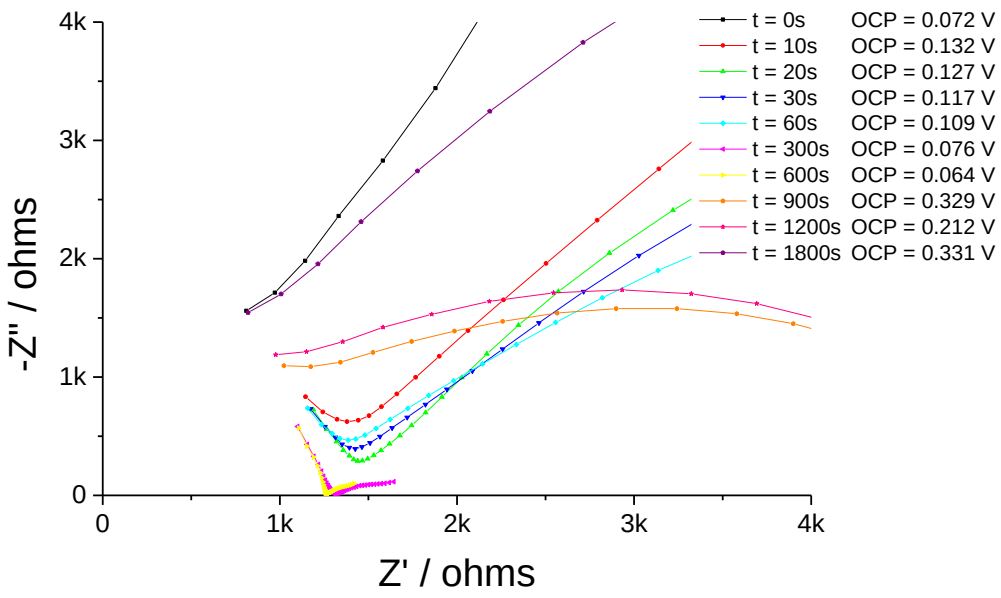

Figure 4.24: Expanded Nyquist plots of impedance spectroscopy at OCP of a liquid mercury electrode during deposition of Cu.

Figure 4.24 expands on the Nyquist plots in Figure 4.23 so that the solution resistance can be examined. Again, unlike previous plots the solution resistance did not exhibit a discernible trend, first increasing, then decreasing.

Repeated attempts to determine a trend in the EIS spectra of copper deposition at a mercury microelectrode as a function of time resulted in a similar pattern of inconsistency. This implies that the mechanism for such extended dendritic growth at the surface of a liquid microelectrode is complex, and not yet understood.

4.7 Conclusions and Further Work

It has been possible to study an aqueous liquid cathode system as an analogue to the liquid cathode in a molten salt reprocessing system to avoid the technological complications of such systems at elevated temperatures and sealed atmospheres.

The deposition of zinc at a liquid metal cathode constructed from a large mercury pool was used to investigate the mechanism for deposition and amalgamation of species that are expected to alloy readily with the liquid electrode in the molten salt process.

The zinc was first observed to undergo a diffusion limited reduction at the metal surface, where the rate of diffusion of zinc into the bulk mercury controlled the reaction rate. Upon re-oxidation of the zinc, the current initially followed a rate limited diffusion curve as the zinc diffused out of the liquid mercury and away from the electrode. This diffusion was truncated, as the zinc had only diffused part way into the electrode, and not fully throughout the whole bulk of the mercury.

Whilst it was not possible to fit the current-time curve to the bounded Cottrell equation, this confirms that the rate of reaction is governed by the diffusion of zinc in the liquid mercury, rather than zinc in the aqueous solution. Future work should investigate this effect and determine the fundamental principles of diffusion of an alloyed species in a liquid electrode.

Copper was also reduced at a liquid mercury cathode, and the formation of dendrites observed both optically and electrochemically. Diagnostic behaviour for the formation of dendrites was identified in correlation with the visual inspection of dendrite growth, so that a method of electrochemically detecting when dendrites form can be developed. This will prove an important tool when operating a molten salt system with a liquid cathode, as it will not be possible to visually monitor the electrode surface for dendritic growth.

The reduction of zinc and copper at micro-scale liquid electrodes was then investigated to support the development of sensors for detecting dendritic growth in a molten salt reprocessing system. First mercury was deposited onto 500 μm platinum electrode before being photographed under a microscope and used to study the deposition of zinc and copper.

With zinc, it was possible to drive the reduction of zinc to the point that a solid alloy was formed between the zinc and the mercury. Whilst dendrites were not observed to grow from the electrode surface, the growth of a solid crust over a liquid electrode in a molten salt process is equally damaging, as the required amalgamation will not be achieved and the target species shall plate out as solids. Changes in both the chronoamperometry and EIS spectra were highlighted as being distinctive for the formation of a solid reduction product, and are proposed as characteristic indicators for solid deposition at a liquid cathode.

The reduction of copper at the liquid microelectrode also resulted in a solid deposition. In this instance dendrites grew extensively from the electrode surface, visibly protruding into the solution. Even when the electrode was removed from the solution, much of the dendrites remained attached. Chronoamperometry to induce reduction and oxidation of copper on the microelectrode are consistent with observations on macroelectrodes, although the oxidation of copper from the microelectrode appeared to be much more ordered. The reason for why the current response during oxidation is not clear, and should be the subject of future work, along with the destruction of the liquid metal deposited on the surface.

The electrochemical impedance spectra recorded during the deposition of copper on the liquid microelectrode were not consistent with those previously measured on micro and macro scale liquid electrodes. Further work is required in order to understand whether this is characteristic for dendritic growth beyond a limit, or a random occurrence.

Comparisons of the characteristic response for dendritic growth identified in this chapter under aqueous conditions at room temperature, to the molten salt systems they were to model, shall be discussed in chapter 7.

4.8 References

1. N. Brockie, *Applications of Liquid Cathode Electrochemistry towards the Nuclear Industry* (2011), PhD Thesis, University of Edinburgh
2. N.K. Sarkar, J.–R. Park; *J. Dent. Res.*, 1988, **67,** (10), 1313
3. H. Moriyama, K. Moritani, T. Sasaki, I. Takagi, K.Kinoshita, H. Yamana, *Recent Advances in Actinide Science*, 2005, 545
4. Z. Galus; *Pure & Appl. Chem*., 1984, **56**, (5), 635
5. H. Okamoto, *J.Phase Equilib*., 2002, **23**, 196
6. C. S. Barrett, *Acta Crystallogr*., 1957, **10**, 58-60
7. M. Puselj, Z. Ban, A. Drasner, *Z. Naturforsch. B*, 1982, **37**, 557-559
8. Vegard L, *Skr. Nor. Vidensk.-Akad., Kl. 1: Mat.-Naturvidensk. Kl.*, 1947, **2**, 1-83
9. D. J. Chakrabarti, D.E. Laughlin, *Binary Alloy Phase Diagrams*, 2nd Ed., 1990, **2**, 1419-1421
10. T. Lindahl, S. Wetman, *Acta Chem. Scand.*, 1969, **23**, 1181-1190
11. H. Okamoto, Phase Diagrams for Binary Alloys, Desk Handbook, Vol. 1, 2000
12. E. B.-T. Tay, S.-B. Khoo, S.-W. Loh, *Analyst*, 1989, **114**, 1039-1042.

13. E.E. Ferapontova, J.G. Terry, A.J. Walton, C.P. Mountford, J. Crain, A.H. Buck, P. Dickinson, C.J. Campbell, J.S. Beattie, P. Ghazal, A.R. Mount; *Electrochem Comms*, 2007, **9**, 303-9.
14. S.W.J. Ember, H. Schulze, A.J. Ross, J. Luby, M. Khonddoker, G. Giraud, J.G. Terry, I. Ciani, C. Tilli, J. Crain, A.J. Walton, A.R. Mount, P. Ghazal, T.T. Bachmann, C.J. Campbell, *Analytical and Bioanalytical Chemistry*, 2011, **401**, (8), 2549-2559
15. N.J. Freeman, R. Sultana, N. Reza, H. Woodvine, J.G. Terry, A.J. Walton, C.L. Brady, I. Schmueser, A.R. Mount, *Phys. Chem. Chem. Phys*, 2013,**15**, 8112-8118.

5 Contact Angles of LKE on Surfaces of Interest

5.1 Introduction

When designing and fabricating an electrode, or indeed a processing plant, it is important to consider how the materials will interact with the liquids or solutions that it comes into contact with. This is the case when considering materials for fabricating a solid microelectrode to be used in a molten salt and these materials' interactions become even more important when considering how a liquid microelectrode may be prepared. In any practical design the liquid metal will need to be contained in a specified location over an underlying metal through which electrical connection will be made. The liquid metal microelectrode will therefore need to be fabricated of materials such that: the passivation layer which forms the boundary of the container will be wetted by the LKE, but not by the liquid metal; the underlying metal will be wetted by liquid metal, but less so by the LKE; and that the liquid metal and the LKE form a stable interface.

Unlike for aqueous systems, there is a lack of fundamental knowledge of how molten salts wet different materials. This chapter will seek to address, at least in part, this issue by investigating the wetting of LKE on possible passivation layers and likely electrode metals. In order to achieve this, a suitable contact angle measurement system needs to be established. Measurements also need to be taken in an inert atmosphere to ensure that the potentially detrimental effects of oxide formation on the substrates due to elevated temperatures do not influence the measurements and therefore the obtained results. The production, validation and use of such a system is the subject of this chapter.

5.2 Method Substantiation

The details of the apparatus constructed to measure molten salt contact angles are given in Section 3.2.3 and shown again in Figure 5.1. This section covers initial testing to prove its robustness, before carrying out measurements of molten salt at elevated temperatures.

Initially, a series of experiments are reported to verify the suitability of the method, the repeatability of the measurements, and the rigour of exclusion of oxygen in the apparatus.

Once the experimental system and method was validated, molten salt contact angles on selected surfaces were measured.

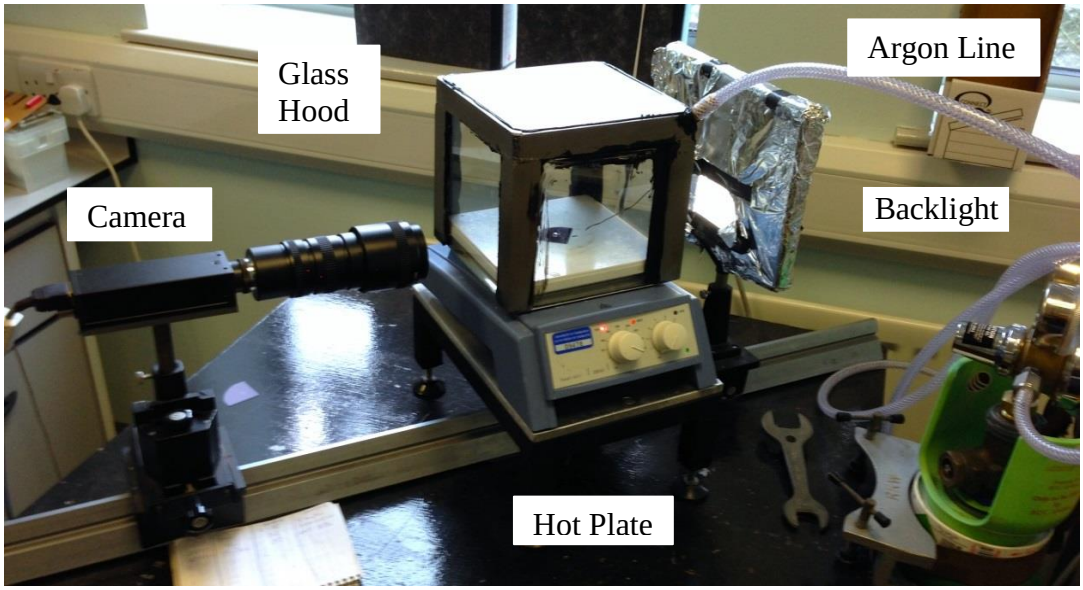

Figure 5.1: Experimental set-up for angle measurements of molten salts.

As explained in Section 3.2.4, 16 measurements were taken for each sample. Once these angles had been measured the anomalies were excluded. Anomalous measurements were deemed to be those where imperfections and deformities across the droplet surface were evident, or where the angle on each side of the droplet differed by more than 10 ° (e.g. where the sample was not level). The remaining angles were averaged to determine a representative contact angle for each of the surfaces. These averaged measurements are reported in this chapter, along with the standard deviation of the data set.

5.2.1 Accuracy

The first issue to be addressed is the potential for distortion of the contact angle caused by reflection or refraction of light through the glass hood. In order to test this, images were captured at ambient temperatures of a 5 µL droplet of deionised water on a 1 µm unpolished thermal oxide surface without, and then with the glass hood in place (Figure 5.2).

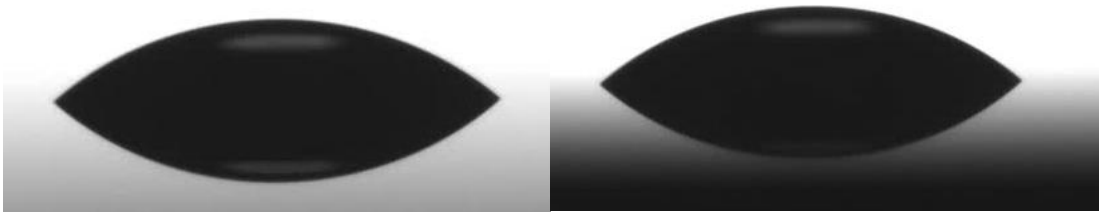

Figure 5.2: Image of a 5 µL DI water droplet on an unpolished 1 µm thermal oxide without (left) and with (right) the glass hood over the hotplate/stage.

In both images the measured contact angle was identical and when the images were superimposed, no distortion could be observed. Some shadowing, and a slight darkening of the image was observed when the hood was in place, however this can be attributed to the reduction in light owing to reflection off the steel frame covering the top of the chamber. Therefore, assuming no temperature-dependent optical effects, optical distortion from the glass was not a concern.

Whilst the native oxides were not removed from the surfaces prior to the measurements, the second issue was the ability of the apparatus to maintain an inert, oxygen free environment. This was of particular concern with respect to the metal surfaces to be investigated, as heating of these surfaces in the presence of air would result in further oxidation or hydration of the surfaces, and influence the contact angle[1]. The presence of air whilst measuring liquid metal contact angles would also lead to further oxidation of the liquid metal surface, to be discussed further in Section 5.5.

In ambient air, either the metal, M, can be oxidised through the process,

$$xM + \frac{y}{2}O_2 \rightarrow M_xO_y$$

Equation 1

or the metal oxide can be hydrated through the process,

$$M_xO_y + yH_2O \rightarrow M_x(OH)_{2y}$$

Equation 2

In both these cases a chemical change takes place at the surface of the metal, which would result in a change in the wetting interaction with the molten salt.

By measuring how the contact angles differed with the ingress of ambient air, the existence of oxygen in the chamber could be readily identified, and also the efficacy of the glass hood to maintain an inert environment.

In measuring contact angles within the chamber, stopping the argon flow, and allowing oxygen to enter the chamber before re-measuring the angle, it was possible to observe the influence of ambient air ingress on the contact angles. Figure 5.3 shows how the contact angle of LKE changes on the native titanium metal surface with the ingress of ambient air into the glass hood at 400 ºC.

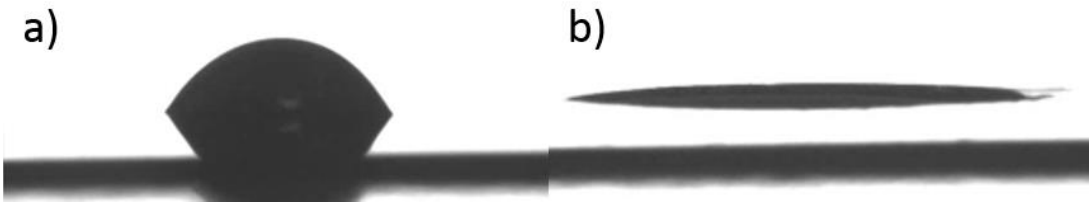

Figure 5.3: Images of the change in contact angle of LKE on titanium surfaces in a) argon and b) after ingress of ambient air at 400°C where the titanium surface was oxidised.

In all cases during these tests, it was found that the presence of ambient air in the chamber had a significant influence on the contact angle of the molten salt on the surfaces. This is seen in Figure 5.3, where the contact angles of LKE on titanium surfaces in argon (Figure 5.3a) are clearly greater compared to the contact angle in air (Figure 5.3b). Under the inert argon blanket, the contact angle of titanium is consistently around 51°; however, in air the LKE spreads rapidly across the titanium surface indicating a greater wetting interaction between the molten salt and the oxidised and/or hydrated surface. In air, titanium is known to readily form a stable oxide[2-5] and the Figure 5.3b is likely to be a measurement of the contact angle on titanium oxide.

Given the difference in observed contact angles, not only does this result demonstrate that titanium metal is relatively non-wetting compared to the titanium oxide surface inevitably forming in air, but also confirms that the apparatus is maintaining an inert atmosphere. If this

were not the case then the titanium surface would be oxidised in both cases and the LKE only observed to be spreading. Even if there was a small ingress of oxygen during the measurements, the titanium surface would slowly oxidise, and the droplet observed to slowly spread across the surface. This was not the case so it can be rationalised that the glass hood arrangement to exclude air was successful.

Despite confirming that ambient air was not entering the glass hood, a number of abnormalities in the droplet shape were observed during the course of measurements of the contact angles of LKE on surfaces. Figure 5.4 shows examples of the abnormal shapes that were observed.

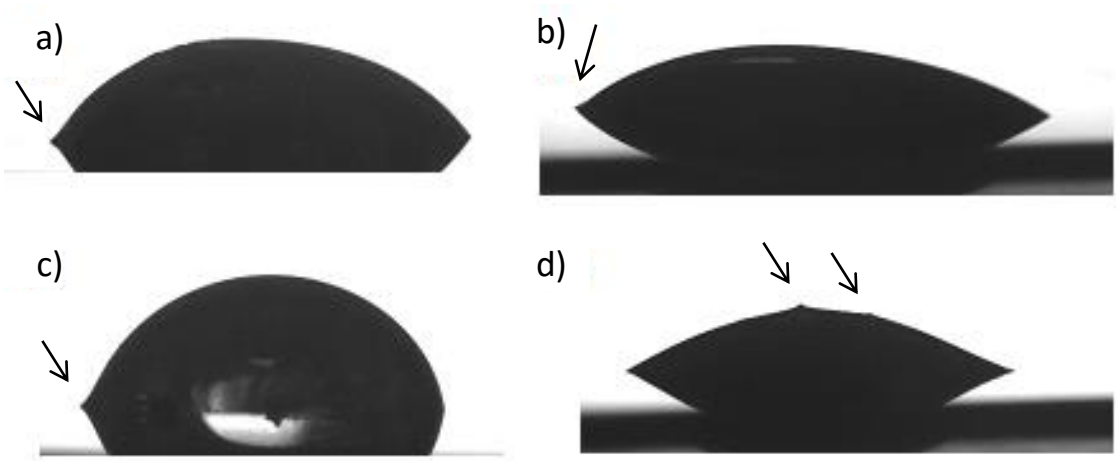

Figure 5.4: Abnormalities observed in molten LKE droplets during measurement of contact angles on silicon substrates. a, b and c are apparent "tail" effects, thought to be related to either an impurity on the surface, or potentially due to the stage not being level. Image d shows small defects in the shape of the droplet.

The abnormalities or irregularities in the shape of the droplets of molten salt could be indicative of a surface defect/ contaminant, a contaminant in the molten salt or an effect of oxide present in the atmosphere. In the case of Figure 5.4, a, b and c have pronounced “tail-like” features to one side of the droplet. Typically, such a shape would be due to the droplet wetting the surface. This is still considered to be the case in these examples, however, as the droplets show largely incomplete wetting, it could be due to a small contaminant on the surface, or a point of oxidation, which is wetted by the LKE. Alternatively, there could be a defect on the surface (i.e. a scratch or pitting) layer, resulting in the underlying substrate being exposed, which would exhibit a different wettability to the surface of interest. Droplets a) and

b) also exhibit a shift in the bulk of droplet towards the left side. This was caused by the hotplate, which was acting as the stage, not being level. As such, the slant on the substrate with respect to horizontal results in the droplet proceeding towards the lower edge. In more advanced contact angle measurements, the pitch of the stage can be deliberately altered to measure dynamic contact angles. This more complex situation was beyond the scope of this work, and in the instances where the stage was seen to not be level (usually at the start of a series of measurements) the stage was returned to level using a digital spirit level.

Abnormalities such as those seen in Figure 5.4 d, could also be explained by the presence of solid contaminants. Occurrence of this irregularity was rare, reserved to only two instances, however visual inspection of these droplets revealed small, solid grains of a contaminant floating on the surface of the molten salt. It is thought that these small grains were shards of glassy carbon introduced to the molten salt whilst the salt was prepared using the technique described in Chapter 7 owing to minor damage (chips and impact pitting) sustained to the crucibles over multiple uses.

In all instances where either an irregular droplet shape, or a droplet with unsymmetrical contact angles due to possible surface contaminants or defects were observed, the measurements were excluded from the data to preclude erroneous results due to potential contaminants or surface defects.

5.3 Wettability of Selected Metal Surfaces

The wettability of a number of predominantly metal surfaces has been measured using the procedure described in Chapter 3.

These surfaces were chosen as they are materials either used in fabricating electrodes for use in molten salts, or have been used in previous molten salts studies. Tungsten, titanium and titanium nitride were selected as they are all materials used in electrode fabrication by the SMC. Despite not being a metal, vitreous carbon (SIGRADUR®) was also investigated as it is the crucible material used in molten salts experiments at the University of Edinburgh and at NNL. The sample of vitreous carbon was attained from a broken crucible which had been used but was no longer required, and was in a representative condition of the crucibles in use. The two stainless steel samples were investigated as the Molten Salts Dynamics Rig (MSDR) at

NNL is constructed from stainless steel, and the results of this study may be of future practical use in either the re-commissioning or replacement of the MSDR.

Both mirrored and brushed samples of stainless steel were investigated because although, as discussed in chapter 2, contact angles are only accurate when the surface is as smooth as possible, the MSDR has been constructed out of a brushed steel.

Images of the contact angles of LKE on these surfaces are shown in Figure 5.5, with the contact angles of deionised water and LKE presented in Table 5.1.

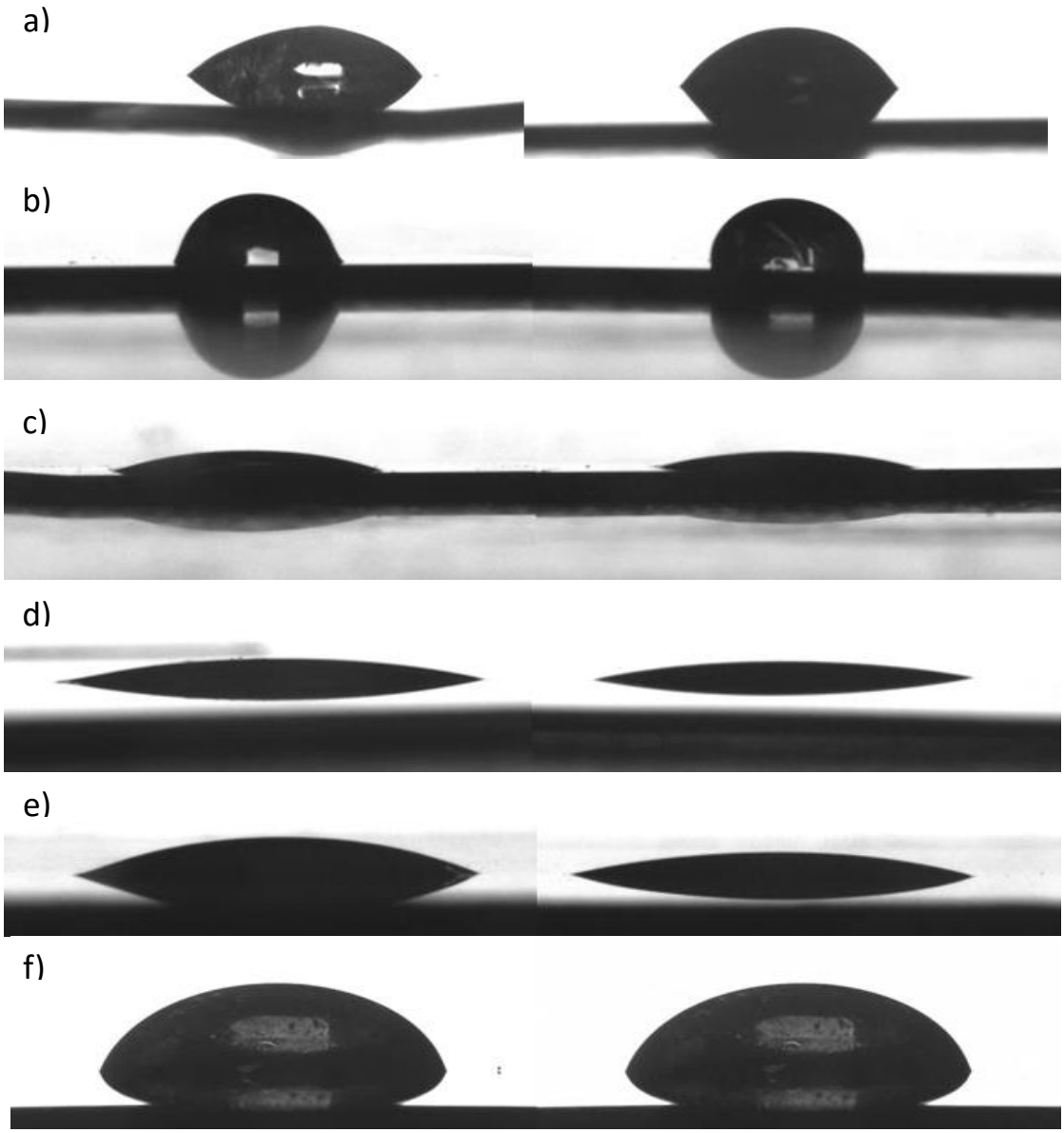

Figure 5.5: Typical contact angle images of LKE in Argon at 400ºC on surfaces of a) titanium, b) titanium nitride, c) tungsten, d) mirrored 316 stainless steel, e) brushed 316 stainless steel, and f) glassy carbon.

Surface	Contact angle of 5µL deionised water (°)	LKE Contact Angle (°)
Tungsten (native oxide)	22 ± 1	21 ± 2
Titanium (native oxide)	38 ± 1	51 ± 2
Mirrored Stainless Steel (316SS, native oxide)	97 ± 1	16 ± 2
Brushed Stainless Steel (316SS, native oxide)	101 ± 1	22 ± 3
Titanium Nitride	66 ± 1	55 ± 5
Vitreous Carbon	55 ± 1	70 ± 1

Table 5.1: Mean contact angles of deionised water and LKE at 400 °C measured on surfaces of interest. Uncertainty is in degrees for 16 measurements.

From this dataset there were some notable results of interest. Contact angles on each of the surfaces were relatively stable and repeatable. The only exceptions to this were the brushed stainless steel, where it is likely surface roughness affected the measurements, and the titanium nitride, which had large variations in the contact angle.

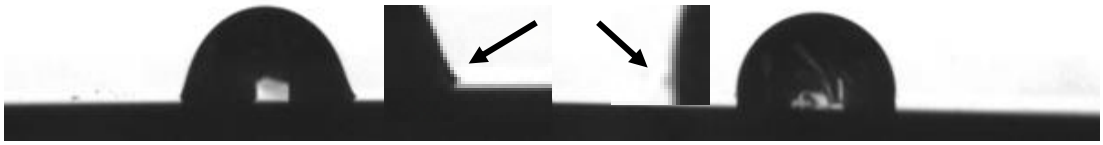

Figure 5.6: Contact angle images of LKE on titanium nitride surfaces in argon at 400°C with expanded three-phase point (inset).

At a cursory glance of the titanium nitride surface images (Figure 5.6b), it would appear that the molten salt is largely non-wetting, and that the droplets seem to be similar in shape. However, on closer inspection of these images, it is clear that there is a small tail-like feature at the three-phase contact point (Figure 5.6) where the salt appears to be more wetting on the surface. This could be due to either surface contamination or due to a surface roughness effect; however, this effect is apparent in almost all the images collected on TiN, so contamination is unlikely as it would not be consistent across all the samples. Furthermore, TiN is a very low

stress film, used in microfabrication as a seed layer for high stress films, and is known to deposit as a very smooth surface, so surface roughness effects are unlikely.

The cause of TiN generally having a relatively low contact angle, whilst maintaining the droplet shape of a non-wetting interaction is not clear from this work and further investigation into this unusual phenomenon is required.

The consistency in the contact angle measurements for each of these surfaces, and the stability of the droplets to maintain their shape for at least a few minutes (after which the samples were changed) confirms the rigour of the apparatus and the method.

5.4 Wettability of Silicon-Based Surfaces by LKE

This study of the contact angles of LKE on different insulating materials was motivated by work on developing microelectrodes for use in molten salts. Improved understanding of the wetting behaviour between molten salts and the materials used in electrode fabrication aids the design of more robust and effective electrodes. Observations of the wetting behaviour can be achieved through simple measurement of the contact angles, the results of which are presented here.

5.4.1 Wettability of Unpolished Silicon Surfaces by LKE

Silicon oxide is one of the most commonly used insulators in the semiconductor industry. Its high chemical stability and spontaneous growth on silica in air make it very easy and cheap to grow by thermal oxidation of silicon wafers. Typically, wafers are heated at temperatures between 600 and 1200 °C in oxygen or steam to promote layers thicker than the 1 nm native layer that forms in ambient conditions.

During previous work on microelectrodes for use in molten salts, electrodes have been investigated using silicon oxide and silicon nitride passivation layers[6]. Whilst the results of

this work tested the efficacy of insulator materials in the molten salt, the wetting behaviour of the molten salt on the oxide and nitride films was not investigated.

The contact angles of deionised water and LKE in argon and in air were measured on several silicon oxide and nitride surfaces prepared either by thermal oxidation or by PCVD methods.

The results of the measurements of deionised water on these surfaces, along with the mean surface roughness of these films are recorded in Table 5.2.

Surface (Unpolished)	Average Surface Roughness, R_a (nm)	Contact angle of 5µL deionised water (°)
1µm Thermal Oxide	0.210	33 ± 1
500nm Thermal Oxide	0.287	33 ± 4
500nm PCVD Oxide	1.232	12 ± 1
LPCVD Nitride	0.287	12 ± 1
PECVD Nitride	1.047	24 ± 3

Table 5.2: Mean contact angles of water measured on unpolished silicon surfaces at room temperature (20 °C).

These contact angles are consistent with previous measurements of similar films produced by the SMC. The surface roughness, R_a, is on the angstrom scale and the surfaces could not be considered to be rough. It is therefore expected that these measurements are predominantly determined by the chemistry of the surface rather than the roughness.

The results of the measurements of LKE on these surfaces, along with the mean surface roughness of these films are recorded in Table 5.3.

Surface (Unpolished)	Average Surface Roughness, R_a (nm)	LKE Contact Angle (°)
1µm Thermal Oxide	0.210	34 ± 6
500nm Thermal Oxide	0.287	52 ± 8
500nm PCVD Oxide	1.232	34 ± 2
LPCVD Nitride	0.287	22 ± 4
PECVD Nitride	1.047	Spreading (<10)

Table 5.3: Mean contact angles of lithium chloride-potassium chloride eutectic measured on unpolished silicon surfaces at 400 °C.

These results are similar to the contact angles measured for deionised water. The angles that were measured were less consistent, however, this could be in part due to the variation in the 'droplet' size arising from small differences in the mass of each salt bead.

Variations in the angles between the surfaces can be influenced by either the surface chemistry or the surface roughness. As the roughness measurements show these surfaces are not rough, it is assumed that the wetting behaviour is due to the chemical interaction at the boundary.

5.4.2 Wettability of Polished Silicon Surfaces by LKE

As discussed in chapter 2, the wetting interaction between a liquid and a surface is influenced by the surface roughness, and the properties of the interface, rather than the bulk material. Interfacial properties cannot be easily predicted, so can only be determined through experimental methods, such as contact angles.

To confirm the effect of surface roughness on the contact angle, and that the results in section 5.4.1 were governed by the surface chemistry, the samples were polished to flatten the surfaces and improve the surface roughness of the samples.

The method described in Section 3.2.1.3 was used to polish the surfaces, and the surface roughness and contact angles of deionised water were re-measured for each surface. These results are shown in Table 5.4.

Surface (Polished)	Average Surface Roughness, R_a (nm)	Contact angle of 5µL deionised water (°)
1µm Thermal Oxide	0.290	13 ± 2
500nm Thermal Oxide	0.246	20 ± 4
500nm PCVD Oxide	0.193	Spreading (<10)
LPCVD Nitride	0.342	14 ± 3
PECVD Nitride	0.278	13 ± 1

Table 5.4: Mean contact angles of water measured on polished silicon surfaces at room temperature (20 °C).

These results highlight that even prior to polishing these surfaces were already very smooth, with the surface roughness in most cases being on the angstrom scale. Improvements in surface roughness were only measured on the PCVD oxide and PECVD nitride surfaces, with the roughness of other surfaces not significantly affected. The contact angles of water, particularly on the thermal oxides however seem to have been affected by the polishing procedure. As the surface roughness was largely unchanged, this would suggest that the polishing has led to an unintended chemical change of the surface.

The contact angles of LKE on the polished surfaces are shown in Table 5.5.

Surface (Polished)	Average Surface Roughness, R_a (nm)	LKE Contact Angle(°)
1µm Thermal Oxide	0.290	81 ± 9
500nm Thermal Oxide	0.246	32 ± 3
500nm PCVD Oxide	0.193	24 ± 2
LPCVD Nitride	0.342	11 ± 1
PECVD Nitride	0.278	21 ± 4

Table 5.5: Mean contact angles of lithium chloride-potassium chloride eutectic measured on polished silicon surfaces at 400 °C.

The contact angles of the LKE were also affected by the polishing, however the effect is different to that observed from the deionised water. As the polishing has a different effect with ionic liquids to polar liquids there must have been a chemical change in the surface, either in structure or composition.

As part of the polishing regime, the polished samples were soaked in tetramethylammonium hydroxide (TMAH) to remove the polishing slurry from the surface prior to drying. Basic solutions can react with the oxide trapped in the films and it is likely that rather than the contact angle being influenced by the polishing process itself, the soaking of the substrate in TMAH was chemically changing the surface and hence the charge interaction between the surface and the droplet.

To test this two additional thermal silicon oxide wafers from the same wafer batch and processed using the same method as before were fabricated. The contact angles of 5 µL droplets of deionised water were measured over several points on each of the wafers, before

the wafers were soaked in TMAH for two minutes and washed in a water jet for 1 minute, replicating the cleaning step after the previous used polishing process. The contact angles of 5 µL droplets of deionised water were re-measured across the wafers.

Sample	Contact angle prior to TMAH soak (°)	Contact angle after TMAH soak (°)
1	43 ± 1	Spreading (<10)
2	36 ± 2	Spreading (<10)

Table 5.6: Contact angles of 5 µL droplets of deionised water on thermal oxide wafers before and after soaking in TMAH.

These results support the hypothesis that, rather than a surface roughness change due to the polishing procedure, the chemical treatment of the surface with TMAH has altered the free charge of the surface resulting in a change in contribution to the contact angle from the electrostatic interaction.

This phenomenon can be explained in a similar manner to electrowetting, although rather than an applied potential, the change in charging is caused by a chemical treatment of the surface. The increased spread contact angle measurements, demonstrated by a greater error, can be explained by this effect. Increases in the difference between the surface free charge and the electrolyte free charge have been shown to result in greater variation in the contact angle[7].

The isoelectric point of silicon dioxide is between pH 1.7 and pH 3.5[8] whereas the isoelectric point of silicon nitride is between pH 6 and pH 7. Treatment in a basic solution will have a greater effect on the Stern layer charging of silicon dioxide than that of silicon nitride, and hence the difference which will be measured in the contact angles between the untreated/ treated surfaces.

It is possible that, as with the oxide surfaces, the difference in polished and unpolished PECVD nitride films is due to the chemical reaction with TMAH. As explained in chapter 3, PECVD of nitride films results in a film of SiN with entrapped hydrogen. This hydrogen is likely to chemically react with the TMAH, and the increase in contact angle is a result of the change in surface charge. This is less prominent in the nitride surface results as the entrapped hydrogen is minimal and films are naturally more wetting than the oxide surfaces.

5.5 Liquid Metal Contact Angles

In studies of 3d of printing flexible metal structures Ladd et al observed that in room temperature liquid metals, oxidation of the metal exposed to air forms a solid film on the outer surface[9]. This flexible metal structure can be manipulated in air as the bulk of the metal is liquid, however the shape of its structure is held by the oxidised solid surface. This effect may also explain the two unexpected peaks on the outer surface of the LKE droplet seen in Figure 5.4d, however this is difficult to prove.

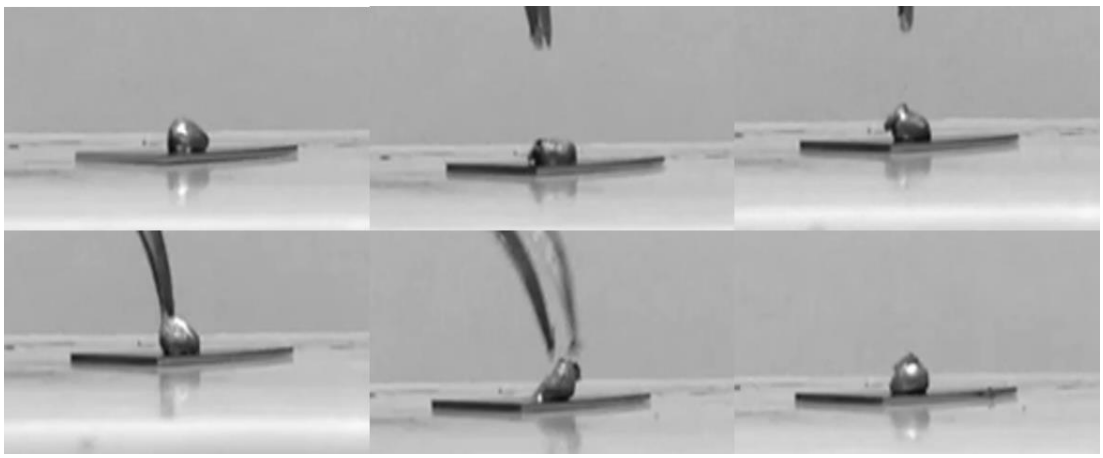

Figure 5.7: Test contact angle images of liquid bismuth on silicon.

Attempts to measure the contact angles of liquid metals (Figure 5.7) were thwarted by similar effects to those reported by Ladd et al[9]. The outer surface of the metal beads purchased for the contact angle experiments had oxidised where the beads were exposed to air during the manufacturing process. This oxide remained solid at the temperature of measurement, obscuring the intrinsic behaviour of the liquid bismuth even in the inert argon atmosphere.

Despite this oxide skin, on removing the glass hood, it was possible to manipulate the bead in open atmosphere to shape the liquid metal as reported in previous observations of other liquid metals[10]. Any attempts to overcome this effect and measure the contact angle of liquid metals will require rigorous exclusion of oxygen from the formation of the bead to the contact angle

measurement, or a process for removing the oxide in an inert environment prior to measuring the contact angle.

5.6 Conclusions

In this chapter a method for measuring the wetting of molten salts on surfaces of interest has been developed and benchmarked against know measurements. The system has been shown to successfully overcome the problem of oxygen ingress causing an oxidative change to the substrate on which the LKE is being measured and maintain an anhydrous atmosphere for the molten salt.

Differences have been shown between contact angle measurements in controlled atmospheres and when the substrate and molten salt are exposed to air and moisture. From these measurements it has been possible to establish that the system is working, and to identify when oxygen and/or water is present in the apparatus.

Using the measurements recorded during this work, it is possible to make informed choices when designing and fabricating molten salt systems. This includes in the fabrication of microelectrode sensors for use in LKE. With these devices, it is essential that the passivating layer of the device is not damaged by the aggressive nature of the salt, and in terms of material interaction, the best way to achieve this is to use a material with poor wetting to the molten salt. This is only one of a number of conditions in choosing a suitable passivation material, and additional consideration will need to be taken in terms of any chemical reaction between the passivation layer and the LKE.

When designing a liquid micro-electrode, it will be important to use an underlying metal which adheres well to the liquid metal and is resistant to wetting by the molten salt. This is important so that the molten salt does not creep on the electrical contact, displacing the liquid metal or creating a short circuit where solid deposition can take place. This can also be avoided if any recess in the device surrounding the underlying solid electrode is lined with a material which is wet by the liquid metal, and not wet by the LKE. Equally, it is important that the liquid metal is non-wetting on the passivating layer of the device so that the liquid metal does not creep, enlarging the electrode area.

Attempts were made to measure the contact angles of liquid bismuth on the surface of interest, however this was not possible owing to the solid native oxide on the bismuth beads, which could not be removed within the apparatus. The melting point of bismuth oxide is well above

the melting point of bismuth metal, and the operating temperature of the hotplate, so the oxide could not be melted. Future work should focus on developing a means to remove the native oxide from the bismuth prior to melting and preventing the oxide from re-forming such that a truly accurate and representative measurement of contact angles of liquid metals on surfaces can be recorded.

In adopting reprocessing systems which employ liquid cathodes and molten salts, the interaction between the liquids and the solid materials used to construct the systems shall become increasingly important to ensure the systems are efficient and robust.

5.7 References

1. M. Humenik Jr., W.K. Kingery, *Journal of the American Ceramic Society*, 1954, **37,** (1), 18-23.
2. I. Vaquila, M.C.G. Passeggi Jr., J. Ferron, *Applied Surface Science*, 1996, **93**, 247-253
3. Y. Wouters, A. Galerie, J-P. Petit, *Solid State Ionics*, 1997, **104,** 89–96
4. I. Vaquila, L.I. Vergara, M.C.G. Passeggi Jr., R.A. Vidal, J. Ferron, *Surface and Coatings Technology*, 1999, **122**, 67–71
5. P. Perez, *Corrosion Science*, 2007, **49** 1172–1185
6. C. L. Brady, *The Development and Characterisation of Microelectrodes for Extreme Environments* (2013), PhD thesis, University of Edinburgh
7. C-P. Lee, B-Y. Fang, Z-H. Wei, *Analyst*, 2013, 138, 2372-2377
8. Marek Kosmulski, *Chemical Properties of Material Surfaces*, 2001, Surfactant Science Series, volume 102.
9. C. Ladd, J-H So, J. Muth, M D Dickey, *Advanced Materials*, 2013, **25**, (36), 5081-5085
10. Q. Xu, N. Oudalov, Q. Guo, H. M. Jaeger, E. Brown, *Physics of Fluids*, 2012, **24**, 063101

6 Developing an Electrochemical Method for Dry Molten Salt Preparation

6.1 The need for dry molten salt

This chapter addresses the issues of maintaining a rigorously dry and pure molten salt in which it is possible to study the electrochemical behaviour of redox species in the melt. An in depth discussion on the development of a novel yet elegantly simple electrochemical method for rigorous removal of molten salt contaminant species arising from entrapped water is also presented. This is of crucial importance in the determination and understanding of thermodynamic and kinetic measurements of redox species in the molten salt through the prevention of competing chemical reduction or oxidation reactions. This method is also demonstrated to be of use in removing the oxide and hydroxide species from the melt in the presence of other redox species. Useful as pre-drying anyway, this important application of the method is of significant importance for the use of pyrochemical nuclear reprocessing system, as it would allow the molten salt to be electrochemically dried should there be an accumulation of water in the salt during operation.

6.2 Current Drying methods

The determination of thermodynamic and kinetic data for the redox reaction of metal ions or metal oxides in molten salts is of crucial importance in the understanding and development of these molten salt processes and in the design of corresponding electrochemical reprocessing reactors. These parameters are often obtained from the redox potentials observed using cyclic voltammetry and chronopotentiometry[1-44]; it is important to ensure the correct speciation, accuracy and reproducibility that these fundamental measurements are performed in a high purity, rigorously dry molten salt[5,6].

As a specific example, the eutectic mixture of LiCl-KCl (LKE) is widely used in molten salt research. This is due to its good thermal stability, wide electrolytic potential window, absence of strongly acidic or basic properties, relatively low operating temperature, high ionic conductivity and high fluidity[5]. However rigorous exclusion of water is a significant challenge. Entrapped water has been established to interact with the salt giving rise to oxy- and hydroxy-

species and also constituent *ad aquo* ion containing species. These undergo uncontrolled reactions with electrodes, container systems and redox species, corroding the electrode and/or container materials and creating new redox active species[7]. Drying of salts is therefore crucial. Although the earliest studies aimed at removing oxygen containing species by heating and evacuation, this becomes progressively more difficult and residual species remain. This is because it is generally accepted[5, 8] that in LKE the following equilibria are established:

$$H_2O_{(l)} + 2LiCl_{(l)} \rightleftharpoons LiOH_{(l)} + HCl_{(g)} + LiCl_{(l)} \rightleftharpoons LiO^-_{(l)} + 2\,HCl_{(g)} + Li^+_{(l)}$$

Equation 1

which results in the loss of HCl under evacuation and the accumulation of first OH^- and then O^{2-} contaminants through further HCl loss. Rigorous drying has therefore necessitated time-consuming purging procedures involving dry hydrogen chloride or dry chlorine gas[5-10]. The use of HCl originates from Laitnen et al.[5], who proposed the salts should be fused under anhydrous HCl gas at atmospheric pressure. This, or HCl purging, shifts the equilibrium to the left, so that water vapour can then be driven off. However, HCl is very soluble in the salt and therefore often remains in the eutectic after evacuation. This leads to a salt which is acidic and chemically oxidizing, which, in extreme cases, as witnessed in previous work, can lead to spontaneous oxidative metal dissolution[11]. An alternative purging method[8] uses reaction with Cl_2 gas

$$2\,LiOH_{(l)} + 2Cl_{2\,(g)} \rightleftharpoons O_{2\,(g)} + 2\,HCl_{(g)} + 2LiCl_{(l)}$$

Equation 2

with subsequent sparging with argon and/or evacuation to attempt to displace the O_2 and HCl formed and any excess Cl_2. However, evacuation again does not remove all the oxidizing species, and indeed upon heating the eutectic becomes red-brown in colour, indicating the presence of chlorine complexes[8]. Such coloured chlorine complexes have been identified spectroscopically in room temperature chloride ionic liquids purged with Cl_2[11] as Cl_3^- and Cl_5^- ions (and indeed Cl_n^-), formed through the reaction

$$Cl^- + 2\,Cl_2 \rightleftharpoons Cl_3^- + Cl_2 \rightleftharpoons Cl_5^- \leftrightharpoons\leftrightharpoons Cl_n^-$$

Equation 3

A previous method for the electrochemical removal of H_2O proposed the use of a sacrificial aluminium working electrode[11] at which an oxidising current was passed to dissolve Al^{3+} ions into the molten salt. These would go on to react with oxygen ions to produce the insoluble product Al_2O_3 through the reaction

$$Al_{(s)} \longrightarrow Al^{3+}_{(l)} + 3\,e^-$$

Equation 4

$$2\,Al^{3+}_{(l)} + 3\,O^{2-}_{(l)} \longrightarrow Al_2O_{3\,(s)}$$

Equation 5

Meanwhile, at the tungsten counter electrode lithium ions reduce water to hydrogen forming another insoluble product, Li_2O through the reaction

$$2\,Li^+_{(l)} + H_2O_{(l)} + 2\,e^- \longrightarrow H_{2\,(l)} + Li_2O_{(s)}$$

Equation 6

During this process, water and hydroxyl species are separated into oxygen and hydrogen with oxygen being removed from the liquid phase as insoluble products, and hydrogen removed as a volatile gas. Whilst this process was effective at removing water from the molten salt without the use of reactive gasses, oxy-containing species and residual Al^{3+} ions remained entrapped in the molten salt. These oxy-containing species were electrochemically detectable in the melt from a small reducing current below -1.00 V. Therefore, whilst this method excluded the use of reactive gases, it did not meet the aim of developing an electrochemical drying method which resulted in a pure molten salt.

Charlotte Brady[12] began work on an electrochemical method based on drying the molten salt using CV cycling. Once fused, the salts were electrochemically treated, using cyclic

voltammetry across the full potential window of the LKE for between twenty and two thousand cycles at either 100 mV s^{-1} or 200 mV s^{-1}. This was found to result in a drier molten salt for conducting electrochemical studies and forms the basis from which this work continues.

6.3 The Concept

The motivation behind this work was to devise a method that avoids the production of either an oxidative or a reductive environment. To avoid this happening, exactly the right amount of oxidising or reducing agent would need to be added to the melt to react with the impurities. This is difficult using reactive-gas drying as it is challenging to deliver a precise amount of HCl or Cl_2 chemically. This is possible to achieve electrochemically by reducing Li^+ to lithium and oxidising Cl^- to chlorine. An electrochemical method is also more convenient for preparing anhydrous chloride eutectics as H_2O is electrochemically active so direct reduction or oxidation of H_2O or associated species is also possible. In this study a novel electrochemical method for this rigorous H_2O removal which utilises the selective electrolysis of water to eliminate H_2 and O_2 and which can be used to avoid oxidizing or reductive environments and the use of reactive gases is demonstrated.

To achieve this, the electrochemical diagnostics and understanding of the drying process has been determined to identify the characteristics of a pure molten salt and allow possible in-situ monitoring of the presence of H_2O in the molten salt. The principle behind this work was to electrochemically generate H_2 and O_2 for evacuation from the salt, to remove H_2O and OH^-.

6.3.1 Electrochemical Drying by Cyclic Voltammetry

In earlier work by Dr Brady[14], the aim was to clean the salt by employing successive reducing and oxidising electrode potentials by cyclic voltammetry. The cathodic reactions at reducing potentials result in the reduction of acidic or aqueous protons and hydrogen evolution. Evacuation then leads to removal of gaseous products of the reactions

$$2\,H^+_{(l)} + 2\,e^- \rightarrow H_{2(g)}$$

Equation 7

$$2\,OH^-_{(l)} + 2\,e^- \rightarrow 2\,O^{2-}_{(l)} + H_2O_{(l)}$$

Equation 8

$$H_2O_{(l)} + 2\,e^- \rightarrow H_{2(g)} + O^{2-}_{(l)}$$

Equation 9

whilst the anodic reactions at oxidising potentials lead to the oxidation of oxide, hydroxide and/or water with the generation of oxygen, which is then removed by evacuation, and protons.

$$2\,H_2O_{(l)} \rightarrow O_{2\,(g)} + 4\,H^+_{(l)} + 4\,e^-$$

Equation 3

$$2\,OH^-_{(l)} \rightarrow O_{2\,(g)} + 2\,H^+_{(l)} + 2\,e^-$$

Equation 11

$$2\,O^{2-}_{(l)} \rightarrow O_{2\,(g)} + 4\,e^-$$

Equation 12

It should be remembered that when the working electrode is performing the cathodic reaction (equations 7, 8 and 9) the counter electrode is performing the oxidative reactions (equations 10, 11 and 12) and *vice versa*.

In an ideal solvent, the only oxidative or reductive currents in a CV can be attributed to the reduction or oxidation of the component species of the solvent. In the case of lithium chloride-potassium chloride eutectic, the only observable peaks should be due to either the redox reactions Cl^-/ Cl, K^+/ K or Li^+/ Li. As potassium is more noble than lithium, the negative solvent limit can be attributed to the reduction and oxidation of lithium, and the positive solvent limit is the oxidation and reduction of chloride ions. At the positive limit, the expected reduction peak will not be observed in the case of chloride through equation 3, as the oxidised species shall go on to react with other chloride ions and form stable complexes.

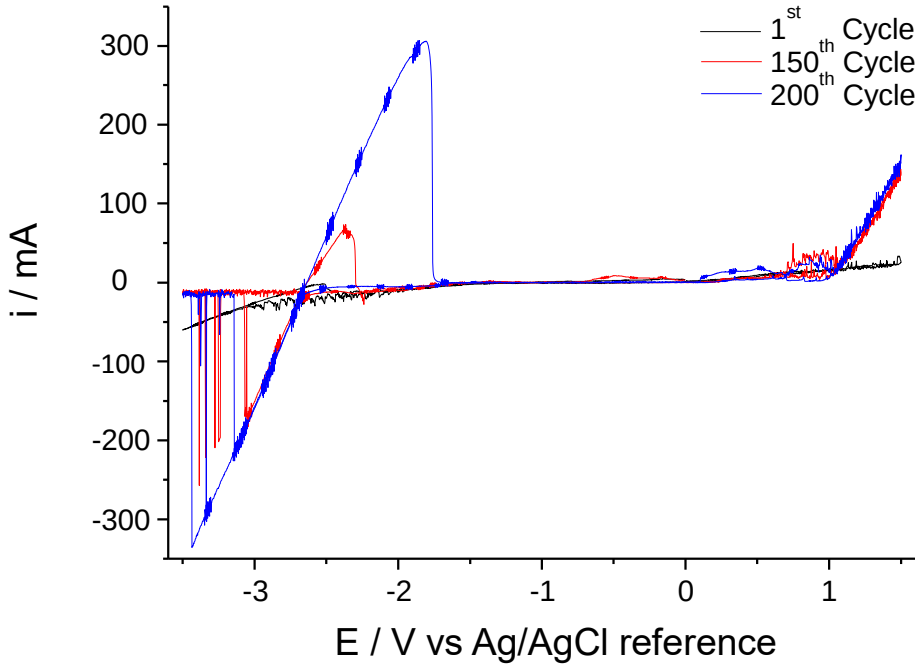

Figure 6.1: Cyclic voltammograms of electrochemical cleaning of LKE using cyclic voltammetry after the 1st (as melted LKE), 150th (partially dried LKE) and 200th (dried LKE) cycles. Cycles consist of sweeping the potential between 1.5 V and -3.5 V at 200 mV s^{-1}.

Figure 6.1 compares the cyclic voltammograms recorded in the molten salt during the cyclic voltammetry cleaning process at the first, 150th and 200th cycle (note that there is repeated periodic noise in the current signal that occurs due to electromagnetic noise generated by the furnace heating element).

In scan 200 on Figure 6.1 the solvent limit is clearly defined as would be expected by the reduction and oxidation of lithium at the negative potential limit (-2.60 V), and the oxidation of chloride and the absence of a corresponding reduction current at the positive potential limit (+1.10 V). A flat current between these limiting reactions would be typical for a pure solvent, and therefore this provides the characteristic signal for a dry molten salt. The charges passed during oxidation and reduction of the lithium in the dry molten salt is equal, indicating the absence of any competing chemical reaction of the lithium with other species in the melt.

In the intermediate CV, scan 150, additional currents are observed between the solvent limits. Between -0.50 V and +1.1 V an oxidising current has been passed, particularly between +0.80 V and +1.0 V. Similarly, a reduction current is passed prior to the lithium peak between

-1.50 V and -2.20 V. Since scan 150 contains some water contamination in addition to the pure LKE as previously described, the oxidising currents between -0.50 V and +1.1 V can be explained by the reactions in equations 10 to 12 and attributed to OH^- and oxygen in the molten salt. Equally, the reducing current between -1.50 V and -2.20 V can be attributed to the reactions in Equations 7 to 9 and attributed to hydrogen in the molten salt.

The noisy responses in the region above +0.80 V is diagnostic of gas evolution as bubbles of gas form and grow blocking active regions on the tungsten electrode surface, reducing the effective electrode area, before detaching from the electrode leading to a spike in current. This could be explained by the oxidation of chloride and the formation of chlorine gas. However, this spiking is not observed in dry molten salt (Scan 200), which would be the case if it was attributed to Cl_2. Therefore, this spiking can only be attributed to the oxidation of oxygen either electrochemically, or chemically by the chloride complexes, resulting in the formation of oxygen gas bubbles.

By comparing the lithium reduction and oxidation charges passed in scan 150, a far greater charge is passed during reduction than oxidation. This suggests that a chemical oxidation of the reduced lithium is occurring before the potential is reversed, and provides further evidence for the presence of contaminant species in the melt.

In the first cycle very little current is passed at all potentials. This can be attributed to the expected resistive native oxide layer on the tungsten electrodes when first inserted to the molten salt. This resistance initially leads to low currents being passed. However, these data show much of this surface oxide film is removed (or becomes porous) during the first reductive scan, which can be attributed to the reaction in equation 13, resulting in recognisable voltammetry in subsequent scans.

$$WO_{x\,(s)} + 2xe^- \rightarrow W_{(s)} + xO^{2-}{}_{(l)}$$

Equation 13

6.3.2 Electrochemical Drying by Alternating Potential Pulsing

Whilst apparently effective at removing water and oxy- and hydroxyl- containing species from the melt without the chemical introduction of reactive gases, the cyclic voltammetry method had the disadvantage of being a time consuming process. This is because for much of the

duration of the drying, the applied potential was between the solvent limits, where little or no reaction was taking place. Therefore, this thesis introduces a pulse sequence method.

The first pulse could either be to a negative or a positive potential. As the native oxide on the electrodes passivates the electrode surface, this must first be removed before the salt can be dried electrochemically. The native oxide is removed by the reaction in equation 13 at negative potentials, and therefore the first pulse needs to apply a negative potential. In addition to reducing the tungsten oxide, lithium is reduced in the first pulse and then the second pulse switches the potential positive to generate chloride species at the working electrode, with the reverse occurring at the counter electrode. The potentials to which the electrodes were pulsed were chosen to be potentials beyond the solvent limit where lithium would be readily reduced, and chloride would be oxidised. The chosen potentials were -2.75 V for the negative potential and +1.50 V for the positive potential as this pair of potentials resulted in similar magnitudes of current in the CV of dry molten salt (Figure 6.1, Scan 200).

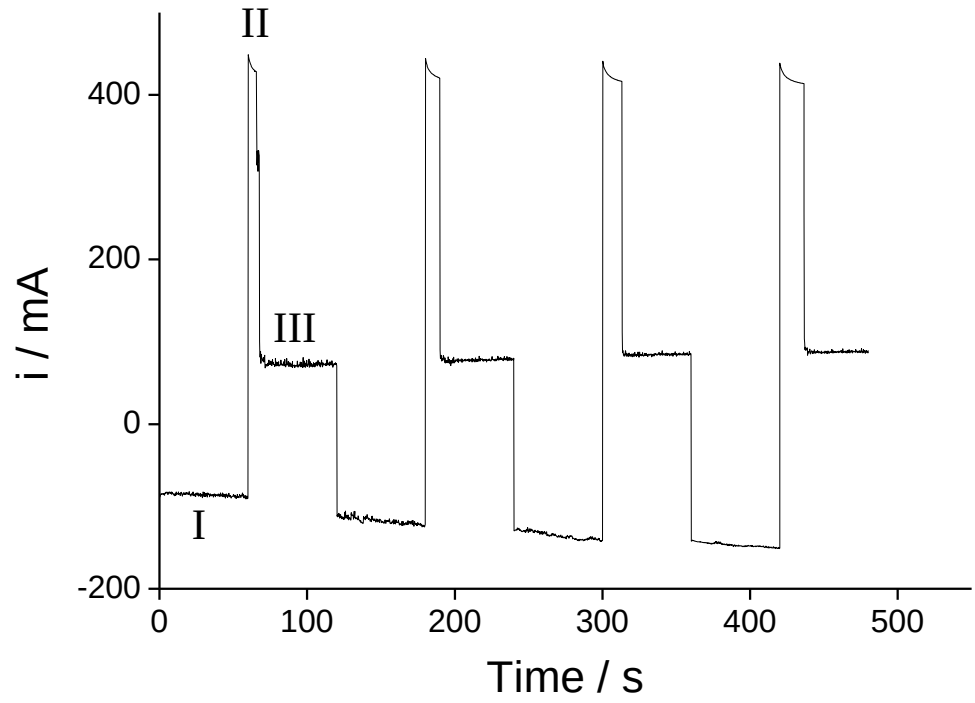

Figure 6.2: The chronoamperogram resulting from pulsing the tungsten working electrode in LKE from -2.75 V to +1.50 V at 60 s intervals for 4 cycles.

Initially eight alternating potential pulses of -2.75 V, where lithium is reduced, and + 1.50 V, where chloride is oxidised, each of 60 seconds in duration were applied to the cell, (

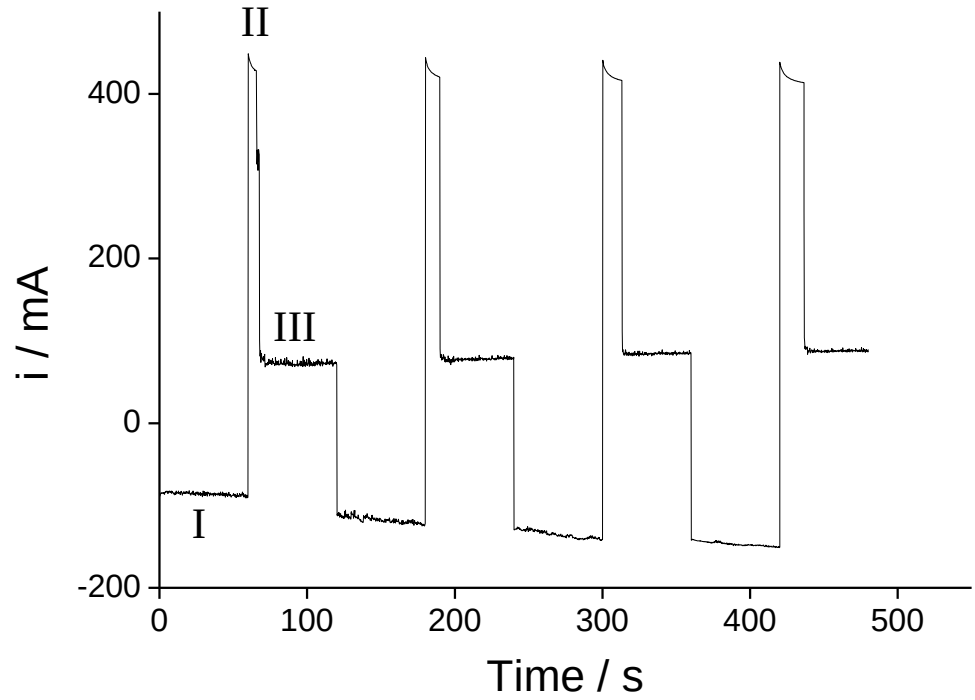

Figure 6.2) leading to first local then widespread generation, liberation and evacuation of first H_2 then O_2 (vice versa from the counter) from H_2O via the electrodes. The pulse cycling was designed to increase drying efficiency, as greater time, and therefore charge, was passed for each reaction; and as the products of the anodic reactions are reagents for the cathodic reactions, and *vice versa*.

The equivalent current response associated with potential pulsing of LKE was also recorded and is shown in

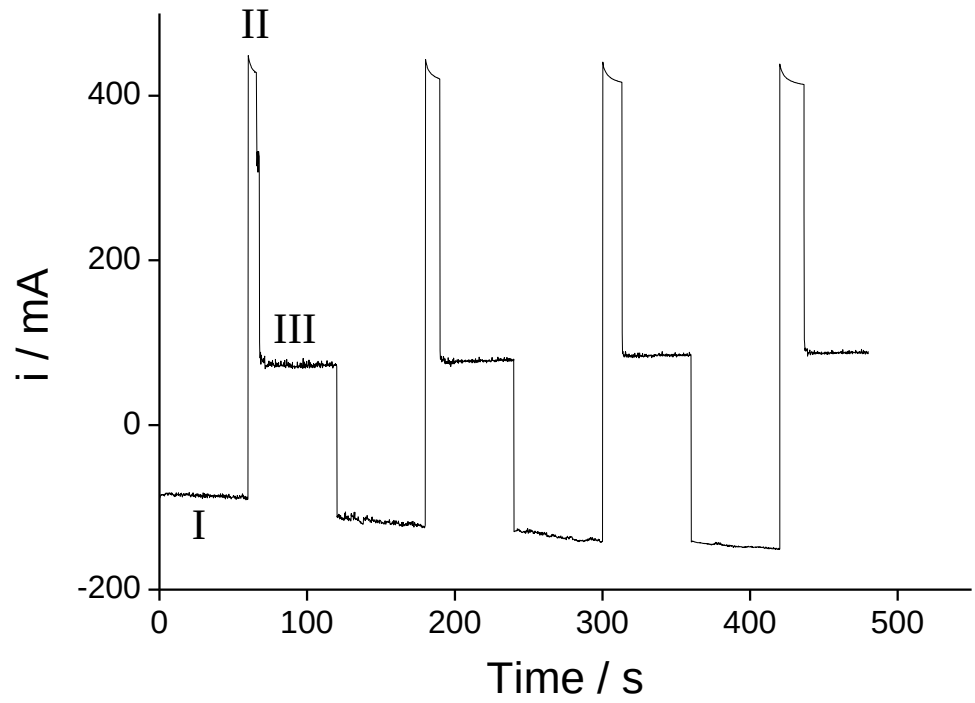

Figure 6.2. Holding the potential at -2.75 V resulted in currents of approximately -80 to -150 mA. The observed current response at this potential is predominantly due to lithium plating on the tungsten wire electrode (I). The magnitude of the current in the first pulse is consistent with rapid initial tungsten oxide reduction, with the additional current related to this reduction (Equation 13) lost within the lithium reduction. Switching the potential to +1.50 V results in an initially large current (~450 mA) which is due to lithium oxidation (III); following the removal of this plated lithium the current drops to a steady state value of ~ 75 mA; this current is similar in magnitude to that that found at this potential in CVs and can be attributed to chloride oxidation at the tungsten wire electrode (III). It is to be expected that the lithium and chlorine complex produced will act as reducing and oxidising agents respectively, reacting with the aqueous species to again generate hydrogen and oxygen gas products which will be removed *in vacuo*. As expected in this case, across the time course of the experiment the current associated with lithium plating (I) increases in magnitude. As with the CV experiments this suggests a cleaner tungsten electrode free of oxide due to a drier salt system; that this is not an increase in effective electrode area can be seen by the constancy of current (III) with each successive pulse. The increased current (II) has a progressively increasing time duration

(charge). This is consistent with reduced chemical loss of lithium owing to reoxidation by other species in the melt through the reaction

$$2\,Li_{(l)} + 2\,H^{+}{}_{(l)} \rightarrow\ 2\,Li^{+}{}_{(l)} + H_{2(g)}$$

Equation 14

Indeed, integration of the charges passed during lithium oxidation (II) and lithium plating (I) gave an initial ratio of charge passed of 40% as the reduced lithium chemically reacts to reduce other species in the melt and is not then electrochemically oxidised on the reverse pulse. After the four successive pulses shown the charge ratio increases 85% as less of the reduced lithium is chemically reoxidised by other species in the melt. This increase in efficiency of oxidation again indicates drying of the electrolyte and removal of the reactive aqueous contaminants by this pulsing process.

After the initial electrolysis pulse sequence, a further pulse sequence was applied to ensure complete drying of the molten salt was achieved.

Having electrochemically treated the melt, the next aim was to demonstrate its dryness. Figure 6.3 compares the cyclic voltammograms (CVs) of LKE that has been fused under vacuum (I), treated with the potential pulse sequence of eight alternating potential steps shown in

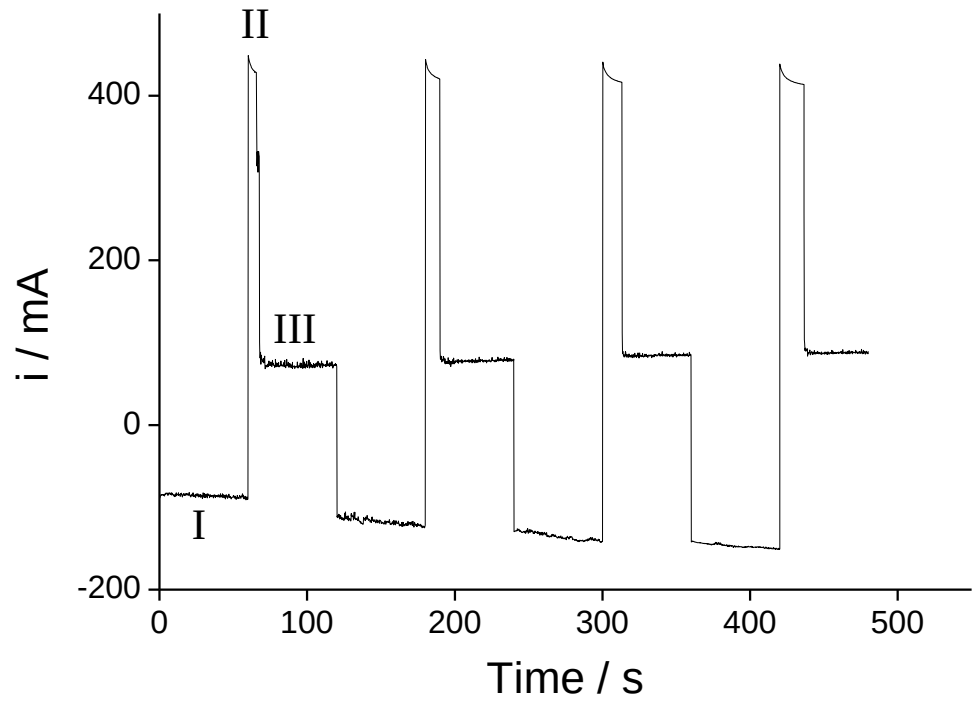

Figure 6.2(II) and then treated with a second series of potential pulses (III).

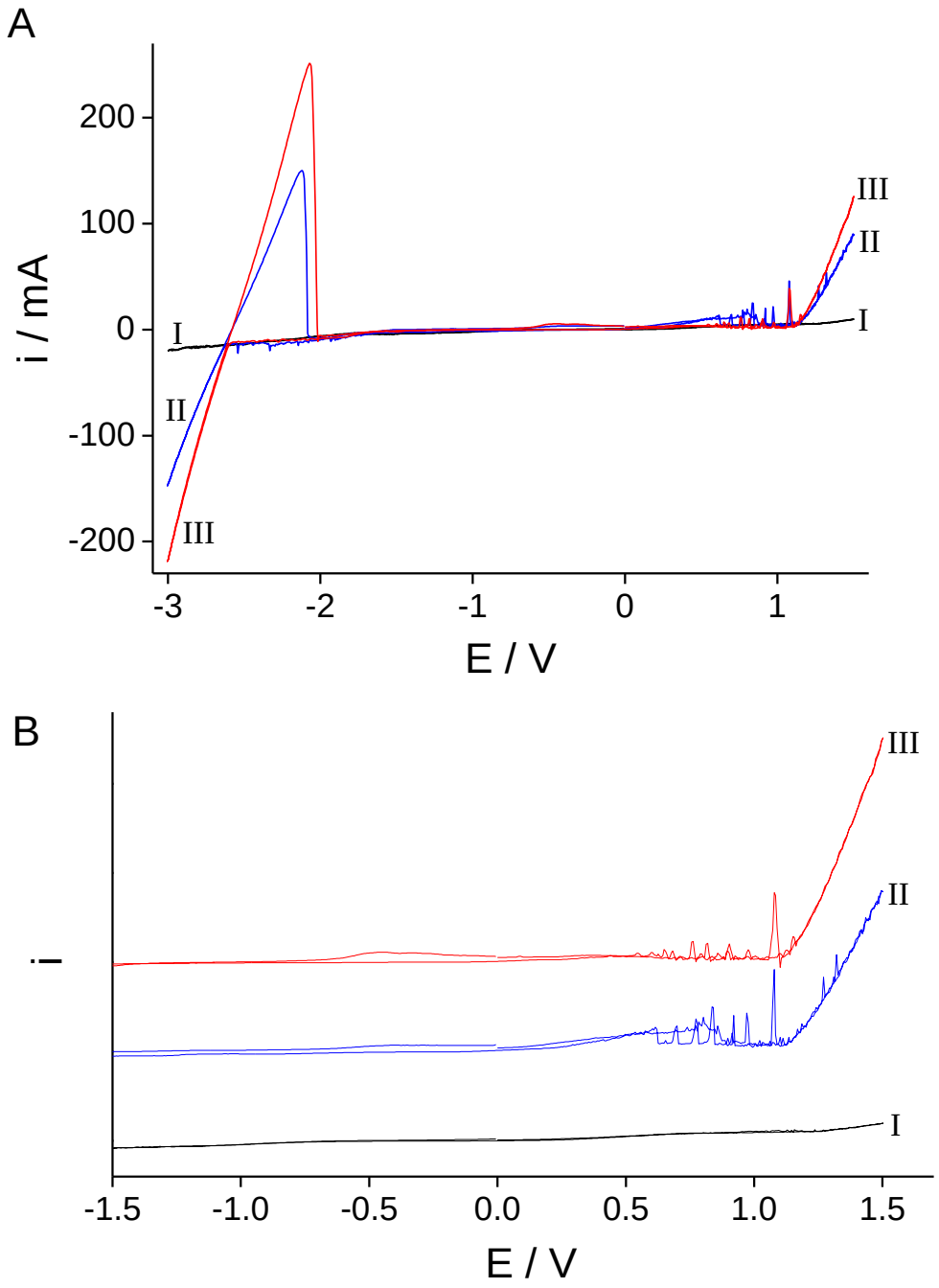

Figure 6.3: A) CVs recorded on a tungsten wire of I) previously untreated, fused salt, II) salt subjected to 4 x 60 s reductive and 4 x 60 s oxidative cleaning pulses, III) Salt subjected to an additional 5 x 30 s reductive and 30s oxidative potential pulses. B) Expanded sections of CVs from Figure 3(A) over the region -1.50 V to 1.5 V. I, II and III have been offset from each other by 50 mA for clarity.

The final CV (III) in Figure 6.3 is comparable to Cycle 200 in Figure 6.1 with the solvent limit clearly defined by the Li^+/ Li peaks, and the chloride oxidation current. Between these

potentials the CV is largely featureless with almost no current passing, typical of a pure system with no other electrochemically active species.

In CV (II) the spikes in the oxidation current between +0.50 V and +1.20 V are again indicative of the change in electrode area. This diagnostic of oxygen gas bubble generation, evolution and detachment is observed to a much lesser extent in the drier salt in CV (III), and to a much greater extent in the CVs of molten salt cleaned using the cyclic voltammetry method. As the oxygen (generated by the schemes described in Equations 10 to 12) is removed *in vacuo* (particularly seen after the final electrolysis (III)) the gas evolution peak heights decrease and they shift to higher potential, between 0.75 V and 1.00 V. This is consistent with decreasing reagent activities (reflecting both decreasing concentration and activity coefficients, the latter arising from increasing interaction between reagent and molten salt ions) that makes the oxidation reactions progressively less favoured. In addition, the lithium plating and stripping redox features below -2.00 V increase in magnitude and area from CV (III) to CV (II), and the charge ratio between oxidation and reduction approaches 1. These changes reflect the decrease in lithium chemical oxidation through the progressive removal of O_2. The previously observed hydrogen reduction wave below -1.00 V attributable to Equations 7 to 9 is also less apparent, indicating that there is less hydrogen in the melt.

It is clear that prior to the cleaning, in CV (I), the low currents observed are indicative of high electrode resistance expected from the presence of passivating tungsten oxides (WOx) on the electrodes, as previously seen in the cyclic voltammetry method already discussed.

Together the CVs in Figure 6.3 are diagnostic of progressive molten salt drying, indicating that not only can water be removed from the molten salt using the method developed here, but that the presence of water can be identified from the corresponding peaks and waves in the CV.

Of course, the CV of dry molten salt does not preclude the presence of either an oxidising of reducing environment, as is the case arising from molten salt dried using reactive gas purging. If the salt is either oxidising or reducing, chemical reactions in the melt would proceed in parallel to the electrochemical study, and species which were electrochemically reduced would be chemically oxidised or vice versa. This would be apparent in the CVs, as reactions would, in the extreme instance, appear to be irreversible. An alternative means of testing this would be to deliberately fix the potential of the cell by depositing lithium on the electrode and

monitoring the potential as if it were a reference electrode. If the salt was oxidising, the lithium metal would be chemically oxidised, and the Li/Li^+ potential lost.

Figure 6.4 demonstrates the stability of the measured open circuit potential following lithium plating at the tungsten wire electrode in salt that has A) been dried using reactive gas purging, and B) been dried using the pulsed potential method described earlier in this chapter.

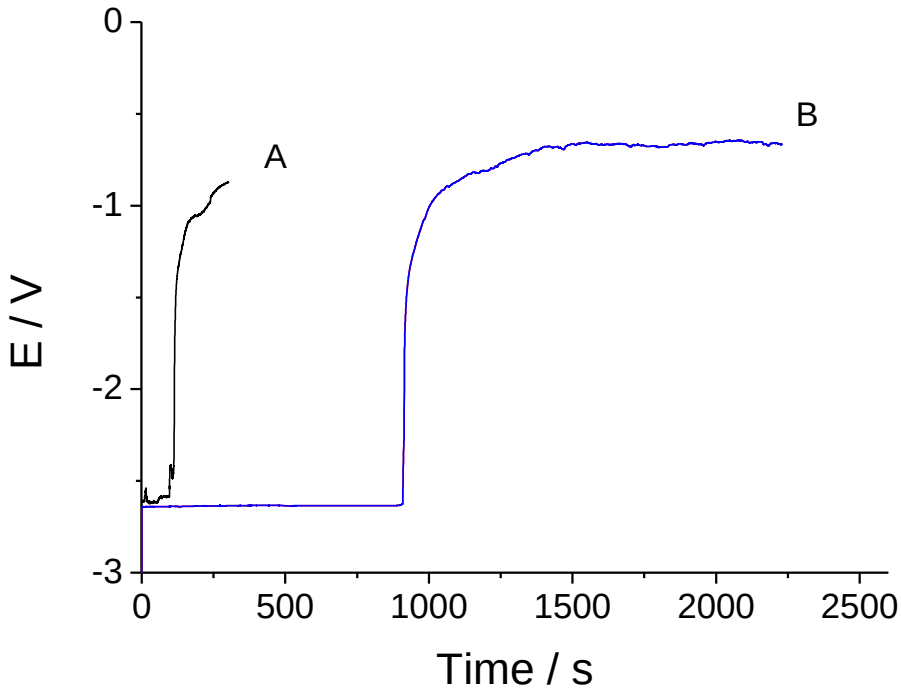

Figure 6.4: The variation in the open circuit potential, E, after 120 second plating of Li at a tungsten wire in A) reactive gas dried LKE (Sigma Aldrich) and B) pulsed potential dried LKE.

Initially, the zero current potential is always near -2.65 V, diagnostic of the expected Li/Li^+ redox potential set up between the deposited Li and the high and constant activity of Li^+ ions in the melt. However, in the reactive gas dried salt (A) (as purchased from Sigma Aldrich, UK), this potential changes rapidly to be more oxidative within a couple of minutes. The change in potential could be due to: progressive mechanical loss of the deposited lithium; the short circuit reaction of oxidised chloride product from the counter electrode reaction re-

combining with the lithium (Equation 17); or the end point of the chemical oxidation reactions by H_2O, OH^- or Cl_2 which cause the complete removal of Li;

$$Li_{(l)} + H_2O_{(l)} \rightarrow Li^+_{(l)} + OH^-_{(l)} + ½\, H_{2\,(g)}$$

Equation 15

$$Li_{(l)} + OH^-_{(l)} \rightarrow Li^+_{(l)} + O^{2-}_{(l)} + ½\, H_{2\,(g)}$$

Equation 16

$$Li_{(l)} + \frac{1}{2} Cl_{2\,(l)} \rightarrow LiCl_{(l)}$$

Equation 17

In contrast to salt (A), in electrochemically dried salt (B), a steady potential is held for at least 15 minutes. If the loss of potential in salt (A) were due to either progressive mechanical loss, or the short-circuit reaction, we would expect the loss of fixed potential to occur on the same time scale in both salts as these losses would be governed by diffusion of either Li or chloride in the melt.

Of course, a possible argument for the eventual observed change in potential in the electrochemically dried salt could be the presence of a lower level of residual moisture. Equation 18 shows the approximate calculation that based on the electrode separation of about 50 mm and typical diffusion coefficients of the order 10^{-5} cm^2 s^{-1} the diffusion time for the Cl_2 from the counter electrode to the working electrode is approximately 1000 seconds.

$$\frac{l\,(m)^2}{D(cm^2 s^{-1})} = t\,(s)$$

$$\frac{(0.05\,m)^2}{(10^{-5}\,cm^2\,s^{-1})} \approx 1000\,s$$

Equation 18

Given that the loss of potential is observed at around the time that the Cl_2 (or other chlorine complex as defined in Equation 3) would take to diffuse to the working electrode and undergo the short circuit reaction (Equation 17), this is most likely explanation for the loss of a stable Li/Li^+ potential. It is therefore likely that this is also an upper time limit to the stable potential,

determined by the removal of liquid lithium by chlorine generated at the counter electrode during the lithium deposition diffusing to the working electrode and diagnostic of rigorously dry LKE. If a frit were to be introduced between the working and counter electrodes, it should be possible to prevent the short circuit reaction and hold the potential indefinitely. This thesis has not investigated this experiment, however future investigation of this would be desirable to further prove the rigour of the drying method proposed.

The ability to hold this diagnostic Li/Li^+ potential for the time required for the short circuit reaction to occur is a clear demonstration of the ability to produce LKE free of an oxidising environment. Equally it could be considered that if the salt were a reducing environment, the short circuit reaction could not take place as the product at the counter electrode would be reduced before it could diffuse to the working electrode. It has therefore been demonstrated that the aim of developing an electrochemical method of drying molten salt without introducing a reducing or oxidising environment has been achieved, and that using cyclic voltammetry it is possible to determine the presence of water and related oxy-/hydroxyl-species.

6.4 Redox Studies in Electrochemically Dried Molten Salt

Up until this point, the dried molten salt has not been tested using a redox agent. To further demonstrate the production of rigorously dry salt, a redox agent was added to the melt post drying. If the dried salt was in an overall reducing state, it would be expected that the species would be chemically reduced, precluding its electroanalysis. If the dried salt was in an overall oxidising environment, any reduction of the species would not be accompanied by the expected, corresponding oxidation peak, as it would be chemically oxidised prior to the potential sweep being reversed. To exclude this possibility, the electroanalysis of silver (I) in electrochemically dried LKE was demonstrated.

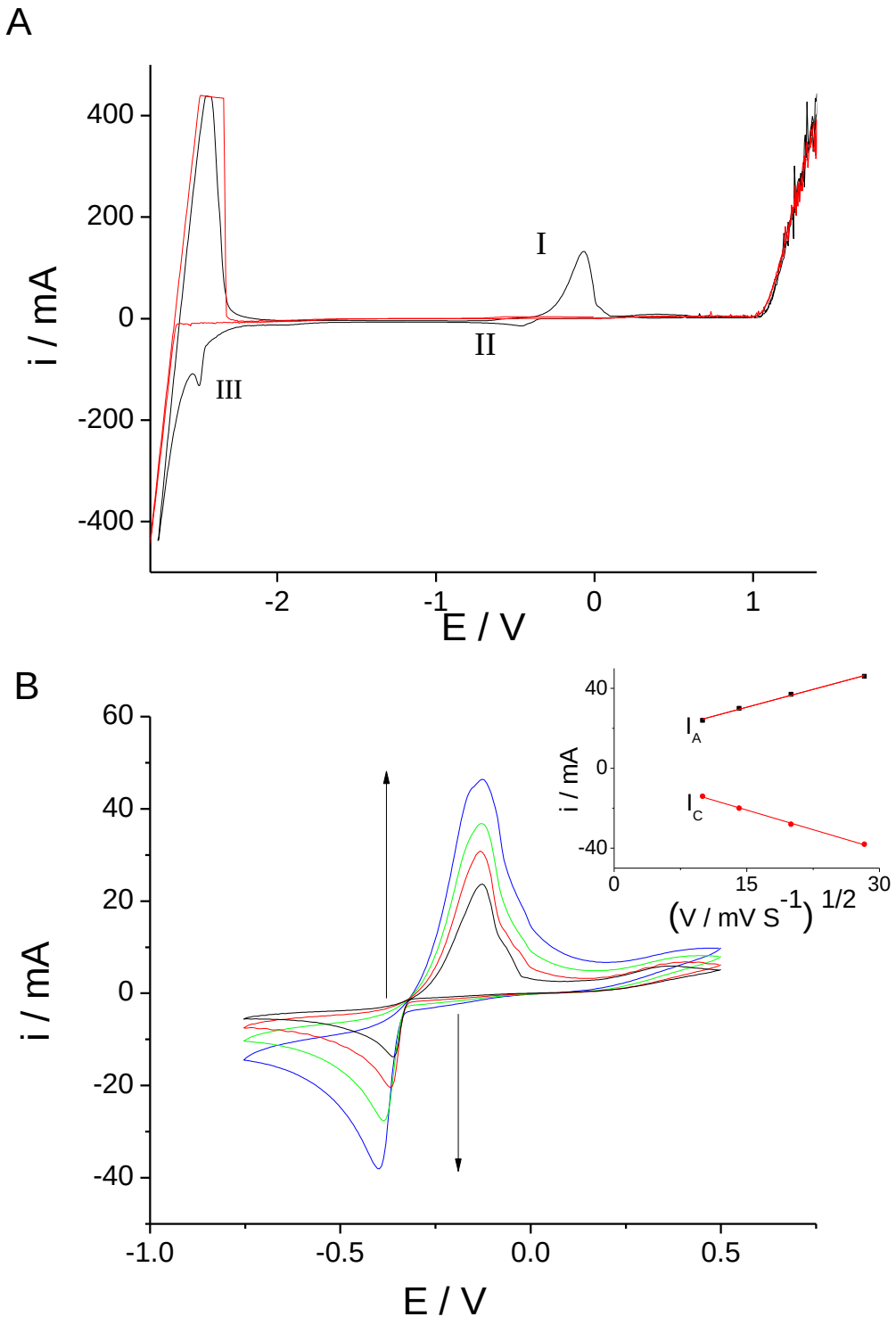

Figure 6.5: (A) Cyclic voltammetry in electrochemically dried LKE with and without 0.063 M kg^{-1} AgCl. Starting at 0 V the potential was scanned firstly to +1.50 V and then back to -2.75 at a scan rate of 200 mV s^{-1}. (B) Silver stripping and plating in LKE + 0.035 M kg^{-1} between potential limits of -0.75 V and 0.50 V with scan rate increasing as shown by the arrows (100 mV s^{-1}, 200 mV s^{-1}, 400 mV s^{-1}, 800 mV s^{-1}). Inset shows plots of anodic and cathodic peak currents, i_A and i_C, vs $V^{1/2}$.

Figure 6.5A shows two cyclic voltammograms, one from LKE (Red) and one from LKE with added (0.063 mol kg^{-1}) AgCl (Black). Features in the voltammogram resulting from silver oxidation (I), reduction (II) and a lithium on silver deposition (III)[13] were only present in the electroanalysis of LKE with AgCl added. Figure 6.5B shows silver stripping and plating in LKE for a range of scan rates. Consistent with a lack of a reducing environment, no silver was observed in the salt pellet following cooling and fusion. It can also be seen that the diagnostic silver plating/stripping system was observed on the addition of silver(I) near 0 V (B) as expected (not at 0 V due to the slight differences in silver ion activity in melt and reference electrode). The characteristic diffusion-limited silver plating peak was observed, with the expected square-root dependencies of peak heights to sweep rate (see Figure 6.5B inset), consistent with a stable solution of silver(I) of constant concentration. The AgCl concentration in the melt, calculated using the Randles-Sevcik equation[14,15] and the literature diffusion coefficient of Ag(I) in LKE (2.39 $x10^{-5}$ cm^2 s^{-1})[16] was 0.048 M, consistent with the expected value of 0.050 M. The charges passed during silver plating and stripping are also equal at all sweep rates. Together these observations indicate the lack of a reducing or oxidizing solution environment. It is interesting that there is an additional reduction peak (III) seen during lithium plating at -2.50 V with silver chloride in the melt, which is attributable to either the underpotential deposition of lithium on silver, or the deposition of lithium into the deposited silver.

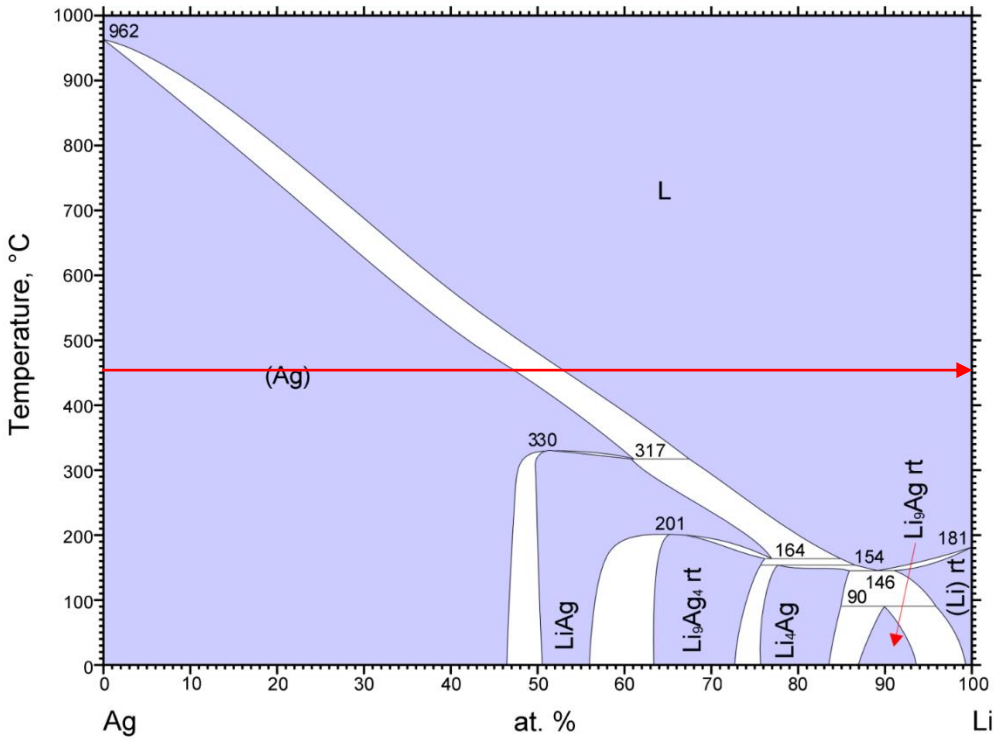

Figure 6.6: Binary phase diagram for the silver – lithium system[17] indicating the Li-Ag mixture at 450°C (marked by the red arrow).

Figure 6.6 shows the phase diagram for the silver-lithium system, with the red arrow indicating the increasing proportion of lithium at 450 °C. Looking at the phase diagram, we see that as the ratio of lithium to silver reaches approximately 45:55, there is a transition from a mixed phase to a single phase, and again a ratio of 55:45 there is another transition back to a mixed phase. The transition from Li accumulating at the silver electrode into the single Ag-Li phase could explain the peak feature observed at (III).

In conclusion it has been shown that a pulsed potential method can be used to electrochemically remove water from lithium chloride-potassium chloride eutectic. This method eliminates the requirement for purging with reactive gases that typically result in either oxidising or reducing environments, and enables on-line diagnostics of LKE to determine the presence of water. Whilst this method has demonstrable advantages over previous drying methods, it would still be desirable for molten salt to be dried with the redox agent in-situ. Should a molten salt reprocessing system suffer from an accumulation of water during

operation, an ideal method would allow the removal of water, without significantly affecting the species in the melt.

6.5 *In-situ drying of LKE containing a redox agent*

Having a pure and rigorously dry molten salt is a vital foundation for accurately and reliably studying the electrochemical behaviour of redox species in the melt. The process of adding a redox species to the melt however can be fraught with problems in maintaining a sealed system, and preventing the ingress of air and moisture. In addition to this, continual operation of molten salt processing systems whilst avoiding the accumulation of water is fraught with difficulties. As a means of overcoming this, it was desirable to test the pulsed potential cleaning method on a molten salt to which a redox agent had been added. One of the complexities of this process is the ability of retaining the desired oxidation state of the species which was to be added to the molten salt to be studied.

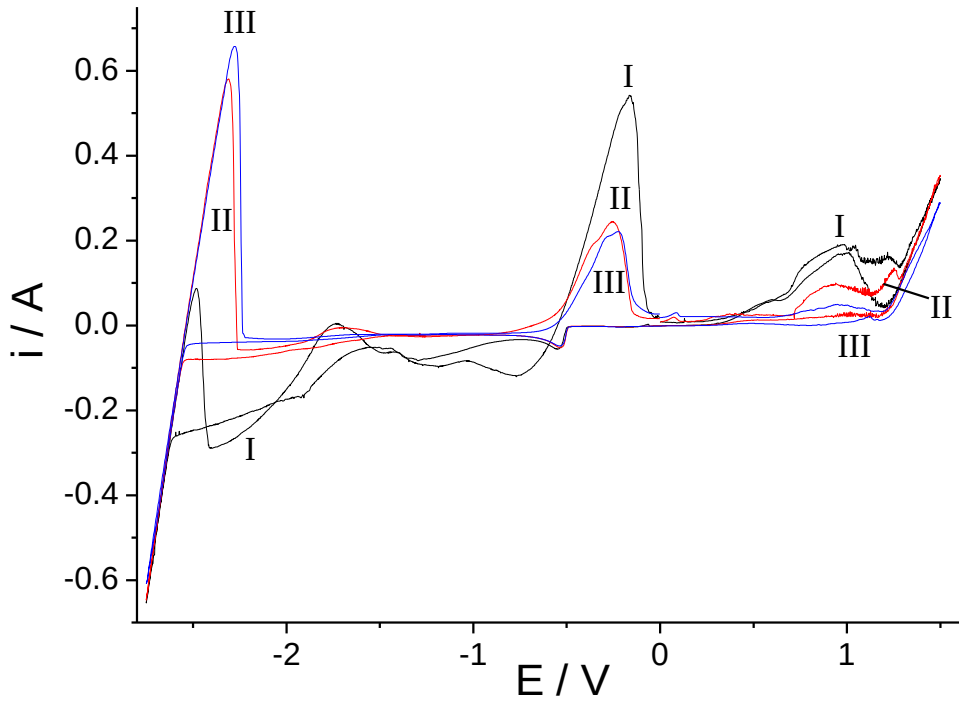

Figure 6.7: CVs recorded on a tungsten wire vs Ag/AgCl reference of LKE containing 5 mM Fe(II)Cl_2.6 H_2O with I) no previous treatment, II) salt subjected to 8 x 30 s oxidative and 8 x 30 s reductive cleaning pulses, III) Salt subjected to an additional 4 x 15 s oxidative and reductive potential pulses.

Figure 6.7 compares the cyclic voltammograms (CVs) of LKE containing 5 mM $FeCl_2.6\ H_2O$ that has been fused under vacuum (I), treated with an initial potential pulse sequence of eight alternating potential steps (II) and then additionally treated with a further sequence of 4 shorter potential pulses (III). It is noteworthy that by adding a precise quantity of hydrated redox agent to a thoroughly dried eutectic, it is possible to deliver a known quantity of water to the eutectic, which could be used to relate the quantity of water in the melt with the oxygen oxidation peak in the CV.

As with Figure 6.1 and Figure 6.3 the oxidation of oxygen is observed above 0.50 V and reduces in magnitude from I to III as oxygen gas is evolved and removed from the salt. Furthermore, the H^+ reduction wave around -1.80 V, a common feature of pre-prepared LKE purchased from Sigma Aldrich, having been purged with HCl during fusion, reduces in magnitude as H_2 gas is evolved and removed from the melt. In the first CV (I), prior to any electrochemical treatment being applied to the salt, the reduction of Fe^{2+} initially occurs at about -0.50 V as would be expected. At potentials more negative of this, an additional reduction of Fe^{2+} is observed and when potential is swept positive of -0.50 V a large oxidation peak for Fe is observed. The increased reduction current could be due to alloy formation between Fe and Li. Alternatively, as this feature occurs around the point at which hydrogen is reduced, the hydrogen gas could be acting as a chemical oxidant at the electrode, resulting in an apparent increased concentration of Fe^{2+}. The increase Fe concentration at the electrode will then be observed electrochemically as it deposits at the electrode. When the applied potential is swept above the hydrogen reduction potential, this chemical oxidation ceases, resulting in the observed reduction current of iron firstly dropping off before diffusion limited deposition of iron at the electrode is restored. After the initial pulse sequence to remove aqueous species is applied, (II) the redox behaviour of the $FeCl_2$ reflects the 2 electron reduction and oxidation that would be expected in the absence of chemically active reducing or oxidising species. A final, shorter cycle of pulses resulted in the removal of the oxygen oxidation (0.80 V) and hydrogen reduction (-1.80 V) waves that were present in CV II, as shown by CV III. In this CV, the charge passed for both the Li^+ and Fe^{2+} reduction and oxidations were equal indicating an absence of either oxidising or reducing contaminants.

It was interesting to note that the oxidation of Fe^{2+} to Fe^{3+} is not observed in any of the CVs recorded in Figure 6.7 suggesting that this method is suitable for removing aqueous contaminants, whilst retaining the intended oxidation state of the species to be studied.

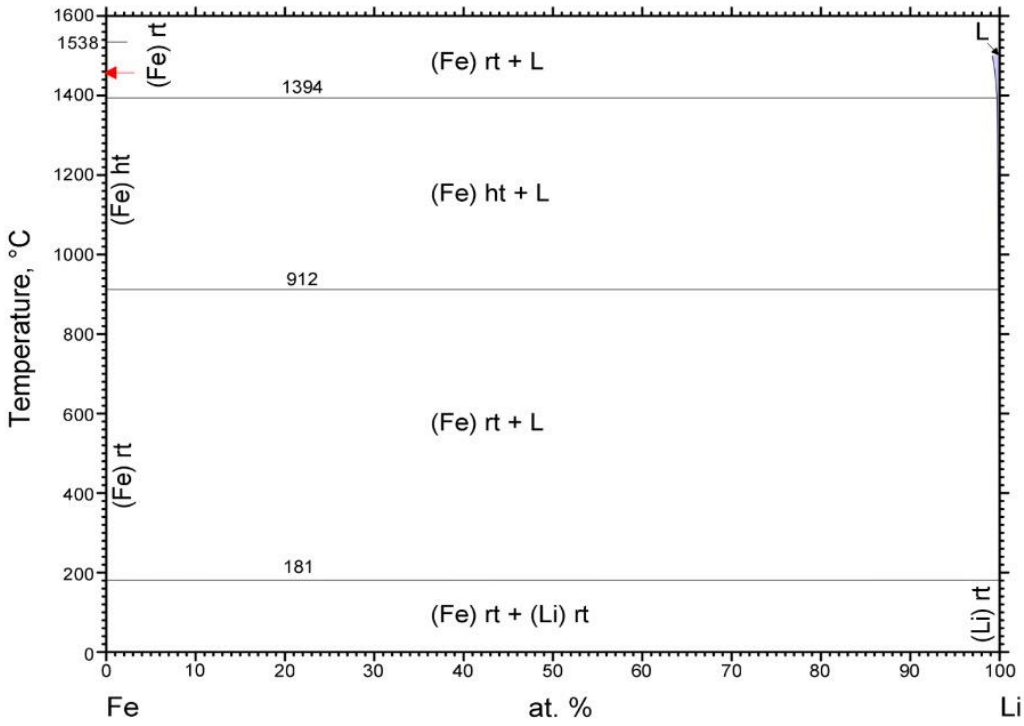

Figure 6.8: Binary phase diagram for the iron – lithium system[18].

Figure 6.8 shows the phase diagram of the iron-lithium binary system. This diagram does little to immediately explain the redox peaks about -2.00 V in Figure 6.7 CV (I) in terms of Fe-Li formation. Furthermore, the absence of this feature in CV (III), and its lesser prominence in CV (II) would suggest that this may be a result of the presence of water. Additionally, there is no lithium pre-peak as was the case with silver, and the solvent limit peaks are observed at the expected potential suggesting that this feature is not lithium depositing on iron.

As this feature occurs around the point at which hydrogen is reduced, the increased reduction current may be due to the hydrogen gas acting as a chemical oxidant at the electrode, resulting in an apparent increased concentration of Fe^{2+} at the electrode which will then be electrochemically reduced. When the applied potential is swept above the hydrogen reduction potential, this chemical oxidation ceases, resulting in the observed reduction current of iron firstly dropping off before diffusion limited deposition of iron at the electrode is restored.

This is a further demonstration of the ability of the electrochemical drying method to remove water from the molten salt, but more significantly demonstrates that it is possible to do this whilst redox agents are present in the melt. This is important because of its potential

application in recovering molten salt reprocessing systems which are subject to water accumulation without the use of reactive gases which would also chemically react with the redox species in the melt.

In serendipitous circumstances, data from Dr Damion Corrigan on measuring multiple redox species in a molten salt further demonstrates the potential for this drying method. In an experiment where $ZnCl_2$ and $CeCl_3$, which had been exposed to air during storage in the lab, had been added to LKE it was apparent that the cerium had partially decomposed to the oxide product, CeO^+.

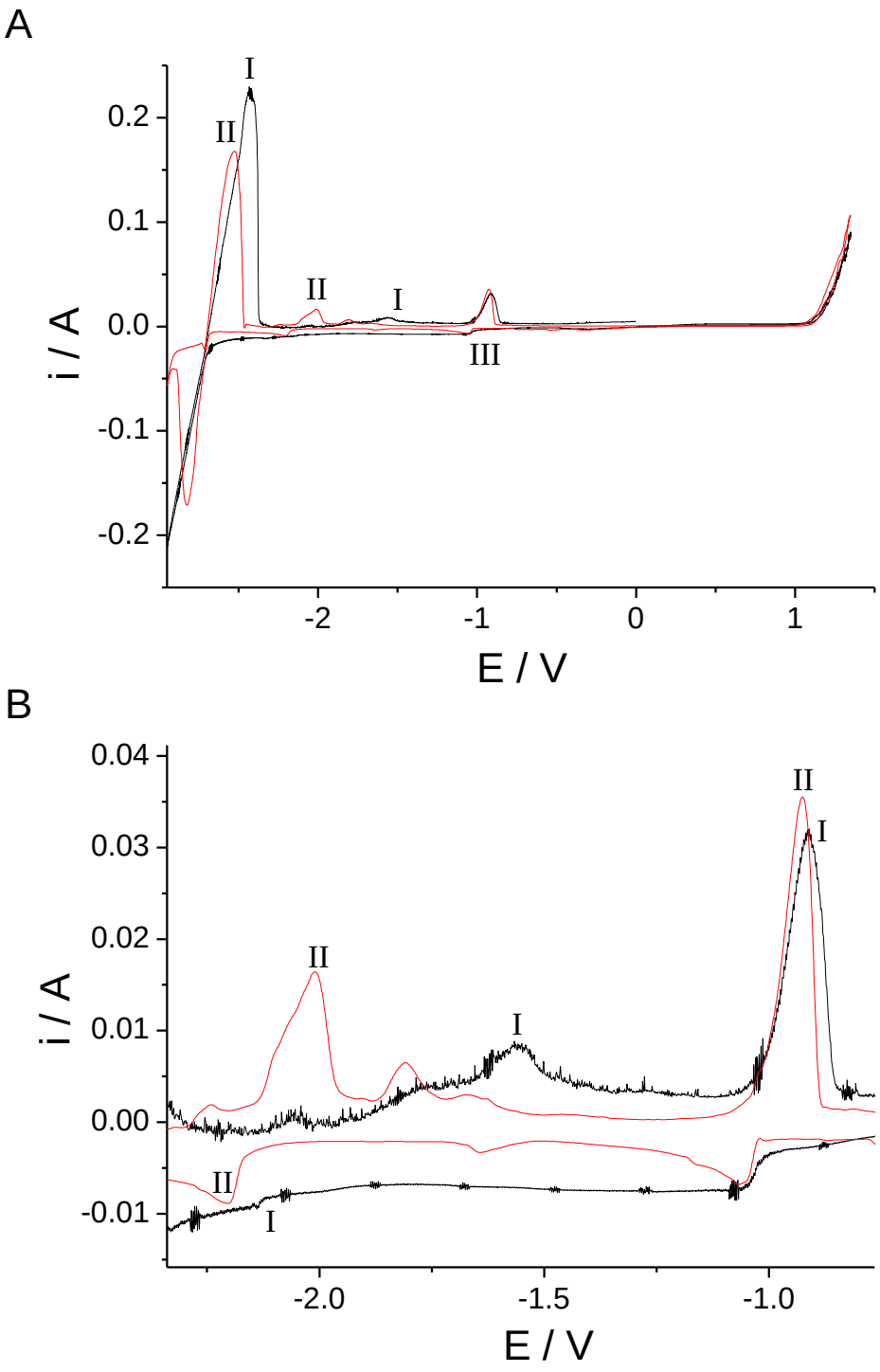

Figure 6.9: CVs recorded on a tungsten wire vs Ag/AgCl reference of I) prepared LKE an $Zn(II)Cl_2$ to which 1 mM partially hydrated $Ce(III)Cl_3$ has been added, II) salt subjected to 4 x 60 s oxidative and 4 x 60 s reductive cleaning pulses, II) Salt subjected to an additional 5 x 30 s oxidative and reductive potential pulses.

Figure 6.9, from Dr Corrigan, compares the CVs of the LKE with 1 mM of each of the redox species prior to any electrochemical drying (I) and after the pulsed potential drying method had been applied to the salt (II). The reduction and oxidation peaks of $ZnCl_2$ can be observed about -1.00 V (III) in both CVs and are broadly the same.

In Figure 6.9B, CV (I) shows a response in the oxidation sweep that has unusual fluctuations in current. Whilst this is partially from periodic electromagnetic noise from the heating coil of the furnace, the continuous fluctuations, especially those in the positive sweep, may be considered to be indicative of some gas evolution. At this potential, below -1.00 V, this is possibly the evolution of hydrogen gas bubbles. Additionally, on the reduction sweep, the reduction of zinc below -1.00 V continues at a steady current above that expected, indicating that, as with the Fe^{2+} in Figure 6.7 (I), a reducing species may be present in the melt.

A small reduction wave can be seen below -2.00 V, where the corresponding oxidation peak is present at -1.50 V. These potentials are close to the previously reported[19] peaks corresponding to the reduction and oxidation of CeO^{+} at -2.00 V and -1.39 V rather than the peaks of Ce^{3+} that have been reported as -2.18 V and -1.98 V respectively. Once the salt had been cleaned using a cycle of pulsed potentials to remove the hydroxyl- and oxy- species from the melt CV (II) showed reduction and oxidation peaks closer to their literature potentials. This variation in redox potentials for oxides and chlorides of the same metal and oxidation state has also been previously reported in uranium and other rare-earth metals[20].

In Figure 6.9A, the lithium reduction and oxidation shows different behaviour in the cleaned salt (II) due to the formation of a zinc-lithium alloy as noted in the binary phase diagram[21] (Figure 6.10).

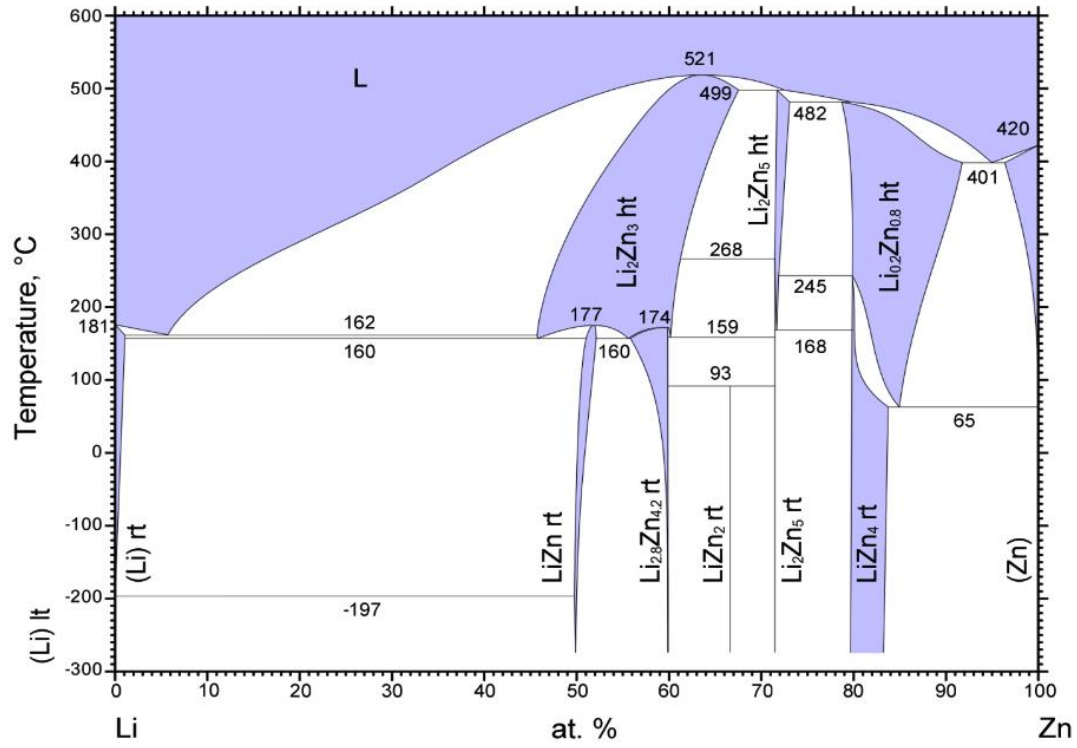

Figure 6.10: The binary phase diagram of lithium and zinc indicating the existence of several alloys, particularly the Li2Zn3 alloy at 500 °C.

6.6 Conclusions

The method of electrochemical drying demonstrated in this chapter offers a number of advantages over the traditional chemical methods hitherto employed for drying lithium potassium eutectic. Firstly, this can be achieved without creating an oxidizing or reducing environment. This is because the electrochemical signatures associated with the cyclic voltammetry and potential pulsing experiments provide direct monitoring of the dryness of the salt, enabling a diagnosis as to when complete dryness has been achieved and *in vacuo* conditions can be removed. Furthermore, this endpoint is self-limiting, as pulsing *in vacuo* first leads to the overall removal of H_2 and O_2 gas (beneficial drying), whereas further pulsing once dry *in vacuo* overall leads to the oxidation of Cl^- to the stable Cl_5^- (Equation 3) and reduction of Li^+ to Li metal, which simply results in the spontaneous regeneration of LiCl and the retention of a dry LKE which is neither oxidizing nor reducing. There is also further benefit to this method when oxides are present. One of the difficulties associated with maintaining a dry and pure melt is the dissolution of metal oxide species into the salt following chemical

cleaning. The work with tungsten demonstrates the concomitant removal of surface oxides and the work with hydrated redox agents demonstrates the removal of solution based oxides and hydroxides during the pulsing cycles, which then enables the removal of these aqueous contaminants from the system as oxygen and hydrogen gases. The concomitant removal of surface oxides on liquid cathodes has also been observed, and shall be discussed in Chapter 7.

It was also worth noting that the hygroscopic nature of the salts was such that even the highest purity "anhydrous" salts as received and packed under argon often evolved water vapour during heating and evacuation. Evidence of trace moisture could also be seen in the CV prior to electrochemical cleaning of "anhydrous" eutectic salt, sold having been fused and chemically treated to remove entrapped water.

Together, these characteristics make this method of real value in the production and monitoring of rigorously dry and oxide free LKE.

6.7 References

1. Y. Castrillejo, M. R. Bermejo, E. Barrado, A. M. Martinez, P. D. Arocas, *Journal of Electroanalytical Chemistry*, 2003, **545**, 141
2. S. P. Fusselman, J. J. Roy, D. L. Grimmett, L. F. Grantham, C. L. Krueger, C. R. Nabelek, T. S. Storvick, T. Inoue, T. Hijikata, K. Kinoshita, Y. Sakamura, K. Uozumi, T. Kawai, N. Takahashi, *Journal of the Electrochemical Society*, 1999, **146**, 2573
3. J. Serp, M. Allibert, A. Le Terrier, R. Malmbeck, M. Ougier, J. Rebizant, J. P. Glatz, *Journal of the Electrochemical Society*, 2005, **152**, C167
4. O. Shirai, K. Uozumi, T. Iwai, Y. Arai, *Journal of Applied Electrochemistry*, 2004, **34**, 323
5. H. A. Laitinen, W. S. Ferguson, R. A. Osteryoung, *Journal of the Electrochemical Society*, 1957, **104**, 516
6. N. Q. Minh, B. J. Welch, *Australian Journal of Chemistry*, 1975, **28**, 965
7. G. Z. Chen, D. J. Fray, *Journal of the Electrochemical Society*, 2002, **149**, E455
8. D. L. Maricle, D. N. Hume, *Journal of the Electrochemical Society*, 1960, **107**, 354
9. Y. Castrillejo, M. R. Bermejo, A. I. Barrado, R. Pardo, E. Barrado and A. M. Martinez, *Electrochimica Acta*, 2005, **50**, 2047
10. D. L. Hill, J. Perano and R. A. Osteryoung, *Journal of the Electrochemical Society*, 1960, **107**, 698

11. N. Brockie, *Applications of Liquid Cathode Electrochemistry towards the Nuclear Industry* (2011), PhD Thesis, University of Edinburgh
12. C. L. Brady, *The Development and Characterisation of Microelectrodes for Extreme Environments* (2013), PhD Thesis, University of Edinburgh
13. J.A. Rodriguez and J Hrbeck, *The Journal of Physical Chemistry*, 1994, **98**, 4061
14. J. E. B. Randles, *Trans. Faraday Soc.*, 1948, **44**, 327
15. A. Sevcik, *Collect. Czech. Chem. Cornman*., 1948, **13**, 349
16. W.K. Behl., *J. Electrochem. Soc*., 1973, **120**, 1692
17. A.D Pelton., *Binary Alloy Phase Diagrams*, II Ed., 1991, **1**, 51
18. J. Sangster, C. W. Bale, *Binary Alloy Phase Diagrams*, II Ed., 1990, **2**, 1718-1720
19. R. P. Campbell-Kelly, T. J. Padget, *Proceeding of the First ACSEPT international Workshop*, 2010
20. S.A. Kuznetsov, H. Hayashi, K. Minato, M. Gaune-Escard, *Electorchimica Acta*, 2006, **51**, 2463-2470
21. Y. Liang, Z. Du, C. Guo, C. Li, *J. Alloys Compd.*, 2008, **455**, 236-242

7 Detection of Dendritic Growth at Liquid Metal Cathodes in a Molten Salt

7.1 Introduction

In chapter 4, the characteristic electrochemical response for dendrite growth on a liquid electrode at ambient temperatures in aqueous solutions was investigated as an analogue for developing diagnostic tools for a pyrochemical fuel reprocessing system.

In this chapter, molten bismuth held within a ceramic crucible is used to investigate the deposition of metals at a liquid metal cathode in the lithium chloride-potassium chloride eutectic (LKE) molten salt. The molten salt experimental cell is described in Section 3.1.3, and is geometrically similar to that used in the ambient temperature experiments with mercury, with identical ceramic crucibles and tubes used to construct the liquid metal cathode.

Preliminary investigations into dendrite growth at a liquid electrode in a molten salt are reported, with comparisons drawn between the electrochemical responses of the bismuth cathode to the observations made on the mercury cathode in Chapter 4.

7.2 Stability of a Bismuth Liquid Pool at the Bi-LKE Interface

Molten salts are of great interest in electrochemical technologies owing to their ability to dissolve many different compounds, including reactive metals, at high concentrations and stabilise oxidation states that are not accessible in aqueous solutions[1]. One of these processes of interest is in the reprocessing of spent nuclear fuels to recover the energy rich uranium for re-enrichment, and collectively removing the other fission products for safe, proliferation resistant disposal as a minimised volume.

Liquid metal electrodes have been proposed as ideal cathodes for the concurrent recovery of practically all of the fission products as deposition of these elements is stabilised by the formation of alloys with the liquid metal at the cathode[2, 3]. Studies on this alloy formation of fission products for recovery has predominantly used cadmium as the liquid metal. In practice the use of cadmium has disadvantages that add barriers to routine studies. Cadmium is toxic,

and listed in the European Restriction of Hazardous Substances directive[4] as a restricted substance. It also has a high vapour pressure at the temperatures used in molten salt experiments[5], which would require additional safeguards for atmospheric control in the molten salt experiment cell, and monitoring on the gas discharge line.

To overcome these issues, the liquid metal used in this work was replaced with bismuth. Bismuth, with a melting point of 271 °C, is also liquid at the desired temperature. It is not considered toxic, and has a much lower vapour pressure[6] than cadmium, negating the need for stringent controls to prevent the release of vapours from the gas line on the molten salt cell. Bismuth alloys have also been well studied, so it is possible to select suitable species for depositing at the liquid cathode which should, and should not, form alloys and hence it should be possible to predict when dendritic growth may occur.

Whilst dissolution of metals is a desirable property for molten salts in dissolving the spent fuel, it would be undesirable that either the containment vessel, or the system components including the electrodes are solubilised by the molten salt. To establish whether the molten salt may react with the liquid metal, the phase diagram can be considered for potential alloys between the two species.

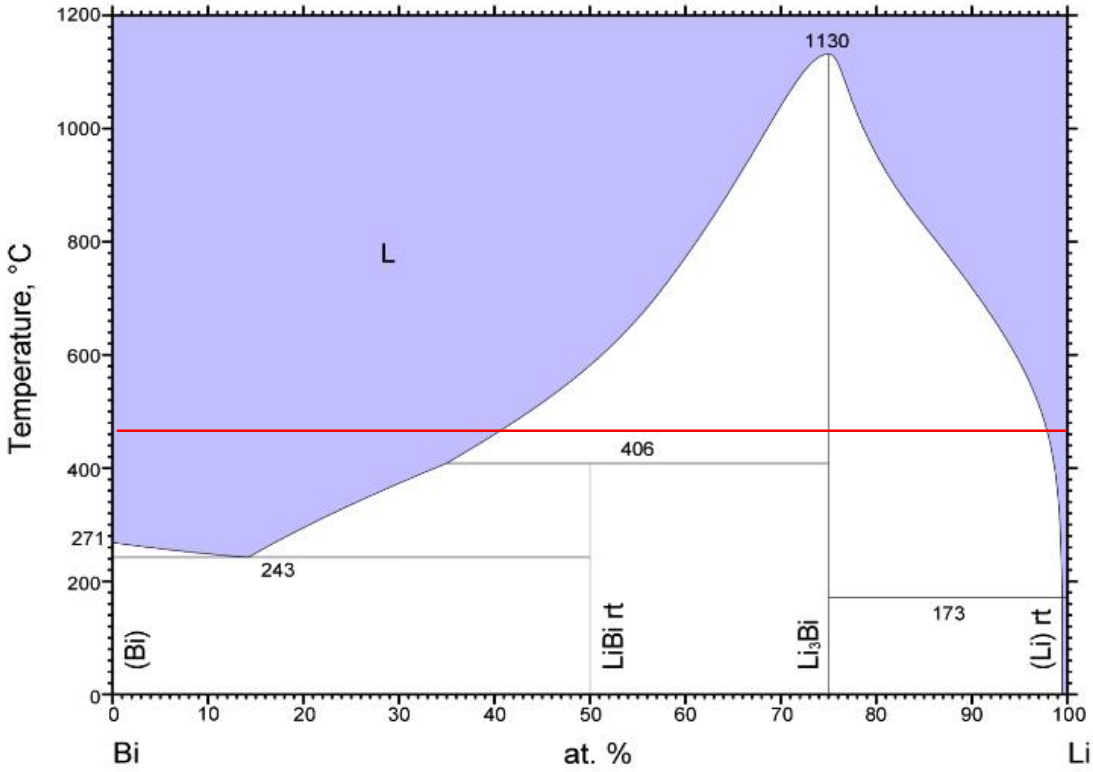

Figure 7.1: Binary phase diagram of bismuth-lithium system[7], with the concentration of lithium increasing from left to right. The red line indicates the temperature at which molten salt experiments are carried out (500 °C).

Figure 7.1 shows the binary phase diagram of bismuth and lithium, with the lithium concentration increasing from left to right. The phase diagram of lithium-bismuth has been shown over the potassium-bismuth phase diagram as lithium is the more reactive of the two metals. Therefore, if a spontaneous reaction were to take place between the molten salt and the bismuth, it would most likely be with the lithium. During experiments at 500 °C, indicated by the red line, one alloy forms between the bismuth and the lithium. In these experiments it is expected that the atomic percentage of lithium will be far greater than that of bismuth (i.e. to the right of the phase diagram) and that a mixture of the lithium and the Li_3Bi alloy will be present. As there will be other species in the system, it is important to test whether any reaction takes place, and whether a stable interface can be formed between the molten salt and the liquid bismuth cathode.

To test this, a ceramic crucible filled with 41.9380 g beads of bismuth was placed in the bottom of 50.2332 g LKE and held at 500 °C for 2 hours. The LKE was electrochemical dried using the method described in chapter 6, and electrochemical measurements were taken at intervals

during the course of the experiment. A CV of 1.276 g $BiCl_3$ in 50 g LKE was then measured as a reference for the Bi^{3+}/Bi^0 redox potential and superimposed upon the time-dependent bismuth metal in LKE CVs.

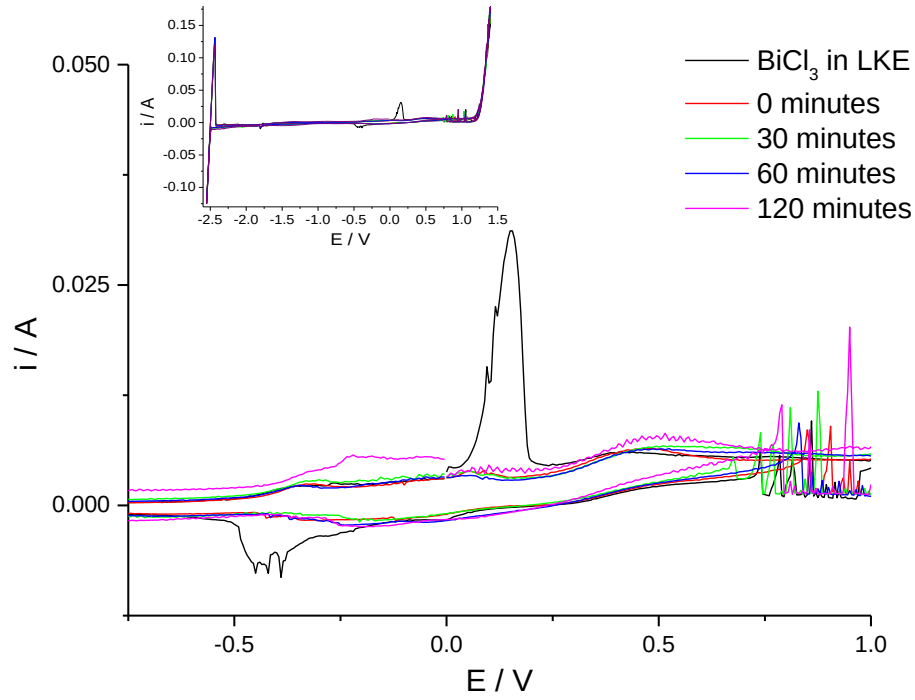

Figure 7.2: Comparison of CVs at a tungsten electrode in LKE at a sweep rate of 200 mV s^{-1}. The first sweep is of LKE with $BiCl_3$, and the subsequent sweeps are of LKE with a bismuth liquid pool immediately after the LKE was electrochemically dried and 30, 60 and 120 minutes after electrochemical drying.

Figure 7.2 shows the CVs recorded in LKE with the Bi pool at the bottom of the crucible on a tungsten electrode at a sweep rate of 200 mV s^{-1} vs an Ag/AgCl reference electrode. The LKE was electrochemically dried using the method described in chapter 6, and electrochemical measurements were taken at intervals during the course of the experiment: immediately after drying, and after 30, 60 and 120 minutes. An additional CV was later measured of 1.276 g $BiCl_3$ in 50 g LKE at a tungsten electrode at a sweep rate of 200 mV s^{-1} vs an Ag/AgCl reference electrode and has been superimposed over the CVs recorded with the Bi pool in the LKE. The inset CV shows the full scan range, with the negative solvent limit having narrowed to -2.40 V in the CV of $BiCl_3$ in LKE rather than the typical -2.65 V seen in Chapter 6 for the electrochemical drying of LKE. This narrowing of the potential window is due to the formation of the Li_3Bi alloy, which has a stabilising effect over the reduction of Li^+ at the solvent limit,

where Bi has already been plated at the working electrode. When the LKE with $BiCl_3$ was cooled, a thin film of bismuth was found to have lined the bottom of the crucible, where liquid bismuth which had deposited on the working electrode had dropped off.

In Figure 7.2, the main oxidation and reduction peaks at 0.2 V and -0.4 V respectively are of the $BiCl_3$ in LKE without the liquid bismuth metal in the salt. The sharp peaks between 0.75 V and 1.00 V in the remaining CVs is due to the residual oxidation of oxygen where the salt was not thoroughly dried in the initial drying stage.

Visual inspection of the bismuth pool in the molten salt appeared to indicate that a clear and stable boundary had formed between the two liquids, as could be expected given the significant difference in their densities (approximately 1.6 g cm^{-3} for LKE and approximately 10 g cm^{-3} for bismuth).

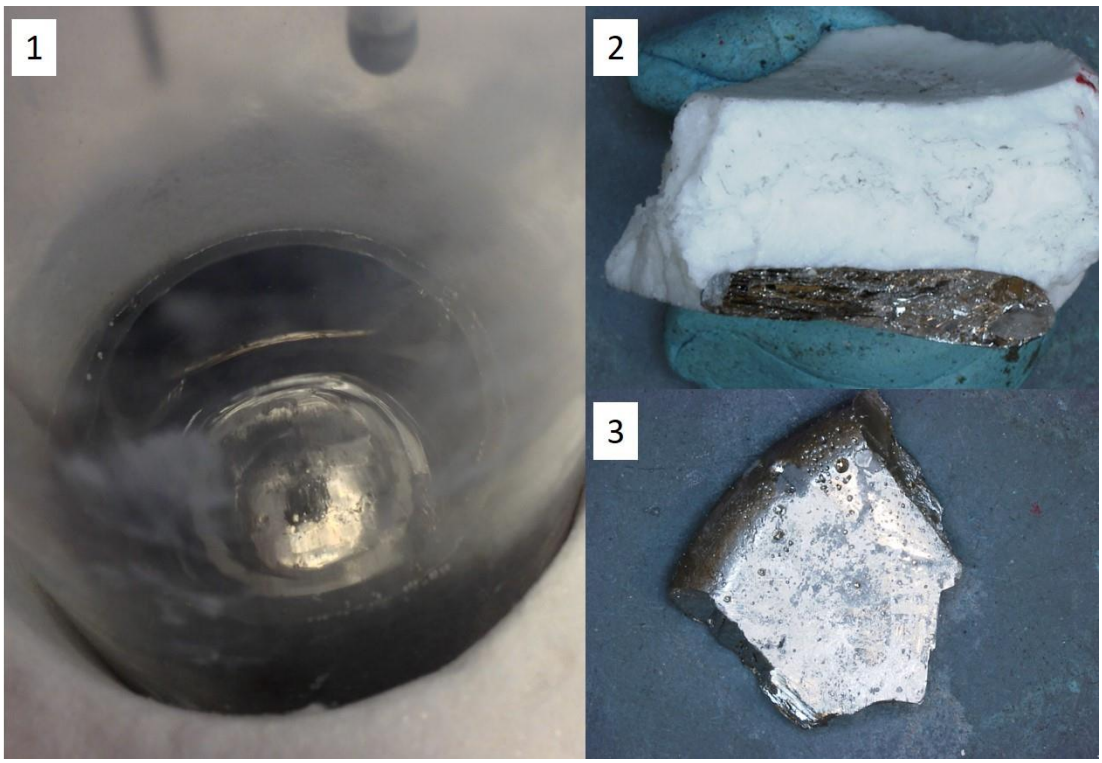

Figure 7.3: Images of 1) a liquid bismuth pool in LKE at 500 °C, 2) cross-section of Bi pool in LKE once cooled and 3) solidified Bi surface from Bi-LKE interface.

Figure 7.3 shows images of the liquid bismuth at the bottom of the molten LKE in the glassy carbon crucible at 500 °C, the clear boundary between the two once the salt and metal were frozen under cooling, and the surface of frozen bismuth when separated from the solidified LKE. As the two liquids both solidify at different temperatures, 353 °C for LKE[8] and 271 °C for bismuth, the surface of the bismuth in image 3 may have been influenced by the solidifying of the LKE. The relative smoothness, and lack of adhesion between the bismuth and the LKE would suggest that there was no interaction between the two liquids; however it is possible that some reaction had taken place despite them being immiscible.

Five samples were extracted from this LKE pellet at varying points across the pellet, and analysed for their bismuth content using ICP-AES. A further sample was collected from the bismuth, and analysed for its lithium and bismuth content. In each of these 5 LKE samples it was not possible to detect any bismuth within the 1 ppm detection limit of the ICP instrument. Furthermore, lithium and potassium were not detected in the bismuth sample above the 5 ppm limits specified in the specification sheet for the bismuth from sigma-aldrich.

These results demonstrate that the liquid bismuth-LKE interface is stable, and no reaction is taking place between the two. This demonstrates that bismuth is an ideal liquid to use as a liquid metal cathode on the grounds of its physical properties, and can be easily used for fundamental studies of the deposition of species at a liquid cathode in a molten salt.

7.3 Deposition of Lanthanum at a Liquid Bismuth Cathode

In the molten salt reprocessing system for selective separation and recovery of spent nuclear fuel, a liquid cathode in utilised to selectively alloy with transuranic elements and facilitate their recovery through electrodeposition. The alloy formation is proposed to reduce the energy required to recover these species, with the species, or its alloy, dissolving into the bulk liquid metal.

As observed in Sections 4.2 and 4.4 during the ambient temperature experiments using a mercury cathode in aqueous solutions, the deposition of a metal and resulting formation of an alloy with the liquid metal exhibits a characteristic current response. To verify that this response was not unique to the Zn-Hg amalgam in aqueous solutions, the phase diagrams of

bismuth with a number of other metals were considered to find a suitable pairing which would form one or more alloy with the bismuth.

Of those identified, lanthanum was chosen because of its direct relevance to the molten salt processing system, which would require the selective recovery of lanthanum at a liquid cathode as part of the separation process.

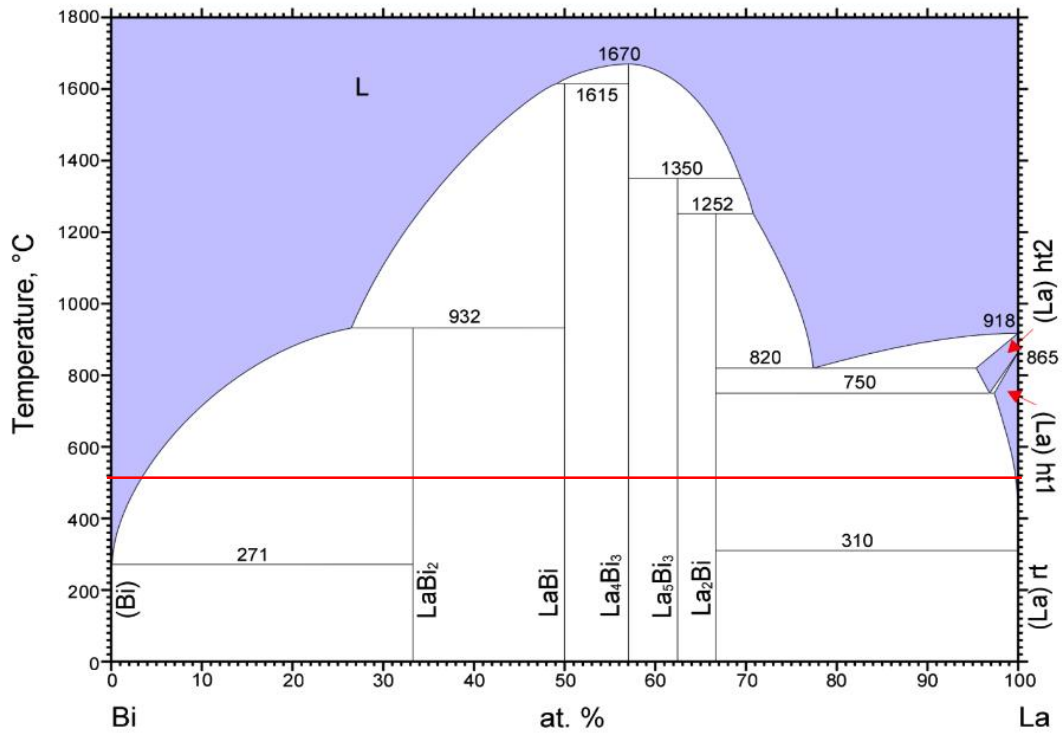

Figure 7.4: Binary phase diagram of bismuth-lanthanum system[9], with the concentration of lanthanum increasing from left to right. The red line indicates the temperature at which molten salt experiments are carried out (500 °C).

Figure 7.4 shows the binary phase diagram of lanthanum and bismuth. At the temperature of interest, 500 °C (indicated by the red line), there are five known alloys of bismuth and lanthanum. With increasing concentration of lanthanum, these are $LaBi_2$, LaBi, La_4Bi_3, La_5Bi_3 and La_2Bi. As with the Zn-Hg alloys, the liquid metal has the greater density, and the density of these alloys decrease with increasing lanthanum concentration. As these alloys are less dense than the liquid bismuth, it can be expected that these alloys will float on the surface of the liquid cathode as they form. As each alloy remains at or close to the electrode surface,

further reduction of lanthanum is likely to promote the formation of the next alloy. As the less dense, solid alloys build up at the surface of the electrode, a solid crust will form and potentially lead to dendritic growth.

The propensity for dendritic growth will be a function of the rate of dissolution of the alloy into the liquid bismuth compared to the rate of deposition at the electrode surface. In the case of zinc deposition at the mercury cathode, the formation of dendrites was more readily achieved on the microelectrode, and evidence for the the formation of the alloys in the current-time transient was more prominent. In the Zn-Hg case, the microelectrode benefitted from enhanced diffusion of Zn ions to the electrode surface, and hence Zn ions were deposited at the electrode surface faster than the alloy could diffuse into the bulk mercury. On the macro electrode, the alloy formation was not observed in the current-time transient as an insufficient amount of zinc was reduced at the electrode surface to promote formation of the second alloy.

In the molten salt experiments in this chapter, only macro electrodes were used, and formation of the different alloys may not be possible if the alloys diffuse into the bulk at a greater rate than the diffusion of La to the electrode surface.

To establish the potential at which the lanthanum would deposit at the bismuth cathode, CVs of $LaCl_3$ in LKE were measured at tungsten and bismuth electrodes against a silver/silver chloride reference electrode.

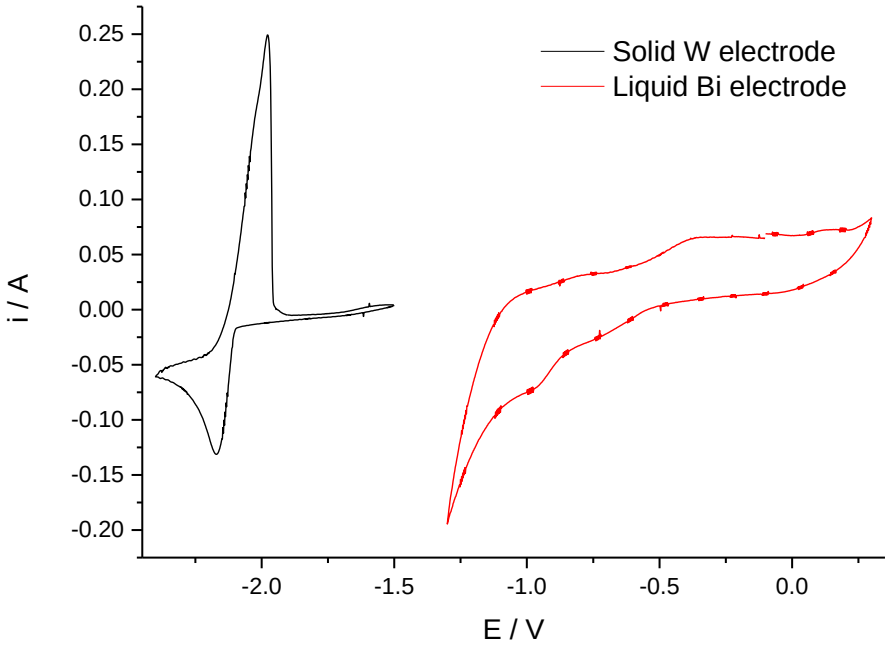

Figure 7.5: CVs of 1.5490 g $LaCl_3$ in 75.8649 g LKE at a sweep rate of 200 mV s^{-1} vs Ag/AgCl reference electrode at a solid tungsten electrode and a liquid bismuth electrode.

Figure 7.5 shows the CVs of lanthanum on each of the electrodes, and a clear decrease in the reduction potential of lanthanum was observed on the bismuth cathode. On the tungsten electrode, the reduction potential of lanthanum was consistent with previously reported value[10] and measured as -2.10 V. On the bismuth electrode, 3 reduction waves were observed at -0.57 V, -0.85 V and -1.08 V with corresponding oxidation waves at -0.90 V, -0.71 V and 0.06 V. As bismuth metal has already been shown to be stable in the melt, these reduction waves could only be due to the reduction of lanthanum forming an alloy with bismuth or possibly with the lithium in the eutectic.

As observed in the CV of $BiCl_3$ in Figure 7.2, bismuth can be oxidised in LKE at 0.2 V, so the positive limit of the sweep was limited to this potential as to not strip any of the cathode metal into the molten salt. In Figure 7.2 the reduction potential of Bi in LKE was also measured as -0.40 V. Whilst a small oxidation peak is observed at the positive limit of the CV sweep, any corresponding reduction of bismuth is not observed in the CV at the liquid electrode, and the

magnitude of the reduction waves negative of -0.50 V are too large to be attributed to a small contamination of bismuth oxidised from the cathode.

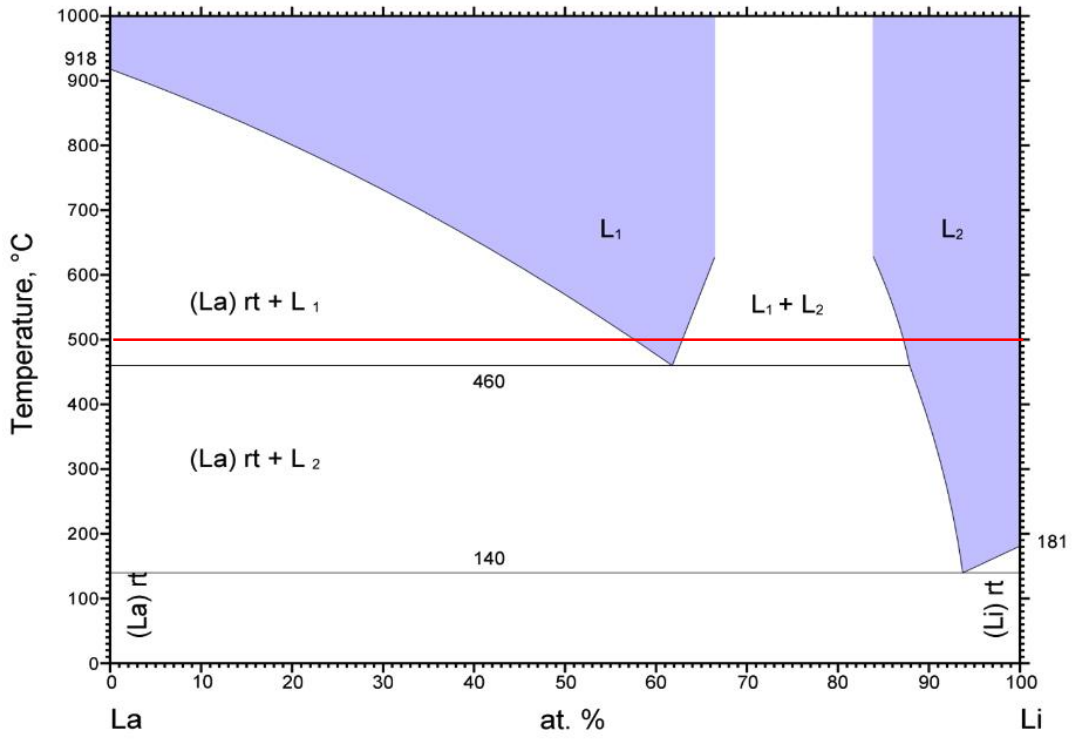

Figure 7.6: Binary phase diagram of lanthanum-lithium system[11], with the concentration of lithium increasing from left to right. The red line indicates the temperature at which molten salt experiments are carried out (500 °C).

Figure 7.6 shows the binary phase diagram of lanthanum and lithium, with the temperature of the molten salt, 500 °C, indicated by a red line. Crucially, the phase diagram shows that at all concentration ratios at this temperature, and indeed between 0 °C and 1000 °C there are no known alloys of lithium and lanthanum. This confirms that the reduction waves observed in the CVs of $LaCl_3$ at a liquid bismuth cathode in Figure 7.5 are due to the reduction of lanthanum.

The three distinct oxidation and reduction waves are due to the reduction of La^{3+} to La^0 and subsequent formation of $LaBi_2$ alloy. This was previously reported during investigations using cyclic voltammetry into concurrent recovery of La and Pu at a bismuth film electrode[12], where

Pu was found to preferentially alloy with Bi under current-controlled deposition, despite having a more negative reduction potential.

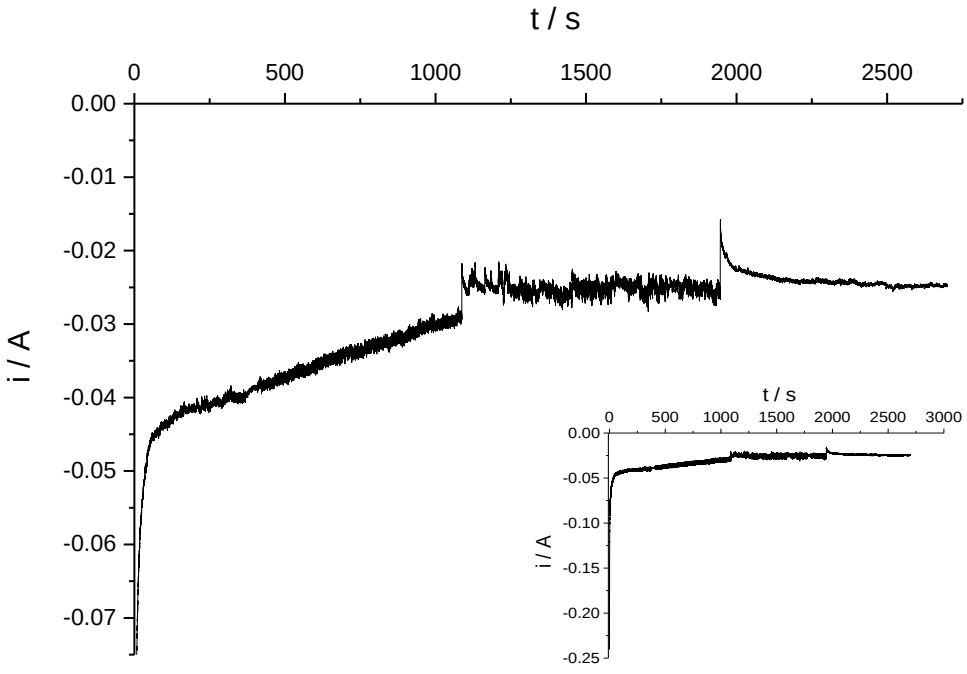

Figure 7.7: Current -time transient for the reduction of La (III) at a Bismuth electrode at -1.00 V vs Ag/AgCl from 1.5490g $LaCl_3$ in 75.8649g LKE.

Figure 7.7 shows the current-time transient of the reduction of lanthanum at a bismuth liquid cathode at a potential of -1.00 V over 2600 seconds. During the reduction, distinct phases can be observed in the current response.

Initially the current spikes as the double layer is charged, before decaying to -0.04 A by 250 seconds. Between 250 and 1000 seconds, the current decays linearly to 0.03 A with the small fluctuations in the current between data points, which are largely within the measurement error of the potentiostat. After 1000 seconds, the current suddenly drops before oscillating at about 0.025 A until 1900 seconds, when there is a further drop in the current to 0.015 A, which quickly returns to a steady current of 0.023 A.

The initial phases of current decay are likely to be caused by diffusion limited control. Initially, the double layer charge is established, and the current drops to steady state where the lanthanum diffuses to the electrode surface. After approximately 250 seconds, the surface of

the liquid electrode is saturated with the $LaBi_2$ alloy, which then diffuses into the bulk bismuth. Between 250 and 1000 seconds, the reduction of La is controlled by the reaction with the reduced La.

In studies of concurrent recovery of Pu and Li at a bismuth pool[12], exceeding the solubility limit of Pu at the Bi-LKE interface was found to lead to an accumulation of solid intermetallics, which blocked the electrode. After 1000 seconds, the drop in current is indicative of a similar formation where the saturation limit of La at the Bi-LKE interface is exceeded and the electrode behaves as a solid $LaBi_2$ cathode. Solid deposition of La at the alloy then occurs at a rate controlled by La diffusing to the solid electrode.

The fluctuations in the current between 1000 and 1900 seconds are typical of dendritic growth, however the current does not rise continuously over this time. It is possible that in this phase of the reduction, small dendrites are growing and detaching at a similar rate, such that there is no overall increase in electrode area. This would be possible if the dendrites had poor mechanical strength, combined with the elevated temperature in the molten salt, greater natural convection and vibrations from the equipment in the lab.

The reason for the sharp drop in current at 1900 seconds is unclear, but could have been due to an external disturbance (as the molten salt experiments were carried out in an open lab) or due to a temporary passivation or disturbance in the electrode surface. After the immediate drop in current, the current returns to a similar value as before the disturbance, but is far more stable. It is most likely that at 1900 seconds an external disturbance displaces the fragile dendrites, and cleared the surface of the electrode with La to continuing to deposit at the smoothed surface.

After 2600 seconds of La deposition, the electrodes were withdrawn and the experimental cell was cooled under argon to freeze the salt and the cathode. The cell was then disassembled in an argon glovebox and the salt pellet dissected with images taken of the salt pellet, the solidified cathode. A fragment of the salt pellet was then removed from the glove box and dissolved in de-ionised water.

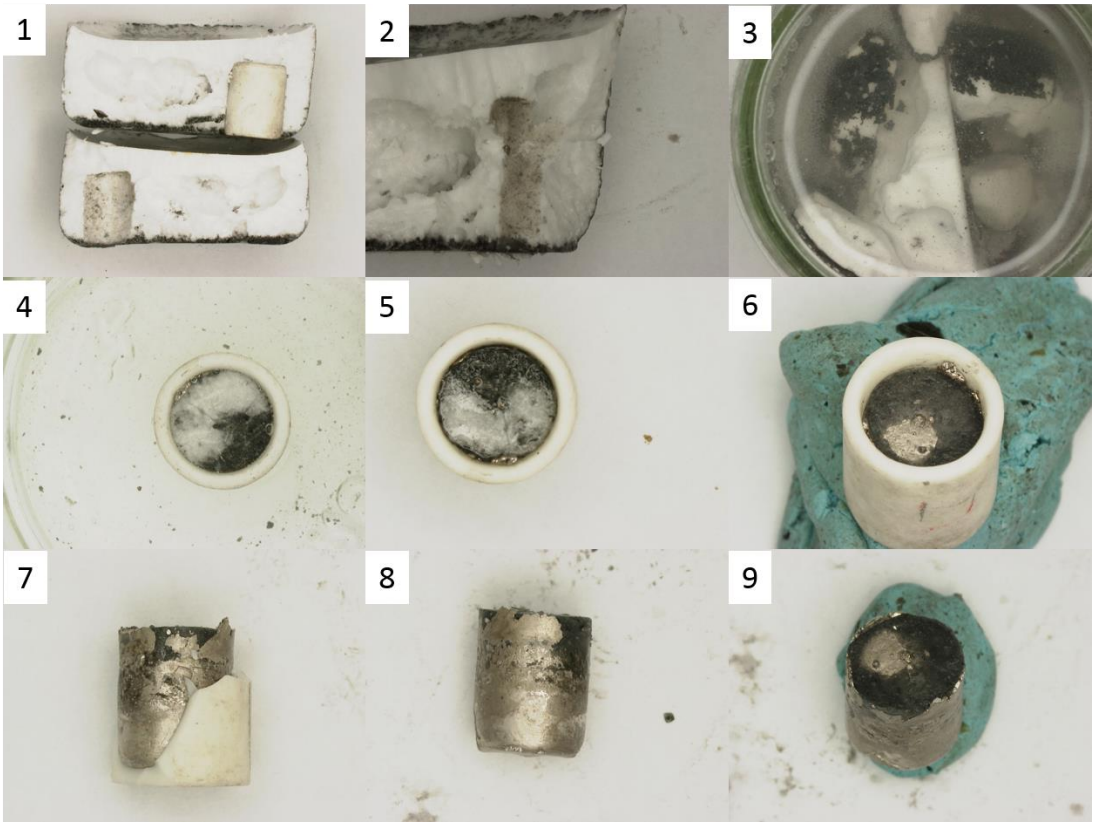

Figure 7.8: Images of lanthanum dendrites and Bi-La alloy formed at a liquid bismuth electrode in LKE after the salt had been frozen, removed from the crucible, and dissected (under argon).

Figure 7.8 displays the images captured of the frozen LKE and solidified cathode. Images 1 and 2 show cross-sections of the LKE, with a thin layer of grey-black particles visible along the lower face of the LKE. Image 3 shows the LKE pellet dissolving in water, freeing the particles which darken in colour as they settle in the bottom of the salt solution. Images 4 to 9 are of the solid bismuth as the salt is picked off and the bismuth is removed from the ceramic crucible.

In Figure 7.8 images 5, 6 and 9, the face of the cathode which was exposed to the molten salt is visible. It is possible to discern where the sheathed electrical connection to the liquid metal was during the experiment from the bright, silver circle visible on the surface. Surrounding this circle, where the bismuth formed the electrode surface, a dull, blue-grey roughened surface has formed, and this is robust to picking and scratching with a sharpened blade and pick showing that it is embedded it the solid metal.

The side-on pictures of the bismuth in Figure 7.8 images 7 and 8 reveal a layered structure to the solidified cathode, with the expected silver-grey bismuth to the bottom of the cathode, capped by blue-grey layer, roughly half the depth of the electrode. This layer of an intermetallic compound is the $LaBi_2$ alloy which had become saturated at the surface of the Bi pool, which inhibited diffusion of Bi to the electrode-LKE interface, and hence further alloy formation.

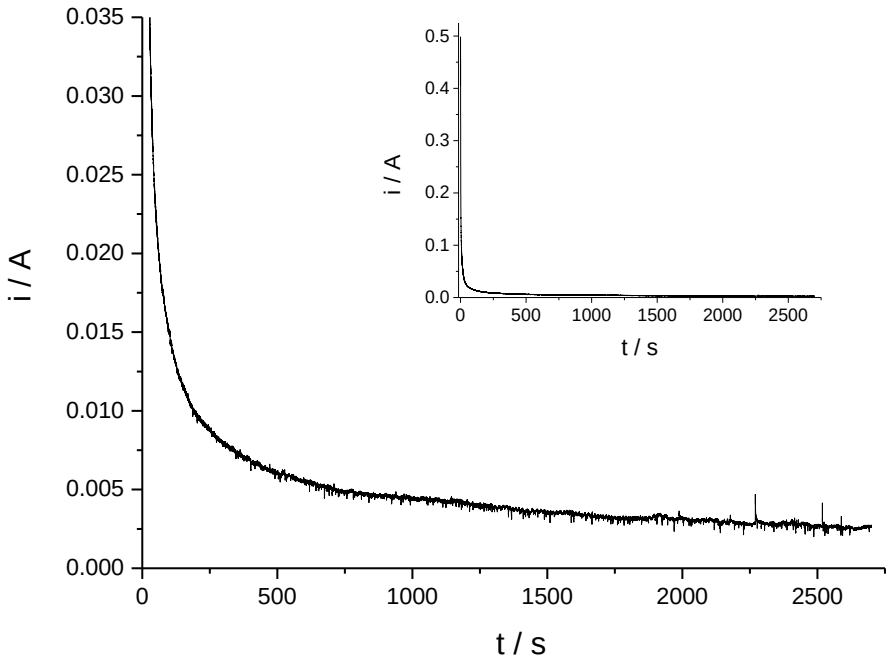

Figure 7.9: Current -time transient for the oxidation of La (III) from a liquid bismuth electrode at -0.20 V vs Ag/AgCl.

Figure 7.9 shows the current-time transient of the re-oxidation of lanthanum which had been deposited at a bismuth cathode using the same method to that used when measuring Figure 7.7. The potential for oxidising the lanthanum was held at -0.20 V to avoid inadvertently oxidising bismuth from the cathode, which would cause an error in the measurement.

During this oxidation, significantly less charge is passed than during the reduction and the current-time transient is largely featureless beyond the charging of the double layer and decay to steady-state current. It is possible that the alloy formed with the bismuth is so stable that a more positive potential is required to strip the lanthanum from the electrode. However, shifting

the potential more positive could equally result in the bismuth being oxidised, resulting in a false reading.

When the cell was cooled and the bismuth removed, the solidified bismuth, although having a smoother, brighter appearance on the exposed face, still had a layered cross section, supporting the idea that the alloy remained stable at the applied potential.

Compositional analysis of the metal was not carried out. However, in future work it would be beneficial to confirm the composition and structure of the solidified cathode product as this may give a useful insight into the formation of alloys in a liquid cathode.

In a reprocessing system, mechanical stirring could be used to overcome the problem of saturation at the surface of the liquid metal. However, the diagnostic responses identified in this work are crucial to understanding when mechanical stirring is required. Understanding how and when stirring should be employed is a key step to building a molten salt re-processing system, and with suitable sensors and an understanding of when dendritic or solid growth is occurring, should be the subject of future work.

7.4 Growth of Iron Dendrites at a Liquid Cathode in LKE

Having established that it is possible to identify when a solid alloy is forming at a liquid electrode-LKE interface, additional work was carried out to identify when dendritic growth from the electrode surface was taking place. In Section 7.3, the diagnostic response in the current-time transient for alloy formation identified at a mercury cathode in aqueous solutions were seen to also be representative of alloy formation at a liquid metal cathode in LKE. In this section, the electrochemical response of dendrite formation at a liquid cathode in LKE will be investigated and compared to the observations of dendritic growth made in chapter 4.

In studying dendritic growth at a liquid cathode in LKE it was important to choose a redox species, which when deposited at the cathode surface would not form an alloy with the liquid cathode, or be soluble in the liquid metal. Historically, iron deposition in molten salts has been extensively studied for powder metallurgy applications and in effort to develop a commercially viable electrorefining and electrowinning process to extract iron from scrap iron, pig iron and its ores[13-21]. From these studies, iron has a known tendency to deposit as dendritic growth, and whilst methods have been established to reduce dendritic growth and obtain high purity iron

deposits with good current efficiency[18, 22], dendritic growth is the prevailing mechanism of deposition. As iron is one of the likely components in the spent fuel that will be dissolved in the molten salt during re-processing, dendritic growth at the liquid cathode will disrupt the separation and recovery processes. This makes it an ideal candidate for study at a liquid cathode in LKE, as the observation of dendritic growth will be directly comparable to that which may occur in the reprocessing system.

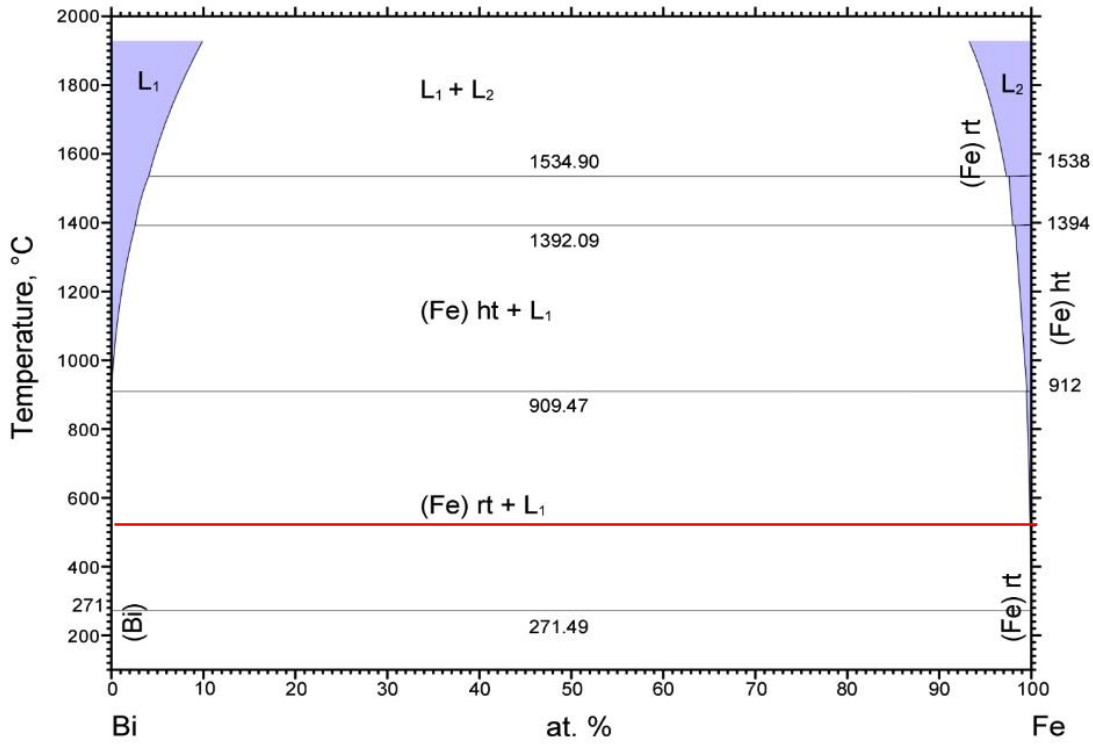

Figure 7.10: Binary phase diagram of bismuth-iron system[23], with the concentration of iron increasing from left to right. The red line indicates the temperature at which molten salt experiments are carried out (500 °C).

Figure 7.10 shows the binary phase diagram for bismuth and iron. The temperature of the molten salt experiments, 500 °C, is indicated by a red line across all compositions. This phase diagram confirms that there are no known alloys of bismuth and iron, and that at 500 °C a mixed phase of the liquid bismuth and the iron in its room temperature structure will exist. The density of solid iron in this structure is 7.89 g cm^{-3}, which is less dense than the bismuth, so deposited iron should float on the surface of the liquid bismuth pool.

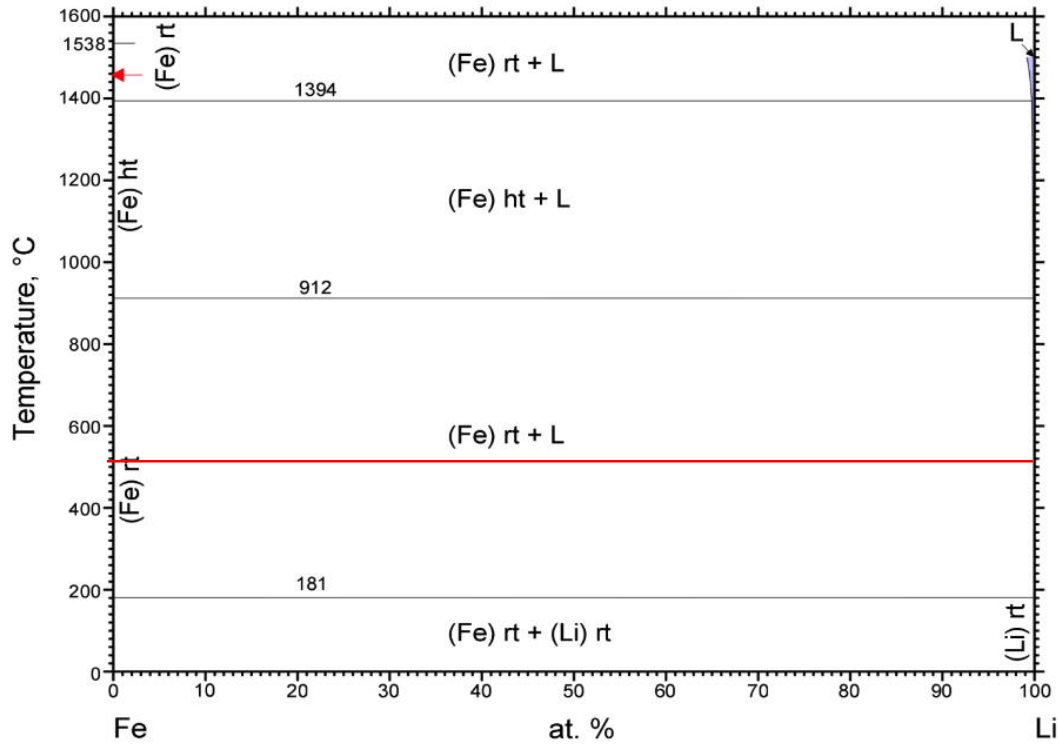

Figure 7.11: Binary phase diagram of iron-lithium system[24], with the concentration of lithium increasing from left to right. The red line indicates the temperature at which molten salt experiments are carried out (500 °C).

The binary phase diagram for lithium and iron in Figure 7.11 also shows that there are no known alloys between iron and lithium, so any electrochemical response measured between the negative solvent limit and the oxidation potential of bismuth can be attributed to the reactions of iron.

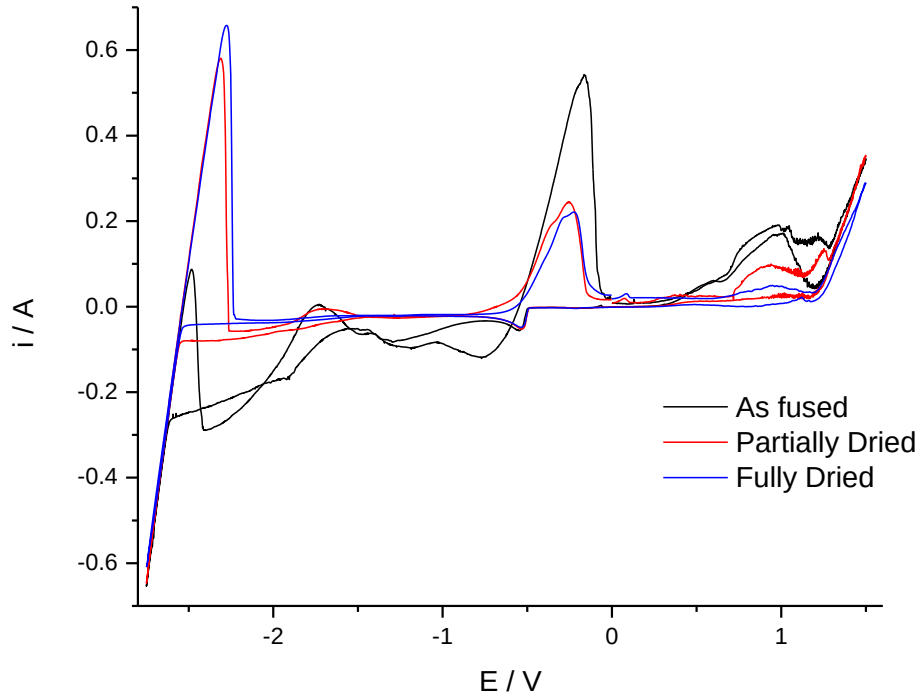

Figure 7.12: CVs over the full LKE solvent window of 0.6685 g $FeCl_2$ in 80.3127 g LKE at a tungsten cathode vs an Ag/AgCl reference electrode at a sweep rate of 200 mV s^{-1}. The LKE was electrochemically dried using the methodology described in Chapter 6.

In Figure 7.12 the CVs of $FeCl_2$ in LKE at a tungsten electrode vs an Ag/AgCl reference electrode are shown pre- and post- electrochemical drying using the method described in Chapter 6. In the as-fused and partially dried LKE, the wave for the oxidation of oxygen can be seen between 0.50 V and the solvent limit at 1.25 V and a wave for the reduction of hydrogen can be seen at about -1.60 V. In the as-fused LKE, the reduction of hydrogen at the electrode surface enhances the deposition of iron, resulting in a large reduction wave of hydrogen and iron below -1.50 V and an associated increased oxidation peak for the iron at -0.15 V.

In each of the three CVs, the iron is seen to be reduced in a single, 2-electron process with reduction peaks at -0.50 V and corresponding oxidation peaks as -0.20 V.

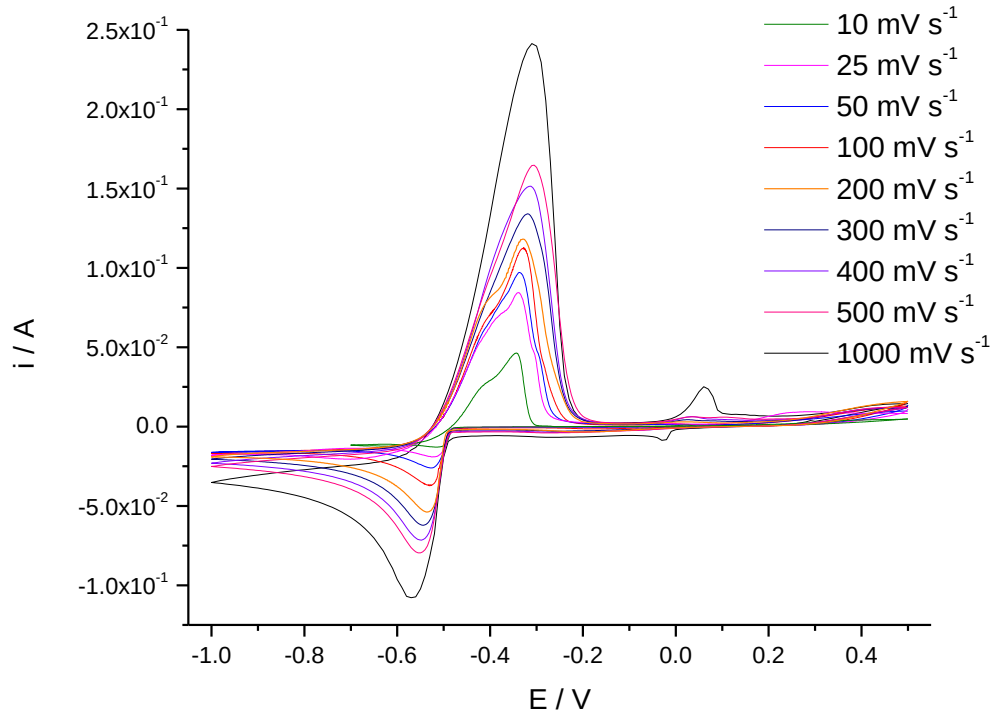

Figure 7.13: CVs of 0.6685 g $FeCl_2$ in 80.3127 g LKE at a tungsten cathode vs an Ag/AgCl reference electrode.

Figure 7.13 shows additional CVs of $FeCl_2$ in LKE at a tungsten working electrode with varying sweep rates. At slower sweep rates a pre-peak is visible in the oxidation peak, where iron is first stripped from underlying iron, and then stripped from the tungsten surface. As the sweep rate is increased, less iron is deposited, and the feature in the oxidation peak becomes less prominent.

Having established the redox potentials of the $FeCl_2$ on the solid tungsten electrodes, it was necessary to identify where iron would be reduced and oxidised on the liquid bismuth electrode.

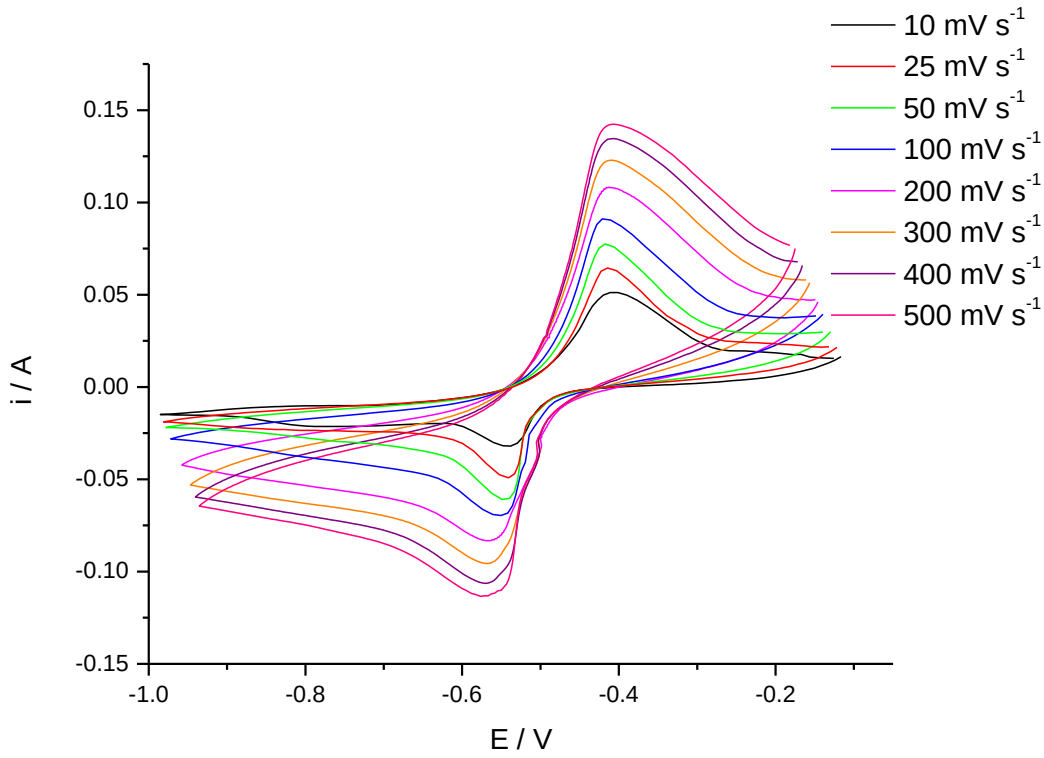

Figure 7.14: CVs of 0.6685 g $FeCl_2$ in 80.3127 g LKE at a liquid bismuth cathode.

Figure 7.14 shows the CVs of $FeCl_2$ in LKE at a bismuth pool electrode vs an Ag/ AgCl reference electrode at varying sweep rate. In these CVs, the reduction peak was measured at -0.55 V and the oxidation peak was measured at -0.40 V equating to a negative shift in the required potential to reduce iron at the liquid bismuth cathode over the solid tungsten cathode.

Having established the potential required to reduce iron at the liquid electrode, the current-time transient of iron deposition was recorded over 4000 seconds, with the potential of the bismuth cathode held at -0.65 V.

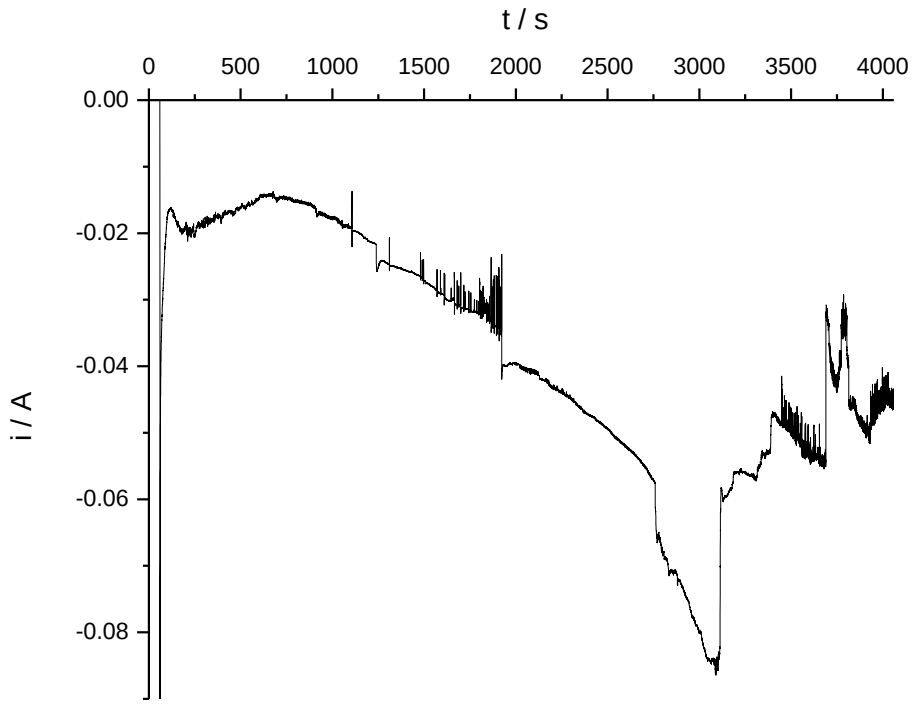

Figure 7.15: Current -time transient for the reduction of Fe (II) at a bismuth electrode at -0.65 V vs Ag/AgCl from 0.6448 g $FeCl_2$ in 71.3981 g LKE.

Figure 7.15 shows the current-time transient recorded during the reduction of Iron at the liquid cathode. Between 0 and 60 seconds the potential was held at 0 V to ensure that any iron which may have deposited on the liquid cathode was re-oxidised whilst not oxidising any bismuth from the cathode into the LKE. At 60 seconds the potential was switched to -0.65 V and the current spikes negative to -0.16 A as the double layer is charged. Within the first 60 seconds of deposition (120 seconds in Figure 7.15) the current decays to -0.017 A as iron depositing on the electrode surface is limited by the rate of diffusion to the electrode. Once a number of nucleation sites have deposited on the surface of the electrode, the current begins to rise, as the iron deposits grow dendrites from the surface of liquid pool. Between 120 and 1060 seconds, the current remains fairly stable as the dendrites grow within the boundary of the ceramic crucible, but above the liquid surface. After 1060 seconds, the current continues to rise progressively to -0.085 A over 3000 seconds as the dendrites spread outwardly into the molten salt. After 3000 seconds an event, likely to be detachment of dendrites from the

electrode, causes the current to drop to -0.060 A. The current then follows a similar pattern of growth and drops until the applied potential was disconnected after 4060 seconds.

This pattern of current growth is representative of the dendrites growing away from the surface of the bismuth pool and increasing the effective electrode area. The drops in magnitude of the current are typical of dendrite detachment seen in the aqueous experiments in Chapter 4 and could be triggered by enhanced convection at the elevated temperatures or vibration from an external source. Sharp increases in the magnitude of current also occur at 1250, 1900, 2700 and 3800 seconds. These increases could equally be due to dendrites either re-attaching to the electrical connection, or a geometric change in the dendrites owing to convection, which results in a greater area being exposed to the bulk $FeCl_2$-LKE mixture.

After 4000 seconds of deposition, the sheathed electrode was withdrawn just enough to remove it from the bismuth pool so as not to significantly disturb the dendrites, and the molten salt cell was cooled under argon to freeze the LKE and liquid bismuth. The experimental cell was then transferred to an argon glovebox and frozen LKE pellet removed from the glassy carbon crucible. The pellet was carefully dissected under argon, and images were captured of the solidified LKE and contents trapped in a matrix in the salt.

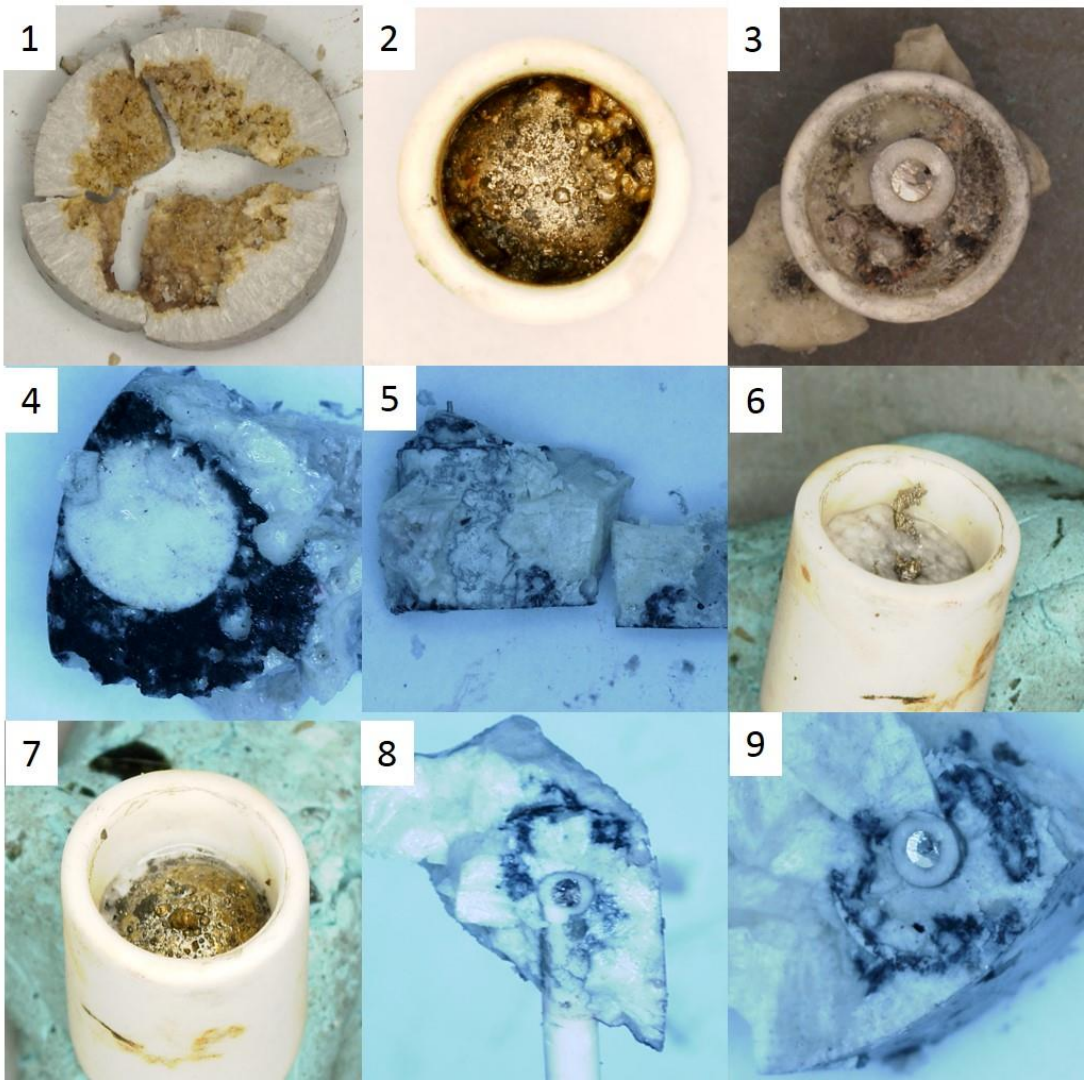

Figure 7.16: Images of iron dendrites at a liquid bismuth electrode in LKE after the salt had been frozen, removed from the crucible, and dissected (under argon).

Figure 7.16 shows images of iron deposits within the LKE and deposited at the liquid bismuth surface as the frozen salt from the deposition in Figure 7.17 was dissected under argon. In images 1, 3, 5, 8 and 9 a network of dendrites can be seen to be trapped within the salt. Images 2 and 7 show bright yellow-brown deposits on the surface of the normally silver-grey bismuth, and in image 6, a metallic, yellow growth can be seen projecting from the electrode surface as the salt was scraped away. Image 4 shows the underside of the LKE pellet, with the bottom of the ceramic crucible surrounded by black particles trapped in the molten salt as seen in Figure 7.8 image 1 of La deposits at the bottom of the crucible.

In image 1, a horizontal cross-section from the LKE above the bismuth filled crucible, the fine, yellow-brown dendrites can be seen to spread from above the working electrode at the bottom of the picture, across the solidified salt to where the counter and reference electrodes were located. The location of the working electrode can be identified, even if the location was not already known, as the coloration of the LKE directly above the working electrode, is darker and the dendrites are visible in a greater density. The absence of coloration around the perimeter of the pellet and in other areas of the LKE confirm the coloration is not due to the $FeCl_2$ having been dissolved throughout the LKE, as this would result in a homogeneous colour.

Having confirmed that the electrochemical indicators of dendritic growth during deposition in the current response is similar to the diagnostic behaviour observed under ambient temperatures in aqueous solutions, attention was drawn on the indicators in the electrochemical impedance spectroscopy.

During the reduction of iron at the liquid bismuth cathode shown in Figure 7.15, concurrent EIS measurements were recorded at defined intervals to measure changes at the surface of the liquid bismuth electrode.

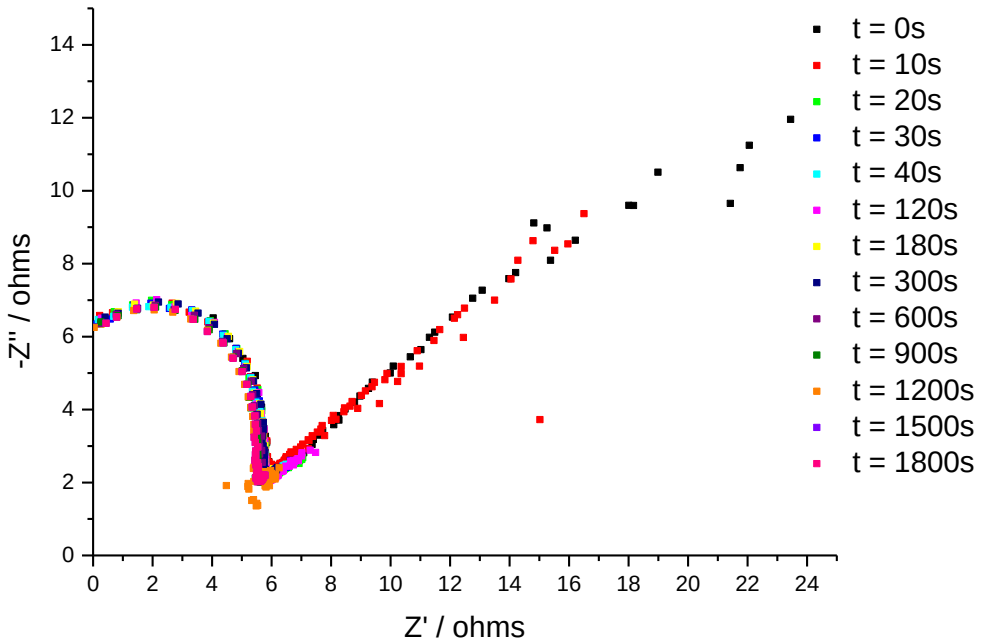

Figure 7.17: Nyquist plots of impedance spectroscopy at OCP of a liquid bismuth electrode during deposition of Fe at -0.65 V vs Ag/AgCl from 0.6448 g $FeCl_2$ in 71.3981 g LKE.

Figure 7.17 shows the Nyquist plots of the impedance measurements on the electrode during the deposition of Fe dendrites. Unlike in chapter 4, there is no immediately obvious change between the plots. However, the length of the Warburg line does decrease significantly after a short time, indicating that the overall resistance is decreasing as the dendrites form at the electrode surface. A decrease in resistance can be directly related to an increase in electrode area, therefore indicating dendritic growth at the liquid electrode.

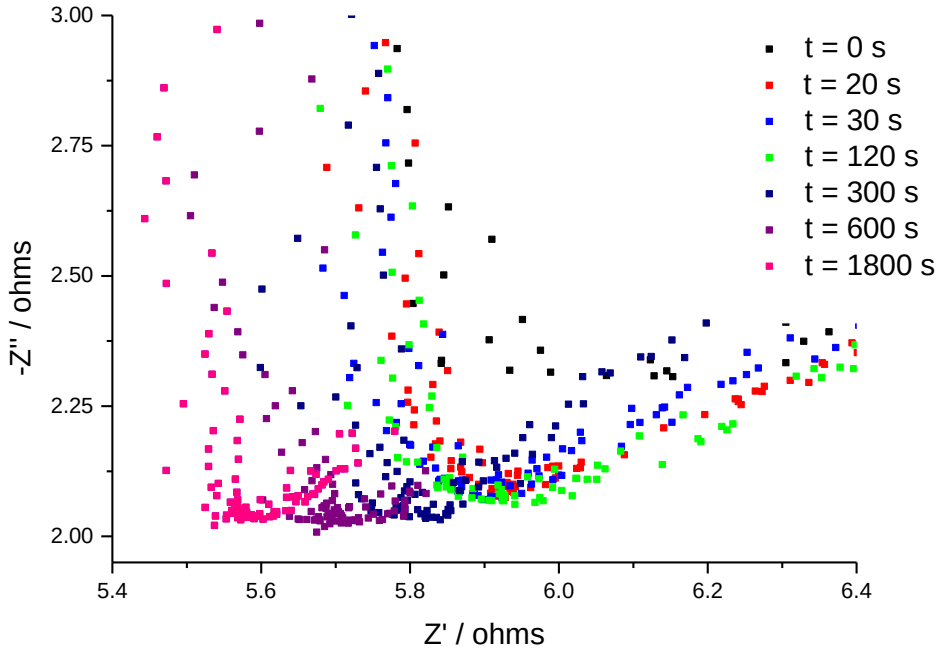

Figure 7.18: Expanded Nyquist plots of impedance spectroscopy at OCP of a liquid bismuth electrode during deposition of Fe to show R_S values on the Z' axis.

Figure 7.18 shows an expanded view of the Nyquist plot in Figure 7.17 to emphasise the reduction in solution resistance measured using EIS during the dendrite growth. Prior to any deposition taking place, the solution resistance was measured as approximately 6 Ω. After 600 seconds of iron deposition, at about the point in the current-time transient when the current is at a minimum, the solution resistance showed a marked decrease to 5.7 Ω and continues to decrease with further dendrite growth.

Throughout the deposition experiments at both mercury cathodes in aqueous solutions and liquid bismuth cathodes in molten salts, the solution resistance measurements provide a good indication of when dendritic growth is occurring. This characteristic behaviour is easily monitored during deposition, and can be used to provide an early warning to dendritic growth in a molten salt reprocessing system.

7.5 Conclusions and Further Work

In this chapter the electrochemical behaviour of deposition at a liquid metal cathode has been studied to identify potential diagnostic signals that can be used to identify when dendritic growth is taking place in a molten salt reprocessing system.

Lanthanum was investigated as it readily forms an alloy in the desired process for enhanced recovery from a molten salt at a liquid cathode. The use of liquid cathodes in the molten salt reprocessing systems is desirable as the reduction potentials of actinides and lanthanides is shifted positive at liquid electrodes when compared to solid inert electrodes[25]. Furthermore, the reduction potentials of actinides and lanthanides are compressed, increasing the efficiency of concurrent actinide and lanthanide recovery by electrolysis. Lanthanum was seen to form a stable alloy with the liquid bismuth metal, and was reduced at the liquid cathode at a more positive potential than at a solid tungsten electrode.

During the deposition of La at the bismuth cathode, it was possible to saturate the Bi-LKE interface with the $LaBi_2$ alloy, blocking further alloying from taking place, and promoting solid growth at the cathode surface. During the reprocessing of spent fuel in a molten salt this could be avoided through mechanical stirring of the liquid metal, however it is necessary to know when this saturation point is being reached so that mechanical stirring, or another mitigating step can be taken. A diagnostic rate change of deposition, and fluctuating current during reduction has been identified for indicating when this limit is reached.

Future work should focus on using these indicators to determine the factors which influence the rate at which the saturation limit is reached; investigate how the deposition rate could be controlled to avoid saturation; and be used to determine the ideal conditions for mechanical stirring of the liquid metal.

By investigating the behaviour of iron deposition at the liquid bismuth cathode, it was possible to confirm that the indicators of dendritic growth that had been identified in the deposition of copper dendrites at a mercury cathode. These indicators include period of steady current followed by an erratic, "noisy" but continually rising current, with sudden drops in current when dendrites detached from the electrode, and a measurable decrease in the solution resistance.

As solution resistance is typically fixed in a given solution for a given electrode area and fixed distance between electrodes, the drop in solution resistance is indicative of either an increased electrode area, a reduced distance between the working electrode and the reference electrode, or both. When dendrites form, they grow outwardly from the electrode surface, which increases the electrode area, and usually decreases the distance between the working electrode and the reference electrode.

Having identified that a reduction in the solution resistance at a liquid cathode is a diagnostic indicator of dendritic growth in a molten salt, further work should look to identify how geometric arrangement of the electrodes could promote an early indication of dendritic growth.

7.6 References

1. S. V. Volkov, *Chem. Soc. Rev.*, 1990, **19**,21-28
2. J.P. Ackerman, J.L. Settle, *J. Alloys Comp.*, 1993, **199**, 77
3. J.P. Ackerman, *Ind. Eng. Chem. Res.*, 1991, **30**, 141
4. European Restriction of Hazardous Substances directive, www.eur-lex.europa.eu, L37, 13 February 2003, pp. 19–23
5. R. C. Paule, J. Mandel, *Pure Appl. Chem.*, 1972, **31** (3), 395-432
6. A.K Fischer, *J. Chem. Phys.*, 1966, **45**, 375
7. W. Gasior, Z. Moser, W Zakulski, *Arch. Metall.*, 1994, **39**, 355-369
8. A. S. Basin, A. B. Kaplun, A. B. Meshalkin, N. F. Uvarov, *Russian Journal of Inorganic Chemistry*, 2008, **53** (9), 1509-1511
9. K.A. Gschneidner Jr., F.W. Calderwood, *Binary Alloy Phase Diagrams*, II Ed., 1990, **1**, 754-756
10. P. Masset, R. J. M. Konings, R. Malmbeck, J. Serp, J-P. Glatz, *Journal of Nuclear Materials*, 2005, **344**, (1–3), 173–179

11. I. N. Ganiev, A. D. Shamsiddinov, K. M. Nazarov, M. D. Badalov, *Metally*, 1996, **4**, 163-167 (in Russian)
12. J. Serp, P. Lefebvre, R. Malmbeck, J. Rebizant, P. Vallet, J.-P. Glat, *Journal of Nuclear Materials*, 2005, **340**, (2–3), 266–270
13. L. Andrieux, G. Weiss, *Comptes Rendu*, 1944, **217**, 615
14. S. Ziolkiewitcz, *Comptes Rendu*, 1958, **247**, 1604
15. S. Ziolkiewitcz and A. Rimsky, *Comptes Rendu*, 1958, **247**, 1727
16. C. Goillot and S. Ziolkiewitcz, *Comptes Rendu*, 1961, **252**, 879
17. A. B. Suchkov, T. N. Ermakova, V. B. Akimenko, *Powder Metallurgy*, 1968, **6**, 1
18. T. N. Ermakova, A. B. Suchkov, V. B. Akimenko, *USSR Proc. Acad. Sci. Metals*, 1968, **6**, 63
19. A. B. Suchkov, T. N. Ermakova, Z. A. Tubyshkina, A. L. Sozina and B. F. Kovalev, *USSR Authors Certificate, No. 323463*, 1972, C 22d 1/24
20. A. B. Suchkov, T. N. Ermakova, L. V. Ryumina, Z. A. Tubyshkina, *Metallurgiya*, 1974, **1**, 148
21. A. I. Demidov, I. A. Simikov, A. G. Morachevskii, A. V. Klevtsov, *Russ. J. Appl. Chem.*, 1987, **60**, 948
22. G. M. Haarberg, E. Kvalheim, S. Rolseth, T. Murakamic, S. Pietrzykd, S. Wange, *ECS Transactions*, 2007, **3**(35), 341-345
23. D. Boa, S. Hassam, G. Kra, K. P. Kotchi, J. Rogez, *CALPHAD: Comput. Coupling Phase Diagrams Thermochem.*, 2008, **32**, 227-239
24. J. Sangster, C. W. Bale, *Binary Alloy Phase Diagrams*, II Ed., 1990, **2**, 1718-1720
25. Y. Sakamura, T. Inoue, O. Shirai, T. Iwai, Y. Arai, Y. Suzuki, *GLOBAL 99*, 1999, Jackson Hole, USA.

8 Conclusions and Further Work

This work has investigated a number of advancements in using liquid metals as cathodes in molten salts. These developments are crucial in the research, design and implementation of a molten salt reprocessing system for the separation and recovery of spent nuclear fuel and enabling a closed loop fuel cycle.

This work addresses three key issues to be overcome in the development of reprocessing spent fuel in a molten salt refiner, namely:

- Significantly, how dendritic growth at liquid cathodes can be detected through the electrochemical response during deposition.
- How molten salts can be prepared through electrolysis of water instead of using reactive gasses to prevent an oxidising or reducing environment and record accurate, reliable electrochemical measurements.
- The wetting behaviour of LKE of metals and other semi-conductor materials that can be used to develop microelectrodes suitable for online analysis.

Initially this work focussed on progressing previous work on ambient condition liquid cathodes in aqueous solutions as analogue systems for liquid metal cathodes in high temperature molten salts. Efforts then focussed on developing the molten salt experimental system, tools and associated methodologies before testing liquid cathodes in a molten salt. These liquid cathodes were then used measure the deposition of alloying species and dendritic growth at a liquid cathode for comparison to the aqueous experiments.

In Chapter 4 an aqueous liquid cathode system was studied as an analogue to the liquid cathode in a molten salt reprocessing system to avoid the technological complications of such systems at elevated temperatures and sealed atmospheres.

The deposition of zinc at a liquid metal cathode constructed from a large mercury pool was used to investigate the mechanism for deposition and amalgamation of species that are expected to alloy readily with the liquid electrode in the molten salt process.

The zinc was first observed to undergo a diffusion-limited reduction at the metal surface, where the rate of diffusion of zinc into the bulk mercury controlled the reaction rate. Upon re-oxidation of the zinc, the current initially followed a rate-limited diffusion curve as the zinc

diffused out of the liquid mercury and away from the electrode. This diffusion was truncated, as the zinc had only diffused part way into the electrode, and not fully throughout the whole bulk of the mercury.

Whilst it was not possible to get a good fit of the current-time curve to the bounded Cottrell equation, this confirms that the rate of reaction is governed by the diffusion of zinc in the liquid mercury, rather than zinc in the aqueous solution. Future work should investigate this effect, including considerations of whether the Fick's law derived Cottrell equation is the appropriate equation for fitting, or whether modification is required to model the diffusion in the liquid cathode as well as in the diffusion double layer. Future work should also investigate the fundamental principles of diffusion of an alloyed species in a liquid electrode and the influence of mechanical stirring on species reduction and subsequent alloy formation.

Copper was also reduced at a liquid mercury cathode, and the formation of dendrites observed both optically and electrochemically. Diagnostic behaviour for the formation of dendrites was identified in correlation with the visual inspection of dendrite growth, so that a method of electrochemically detecting when dendrites form can be developed.

This is an important characteristic when operating a molten salt system with a liquid cathode, as it will not be reasonably practicable to visually monitor the electrode surface for dendritic growth.

The reduction of zinc and copper at micro-scale liquid electrodes was then investigated to support the development of sensors for detecting dendritic growth in a molten salt reprocessing system.

With zinc, it was possible to drive the reduction of zinc to the point that a solid alloy was formed between the zinc and the mercury. Whilst dendrites were not observed to grow from the electrode surface, the growth of a solid crust over a liquid electrode in a molten salt process is equally damaging, as the required amalgamation will not be achieved and the target species shall plate out as solids. Changes in both the chronoamperometry and EIS spectra were highlighted as being distinctive for the formation of a solid reduction product, and are proposed as characteristic indicators for solid deposition at a liquid cathode.

The reduction of copper at the liquid microelectrode also resulted in a solid deposition. In this instance dendrites grew extensively from the electrode surface, visibly protruding into the solution. Even when the electrode was removed from the solution, much of the dendrites

remained attached. Chronoamperometry to induce reduction and oxidation of copper on the microelectrode are consistent with observations on macroelectrodes, although the oxidation of copper from the microelectrode appeared to be much more ordered. The reason for why the current response during oxidation is not clear, and should be the subject of future work, along with understanding the destruction of the liquid metal deposited on the underlying micro-square.

The electrochemical impedance spectra recorded during the liquid cathode experiments were not fit to an equivalent circuit, and the raw measurements were used for data analysis and interpretation. Attempts to fit these spectra to simple circuits did not yield meaningful results, with the liquid cathode's electrical response characteristics not appropriately represented by inclusion of a capacitor, resistor or constant phase element in typical circuits. Future work should consider the correct equivalent circuit and appropriate fitting for these measurements, and analyse any subsequent features arising from correctly fitting the data.

Given these observations, there are three clear electrochemical indicators which can be used to indicate when dendritic growth is taking place. These principle indicators are:

1. The rapid increase in current flow as surface area increases significantly due to fern like growth.
2. High frequency fluctuations in current as dendrites mechanically detach and reattach to the electrical circuit.
3. Reduction in the solution resistance measured by EIS, as the concentration of depositing metal at the surface of the liquid increases, and subsequent nucleation of dendritic growth occurs.

Having established the principle indicators for dendritic growth and the formation of alloys at the liquid cathodes under ambient conditions, a molten salt system needed to be developed for comparative experiments in molten salts and validation of the analogue system.

In chapter 5 a method for measuring the wetting of molten salts on surfaces has been developed and benchmarked against known measurements. Differences have been shown between contact angle measurements in controlled atmospheres and when the substrate and molten salt are exposed to air and moisture. The system has been shown to successfully overcome the

problem of oxygen ingress and maintain an anhydrous atmosphere for the molten salt and metal surfaces which could be oxidised in air at elevated temperatures.

Using the measurements recorded during this work, it is possible to make informed choices when designing and fabricating molten salt systems. This includes, but is not limited to the structural and containment components of a reprocessing system, in the fabrication of microelectrode sensors for use in LKE and in auxiliary equipment required to operate the system.

Understanding the interaction between molten salt and these materials is important to build a robust and efficient system, just as the interaction between the construction materials and the liquid metal used for the cathode will be important in corralling the liquid cathode.

Having developed the system to measure the contact angles of molten salts on surfaces at 450 °C, the system should be used to measure the interaction of LKE with wider range of materials, and the influence of surface preparation should be investigated. Crucially these measurements could be used to measure the surface tension of molten salts.

Modifications to the system should also be considered to facilitate the measurement of liquid metal contact angles on these surfaces. These measurements, and investigations into surface treatment effects on the wetting by liquid metals will inform the design of a microelectrode where the liquid electrode can be corralled into a micro-droplet for use as sensing tool in a reprocessing system.

In Chapter 6, the method of electrochemical drying demonstrated offers a number of advantages over the traditional chemical methods employed for drying lithium potassium eutectic. Furthermore, it is anticipated that this drying method may also be suitable for a number of other air and water sensitive molten salts.

The method removes oxygen and water contamination from the salt without creating an oxidizing or reducing environment. The associated electrochemical signatures provide direct monitoring of the dryness of the salt, enabling a diagnosis as to when complete dryness has been achieved. Furthermore, this endpoint is self-limiting, as pulsing *in vacuo* first leads to the overall removal of H_2 and O_2 gas (beneficial drying), whereas further pulsing once dry *in vacuo* overall leads to the oxidation of Cl^- to the stable Cl_5^- and reduction of Li^+ to Li metal,

which simply results in the spontaneous regeneration of LiCl and the retention of a dry LKE which is neither oxidizing nor reducing.

This method has also been shown to remove oxygen and water from the salt in the presence of metal oxides and hydrated redox agents. This eliminates one of the difficulties associated with maintaining a dry and pure melt when adding redox agents to the molten salt following chemical cleaning. The work with tungsten demonstrates the concomitant removal of surface oxides and the work with hydrated redox agents demonstrates the removal of solution based oxides and hydroxides. These aqueous contaminants are then removed from the system as oxygen and hydrogen gases.

The concomitant removal of surface oxides on liquid cathodes has also been observed, and should be investigated further to establish a quantitative relationship between the electrode area, oxide thickness and oxidation current required to prepare the liquid surface for use.

Together, these results make this method of real value in the production and monitoring of rigorously dry and oxide free LKE. Future work should focus on quantitatively confirming the relationship between the characteristic response of oxygen and hydrogen such that an accurate tool for monitoring the contamination of molten salts with water and oxygen can be developed. Such a tool would be advantageous in a reprocessing system to understand when the oxygen and/or water contamination may disrupt the process and when salt may need to be electrochemically dried.

In chapter 7 the electrochemical behaviour of deposition at a liquid metal cathode has been studied in electrochemically dried LKE to validate the diagnostic signals established in Chapter 4 to identify when dendritic growth is taking place in a molten salt reprocessing system.

Lanthanum was investigated as it readily forms an alloy in the desired process for enhanced recovery from a molten salt at a liquid cathode. During the deposition of La at the bismuth cathode, it was possible to saturate the Bi-LKE interface with the $LaBi_2$ alloy, blocking further alloying from taking place, and promoting solid growth at the cathode surface.

During the reprocessing of spent fuel in a molten salt blocking of the electrode surface through solid alloy formation could be avoided through mechanical stirring of the liquid metal. For this to be implemented it is necessary to know when this saturation point is being reached so that mechanical stirring, or another mitigating step can be taken. A diagnostic rate change of

deposition, and fluctuating current during reduction has been identified for indicating when this limit is reached.

Future work should focus on using these indicators to determine the factors which influence the rate at which the saturation limit is reached; investigate how the deposition rate could be controlled to avoid saturation; and be used to determine the ideal conditions for mechanical stirring of the liquid metal.

By investigating the behaviour of iron deposition at the liquid bismuth cathode, it was possible to confirm the indicators of dendritic growth that had been identified in Chapter 4. These indicators include period of steady current followed by an erratic, "noisy" but continually rising current, with sudden drops in current when dendrites detached from the electrode, and a measurable decrease in the solution resistance.

Having identified that a reduction in the solution resistance at a liquid cathode is a diagnostic indicator of dendritic growth in a molten salt, further work should look to identify how geometric arrangement of the electrodes could promote an early indication of dendritic growth.

Throughout this work, the emphasis has been to develop the use of liquid metal cathodes in a molten salt to facilitate the recovery of fission products in a spent fuel reprocessing system. By identifying key indicators of when such a system may or may not be functioning correctly, this work has developed the tools for fundamental investigation into electrodeposition at liquid cathodes in molten salts. These tools are:

- An electrochemical method for *in-situ* drying of a molten salt including the removal of oxides and hydrates arising from redox agents and native oxides on metals. This is of particular use, as the methodology can be used to restore a system after an exposure event, as well as in the initial preparation.
- A potential electrochemical method for identifying the alloying of species deposition at a liquid electrode.
- A comparison of electrochemical and optical observations of dendritic growth at a liquid cathode in both aqueous and molten salt systems.
- A method for measuring the static contact angle of molten salts on selected surfaces at 450 °C in a controlled atmosphere.
- An enhanced understanding of how LKE wets on a number of materials used in the fabrication of a molten salt system and associated tools.

Having developed these tools it is now possible for fundamental measurements of alloying and recovery of fission products to be measured, and accurate sensors for use in reprocessing systems to be characterised. Investigations into how molten salts and liquid metals wet on a range of surfaces are also possible, the results of which can be used to inform the design of the final reprocessing system.